

Measurement and Interpretation of Stable and  
Unstable Alfvén Eigenmodes in the Presence of  
Fast Ions in Alcator C-Mod

by  
Jason A. Sears

B.A.Sc., University of Toronto (2001)  
S.M., Massachusetts Institute of Technology (2003)

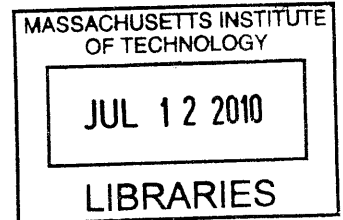
Submitted to the Department of Electrical Engineering and Computer  
Science

in partial fulfillment of the requirements for the degree of  
Doctor of Philosophy in Applied Plasma Physics  
at the

MASSACHUSETTS INSTITUTE OF TECHNOLOGY

June 2010

© Massachusetts Institute of Technology 2010. All rights reserved.



**ARCHIVES**

Author .....  
Department of Electrical Engineering and Computer Science  
May 11, 2010

Certified by .....  
R. R. Parker  
Professor, Department of Nuclear Science and Engineering and  
Department of Electrical Engineering and Computer Science  
Thesis Supervisor

Certified by ...  
J. A. Snipes  
Senior Scientific Officer Integrated Scenarios, ITER Organization  
Thesis Supervisor

Accepted by .....  
Terry P. Orlando  
Chairman, Department Committee on Graduate Students

# Measurement and Interpretation of Stable and Unstable Alfvén Eigenmodes in the Presence of Fast Ions in Alcator C-Mod

by

Jason A. Sears

Submitted to the Department of Electrical Engineering and Computer Science  
on May 11, 2010, in partial fulfillment of the  
requirements for the degree of  
Doctor of Philosophy in Applied Plasma Physics

## Abstract

The stability of two types of lightly damped resonant eigenmodes in the presence of energetic ions is studied in Alcator C-Mod. Global Alfvén eigenmodes (GAEs) can exist at frequencies between the continua of adjacent poloidal mode numbers to avoid strong continuum damping. Toroidicity-induced Alfvén eigenmodes (TAEs) exist in gaps in the frequency continuum induced by toroidal coupling. Passing and trapped fast ions can resonantly excite AEs, which saturate at significant amplitude and redistribute the ions. There is evidence that consequent losses of D-T alpha particles could degrade the fusion burn. Unstable TAEs driven by ICRF-heated fast ions are observed in Alcator C-Mod with toroidal mode numbers of  $n = -4$  and  $n = 6$ . Positive mode numbers indicate that modes are driven by fast ions having hollow pressure profiles, in agreement with measurements using the Compact Neutral Particle Analyzer (CNPA). In the absence of sufficient fast ion drive, eigenmodes are detected by exciting them with antennas close to the plasma boundary and monitoring the plasma frequency response with an array of magnetic probes, a method called active MHD excitation. This thesis reports for the first time that TAEs of various toroidal mode numbers are excited with a wide-toroidal-spectrum antenna and observed using a fully resolved toroidal array of probes. GAEs with  $n = 0$  and damping rates around  $\gamma/\omega_0 = -1\%$ , and TAEs with  $n = 1$  and damping rates around  $\gamma/\omega_0 = -1.5\%$  are observed. Rigorous calibration is applied to the magnetic probes to reject the system response of the diagnostic. Measurements demonstrate that even with a wide-spectrum antenna, the range of AEs that are accessible to the diagnostic for any particular equilibrium remains quite limited, subject to the modes' proximity to the plasma edge. A composite spectrum of observed stable and unstable modes, and the stability spectrum calculated by NOVA-K, shows that for fast ions with approximately 150 keV effective temperature, the most unstable mode number tends to be around  $n = -5$ . In comparison, the simple scaling of fast ion drive for  $k_{\theta}\rho_i \approx 1$  predicts unstable modes around  $n = -8$ , demonstrating reasonable agreement with

the measurements. Local islands of stability that are observed in the toroidal mode number spectrum and the fast ion temperature could be exploited by the strong dependence of the AE spectrum on subtle changes in equilibrium parameters to stabilize AEs in burning plasmas.

Thesis Supervisor: R. R. Parker

Title: Professor, Department of Nuclear Science and Engineering and  
Department of Electrical Engineering and Computer Science

Thesis Supervisor: J. A. Snipes

Title: Senior Scientific Officer Integrated Scenarios, ITER Organization

## Acknowledgments

I am indebted to Professor Ron Parker for his patience and insight throughout this work. His experience with the many aspects of tokamak research is greatly appreciated. Professor Parker's unwavering standards have contributed immeasurably to my development as a scientist and as a person. I am also thankful for all the knowledge that Dr. Joseph Snipes shared with me, and the support he offered, as we worked together to develop this experiment. Professor Jeffrey Freidberg helped me to understand Alfvén eigenmodes and other curious MHD phenomena that represent my greatest attraction to plasma studies, in class and in discussions outside of the classroom. I also thank Professor Jeff Lang for his guidance as a member of my thesis committee and for his inspiring role as an instructor in several courses.

I thank Dr. Gerrit Kramer for his willingness to teach me about the NOVA-K code and to share his experience in the field of Alfvén eigenmodes. Discussions with Gerrit are always a pleasure.

I am also grateful for the group of scientists that I have had the chance to work with at C-Mod, including Catherine Fiore, Bob Granetz, Martin Greenwald, Amanda Hubbard, Jerry Hughes, Jim Irby, Brian Labombard, Yijun Lin, Earl Marmor, Miklos Porkolab, John Rice, Bill Rowan, Steve Scott, Jim Terry, Steve Wolfe and Steve Wukitch.

The Alcator C-Mod experiment would not be possible without the support of the engineers and technicians that are responsible for bringing it to life, including the guys in the machine shop, Ed Fitzgerald, Mark Iverson, Bob Silvia, Bill Keating, Charlie Cauley; help from Bill Parkin, Dave Bellofatto, Maria Silveira in the electronics shop; Bob Childs, Tom Toland and Ron Rosati in the vacuum shop; Gary Dekow, Sam Pierson and Rui Vieira on matters concerning the vessel; Josh Stillerman, Brandon Savage, Felix Kreisel, Henry Bergler and Mark London who kept the computers alive; William Burke and Bill Cochran, who built the amplifiers and DC power supplies; and Corrinne Fogg and Jessica Coco for being the glue to hold it all together.

I appreciate the camaraderie that I have shared with fellow graduate students over

the years. My office mates have always been the first to hear any complaints, so I thank Natalia Krasheninnikova, Vincent Tang, Jin Seok Ko, and Liang Lin for their patience. Eric Edlund has always been ready for a rousing discussion, philosophical or otherwise. I have quite enjoyed the opportunity to work closely with Aaron Bader on the CNPA, and with Ted Golfinopoulos on the active MHD experiment. I enjoyed the tradition of rooming with Alex Boxer at the annual APS conference. I appreciate all the conversations over the years with Harold Barnard, Brock Bose, Antoine Cerfon, Istvan Cziegler, Arturo Dominguez, Jennifer Ellsworth, Ian Faust, Marco Ferrera, Will Fox, Mike Garrett, Tim Graves, Zach Hartwig, Alex Ince-Cushman, Grigory Kagan, Istak Karim, Noam Katz, Alex Klein, Ari Le, John Liptac, Ken Marr, Roark Marsh, Rachael McDermott, Orso Meneghini, Bob Mumgaard, Roman Ochoukov, Geoff Olynyk, Alex Parisot, Leonardo Patacchini, Yuri Podpaly, Matt Reinke, Noah Smick, Andrea Schmidt, Balint Veto, Greg Wallace and Howard Yuh.

I have enjoyed the singular company of my MIT Cycling teammates. It has been a privilege to share hardship and triumph with them, most especially with Caitlin Bever.

Finally I would like to thank my grandparents, my parents and my sister Karli for their encouragement along the way. The unconditional love from my parents and their continuous support, at any time of the day, has made this possible.

# Contents

<b>1</b>	<b>Introduction</b>	<b>10</b>
<b>2</b>	<b>Background</b>	<b>16</b>
2.1	Introduction . . . . .	16
2.2	Alfvén Eigenmodes . . . . .	18
2.2.1	The Ideal MHD Model . . . . .	18
2.2.2	Normal Modes of Ideal MHD . . . . .	21
2.2.3	MHD Waves in the Homogeneous Plasma . . . . .	23
2.2.4	Inhomogeneous Slab . . . . .	29
2.2.5	Cylindrical Geometry . . . . .	35
2.2.6	Toroidal Geometry . . . . .	41
2.2.7	Damping of the TAE . . . . .	48
2.2.8	Drive of the TAE . . . . .	49
2.3	Consequences of TAEs . . . . .	53
2.4	Experiment . . . . .	53
2.4.1	Computer Models . . . . .	57
2.4.2	Passive TAE Measurements . . . . .	57
2.4.3	Active MHD Excitation and Measurement . . . . .	58
2.4.4	Active MHD on JET . . . . .	59
2.4.5	Active MHD on Alcator C-Mod . . . . .	60
<b>3</b>	<b>The Active MHD Diagnostic</b>	<b>62</b>
3.1	Principle of Operation and System Overview . . . . .	63

3.2	Excitation . . . . .	64
3.2.1	Amplifiers . . . . .	64
3.2.2	Antennas . . . . .	67
3.2.3	Filters . . . . .	71
3.3	Detection . . . . .	74
3.3.1	Pickup Coil System . . . . .	74
<b>4</b>	<b>Analysis</b>	<b>79</b>
4.1	Signal Processing to obtain the System Response . . . . .	79
4.1.1	Synchronous Detection . . . . .	83
4.1.2	Properties of $H(s)$ . . . . .	85
4.1.3	Parametric Fitting of the System Function $H(s)$ . . . . .	87
4.2	Compensation . . . . .	91
4.2.1	Compensating for Normal Non-Ideal Effects . . . . .	99
4.2.2	Compensating for Pathological Non-Ideal Effects . . . . .	119
4.2.3	Discriminating Plasma Resonances from other Processes . . . . .	125
4.2.4	Conclusion to Equipment . . . . .	130
<b>5</b>	<b>Results</b>	<b>132</b>
5.1	2008 ensemble . . . . .	135
5.1.1	Toroidal mode $n = 0$ . . . . .	142
5.1.2	Frequency . . . . .	144
5.1.3	Damping rate . . . . .	146
5.2	2006 ensemble . . . . .	150
5.3	2007 ensemble . . . . .	152
5.4	Unstable mode observations . . . . .	163
5.5	Conclusion . . . . .	166
<b>6</b>	<b>Summary &amp; Conclusions</b>	<b>168</b>
6.1	Diagnostic Contributions . . . . .	168
6.2	Summary of Observations . . . . .	170

6.3	Conclusions . . . . .	171
6.4	Future Work . . . . .	173
<b>A</b>	<b>Error Analysis</b>	<b>176</b>
A.1	Uncertainty in the system response . . . . .	177
A.1.1	Characterizing the signal and noise . . . . .	179
A.1.2	Quantifying the uncertainty in the system response . . . . .	187
A.2	Propagation of error to quantities of interest . . . . .	196
A.2.1	Confidence interval of polynomial coefficients . . . . .	196
A.2.2	Confidence interval of resonance parameters . . . . .	197
A.2.3	Significance of the toroidal mode number fit . . . . .	198
<b>B</b>	<b>Calibration of Pickup Coils</b>	<b>201</b>
<b>C</b>	<b>Test Shot Procedure</b>	<b>207</b>
	<b>References</b>	<b>209</b>



Each day begins clean and promising in the sweet cool clear green light of dawn. And then the sun appears, its hydrogen cauldrons brimming - so to speak - with plasmic fires, and the tyranny of its day begins.

Edward Abbey, *The Dead Man at Grandview Point*

I conclude, therefore, that this star is not some kind of comet or a fiery meteor, but that it is a star shining in the firmament itself one that has never previously been seen before our time, in any age since the beginning of the world.

Tycho Brahe

# Chapter 1

## Introduction

The fusion of a deuterium nucleus and a tritium nucleus releases a neutron of 14.1 MeV and a helium nucleus (alpha particle) of 3.5 MeV. In bulk, and at a rapid rate, this reaction and others involving those constituents (such as D-D and so on) are a promising source for electric power generation. The required pressures and temperatures to attain an appreciable reaction cross-section inevitably lead the deuterium and tritium fuels to be in the plasma state. The tokamak is one well developed concept to contain a hot, dense plasma for long periods. This thesis reports on experiments performed on deuterium plasmas with minority fractions of hydrogen in the Alcator C-Mod tokamak at MIT.

It has been observed at C-Mod and other toroidal devices that fast ions with energies around 150 keV, produced by heating with ion cyclotron range of frequency (ICRF) heating, can excite lightly damped magnetohydrodynamic Alfvénic eigenmodes (AEs) of the plasma volume. At large amplitudes, the unstable modes saturate and displace the fast particles in configuration as well as phase space. Fast ions born from other means of heating, such as energetic neutral beams or fusion reactions, are equally capable of driving the modes; in C-Mod, the available non-inductive methods of heating are ICRF and lower-hybrid drive.

The redistribution of fast ions by unstable AEs is a legitimate concern for fusion reactors. Direct observations of significant fast ion losses in synchronization with AEs have been reported [1], as well as indirect evidence based on reduced neutron

rate [2] and vessel damage [3]. When multiple unstable modes at different minor radii occur together, they can cause significant degradation of the fast ion pressure. Ultimately, this reduces the fusion burn and is a hurdle on the way to ignition. A complete understanding of AE dependence on plasma parameters can help to mitigate their deleterious effects and even to harness their impact on transport for controlling plasma composition.

Each Alfvén eigenmode has an integer toroidal mode number and comprises a spectrum of poloidal modes, so that individual eigenmodes can be conveniently labelled by their toroidal mode number,  $n$ . Dependence on many of the parameters that contribute to AE damping and also excitation have been studied empirically and theoretically, as reported in the literature, and always with toroidal mode number as an important parameter. Experimental evidence typically takes two forms: firstly, that of unstable modes that appear spontaneously with sufficient fast ion drive; and secondly, of stable modes enunciated by external antennas, as a means to evaluate the eigenmode spectrum. This second method of inspecting the stable mode spectrum is called active MHD excitation.

Both experimental [4] and theoretical [5] studies find that instability peaks approximately when the fast particle orbit is on the order of the wavelength, or  $k_\theta \rho_i \approx 1$ , where  $k_\theta$  is the perpendicular wavevector and  $\rho_i$  is the fast ion gyroradius. (For large  $k_\theta \rho_i$ , the wave-particle interaction is weakened because the orbit is large compared to the wavelength. At small  $k_\theta \rho_i$ , the interaction increases linearly with  $k_\theta \rho_i$  as more fast ions contribute.) It is also generally agreed that the particular modes that come to be expressed in a given equilibrium, and their effects on the fast ion distribution, are sensitively dependent on the equilibrium profiles [6].

Therefore one goal of AE studies is to demonstrate the full AE spectrum for a particular equilibrium. As one example, the code NOVA-K calculates the plasma equilibrium and then finds each mode perturbatively, with the assumption that the modes are independent, and the existence and behavior of every mode of the spectrum can be evaluated one at a time [7]. Similarly, active MHD studies attempt to excite each mode in the toroidal spectrum by sweeping across the relevant band of

frequencies. Doing so assumes linearity, since each mode is excited individually, yet the spectrum is considered as a whole.

To date, though, no experimental observations have covered the entire practical AE spectrum simultaneously. Observations of spontaneous, fast-ion driven modes report only the most unstable of modes, which tend to have moderate toroidal mode numbers. Active MHD experiments, on the other hand, have identified modes over a small range for each plasma shot. On the JET tokamak, this had originally been in the range  $|n| = 0 - 2$  because the active MHD antenna on JET had a narrow toroidal spectrum on account of the antenna geometry; a new antenna has been installed with a broader spectrum [8]. On C-Mod, single modes of moderate toroidal mode number have been observed from shot to shot, occasionally with unstable, moderate- $n$  modes also observed.

In other words, the existing experimental picture of AE behavior is piecemeal. What is lacking is the experimental counterpart to a self-consistent, full-spectrum model of AEs' impact on the fast ion distribution, and the resulting, modified fast ion distribution's effect on the mode spectrum. Partly as a result, there is no final word on whether next-generation fusion reactors will be threatened by AEs.

This thesis examines an important factor in the threat of AEs, namely the stability dependence of a wide- $n$  spectrum (eg  $|n| = 0 - 10$ ) on the fast ion temperature  $T_{fast}$  and distribution  $f_{fast}(r, v)$ . Motivated by analytical theory [5], [4], numerical studies [9] and pioneering experiments [10], [11], [12] that find the mode instability to be peaked for moderate- $n$ , this research seeks inflections in the stability of the spectrum that could be exploited to preserve or modify the fast ion distribution.

While it does not provide a conclusive answer with regard to the ultimate risk of AEs, such knowledge could be useful to attenuate or eliminate particular modes, or to enhance benign modes for purposes of ash removal. The mode control could be effected by precisely shifting any of the equilibrium profiles of safety factor, density, rotation and current, as well as the plasma shape and effective ion mass, all of which strongly influence the AE spectrum.

The experiment is based around the active MHD system of two antennas posi-

tioned very near the last closed flux surface, that excite eigenmodes of the plasma, and an array of magnetic probes that detect the plasma response. The antenna frequency is scanned over the range of eigenmode frequencies to manifest the plasma frequency response and thereby obtain the mode stability, toroidal structure and resonant frequency. Simultaneously, the fast ion distribution is tailored by varying the ICRF coupled power up to approximately 5.5 MW, as well as shifting the resonant deposition layer by adjusting the toroidal magnetic field. The compact neutral particle analyzer (CNPA) measures the ICRF-generated fast ion distribution along three vertical chords. The CNPA's silicon diodes detect core ions that have escaped confinement by gaining an electron in a charge exchange collision with the diagnostic neutral beam.

Over the course of several run campaigns toroidicity-induced Alfvén eigenmodes (TAEs) having toroidal mode numbers of  $n = 1$  and also of moderate  $n$ , and global Alfvén eigenmodes (GAEs) having  $n = 0$  are observed routinely. It is found that the coupling of the active MHD antenna to AEs is strongly dependent on the equilibrium. Modes are observed for the most part only in select equilibria that are used on dedicated rundays, and the modes are found in isolation rather than as a whole spectrum. The system performance was improved by augmenting the toroidal array of probes for better toroidal resolution; and by activating only one of the two antennas to disambiguate the system input. A confident identification of the mode number is achieved by a careful calibration of the magnetic probe response. Since the  $n = 1$  TAEs were only observed in Ohmic conditions, and since  $n = 0$  GAEs do not couple to fast ions, no experimental data is obtained for the interaction of fast ions with stable modes. The damping rate resolution for these modes is found to be strongly degraded by density fluctuations of the plasma.

On the other hand, unstable modes excited by fast ions are also observed in the same shots, and have  $n = -4$  and  $n = 6$ . Positive unstable mode numbers are indicative of a hollow fast ion pressure profile. Furthermore, the NOVA-K code is used to estimate the interaction of fast ions with the measured stable modes and finds reasonable agreement (ie very little excitation for  $n = 0, 1$ ).

A composite spectrum is rendered from the collection of stable and unstable mode observations, and the NOVA-K calculations. This patchwork spectrum displays peaked instability at moderate mode numbers around  $|n| = 5$ . In comparison,  $k_{\theta}\rho_i$  is found to be around  $8^{-1}n$  for protons of 150 keV, indicating the most unstable modes should be around  $|n| = 8$ . Considering the simplicity of that scaling, the agreement is good.

Notably, this experiment has for the first time excited TAEs of various toroidal mode number with a wide-toroidal-spectrum antenna and a fully resolved toroidal array of probes. Measurements demonstrate that even with a wide-spectrum antenna, the range of AEs that are accessible to the diagnostic for any particular equilibrium remains quite limited. In fact, only in an unconnected subset of plasma conditions are modes observable at all. AE behavior is found to be discontinuous across parameter space, so that slightly tweaking a profile can lead to a completely different mode being observed.

The most severe discontinuity arises between stable, linear modes and the necessarily non-linear (saturated) unstable modes. In the unstable regime, the fast ion pressure gradient is modified by the competing actions of recharging by the heating source and depletion by the excited waves; in turn, the destabilized waves also evolve. This interdependency is apparent as a transition of the resonant modes to a modified steady state or as chaotic bursting behavior of multiple, interacting AEs [13], [14]. The linear, stable regime of active MHD, however, does not perturb the fast ion distribution, so the associated observations are not easily extended to predict the amplitude of unstable modes (let alone their specific impact on burning plasmas). Nonetheless, measurements with active MHD can be regarded as initial conditions for the evolution of the instability; and relevant scalings of net damping rate with fast ion temperature, toroidal mode number and plasma shape are achieved by active MHD excitation in this thesis.

The active MHD system is also found to be useful for MHD spectroscopy, in which plasma conditions are deduced from mode behavior. For example, it is found that correlated variations in the mode residue and damping rate indicate otherwise

unmeasured density fluctuations. As another example, the amplitude profile among the toroidal set of probes is correlated with the gap between the plasma and the vessel, and possibly with triangularity and edge shear. While active MHD cannot provide a definitive conclusion as to the threat that AEs pose for burning plasmas, it is still a very useful tool.

The sections of this thesis are as follows. First, background on the physics of AEs and the experimental history is discussed. Then the active MHD diagnostic is described in detail, including the data analysis and compensation methods. Next, results from the 2006, 2007 and 2008 campaigns are presented. Finally, the results are discussed and suggestions for future work given. The appendices contain a thorough example of error analysis, a description of the probe calibration method, and instructions for setting up the diagnostic for operation.

# Chapter 2

## Background

### 2.1 Introduction

Alfvén eigenmodes are global resonant modes of magnetohydrodynamic waves in laboratory plasmas. The eigenmodes exist at discrete frequencies well below the ion cyclotron frequency and are lightly dissipated by mode conversion, radiative damping, electron and ion Landau damping, and coupling to the shear Alfvén frequency continuum. Energetic ions from neutral beams and ICRF heating, and alpha particles from the fusion reaction can act to damp or excite the eigenmodes. When the energetic ion excitation exceeds the combined sources of damping, the eigenmodes appear spontaneously and grow to large, saturated amplitudes. The saturated modes in turn redistribute the energetic ions in velocity and configuration space, degrading the energy confinement of the plasma. The scope of this thesis is restricted to Alfvén eigenmode behavior in tokamaks.

Experiments [15] and numerical calculations [16] have indeed confirmed that energetic particle confinement in tokamaks can be reduced during Alfvén eigenmode activity. This presents a valid concern for burning plasmas such as ITER, where energetic alpha particles that can excite Alfvén eigenmodes will be abundant. Enhanced transport of the alpha particles could reduce the alpha thermalization on core DT fuel, suppressing the fusion burn; and it could increase the thermal load on the reactor vessel wall, causing catastrophic damage to the blanket modules.



The radial structure of the displacement and magnetic field perturbations of the Alfvén eigenmodes, and their damping rate and resonant frequency, are sensitive to the mass density and magnetic pitch angle profiles of the plasma [6]. The mode interaction with energetic ions is further dependent on the ion phase-space distribution. Consequently the severity of Alfvén eigenmode activity is subject to the particulars of the plasma configuration. The central focus of this thesis is to obtain an empirical understanding of this dependency, to enable the prediction and mitigation of Alfvén eigenmode effects.

One way to experimentally interrogate the discrete spectrum of Alfvén eigenmodes is to energize the modes with an external antenna below the onset of energetic particle excitation, and to observe the resultant plasma response with magnetic probes arrayed around the periphery of the discharge. Resonant frequency and net damping rate are apparent from the plasma frequency response extracted from the cross-spectral density function of the antenna current and probe voltages. Toroidal and poloidal mode structure can also be reconstructed from probe signals, although caution must be exercised when interpreting mode localization in the interior of the plasma from strictly external measurements. This diagnostic approach is called active MHD [17]. A detailed description of the active MHD instrumentation that was designed and used in Alcator for the research in this thesis is reserved for the next chapter.

This chapter presents a comprehensive summary of the literature with a threefold purpose. First, it introduces the physical mechanisms of the Alfvén eigenmodes and their interactions with the energetic ions in a tokamak plasma. Secondly, it describes how this joint behavior can enhance the transport of energetic ions, prematurely removing energy from the plasma core. For this reason, Alfvén eigenmodes could represent an important factor in the performance of next generation machines such as ITER. Finally, an account is given of relevant prior experimental work on Alcator and other tokamaks concerning Alfvén eigenmode stability and interaction with energetic ions. The sections of this chapter are roughly divided on the same basis.

Development of Alfvén eigenmode theory and experiment spans more than sixty years since electrical engineer and recipient of the 1970 Nobel Prize in Physics, Hannes

Alfvén, postulated the hydromagnetic wave in 1942 [18]. Throughout that period of incremental maturation (which continues still), important observations were made that remain relevant even though the complete picture has since been refined. For example, the redistribution of energetic ions by saturated AEs was investigated experimentally before the damping mechanisms of AEs were very well understood. While studying the literature, then, it is often illuminating to understand not only the present status of the field, but also the thinking that pervaded at the time of writing. Therefore figure 2-1 presents a graphical timeline of the history of Alfvén eigenmode research. At each key development, the timeline lists a seminal paper that appears to have brought the concept to the attention of the broader community. A comprehensive list of references is given in the bibliography and cited throughout this chapter.

## 2.2 Alfvén Eigenmodes

### 2.2.1 The Ideal MHD Model

The scale of MHD behavior is defined relative to the macroscopic quantities of the plasma minor radius,  $L \approx a$ , and the ion thermal speed,  $u \approx v_{Ti}$ , the fastest single-fluid macroscopic motion possible. The corresponding time scale is the ion thermal transit time of the volume of interest,  $\tau \approx a/v_{Ti}$ . With a substantial magnetic field, the ion cyclotron periods and gyroradii are small enough to be averaged over.

Likewise, other phenomena with periods below the ion thermal transit time and motions with shorter characteristic length than the ion gyroradius are for the most part decoupled from MHD and can be ignored. Therefore several simplifying approximations can be made that restrict our attention to the scales of interest [19].

1. since the MHD frequency is very much smaller than the electron cyclotron and plasma frequencies, the electron inertia can be neglected
2. the Debye length is very small, so the plasma is quasi-neutral.

<b>Topic</b>	<b>Year</b>	<b>Paper</b>
MHD waves	1942	<b>Alfvén H.</b> , Nature 150
Continuous Alfvén spectrum in inhomogeneous plasma	1964	<b>Uberoi C.</b> , Indian J. Pure App. Physics 2
Resonant absorption of Alfvén waves	1973	<b>Tataronis J.</b> and <b>Grossman W.</b> , Z. Physik 261
Alfvén wave dissipation as a heating mechanism	1974	<b>Hasegawa A.</b> and <b>Chen L.</b> , Phys. Rev. Lett. 32
Gaps in Alfvén spectrum due to toroidicity	1978	<b>Pogutse O.</b> and <b>Yurchenko E.</b> , Nucl. Fusion 18
Global Alfvén eigenmodes (GAE) and discrete Alfvén waves (DAW)	1982	<b>Appert K.</b> et al., Plas. Physics 24
Toroidicity-Induced Alfvén Eigenmodes (TAE)	1985	<b>Cheng C.Z.</b> et al., Ann. Phys. 161
Excitation of TAEs by Energetic ions	1989	<b>Fu G.Y.</b> and <b>Van Dam J.W.</b> , Phys. Fluids B 1
Redistribution of energetic ions by TAEs	1991	<b>Heidbrink W.W.</b> et al., Nucl. Fusion 31
TAE Damping mechanisms	1992	<b>Zonca F.</b> and <b>Chen L.</b> , Phys. Rev. Lett. 68
MHD Spectroscopy of tokamak plasmas	1993	<b>Goedbloed J.P.</b> et al., Plasma Phys. Control. Fusion 35
JET Active MHD	1995	<b>Fasoli A.</b> et al., Phys. Rev. Lett. 75
Review: AEs in toroidal plasmas	1999	<b>Wong K.L.</b> , Plasma Phys. Control. Fusion 41
C-Mod Active MHD	2004	<b>Snipes J.A.</b> et al., Plasma Phys. Control. Fusion 46
Review: Alfvén Instabilities driven by energetic particles	2008	<b>Heidbrink W.W.</b> , Phys. Plasmas 15
MAST Active MHD	2008	<b>Gryaznevich M.P.</b> et al., Nucl. Fusion 48

Figure 2-1: Timeline of topics relevant to Alfvén Eigenmodes. Not to scale. A more complete list of publications is presented in this chapter.

3. the electron motion, being much more rapid than the time scale of interest, largely eliminates the displacement current. This is equivalent to setting the permittivity to zero  $\epsilon_0 \rightarrow 0$
4. heat flow is slow compared to the MHD time scale so the behavior is adiabatic and pressure is assumed to be isotropic with  $\gamma = 5/3$ .
5. the plasma is assumed to be collision dominated and can be treated as a fluid.

In summary, these approximations allow the formulation of macroscopic variables that treat the ion and electron constituents of the plasma as a single fluid, as follows:

$$\begin{aligned}\rho &= m_i n \\ \mathbf{v} &= \mathbf{u}_i \\ \mathbf{J} &= en(\mathbf{u}_i - \mathbf{u}_e) \\ p &= p_i + p_e\end{aligned}$$

Furthermore, at large enough scale lengths, the electric field in the plasma frame can be neglected, and the ideal Ohm's law adopted. This implies that the perpendicular motion is dominated by  $E \times B$  drift, wherein the ions and electrons move in the same direction and conserve neutrality. Ideal Ohm's law also forces the fluid elements to conserve magnetic flux, so that the plasma is frozen to the magnetic lines of force. Collisionality must also be low to minimize the resistive term in Ohm's law, and this is always satisfied for fusion plasmas.

How is it that the fluid model which assumes a collision-dominated plasma can be applied to low-collisionality plasmas? It turns out that collisionality only comes into play in the compressive terms of the momentum and energy conservation. Fortunately, since compression is highly stabilizing, it is not important for most MHD phenomena, so the fluid picture remains mostly valid in collisionless plasmas.

Finally, applying the macroscopic variables to Maxwell's equations and the con-

conservation laws of mass, momentum and energy results in the Ideal MHD model:

$$\begin{aligned}
\frac{d\rho}{dt} + \rho \nabla \cdot \mathbf{v} &= 0 \\
\rho \frac{d\mathbf{v}}{dt} &= \mathbf{J} \times \mathbf{B} - \nabla p \\
\frac{d}{dt} \left( \frac{p}{\rho^\gamma} \right) &= 0 \\
\mathbf{E} + \mathbf{v} \times \mathbf{B} &= 0 \\
\nabla \times \mathbf{E} &= -\frac{\partial \mathbf{B}}{\partial t} \\
\nabla \times \mathbf{B} &= \mu_0 \mathbf{J} \\
\nabla \cdot \mathbf{B} &= 0
\end{aligned}$$

The derivation and application of the ideal MHD model is treated with elaborate detail by Freidberg and others in [19] - [22].

### 2.2.2 Normal Modes of Ideal MHD

The ideal MHD equations provide a non-linear description of motions of the plasma that satisfy the assumed length and time scales. For small displacements,  $\xi$ , around a static equilibrium, the equations can be made tenable by linearizing. The linearized ideal MHD equations are:

$$\begin{aligned}
\frac{d\rho_1}{dt} + \rho \nabla \cdot \mathbf{v}_1 &= 0 \\
\rho \frac{d\mathbf{v}_1}{dt} &= \mathbf{J}_1 \times \mathbf{B} + \mathbf{J} \times \mathbf{B}_1 - \nabla p_1 \\
\frac{\partial p_1}{\partial t} + \mathbf{v}_1 \cdot \nabla p + \gamma p \nabla \cdot \mathbf{v}_1 &= 0 \\
\nabla \times (\mathbf{v}_1 \times \mathbf{B}) &= \frac{\partial \mathbf{B}_1}{\partial t} \\
\nabla \times \mathbf{B}_1 &= \mu_0 \mathbf{J}_1 \\
\nabla \cdot \mathbf{B}_1 &= 0
\end{aligned}$$

where the laws of Ohm and Faraday have been combined to eliminate the first order electric field in the plasma frame. Together, these equations specify the normal modes of the ideal MHD plasma. It is convenient to introduce the displacement variable,  $\xi$ ,

$$\xi = \xi(\mathbf{r})\exp(-i\omega t)$$

and to represent all the perturbed quantities in terms of  $\xi$ .

$$\begin{aligned} \mathbf{v}_1 &= -i\omega\xi \\ \rho_1 &= -\nabla \cdot (\rho\xi) \\ p_1 &= -\xi \cdot \nabla p - \gamma p \nabla \cdot \xi \\ \mathbf{B}_1 &= \nabla \times (\xi \times \mathbf{B}) \\ \mathbf{J}_1 &= \frac{1}{\mu_0} \nabla \times [\nabla \times (\xi \times \mathbf{B})]. \end{aligned}$$

The eigenmode equation is then obtained by solving for  $\xi$  in terms of equilibrium quantities, as

$$-\omega^2 \rho \xi = \mathbf{F}(\xi) \tag{2.1}$$

where

$$\mathbf{F}(\xi) = \frac{1}{\mu_0} (\nabla \times \mathbf{B}) \times [\nabla \times (\xi \times \mathbf{B})] + \frac{1}{\mu_0} \{ \nabla \times [\nabla \times (\xi \times \mathbf{B})] \} \times \mathbf{B} + \nabla (\xi \cdot \nabla p + \gamma p \nabla \cdot \xi).$$

The normal mode equation is utilized by applying the equilibrium geometry of interest and searching for eigenmodes and their corresponding eigenvalues. If these eigenvalues have imaginary parts then the eigenmodes are unstable. Before venturing into geometries relevant to fusion devices, it is instructive to review the normal modes of a homogeneous plasma, which are all stable.

### 2.2.3 MHD Waves in the Homogeneous Plasma

Consider an infinite, homogeneous plasma with a straight magnetic field defined by  $\mathbf{B}_0 = \mathbf{e}_z B_0$ . The general normal mode can be represented as  $\xi = \xi \exp(i\mathbf{k} \cdot \mathbf{r} - i\omega t)$ . If the coordinate system is transformed to align the y-axis with the perpendicular part of the wave vector,  $\mathbf{k} = \mathbf{e}_y k_\perp + \mathbf{e}_z k_\parallel$ , one component of the displacement is decoupled. In matrix form the eigenmode equation becomes:

$$\begin{bmatrix} \omega^2 - k_\parallel^2 c_A^2 & 0 & 0 \\ 0 & \omega^2 - k_\perp^2 c_s^2 - k^2 c_A^2 & -k_\perp k_\parallel c_s^2 \\ 0 & -k_\perp k_\parallel c_s^2 & \omega^2 - k_\parallel^2 c_s^2 \end{bmatrix} \begin{bmatrix} \xi_x \\ \xi_y \\ \xi_z \end{bmatrix} = 0 \quad (2.2)$$

where  $c_A = B/\sqrt{\mu_0 \rho}$  is the Alfvén speed and  $c_s = \sqrt{\gamma p/\rho}$  is the adiabatic sound speed. Non-trivial eigenvalues (of which there are three) are the roots of the determinant of the matrix on the left:

$$(\omega^2 - k_\parallel^2 c_A^2) (\omega^4 - (c_s^2 + c_A^2) k^2 \omega^2 + (k k_\parallel c_s c_A)^2) = 0 \quad (2.3)$$

Each eigenvalue corresponds to a normal MHD mode of the homogeneous magnetized plasma. The modes are known as the Alfvén wave, the fast magnetosonic wave, and the slow magnetosonic wave. These are depicted schematically in Figure 2-2. The figure illustrates that for a given wave vector, since the displacements of the three waves are orthogonal, an arbitrary disturbance can be decomposed into a linear combination of these waves. All the waves are dispersionless, since  $\omega/k$  does not depend on  $k$ , but they are strongly anisotropic in most conditions. The anisotropy is best understood from the phase diagrams of Figure 2-3. The waves are investigated in further detail below. In particular, their behavior in the low- $\beta$  regime is noted as the relevant condition for tokamak plasmas. In effect, it is emphasizing the magnetic field force over the plasma pressure in their influence on wave behavior.

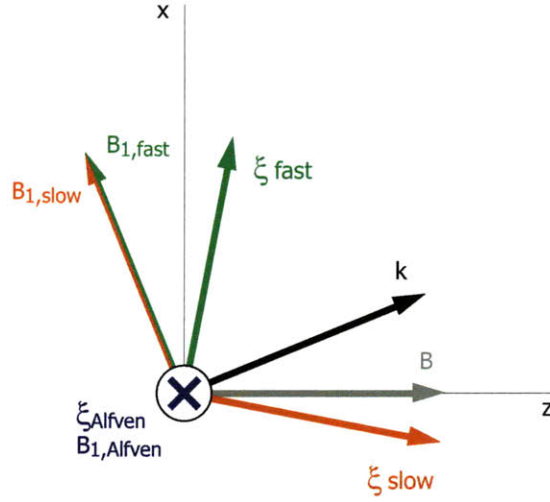


Figure 2-2: The Alfvén wave is characterized by transverse displacement and magnetic field. The magnetoacoustic modes are characterized by displacement and magnetic field in the plane tangent to the wave vector and the background magnetic field. The displacements for these two waves are orthogonal to each other and to the displacement of the Alfvén wave, so that an arbitrary disturbance can be decomposed into components of each wave.

### Alfvén wave

The first root of the dispersion relation, equation 2.3, corresponds to the Alfvén wave [18] and is completely independent of  $k_{\perp}$ .

$$\omega^2 = k_{\parallel}^2 c_A^2 \quad (2.4)$$

Therefore, the Alfvén phase speed  $v_A$  drops to zero for perpendicular wave vectors. Figure 2-3 illustrates the phase velocity of each branch of MHD mode as a function of the angle of the wave vector relative to the magnetic field, and for several values of  $\beta = 2\mu_0 p/B^2$ . Since  $v_{phase} = \omega/k$ , the locus also corresponds to the mode frequency as a function of the angle of propagation, given a fixed wavelength.

The group velocity of the Alfvén wave is always parallel to the magnetic field and there is no communication across field lines. This allows adjacent lines of force to shear across each other, lending the descriptive name *shear* to the Alfvén wave. Figure 2-4 shows the locus of the group velocity for various angles of wave vector; for



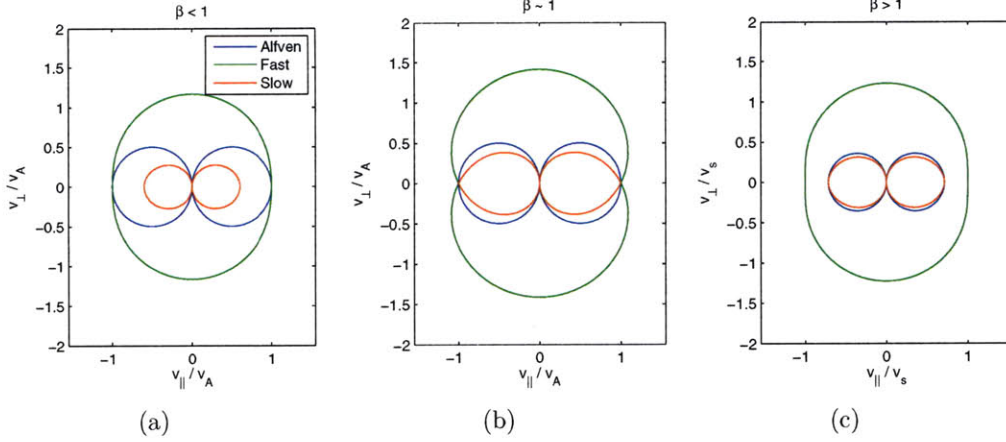


Figure 2-3: Phase diagrams illustrate the wave normal surface of each wave. A point disturbance would evolve into a wave front of these shapes. While they are strongly anisotropic in most conditions (the exception being the fast wave in the low- $\beta$  limit), all the waves are dispersionless, since  $\omega/k$  does not depend on  $k$ .

the Alfvén wave, the locus corresponds to a point.

The displacement of the Alfvén wave is polarized perpendicular to both  $k$  and  $B_0$  for all angles of propagation, as shown in figure 2-5. Since  $k \cdot \xi = 0$ , the displacement is compressionless, hence this wave is also sometimes called the incompressible Alfvén wave. This also explains the Alfvén wave’s insensitivity to  $\beta$ , which may be noted in Figures 2-3 and 2-4.

The perturbed magnetic field is polarized parallel to  $\xi$ . To first order there is no magnetic compression since  $B_0 \cdot B_1 = 0$ . Instead, the magnetic perturbation serves to bend the background magnetic field, working against the inherent tension in the lines of force.

The electric field is perpendicular to the background magnetic field, in the plane of the wave vector, and the plasma displacement corresponds to the resultant  $E \times B$  drift. In comparison to an electromagnetic wave, the electric field is smaller by the ratio  $v/c$ , where  $v \approx \partial\xi/\partial t$  and accounts for only a fraction of the energy of the wave. Instead, the wave motion is a balance between plasma inertia and magnetic field tension, analogous to the dynamics of a stretched, vibrating string. Figure 2-6 shows the balance between the kinetic energy of the fluid motion and the magnetic energy

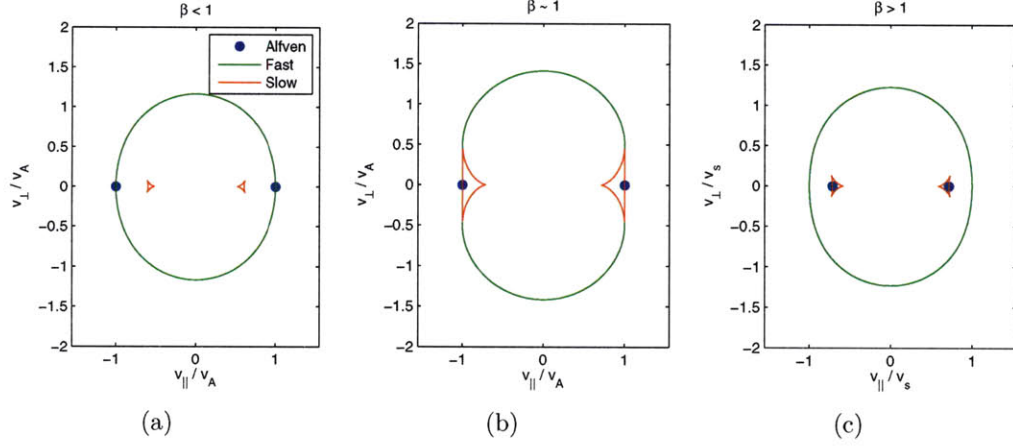


Figure 2-4: Group diagrams illustrate the loci of group velocity, or direction of energy propagation, of the waves as a function of angle of wave vector. None of the waves has their group velocity parallel to their phase velocity in general: the shear wave group velocity is always parallel to the magnetic field, so that there is no communication across field lines; the fast wave group velocity is roughly in a similar direction to the phase velocity; and the slow wave has a group velocity across the magnetic field in the opposite direction of its phase velocity!

of the bent lines of force, as a function of the angle of propagation. The difference represents the energy of the electric field.

### Fast magnetoacoustic wave

Two more roots are obtained from the second term of the determinant given in Equation 2.3. These are,

$$\omega^2 = \frac{1}{2}k^2(c_a^2 + c_s^2)[1 \pm (1 - \alpha^2)^{1/2}],$$

$$\alpha^2 = 4 \frac{k_{\parallel}^2}{k^2} \frac{c_s^2 c_a^2}{(c_s^2 + c_a^2)^2},$$

corresponding to the sound wave (-) and the fast magnetosonic wave (+).

The phase velocity of the fast wave does not vanish for perpendicular propagation (Figure 2-3) and a perpendicular group velocity is possible (Figure 2-4). At parallel propagation, the fast wave and Alfvén wave have the same phase velocity for  $\beta < 1$ . The fast wave is distinguished from the Alfvén wave by having parallel perturbed

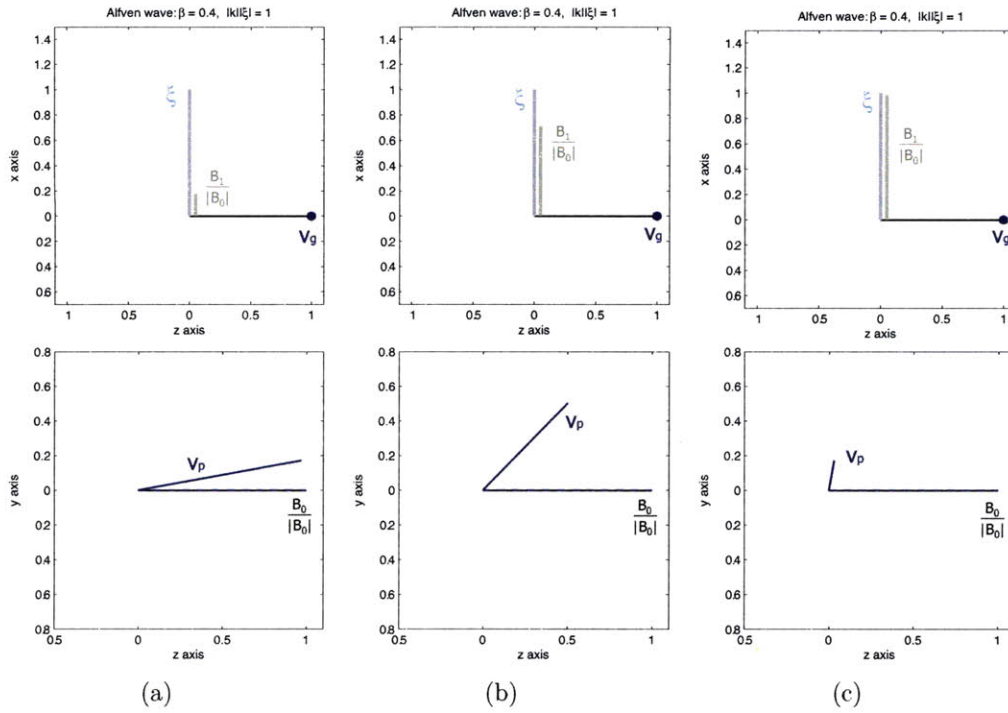


Figure 2-5: The upper figures illustrate the relative magnitudes and directions of the displacement and the perturbed magnetic field for the Alfvén wave, for low beta, at several angles of propagation. The lower figures show the corresponding relative magnitude and angle of the phase velocity.

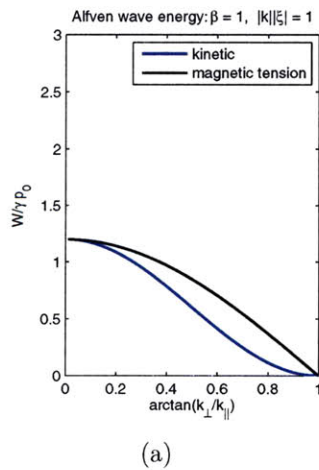


Figure 2-6: For the Alfvén wave, the energy is partitioned among the plasma kinetic energy and the magnetic field bending. The small difference accounts for the weak electric field. The energy vanishes for perpendicular propagation because the mode frequency decreases to zero there.

magnetic field compared to the Alfvén wave’s perpendicular perturbed field.

The polarization of the fast wave is illustrated in Figure 2-7. The displacement is in the plane of the magnetic field and the wave vector. At low  $\beta$ , the displacement is mostly perpendicular for all directions of propagation. Since  $k \cdot \xi \neq 0$ , unlike the shear Alfvén wave, the fast wave is not incompressible.

The magnetic field perturbation lies in the same plane and is perpendicular to the wave vector, since  $\nabla \cdot B_1 = 0$ . The parallel part of  $B_1$  corresponds to magnetic field compression, while the perpendicular part corresponds to magnetic line of force, as in the Alfvén wave. The direction of  $k$  dictates whether magnetic compression or line bending predominates the magnetic energy of the wave. The composition of energy among plasma kinetic and compression and magnetic compression and tension are illustrated in Figure 2-8 for several values of  $\beta$  as a function of the direction of propagation; the tokamak-relevant regime is low- $\beta$  and almost perpendicular propagation. From the figure it is evident that such a wave is predominately supported by kinetic energy and compression of the magnetic field. The fast wave becomes isotropic in the low-beta limit.

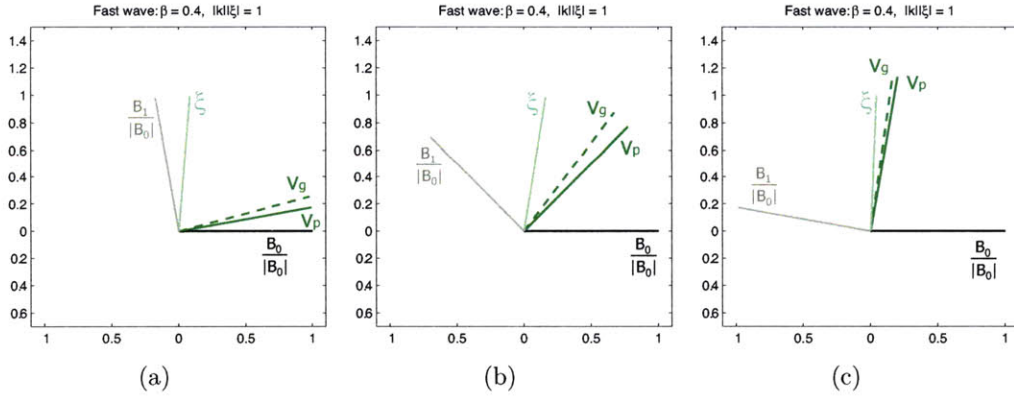


Figure 2-7: The relative magnitudes and directions of the displacement, phase velocity and the perturbed magnetic field for the fast wave, for low beta, at several angles of propagation.

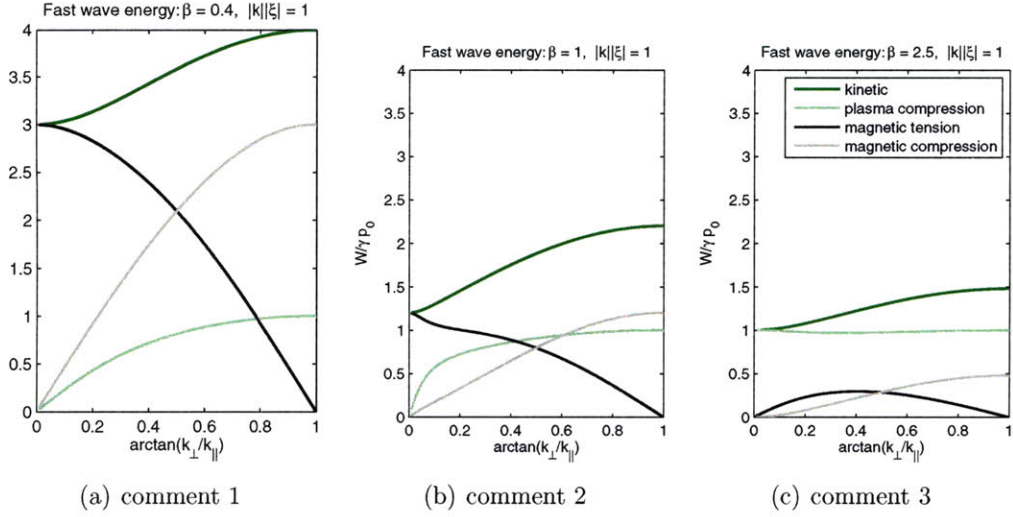


Figure 2-8: The energy of the fast wave is shared mostly between the plasma kinetic energy and magnetic pressure at high  $k_{\perp}/k_{\parallel}$ .

### Slow wave

The smaller frequency branch from the second term in Equation 2.3 describes the slow magnetoacoustic wave. Like the fast wave, it has displacement in the plane of the wave vector and the background magnetic field, but at low beta, the displacement is predominantly parallel to the magnetic field. The magnetic field perturbation is in the same direction as in the fast wave: in the plane of  $B$  and  $k$ , and perpendicular to  $k$ . At low  $\beta$ , the wave energy is found mostly in the plasma kinetic and compressive terms, while the magnetic field accounts for only a fraction of the wave energy. Figure 2-8 illustrates the balance between these terms.

### 2.2.4 Inhomogeneous Slab

New behavior emerges for the MHD waves in inhomogeneous plasma. The dispersion relations of all three modes of ideal MHD depend on the density and the angle of the magnetic field with respect to the wave vector. When either of these quantities has spatial variation, the modes are resonant on the layers where they satisfy the local dispersion relation. Formally, gradient terms appear in the eigenmode problem, Equation 2.2, and the resulting eigenfunctions are not square-integrable. If the as-

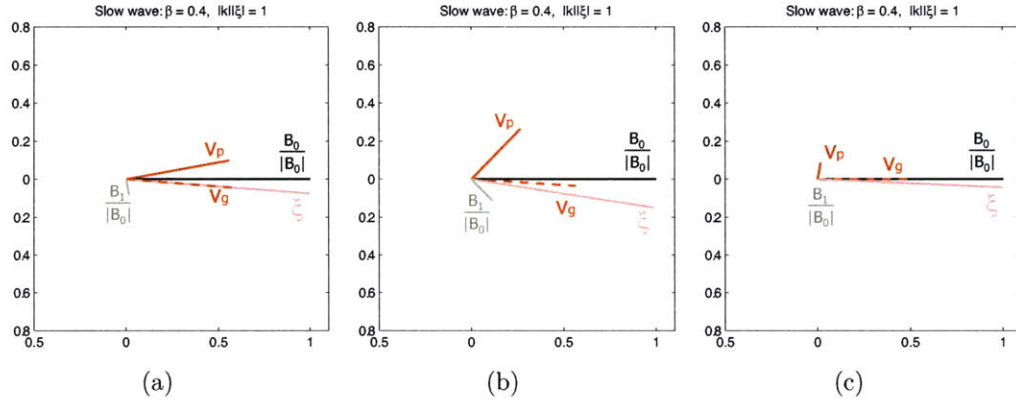


Figure 2-9: The relative magnitudes and directions of the displacement, phase velocity and the perturbed magnetic field for the slow wave, for low beta, at several angles of propagation.

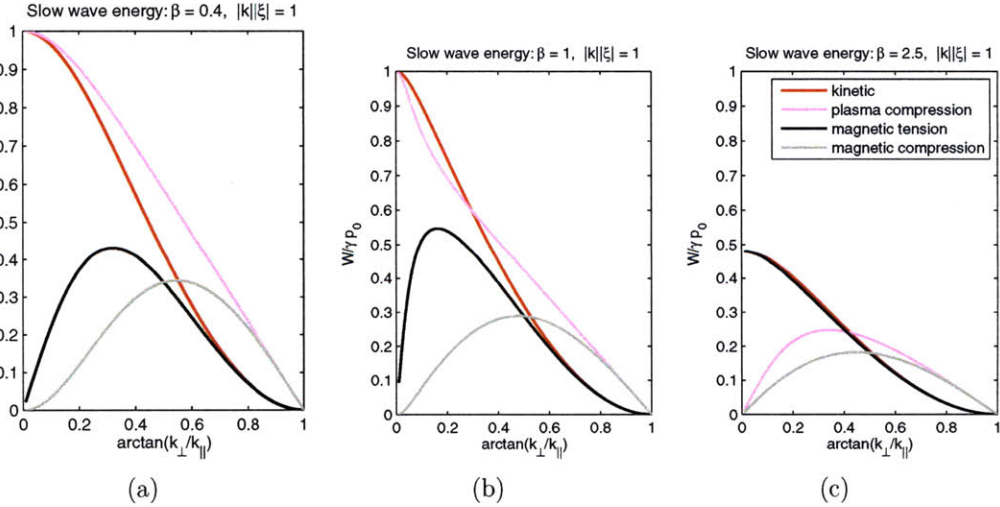


Figure 2-10: For the slow wave, the energy is partitioned mostly among the plasma pressure and plasma kinetic energy, like a sound wave. The energy vanishes for perpendicular propagation because the mode frequency decreases to zero there. The assumptions of Ideal MHD with which these waves were derived are not valid for strongly compressive or high- $k$  (small- $\omega$ ) motions, so these figures are inaccurate for low and high  $k_{\perp}/k_{\parallel}$ .

assumptions of ideal MHD are not relaxed, the modes are found to absorb unbounded energy at the resonance layer, even though the force operator is Hermitian. When the ideal MHD assumptions are relaxed, the energy is dissipated by particle kinetics and mode coupling. The interesting problem of the inhomogeneous plasma can be understood most simply in the infinite cartesian plasma slab with equilibrium gradients restricted to one axis.

Following on the geometry of the previous section, the wave vector is taken to be in the  $y - z$  plane,  $k = k_y + k_z$ . The magnetic field is also assumed to be in the  $y - z$  plane,  $\mathbf{B} = B(x)_y + B(x)_z$ , and a gradient is imposed on the density and magnetic field in the  $x$  direction. (This allows a component of shear in the magnetic field). Furthermore, the displacement is projected into orthogonal components relative to the magnetic field. The displacement along the gradient is called  $\xi$ ; the displacement in the plane of the magnetic field and the wave vector is called tangential, with the parallel component being  $\zeta$  and the perpendicular component,  $\eta$ .

$$\begin{aligned}\xi &= \xi_x, \\ \eta &= i(B_z \xi_y - B_y \xi_z)/B, \\ \zeta &= i(B_y \xi_y + B_z \xi_z)/B.\end{aligned}$$

The first task is to reformulate the eigenmode equation from the force operator, Equation 2.1. In matrix form this is,

$$\begin{bmatrix} \rho\omega^2 + \frac{d}{dx}(\gamma p + B^2)\frac{d}{dx} & \frac{d}{dx}k_\perp(\gamma p + B^2) & \frac{d}{dx}k_\parallel\gamma p \\ -k_\perp(\gamma p + B^2)\frac{d}{dx} & \rho\omega^2 - k_\perp^2(\gamma p + B^2) - k_\parallel^2 B^2 & -k_\perp k_\parallel\gamma p \\ -k_\parallel\gamma p\frac{d}{dx} & -k_\parallel k_\perp\gamma p & \rho\omega^2 - k_\parallel^2\gamma p \end{bmatrix} \begin{bmatrix} \xi \\ \eta \\ \zeta \end{bmatrix} = 0 \quad (2.5)$$

Solving for the transverse component of displacement yields an ordinary differential equation in  $\xi$ ,

$$\frac{\partial}{\partial x} \left[ \frac{\rho(\omega^2 - k_\parallel^2 c_A^2) \left[ (c_A^2 + c_s^2)\omega^2 - k_\parallel^2 c_A^2 c_s^2 \right]}{\omega^4 - k^2(c_A^2 + c_s^2)\omega^2 + k^2 k_\parallel^2 c_A^2 c_s^2} \right] \frac{\partial \xi}{\partial x} + \rho(\omega^2 - \omega_A^2)\xi = 0$$

In the limits of tokamak plasma conditions, the eigenmode problem can be reduced to describe only the shear Alfvén wave. First, the sound wave is decoupled by considering the low- $\beta$  limit, where its phase speed is much lower than that of the Alfvén wave. Secondly, the fast wave is decoupled by considering large  $k_{\perp}/k_{\parallel}$  (see [20]), where its phase speed is much larger than the Alfvén wave phase speed. In effect, for a given wave vector, these limits spread apart the eigenfrequencies of the three modes, isolating the Alfvén wave in the middle. (Goedbloed and Poedts [22] give a treatment of the full wave equation, *keeping  $\beta$  and  $k_{\parallel}/k_{\perp}$  finite*. They find continuous spectra for the Alfvén and sound waves, and discrete modes clustering at infinite frequency for the fast magnetosonic waves.)

In the low- $\beta$  and  $k_{\perp} \gg k_{\parallel}$  limits, the wave equation is

$$\frac{\partial}{\partial x} \left[ \frac{\rho(\omega^2 - \omega_A^2)}{k_{\perp}^2} \frac{\partial \xi}{\partial x} \right] - \rho(\omega^2 - \omega_A^2) \xi = 0 \quad (2.6)$$

where  $\omega_A^2(x) = k_{\parallel}^2(x)c_A^2(x)$  is the local Alfvén frequency for a given wave vector. Equation 2.6 takes the form of the Liouville equation,

$$\frac{\partial}{\partial x} \left[ p(x) \frac{\partial \psi}{\partial x} \right] + (q(x) + \lambda r(x)) \psi = 0,$$

where  $\lambda = 0$  is the Liouville eigenvalue, and

$$\begin{aligned} p(x) &= \rho(\omega^2 - \omega_A^2)/k_{\perp}^2 \\ q(x) &= \rho(\omega^2 - \omega_A^2). \end{aligned}$$

At  $x = x_0$  the mode frequency matches the local Alfvén frequency so that  $p(x_0) = q(x_0) = 0$ , giving rise to a regular singular point of the differential equation (Equation 2.6). At that point the displacement  $\xi(x)$  could be unbounded.

A standard approach to solving the Liouville equation is applicable [23]. With the derivatives distributed, Equation (2.6) is

$$\xi'' p + p' \xi' - q \xi = 0, \quad (2.7)$$



where primes are used to denote the derivative with respect to  $x$ . Next it is convenient to divide all the terms by  $p$  and expand the coefficients in Taylor series about the singular point,  $x_0$ . Setting  $z = x - x_0$ , and defining new coefficients gives,

$$\begin{aligned} P &= \frac{p'}{p} = \frac{1}{z} \sum_{n=0}^{\infty} a_n z^n, & a_0 &= 1 \\ Q &= \frac{q}{p} = \frac{1}{z} \sum_{n=0}^{\infty} b_n z^n. \end{aligned} \tag{2.8}$$

Now the Frobenius series can serve as a trial solution of  $\xi$ . Its derivatives evaluate as,

$$\begin{aligned} \xi &= z^\nu \sum_0^\infty c_n z^n, \\ \xi' &= z^{\nu-1} \sum_0^\infty (\nu + n) c_n z^n, \\ \xi'' &= z^{\nu-2} \sum_0^\infty (\nu + n)(\nu + n - 1) c_n z^n. \end{aligned} \tag{2.9}$$

Substituting series representations 2.8 and 2.9 into the differential equation 2.7 gives,

$$\begin{aligned} \xi'' + P\xi' - Q\xi &= z^{\nu-2} \sum_0^\infty (\nu + n)(\nu + n - 1) c_n z^n \\ &\quad + z^{\nu-2} \sum_0^\infty a_n z^n \sum_0^\infty (\nu + n) c_n z^n \\ &\quad - z^{\nu-1} \sum_0^\infty b_n z^n \sum_0^\infty c_n z^n \\ &= 0. \end{aligned} \tag{2.10}$$

Collecting terms of equal degree yields the indicial equation that constrains  $\nu$ ,

$$z^{\nu-2}(\nu(\nu - 1)c_0 + \nu c_0 a_0) = 0 \quad \rightarrow \nu = \{0, 0\}$$

and the recursion relation that prescribes the Frobenius coefficients,

$$(\nu + n)(\nu + n - 1 + a_0)c_n = - \sum_{k=0}^{n-1} [(\nu + k)a_{n-k} + b_{n-k-1}] c_k. \quad (2.11)$$

The coefficients  $c_n$  can be considered functions of  $\nu$  insofar as they satisfy the recursion relation for *any* value of  $\nu$ . Therefore, the  $\nu$ -derivatives of the recursion relation to all orders are also satisfied.

From the indicial equation, and recalling that  $a_0 = 1$ , we find a 2-fold repeated root,  $\nu = \{0, 0\}$ . Therefore one solution for  $\xi$  is found by substituting  $\nu = 0$  into equation 2.9, with the coefficients  $c_n$  given by solving the recursion relation 2.11,

$$\xi_1 = \sum_0^{\infty} c_n z^n.$$

A second solution is found by differentiating equation 2.10 with respect to  $\nu$  [24]. It has already been shown that the recursion relation remains satisfied after differentiation with respect to  $\nu$ . Also, since  $\nu = 0$  is a repeated root of the indicial equation, it remains a root after differentiation. Therefore the second solution is given by,

$$\begin{aligned} \xi_2 &= \frac{d\xi_1}{d\nu} \\ &= \frac{d}{d\nu} z^\nu \sum_0^{\infty} c_n z^n \\ &= \ln|z| \sum_0^{\infty} c_n z^n + \sum_0^{\infty} \frac{d}{d\nu}(c_n) z^n, \end{aligned} \quad (2.12)$$

where the principal value of the logarithm is taken.

While the transverse displacement,  $\xi$ , has been shown to be unbounded at the singular point where the wave frequency matches the local Alfvén frequency, it is still square-integrable there, so it absorbs only finite energy from the wave. In contrast to the Alfvén wave in homogeneous plasma, however, the displacement is not restricted to the transverse direction.

The tangential components of the shear Alfvén wave,  $\eta$  and  $\zeta$ , are non-zero in an inhomogeneous plasma and they play an important role at the singularity. They are recovered from the full force operator (setting aside the low- $\beta$  and small- $k_\perp/k_\parallel$  assumptions) as follows:

$$\eta = k_\perp \frac{(c_A^2 + c_s^2)\omega^2 - k_\parallel^2 c_A^2 c_s^2 \xi'}{\omega^4 - k^2(c_A^2 + c_s^2)\omega^2 + k^2 k_\parallel^2 c_A^2 c_s^2} \rightarrow -\frac{\xi'}{k_\perp} \gg \xi,$$

$$\zeta = k_\parallel \frac{c_s^2(\omega^2 - k_\parallel^2 c_A^2)\xi'}{\omega^4 - k^2(c_A^2 + c_s^2)\omega^2 + k^2 k_\parallel^2 c_A^2 c_s^2} \rightarrow -\frac{c_s^2 \xi'}{k_\perp} \approx \xi,$$

From this result it is also notable that the Alfvén wave in inhomogeneous plasma is not incompressible and does have some component of the perturbed magnetic field parallel to the background field. Nonetheless the Alfvén wave is still easily distinguished from the fast and slow magnetoacoustic branches by its polarization and eigenfrequency.

It now becomes apparent how the Alfvén wave described by ideal MHD in inhomogeneous plasma can seemingly dissipate energy, despite its origin from a self-adjoint operator. The large displacements immediately to each side of the singular surface are not in phase, and the continued absorption of energy drives the growth of unbounded fields that must necessarily develop to support the discontinuity. This is known as phase mixing [25]. When dissipative effects such as particle kinetics are taken into account they will replace the growth of unbounded fields, and this process is called continuum damping. Interestingly, though, the rate of continuum damping depends on the absorption as described by ideal MHD rather than on the specifics of the dissipation mechanisms themselves [26].

## 2.2.5 Cylindrical Geometry

Some aspects concerning Alfvén waves in toroidal geometry are just as effectively discussed in the simpler cylindrical geometry. Therefore it is convenient to first ignore the bending of the plasma column and treat it as a straight cylinder with length  $2\pi R$  and radius  $a$ , and with the same periodicity constraints that would follow from joining the ends. The resulting plasma column is called a screw pinch. The no-bend

assumption can be made for torii where the inverse of the aspect ratio,  $\epsilon = a/R$ , is large. Alcator C-Mod has a moderately large inverse aspect ratio of around  $\epsilon^{-1} = 3$ .

In a cylindrical screw pinch the magnetic field, having both axial and azimuthal components, is inevitably non-uniform because it is curved. The inverse pitch of the magnetic field is an important factor in the stability of the screw pinch. It is known as the safety factor,  $q$ , defined as,

$$q = \frac{rB_\phi}{RB_\theta} \quad (2.13)$$

where  $r$  is the local minor radius,  $B_\phi$  is the axial field, and  $B_\theta$  is the azimuthal field.

In a cylinder with circular cross-section, the continuous set of concentric, cylindrical surfaces that are tangent to the magnetic field can be labelled by their radii,  $r$ . Alternately those surfaces can be parametrized by the amount of axial magnetic flux,  $\psi$ , they enclose: for that reason they are called flux surfaces. While the parametrization between radius and flux function amounts to a trivial change of variables in the circular cylinder, the flux function is a much more convenient label in the tokamak, where the flux surfaces are neither concentric nor circular, rendering the concept of radius somewhat unclear. Therefore radial profiles of equilibrium parameters, such as density and safety factor, are often given as functions of flux. An equally valid, but different parametrization is to use the poloidal flux. This is calculated as the magnetic flux that passes through a (2D) annulus defined by the portion of the midplane between the magnetic axis and some larger radius. For continuity, poloidal flux will be used as the radial coordinate throughout this chapter.

Eigenmodes of the periodic cylinder can be defined by integer toroidal and poloidal wavenumbers,  $n$  and  $m$ , respectively, a radial eigenfunction  $\xi(\psi)$  and a frequency  $\omega$ . Then the parallel wavevector is,

$$\begin{aligned} k_{\parallel} &= \frac{\mathbf{k} \cdot \mathbf{B}}{B} \\ &= \frac{B_\phi}{B} \frac{1}{R} (n + m/q). \end{aligned}$$

When the inverse aspect ratio is large, it can generally be assumed that the magnetic field is mostly in the toroidal direction, so that,

$$\frac{B_\phi}{B} \approx 1$$

and

$$k_\parallel \approx \frac{1}{R}(n + m/q).$$

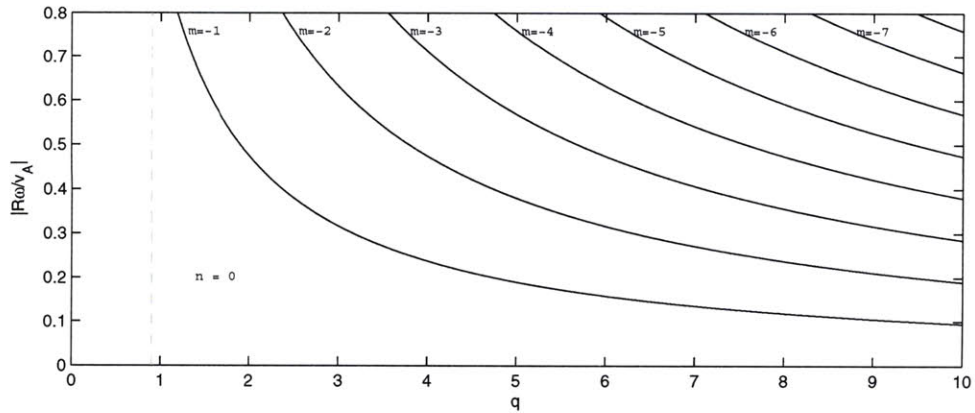
In the cylinder, the local Alfvén speed,  $c_A$ , is a function of the flux parameter, and covers a continuous range as the radius varies from the axis to the plasma edge. Therefore the local Alfvén frequency  $\omega_A$  for a particular wavevector  $k = \{n/R, m/r\}$  is a continuous function of flux, called the Alfvén continuum.

$$\omega_A(r)^2 = k_\parallel^2 c_A(r)^2$$

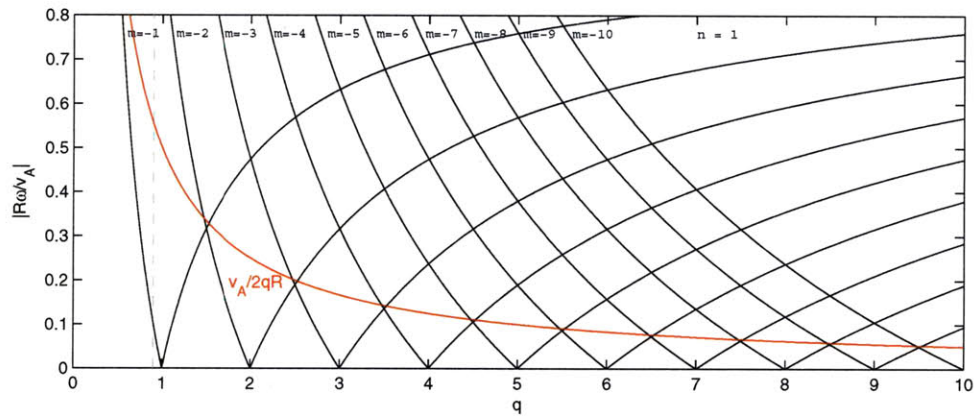
The Alfvén resonance occurs at the minor radius  $r_0$  where the local shear Alfvén dispersion relation is satisfied, that is, where the wave frequency matches the local Alfvén continuum frequency,  $\omega_0 = \omega_A(\psi_0)$  [27] [28]. There, as in the inhomogeneous slab, strong absorption takes place due to continuum damping.

The generalized Alfvén continua for  $n = 0, 1, 2$  and  $m = 0 - 10$  are plotted in Figure 2-11. The continua for the particular equilibrium of shot 1080403010 are plotted in Figure 2-13. The relevant equilibrium profiles of safety factor and Alfvén speed for shot 1080403010 are plotted in Figure 2-12.

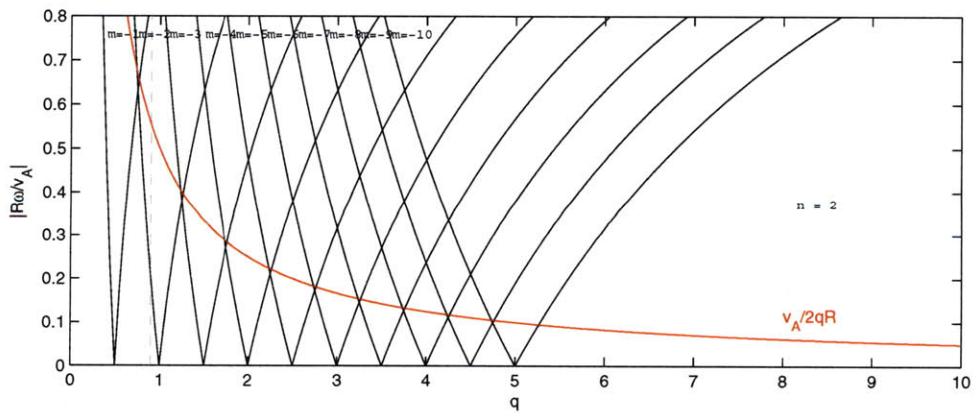
It is evident from Figure 2-13(a) showing the continuum for  $n = 0$  in shot 1080403010, that for some combinations of wavevector and equilibrium profiles, gaps in frequency exist in the continuum across the entire plasma radius. Any discrete eigenmodes of the plasma column that exist in such a gap avoid the strong absorption of continuum damping *despite the inhomogeneity*. If other potential damping mechanisms are weak, such modes can be strongly resonant. Discrete modes that occur at frequencies below or between adjacent continua are called Global Alfvén Eigenmodes (GAEs) [29] [30] [31].



(a) generalized  $n=0$  continuum for the cylinder

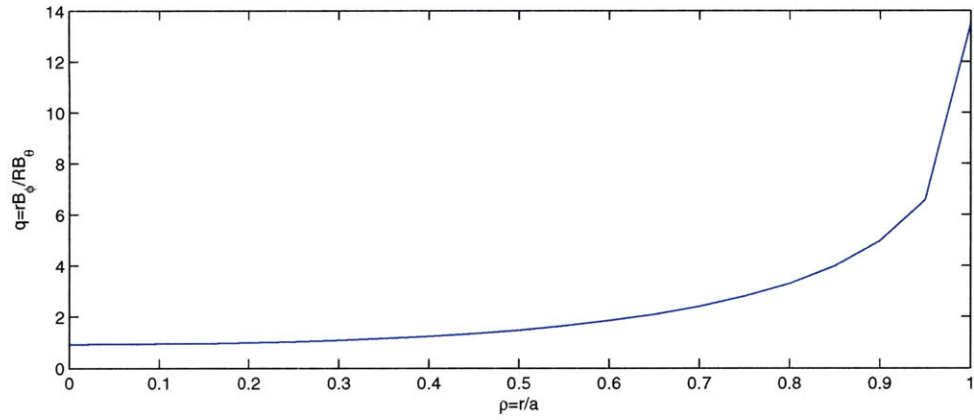


(b) generalized  $n=0$  continuum for the cylinder

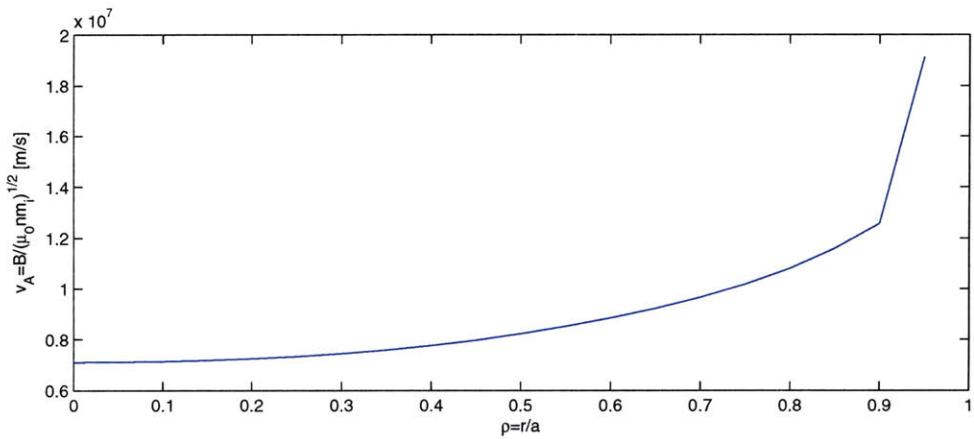


(c) generalized  $n=0$  continuum for the cylinder

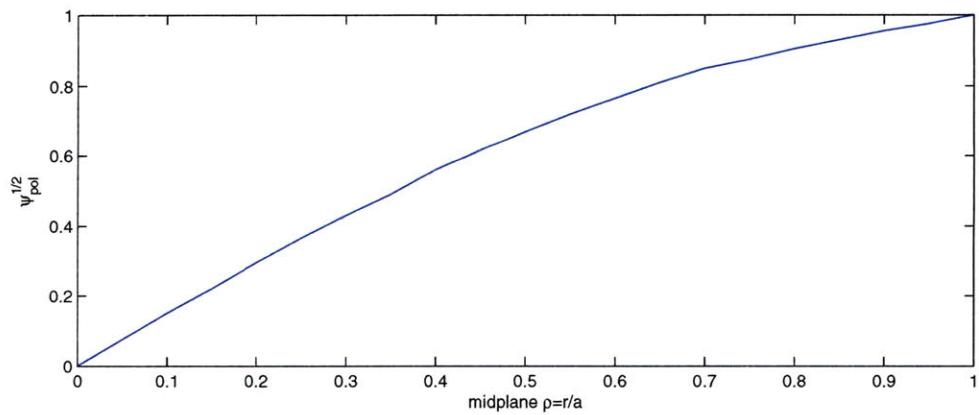
Figure 2-11: Generalized continua for the cylinder. The red line traces the points where poloidal modes are degenerate. The small discrepancy between the approximation  $v_A/2qr$  and the actually crossing points is due to the large aspect assumption, or equivalently  $B_\phi/B = 1$ . The dashed grey vertical line shows the typical minimum  $q$  value.



(a) safety factor

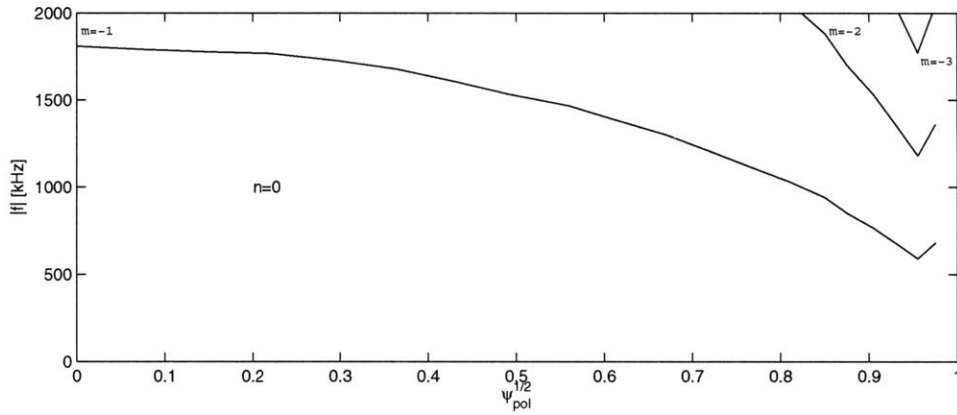


(b) density

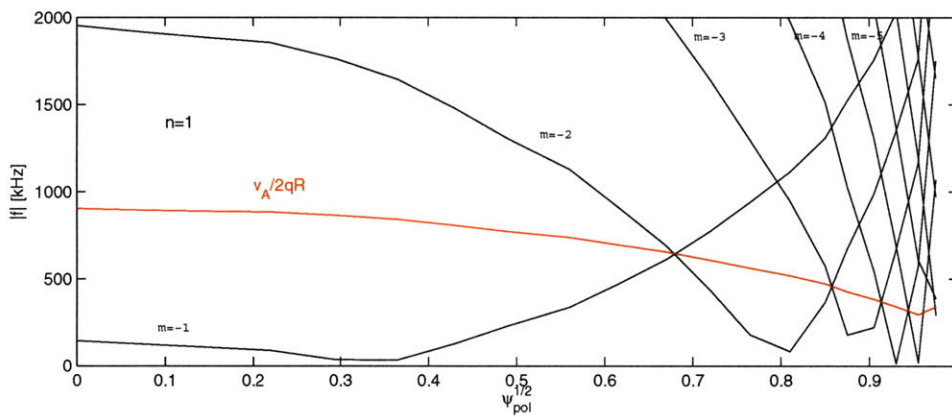


(c) conversion of poloidal flux vs normalized radius at the midplane

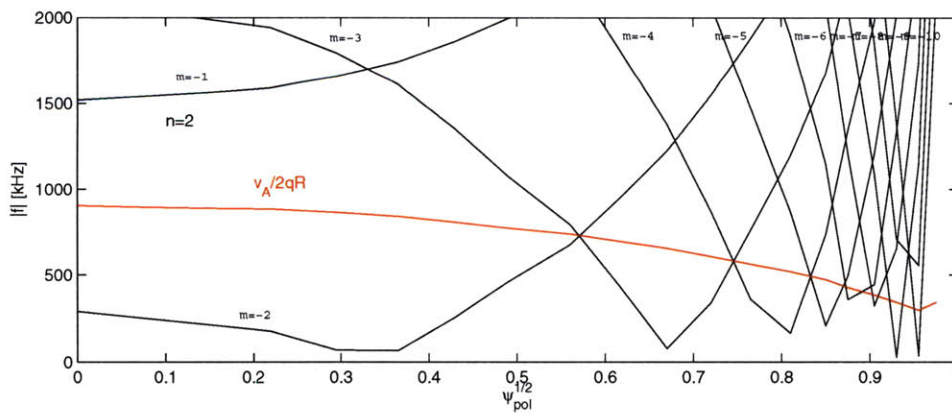
Figure 2-12: Equilibrium profiles for shot 1080403010 that are used to plot the continua for that shot in the next figure.



(a)  $n=0$



(b)  $n=1$



(c)  $n=2$

Figure 2-13: Continua for shot 1080403010. The equilibrium profiles of Figure 2-12 were used to denormalize the general continua of Figure 2-11, without smoothing. The discretization of the continuum, especially near the edge, shows how sensitive the continuum calculation is to the assumed equilibrium profiles.



Figure 2-11 also shows that for finite toroidal mode numbers, the continua of modes having different poloidal wave numbers cross at rational values of the safety factor. For example, where the continuum frequency is satisfied by two distinct poloidal modes  $m$  and  $m + 1$ ,

$$\frac{1}{R} \left( n + \frac{m}{q} \right) = -\frac{1}{R} \left( n + \frac{m+1}{q} \right),$$

the safety factor where those two wavevectors are degenerate is,

$$q = -\frac{2m+1}{2n}. \quad (2.14)$$

The parallel wavevector and Alfvén continuum frequency at the crossing point are, respectively,

$$k_{\parallel} = \frac{-1}{2qR}$$

$$\omega_A^2 = \left( \frac{c_A}{2qR} \right)^2$$

In a screw pinch, modes with distinct wave numbers are orthogonal so both continua can exist at the point of degeneracy.

## 2.2.6 Toroidal Geometry

Bending the cylinder into a finite aspect ratio, circular cross-section torus gives rise to an unavoidable  $1/R$  dependence of the toroidal magnetic field. Then the safety factor is computed as an average over the flux surface,

$$k_{\phi}R = n, \quad n \in \text{integer}$$

$$q = \frac{1}{2\pi} \oint \frac{r}{R} \frac{B_{\phi}}{B_{\theta}} d\theta \approx \frac{rB_{\phi}}{RB_{\theta}}$$

As a result of the  $1/R$  dependence, the magnetic field varies over a poloidal transit on a flux surface. Moreover, that variation acts as a periodic index of refraction that couples the continua of distinct poloidal wavenumbers where they are degenerate.

The mode coupling at the degeneracy creates a forbidden gap in the Alfvén resonance frequency continuum [32], [33]. The approximate location of that gap is shown in Figures 2-11 and 2-13 as a red curve. A more accurate computation of the continuum requires a numerical approach such as is implemented by the code NOVA-K. Figure 2-14 shows the calculated continuum for shot 1080403010, computed by NOVA-K based on the equilibrium profiles in Figure 2-12, overlaid on the simple continuum calculated for the cylinder assumption. That agreement is fairly good.

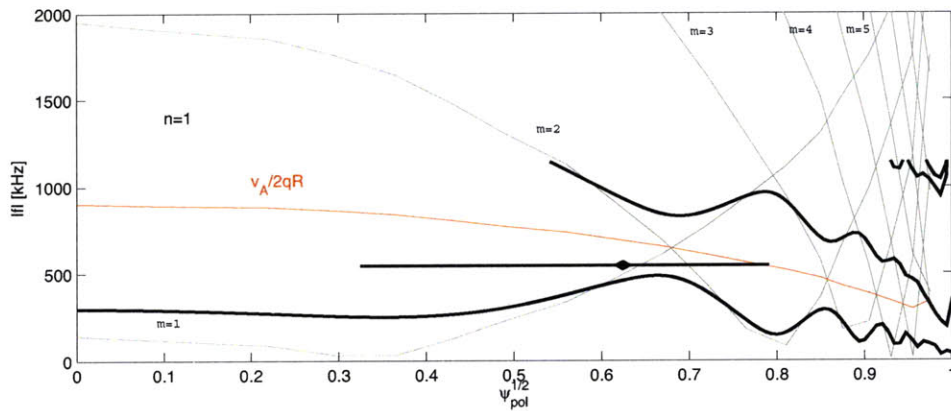


Figure 2-14: The continuum for shot 1080403010 in the cylindrical approximation (thin lines), compared to the continuum calculated by NOVA-K assuming toroidicity (thick lines). The agreement is good. An  $n=1$  mode is indicated with a horizontal line showing the radial extent of half-amplitude.

The appearance of a band gap is typical of periodic structures. A photonic crystal lattice couples the forward and reverse modes of a photon to form a standing wave. In that case, the lattice prohibits propagation of photons with energies in the forbidden range and can be used to form an extremely efficient waveguide cavity [34]. Electron wave functions have analogous behavior in a semi-conductor [35].

The coupling of degenerate modes in the torus is commonly known as ‘poloidal coupling’, ‘toroidal coupling’ [36] or ‘the effect of toroidicity’. However, the mistake should not be made of thinking that the modes couple due to toroidal periodicity; any periodic system must have modes with integer wave numbers. The coupling is due entirely to the unavoidable poloidal variation of the magnetic field strength acting as a periodic potential. Poloidal coupling would also be present in a cylindrical pinch if

the axial field were not uniform over the flux surface [37] and is encountered at higher orders in toroidal plasmas due to non-circular shaping of the cross-section, such as ellipticity [38] and triangularity.

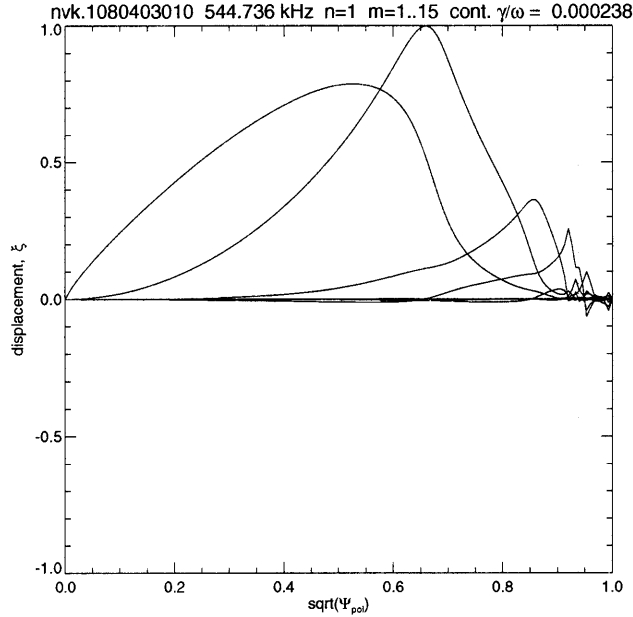


Figure 2-15: Radial eigenfunction for the poloidal components of the  $n = 1$  mode calculated by NOVA-K. The primary components are  $m = -2$  and  $m + 1 = -1$ .

For particular equilibrium profiles, the gap in the continuum may extend across the entire plasma radius. If discrete eigenmodes of the plasma volume exist at frequencies in the gap, they avoid the strong continuum damping. Eigenmodes that exist in the gap caused by toroidicity are called Toroidicity-induced Alfvén Eigenmodes (TAE). The horizontal bar with a central diamond in Figure 2-14 shows the frequency, radial extent and radius of maximum amplitude (of the ensemble of poloidal modes) of a TAE that has been computed by NOVA-K for the equilibrium of shot 1080403010. Figure 2-15 shows the displacement for all the poloidal harmonics that compose the  $n = 1$  mode computed by NOVA-K. The primary harmonics correspond to the ones that are degenerate near the mode in the cylindrical approximation: they are  $m = -2$  and  $m + 1 = -1$ , and the corresponding value of the safety factor is,

$$q = -\frac{m + 1/2}{n} = 1.5$$

It is instructive to examine the propagation space of these two primary poloidal harmonics. Figure 2-16 shows the direction and relative magnitude of the wavevectors of the two harmonics on an unwrapped flux surface; on the same plot are shown the direction and relative magnitude of the velocity vectors. In the cylindrical approximation, the wavevectors are found to have parallel components that are equal in magnitude but opposite in direction. Parallel to the magnetic field, then, the mode structure is a standing wave. However, the waves share the same toroidal wavenumber and have poloidal wavenumbers that differ by 1. This is possible, as Figure 2-16 makes clear, because the waves propagate nearly perpendicular to the magnetic field. For high toroidal wave numbers, such as  $n = 5$  presented in Figure 2-17, the waves propagate even closer to perpendicular.

The red curve in Figure 2-14 traces the points where distinct poloidal modes are degenerate,

$$\omega_A^2 = \left( \frac{c_A}{2qR} \right)^2$$

and therefore marks the center of the toroidicity-induced gap. As such it provides a rough estimate of the expected frequency where TAEs could exist [39]; clearly that estimate depends on the flux surface at which the values of the Alfvén phase speed,  $c_A$ , and the safety factor,  $q$ , are chosen. In lieu of time-consuming numerical hunting for eigenmodes of a given profile, the  $q = 1.5$  flux surface is often chosen as the nominal radial location to expect TAEs because that value allows the densest packing of modes in toroidal wavenumber space: for  $q = 1.5$ , all odd  $n$  can satisfy Equation 2.14.

In many cases the frequency gap may curve near the edge, so that the frequency band that avoids damping in the core is separated from the plasma edge by a continuum. TAEs that are localized in the core can still avoid strong damping if their amplitudes are small where they cross the continuum. For example, in Figure 2-14 it is evident that the TAE amplitude falls off before reaching the continuum near the edge. Modes of higher toroidal wave number tolerate curved gaps even more readily because they tend to be more radially localized.

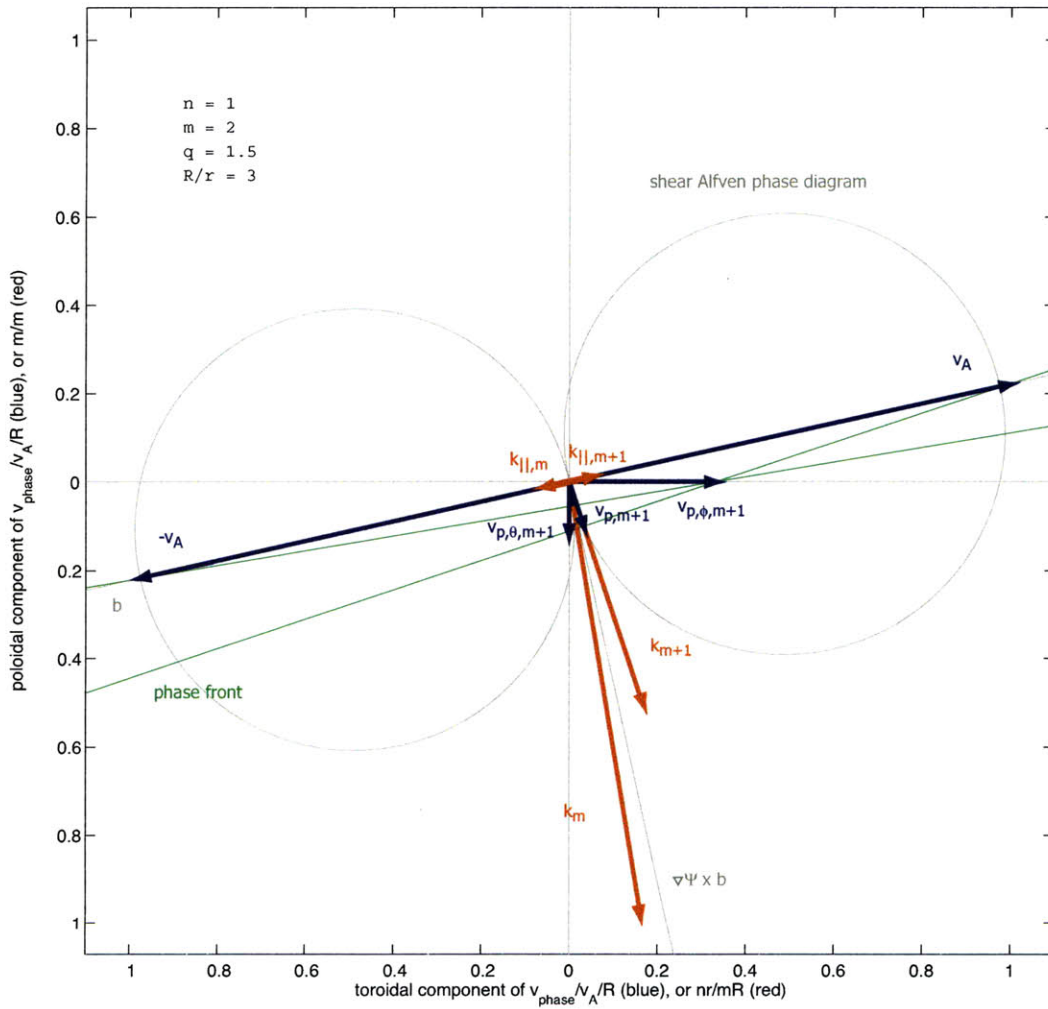


Figure 2-16: For an  $n = 1$  mode, the relative directions and amplitudes of the phase velocities for the two primary poloidal components (blue); and the relative directions and amplitudes of the wavevectors (red).

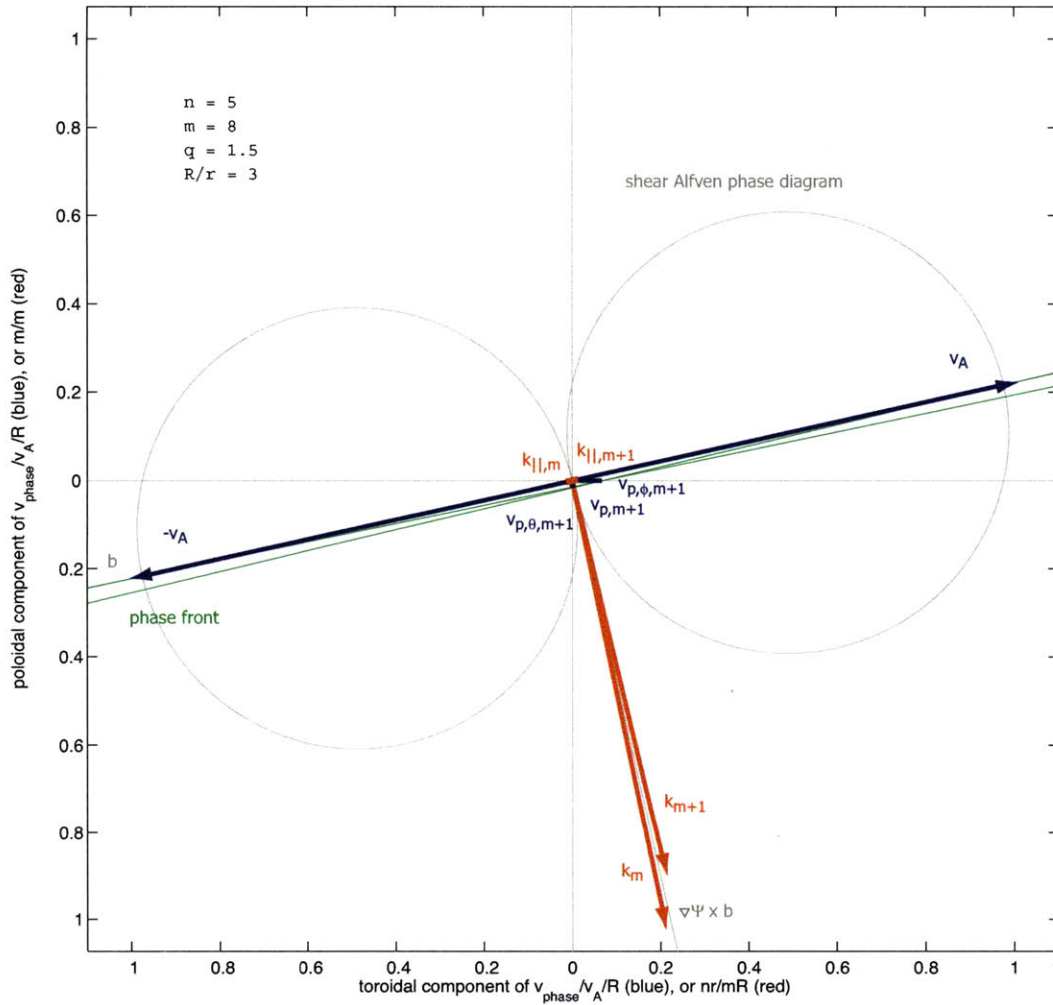


Figure 2-17: For an  $n = 5$  mode the relative directions and amplitudes of the phase velocities for the two primary components (blue); and the relative directions and amplitudes of the wavevectors (red). The phase velocities are even closer to perpendicular to the magnetic field than in the  $n = 1$  case.

The TAE eigenfunction is described by [40]:

$$\left\{ \frac{d^2}{d\theta^2} + \frac{\omega^2}{\omega_A^2} (1 + 2\epsilon \cos\theta) - \frac{s^2}{(1 + s^2\theta^2)^2} \right\} \Phi = 0.$$

where  $\Phi$  is a scalar field related to the Fourier transform of the perturbed magnetic flux,  $\theta$  is the generalized poloidal angle, and

$$s = \frac{rq'}{q}.$$

Two branches arise near the top and bottom of the forbidden gap. The two branches are [41]:

$$\omega_{\pm}^2 = \frac{k_{\parallel m}^2 c_A^2 + k_{\parallel m+1}^2 c_A^2 \pm \sqrt{(k_{\parallel m}^2 c_A^2 - k_{\parallel m+1}^2 c_A^2)^2 + 4\epsilon^2 x^2 k_{\parallel m}^2 c_A^2 k_{\parallel m+1}^2 c_A^2}}{2(1 - \epsilon^2 x^2)}$$

where

$$\epsilon = \frac{3a}{2R},$$

$$x = \frac{r}{a}.$$

The higher frequency branch has a higher amplitude on the high field side; the lower frequency branch has a higher amplitude on the low field side [37], [42].

The modes are peaked between the corresponding mode rational surfaces but are of global radial extent [36] [43]. The corresponding eigenfrequencies vary from the lower end of the gaps when  $s = 0$  to the upper end of the gap when  $s \rightarrow \infty$  [40]. The number of modes is proportional to  $n$  for a given  $q(r)$ . As  $n$  becomes large, the modes fill up the gap. The width of the gap in  $(\omega/\omega_A)^2$  is of order  $r_0/R = \epsilon$  [36] and the radial width of the eigenfunction is  $\epsilon/nq'$  [44].

While TAEs avoid strong continuum damping by existing in a forbidden frequency gap, they have small but finite amplitude where they cross the continuum at the plasma edge. In addition, TAEs are subject to several other damping mechanisms.

### 2.2.7 Damping of the TAE

Growth of TAEs is limited by damping mechanisms which involve both MHD and kinetic effects, including coupling to the heavily damped frequency continuum, ion and electron Landau damping, radiative losses on kinetic Alfvén waves, and collisional absorption. Each mechanism is described briefly.

In the high- $n$  limit the TAEs are highly localized in the radial direction between two mode rational surfaces, decaying exponentially outside this region. While many poloidal harmonics are coupled together to determine a much broader global radial envelope structure, radial variation of  $\omega_A$  acts to localize the envelope. Coupling with the continuum modes occurs to the extent that the TAE exceeds the boundaries of the frequency gap, resulting in weak damping of the TAE on the Alfvén resonances of the continuum [44], for both high [45] [46] and low  $n$  [47]. The damping is independent of the details of the absorption mechanisms for the continuum itself but is very sensitive to the profiles of  $q$  and  $\rho$ . Continuum damping is linked to the radial dependence of the quantity  $1/q\rho^{1/2}$  being constant so that the gaps are aligned. If that quantity varies strongly, continuum damping becomes dominant and leads to damping rates of 5-10% [48], [49]. For instance, the peaked density in H-mode causes modes to coalesce because the gap gets narrower. This may also happen if the modes reach the bottom of the gap [50]. Finite pressure shifts the TAE out of the frequency gap and increases the continuum damping contribution [44] [42].

Ion [51] [44] [52] and electron [41] Landau damping are described respectively by:

$$\frac{\gamma_i}{\omega} \propto \beta_i^{-\frac{3}{2}} \exp\left(-\frac{\beta_i}{9}\right)$$

and

$$\frac{\gamma_e}{\omega} \propto \beta_e \frac{c_A}{v_{thermal,\parallel}}$$

where  $\beta_i = n_i T_i / (B_{tor}^2 / 2\mu_0)$  is the ion beta and  $\beta_e$  is the electron beta.

Collisionless damping on passing electrons and collisional damping on trapped and passing electrons couples the TAE to kinetic Alfvén waves that radiate energy



away from the gap region. This damping rate may be enhanced by nonideal effects of electron inertia and finite ion Larmor radius [53]. It scales as

$$\frac{\gamma_R}{\omega} \propto s^2 \exp\left(-\frac{f(s, \epsilon)}{\rho_i m}\right),$$

where  $f(s, \epsilon)$  is a function of magnetic shear,  $s$  and aspect ratio,  $\epsilon$ , and  $\rho_i$  is ion Larmor radius [54] [55].

Finally, trapped electron collisional absorption is given by

$$\frac{\gamma_e^t}{\omega} \propto \left(\frac{\nu_e}{\omega}\right)^{1/2} [\beta_e q^2 + 0.1 \left(\frac{\rho_s}{\delta_{TAE}}\right)^2]$$

where

$$\nu_e \propto \frac{n_e}{T_e^2}$$

is the electron collision frequency, and

$$\rho_s^2 = \frac{2T_e}{m_i \omega_{ci}^2},$$

$$\delta_{TAE}^2 = \frac{\pi}{64} \left(\frac{r\epsilon}{m}\right)^2.$$

Here,  $\omega_{ci}$  is the ion cyclotron angular frequency,  $\epsilon$  the tokamak inverse aspect ratio and  $m$  the poloidal mode number [56] [57] [58].

### 2.2.8 Drive of the TAE

Global MHD instabilities are known to be caused by interaction with energetic particles, such as injected neutral beam ions [59], ICRF heated minorities, or fusion born alphas [60]. In particular, energetic particles can excite TAEs [61] [62] [63], with the particles' density inhomogeneity providing the free energy source to destabilize the mode [43].

TAE growth due to fast particles is caused by the resonant interaction of the mode with the periodic transit of the passing energetic particles [44] [64] [65] [66] at the Alfvén speed and also at one third the Alfvén speed. The precessional magnetic drift

of trapped particles resonant with the TAE also contribute to its instability [67]. The growth rate of TAEs destabilized by alpha particles is given for the first time in [68]. The growth rate at the peak of the mode (near the center of the forbidden frequency gap) is given by [43]:

$$\frac{\gamma}{\omega_0} \approx \frac{9}{4} [\beta_\alpha (\frac{\omega_{*,\alpha}}{\omega_0} - \frac{1}{2}) F - \beta_e \frac{c_A}{v_e}]$$

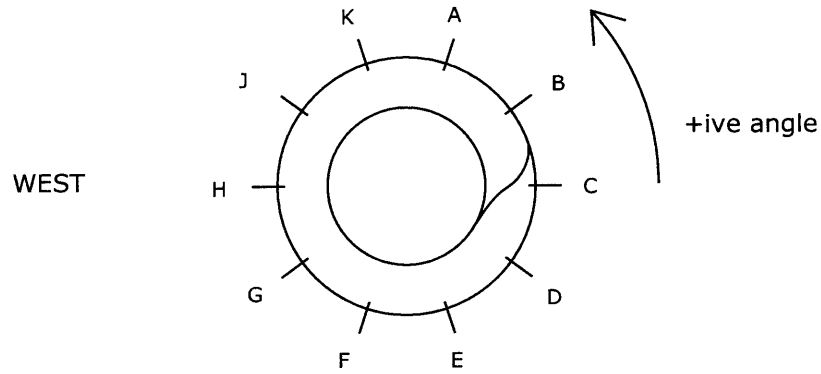
where

$$F(x) = x(1 + 2x^2 + 2x^4)e^{-x^2},$$

$$x = c_A/v_\alpha$$

and  $\omega_{*,\alpha}$  is the alpha particle diamagnetic drift frequency and is proportional to the toroidal mode number,  $n$  [67] [5],  $v_\alpha$  and  $v_e$  are thermal velocities, and  $\beta_\alpha$  and  $\beta_e$  are the ratio of kinetic to magnetic pressures for the respective species. Conditions for unstable TAEs are therefore that the alpha density scale length is small enough ( $\omega_{*,\alpha}/\omega_0 > \frac{1}{2}$ ) and that the alpha particle destabilization overcomes all combined damping effects, to be discussed next. This conclusion has been reached from a kinetic perspective [43] and is in agreement with a fluid/MHD formulation with kinetic modifications [69]. As well, stability criteria have been studied numerically using the computational solver NOVA-K [70], to be discussed shortly.

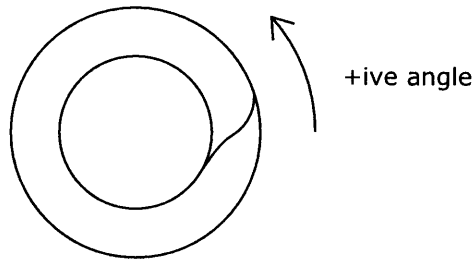
Exact scaling of the stability depends on the actual alpha particle distribution function and the toroidal mode number. For example, ICRF drive for TAEs should decrease as the resonance location moves inboard because the toroidal precession drift frequency decreases [71] [72] [73]. The growth rate induced by the circulating alpha particles increases linearly with the toroidal mode number  $n$  for small  $k_\theta \rho_\alpha$ , and decreases as  $1/n$  for  $k_\theta \rho_\alpha \approx 1$ , where  $\rho_\alpha$  is the alpha particle Larmor radius [5]. Therefore the most unstable modes have moderate toroidal mode number [45] with the mode rotating in the ion diamagnetic drift direction. In JET, modes that rotate in the usual ion diamagnetic drift direction have positive toroidal mode number, so unstable TAEs are expected to have positive  $n$ . When the field and current are reversed in occasional JET experiments to set the ion  $\nabla B$  drift away from the divertor, the



**C-Mod viewed from above**

	<b>usual field</b>	<b>reversed field</b>	
edge helicity		always as shown	
divertor location		bottom	
ion grad-B drift	down	up	Snipes, J.A., EPS 2006
port labelling	-ive	-ive	
magnetic field	-ive	+ive	
plasma current	-ive	+ive	Snipes, J.A., Phys. Plasmas 12, 056102
toroidal component of electron diamagnetic drift	+ive	-ive	
toroidal component of ion diamagnetic drift	-ive	+ive	
$v_{\text{phase}}$ for TAEs with $n > 0$	+ive	+ive	Snipes, J.A., Phys. Plasmas 12, 056102 Snipes, J.A., EPS 2006
$v_{\text{phase}}$ for fast ion-driven TAEs with centrally peaked $f_{\text{fast}}$	-ive	+ive	Snipes, J.A., Fus. Sci. Tech. 51, 437
core plasma rotation (ICRF)	-ive		Snipes, J.A., Fus. Sci. Tech. 51, 437
core plasma rotation (Ohmic)	+ive		Snipes, J.A., Nucl. Fusion 46, 1036

Figure 2-18: Toroidal conventions for C-Mod.



**JET viewed from above**

	usual field	reversed field	
edge helicity		always as shown	
divertor location		bottom	
ion grad-B drift	down	up	
magnetic field	-ive	+ive	
plasma current	-ive	+ive	Pitts, R.A., J. Nucl. Materials 337, 146
toroidal component of electron diamagnetic drift	+ive	-ive	Erents, S.K., Plas. Phys. Con. Fus. 46, 1757
toroidal component of ion diamagnetic drift	-ive	+ive	
v_phase for TAEs with $n > 0$	-ive	-ive	Fasoli, A., Plas. Phys. Con. Fus. 44, B159
v_phase for fast ion-driven TAEs with centrally peaked $f_{fast}$	-ive	+ive	Snipes, J.A., Fus. Sci. Tech. 51, 437

\* Testa, D., Nucl. Fusion 46, 829 contradicts the orientation of positive angle in JET. The orientation of the field and current described in that paper would put the divertor on the top of the machine. Photos online, however, show a person standing on the divertor without anti-gravity devices. The paper is assumed to be in error.

\* Note that the sign convention for the toroidal wavenumber of TAEs on JET is opposite the C-Mod convention.

Figure 2-19: Toroidal conventions for JET.

ion diamagnetic drift direction reverses. Then unstable TAEs are expected to have negative  $n$ . In C-Mod, the polarity convention for  $n$  is exactly opposite. Figures 2-18 and 2-19 elucidate this difference.

The precessional resonance of trapped particles makes a much larger contribution than the bounce resonance [5]. The safety factor profile also plays a role: reversed shear causing merged core modes could enhance alpha destabilization of TAEs [52]. Also, the least stable TAE for a monotonic  $q$  profile is at  $q=1.5$ , halfway between the  $m=1$  and  $m=2$  continua [71] [48] [74].

Since many tokamaks have finite ellipticity but small toroidicity and triangularity, the EAE may have potentially lower stability threshold than the TAE [51].

## 2.3 Consequences of TAEs

If the damping mechanisms are weak, fusion generated  $\alpha$ -particles may destabilize the TAEs in ITER [75], especially for moderate  $n$  [9] [76] and decrease the fusion gain or damage the first wall [77]. They can affect the orbits of the particles leading to anomalous transport [41] [60] [78] [45] and increase the reactivity required for ignition [12] [17]. Threshold TAE amplitudes as low as  $\delta B/B \approx 10^{-3}$  have been shown to cause significant alpha loss, using the simulation code NOVA-K [79]. Reduction in neutron rate and fast particle losses have been observed simultaneously with TAE activity [2]. However, other phenomena may sometimes be difficult to distinguish from TAEs: energetic particle modes in hollow  $q$ -profiles may appear to be TAEs [71] [72].

## 2.4 Experiment

Extensive experiments have been conducted on multiple machines to study the excitation, damping, and effects on fast ion redistribution associated with AEs. Figures 2-20, 2-21, 2-22 present a summary of prior experimental work in table form. A brief description of the primary achievements follows.

Figure 2-20: Table of prior active and passive MHD experimental results, part I.

JET C-Mod	Parameter of interest	Reference	Mode Type	Stability	Heating	Config	Behavior
<b>existence of...</b>							
GAEs		Testa, D., Nucl. Fusion 43, 724	n=0 GAE	stable	NBI	limited	observed for P_NBI > 4MW AMHD antennas in-phase
		Testa, D., Nucl. Fusion 41, 809	n=0 GAE	stable	Ohmic	limited	
Alfven Cascades		Snipes, J.A., Plas. Phys. Cont. Fus. 42, 381	RSAE	unstable	ICRF	current rise	indicates flat or reversed shear
kinetic TAEs		Fasoli, A., Nucl. Fusion 35, 1485	KTAE	stable	ICRF, NBI, LH, Ohmic		modes appear above the TAE gap
<b>radial eigenfunction measurement via...</b>							
bulk rotation profile		Testa, D., Phys. Plasmas 9, 243	n=4-12 TAE	unstable	ICRF, NBI	OS	inferred Doppler shift radially locates mode via measured rotation profile
ECE cross-correlation		Testa, D., Phys. Plasmas 9, 243	n=4-12 TAE	unstable	ICRF, NBI	OS	radial localization via correlation of ECE cords with magnetic signal
relative frequency fluctuations		Fasoli, A., Plas. Phys. Cont. Fus. 39, B287	n=3-6	unstable	ICRF, NBI	OS	differential frequency fluctuations among modes reflect radial separation
<b>damping dependence on...</b>							
$q(r)\rho(r)^{1/2}$ (equilibrium profiles)		Fasoli, A., Phys. Rev. Lett. 75, 645	n=2 TAE	stable	Ohmic	limited	balance of damping mechanisms is extremely sensitive to q, n profiles
ion grad-B drift direction		Testa, D., Nucl. Fusion 46, 829	n =3-10 TAEs	unstable	ICRF	diverted	damping is greater for ion grad-B drift away from the divertor damping is greater for ion grad-B drift away from the divertor damping is weaker for ion grad-B drift away from the divertor
		Testa, D., Plas. Phys. Cont. Fus. 46, S59	n=1 TAEs	stable	Ohmic	limited	
		Snipes, J.A., EPS 2006	TAE	stable	Ohmic	diverted	
$q_0$ (safety factor on axis)		Testa, D., Nucl. Fusion 45, 907	n=1	stable	Ohmic	limited	damping < 2% for $q_0 > 0.9$ and low edge shear
$\langle s_{rot} \rangle$ (eigenfunction-averaged toroidal rotation shear)		Testa, D., Nucl. Fusion 45, 907	n=1	stable	NBI	diverted	damping > 2% for $\langle s_{rot} \rangle > 0.55$ and $P_{NBI} > 6.5$ MW.
$\sigma_{edge}$ (edge safety factor shear)		Testa, D., Plas. Phys. Cont. Fus. 46, S59	n =3-10 TAE	unstable	NBI	div, lim	instability threshold is lower in low-sigma-edge (limited) plasmas than in high-sigma-edge (diverted) plasmas. damping is lower in high-sigma-edge (diverted) plasmas, than in low-sigma-edge (limited) plasmas. no clear dependence
		Snipes, J.A., Plas. Phys. Cont. Fus. 46, 611	n=4 TAE	stable	Ohmic	div, lim	
		Snipes, J.A., Phys. Plasmas 12	TAE	stable	Ohmic	limited	
$\kappa_{95}$ (elongation near edge)		Testa, D., Nucl. Fusion 41, 809	n=1 TAE, n=0 GAE	stable	Ohmic	limited	damping increases with elongation damping decreases with elongation
		Snipes, J.A., Phys. Plasmas 12	TAE	stable	Ohmic	limited	
$\delta$ (triangularity)		Testa, D., Nucl. Fusion 41, 809	n=1 TAE, n=0 GAE	stable	Ohmic	limited	damping increases with triangularity
$\beta_n (2\mu_0\rho/B^2)/(I/aB)$		Testa, D., Nucl. Fusion 43, 724	n=1 TAE	stable	NBI	limited	damping increases with increasing $ \beta_n - 0.4 $ damping increases with increasing $\beta_n$
		Snipes, J.A., EPS 2006	TAE	stable	ICRF		
$\rho_{*e} = \rho/a$ (normalized ion gyroradius)		Testa, D., Nucl. Fusion 43, 479	n=1 TAE	stable	Ohmic	limited	damping decreases (remains constant) for increasing $\rho_{*e} > (<) 3.2e-3$ damping increases with increasing $\rho_{*e}$
		Snipes, J.A., EPS 2006	TAE	stable	Ohmic, ICRF		
$A_{eff}$ (effective ion mass)		Fasoli, A., Phys. Let. A 265, 288	n=1 TAE	stable	Ohmic	limited	damping decreases with increasing effective ion mass.
outer gap		Snipes, J.A., Plas. Phys. Cont. Fus. 46, 611	TAE	stable	Ohmic	limited	damping increases with outer gap > 1cm resonances are detected only for outer gap < 1cm, and damping rate is independent.
		Snipes, J.A., Plas. Phys. Cont. Fus. 46, 611	TAE	stable	Ohmic	diverted	
$\nu_{*e}$ (collisionality)		Snipes, J.A., EPS 2006	TAE	stable	Ohmic		no dependence damping decreases with increasing $\nu_{*e} < 0.1$
		Snipes, J.A., EPS 2006	TAE	stable	ICRF		
$f_{fast}$ (fast particle distribution)		Fasoli, A., Plas. Phys. Cont. Fus. 39, B287	n=0 GAE	stable	ICRF	limited	waves Landau damp on sub-resonant ions

Figure 2-21: Table of prior active and passive MHD experimental results, part II.

JET C-Mod	Parameter of interest	Reference	Mode Type	Stability	Heating	Config	Behavior
<b>f_fast excitation dependence on...</b>							
	multi-frequency ICRF	Testa, D., Plas. Phys. Cont. Fus. 46, S59	EAE, TAE	unstable	ICRF		polychromatic heating flattens f_fast and bears TAEs of lower amplitude
	T_fast	Testa, D., Plas. Phys. Cont. Fus. 46, S59	n=5-8 TAE	unstable	ICRF		T_fast is lower and TAE drive is weaker at high densities.
	radial fast ion redistribution	Testa, D., Plas. Phys. Cont. Fus. 46, S59	n=3-5 TAE, EAE	unstable	ICRF		error-field-induced radial redistribution of fast ions reduces eigenmode excitation more effectively in the core.
	radius of ICRF deposition	Snipes, J.A., Phys. Plasmas 12, 056102	TAE	unstable	ICRF		f_fast from inboard RF deposition delivers less excitation than f_fast from on-axis or outboard.
	ICRF power	Snipes, J.A., EPS 2006 Fasoli, A., Plas. Phys. Cont. Fus. 39, B287	TAE n=1 TAE	stable stable	ICRF ICRF	limiter	no clear dependence excitation increases with P_ICRF
	particle drive optimization	Fasoli, A., Phys. Plasmas 7, 1816 Fasoli, A., Phys. Plasmas 7, 1816	TAE TAE	unstable unstable	ICRF ICRF, NBI	OS OS	ITB and large q(0) permit strong nonlinear evolution, with drive >> damping. transient growth by sweeping across f_fast to avoid depletion
	Y_excitation distinguished from Y_damping	Fasoli, A., Plas. Phys. Cont. Fus. 39, B287	AE	stable	ICRF, NBI		compare standing waves: excitation depends on n/ n , while damping does not.
<b>MHD spectroscopy of...</b>							
	q_min(r) evolution	Testa, D., Rev. Sci. Inst. 74, 1694 Snipes, J.A., Phys. Plasmas 12, 056102	Alfven Cascades Alfven Cascades	unstable unstable	ICRF ICRF	current rise current rise	AC onset signals rational q_min AC onset signals rational q_min
	reversed current	Testa, D., Rev. Sci. Inst. 74, 1694	Alfven Cascades	unstable	ICRF	current rise	negative helicity ACs indicate reversed current
	sawtooth inversion localization	Snipes, J.A., EPS 1999	TAE	unstable	ICRF		core TAE frequency increases after collapse
	sawtooth redistribution of f_fast	Fasoli, A., Plas. Phys. Cont. Fus. 44, B159	TAE	unstable	ICRF		mode attenuation indicates flattened beta_fast at sawtooth crash
	alpha(r) (shear profile)	Snipes, J.A., Phys. Plasmas 12, 056102	-10 < n < -8 TAEs	unstable	ICRF	double null	coalescing of mode frequencies, narrowed gap, indicate peaked current density
	q(0) (safety factor on axis)	Fasoli, A., Plas. Phys. Cont. Fus. 44, B159	n=1 TAE	stable	Ohmic	limited	frequency separation of multiple modes reveals gap width, evidence for q(0)
	fast particle sawtooth stabilization	Snipes, J.A., Fus. Sci. Tech 51, 437	TAE	unstable	ICRF	double null	destabilization of TAEs shortly precedes sawtooth stabilization
	ICRF absorption regime	Snipes, J.A., Fus. Sci. Tech 51, 437 Fasoli, A., Plas. Phys. Cont. Fus. 44, B159 Fasoli, A., Plas. Phys. Cont. Fus. 44, B159	TAE TAE TAE	unstable unstable unstable	ICRF ICRF ICRF, NBI	diverted	disappearance of unstable modes at high H/D signals electron heating via mode conversion disappearance of unstable modes indicates weakened H minority heating unstable mode onset implies sufficient NB seed ion energy in He^4 3rd harmonic heating
	hollow f_fast	Snipes, J.A., Fus. Sci. Tech 51, 437 Eriksson Phys. Rev. Lett. 81, 1231	TAE TAE	unstable unstable	ICRF ICRF	diverted OS	rotation in electron diamagnetic drift direction is hastened by outward-directed local grad-f_fast rotation in electron diamagnetic drift direction is hastened by outward-directed local grad-f_fast
	f_fast phase space diffusion	Fasoli, A., Plas. Phys. Cont. Fus. 44, B159	n=7 TAE	unstable	ICRF		amplitude evolution depends on fast particle phase space depletion/restoration
	T/D ratio	Fasoli, A., Plas. Phys. Cont. Fus. 44, B159	n=1 TAE	stable	Ohmic	limited	T concentration derived from mode frequency normalized by D-D calibration.
	D-T alpha production	Fasoli, A., Phys. Plasmas 7, 1816	TAE	unstable	fusion		absence of AEs implies below-threshold alpha production
	pellet-induced rotation and density fluctuations	Fasoli, A., Phys. Plasmas 7, 1816	TAE	unstable	ICRF, NBI		fluctuations are derived from differential frequency variation among modes of various n

Figure 2-22: Table of prior active and passive MHD experimental results, part III.

ASDEX DIII-D NSTX TFTR	Parameter of interest	Reference	Mode Type	Stability	Heating	Config	Behavior
<b>fast ion transport induced by...</b>							
TAE-induced beam ion loss		Garcia-Munoz, M., Rev. Sci. Inst. 80	TAE	unstable	ICRF, NBI		lost-ion scintillator spectrogram clearly shows TAE decreased neutron emission (scintillator), increased fast ion losses (bolometer). graphite redeposition are repeatedly coincident with intense TAE
		Duong, H.H., Nucl. Fusion 33, 749	TAE	unstable	NBI	limited	
		Fredrickson, E.D., Phys. Plasmas 13	n=3,4 TAE	unstable	NBI	ST	
TAE-induced loss of ripple trapped ions		White, R.B., Phys. Plasmas 2, 2871	TAE	unstable	ICRF		vessel components were melted, coincident with TAE activity. fast ion losses are implicated.

**Notes**

1. It is given that toroidally-distributed active MHD systems can measure the complex frequency coordinates and toroidal structure of stable modes. Thus no references are provided for these tasks.
2. Some results may previously have been achieved on TCA, PETULA and TEXTOR active MHD systems.
3. While MAST has recently installed an active MHD system, first physics results beyond Gryaznevich, Nucl. Fusion 48, 084003 have yet to be published.
4. This table is not exhaustive, especially when it comes to observations of fast-particle-driven unstable Alfvénic activity. It does, however, demonstrate the wide variety of plasma parameters that can affect Alfvén activity, the significant attention the subject has received, and the maturity of the field.
5. Where conditions have not been reported in the referenced publication, they are left blank in the table.
6. OS: the Optimized Shear configurations in JET have flat or reversed shear that facilitates the formation of an internal transport barrier (ITB).
7. ST: NSTX is a Spherical Tokamak, characterized by a low aspect ratio and high beta.



### 2.4.1 Computer Models

Several numerical codes have been assembled to simulate tokamak plasmas [71]. A brief description of each is given.

NOVA-K [80] is a nonvariational kinetic-MHD stability code based on the original ideal-MHD code NOVA [81]. It can predict finite drift orbit width and Larmor radius effects [71] [82]. Slightly distinct versions are maintained by N. Gorelenkov and G. Kramer, both of PPPL.

The MISHKA-H code includes indirect effects of hot ions in an MHD approach [83] based on the ideal-MHD code MISHKA-D [84]. MISHKA-D included the finite gyroradius stabilizing effect of ion diamagnetic drift frequency. The original ideal-MHD version was MISHKA-1 [85].

TRANSP is a comprehensive time-dependent transport analysis code incorporating many dedicated components, seemingly originating from [86] and [87], and summarized in [88]. The best source of references is [89].

To predict the effects of ICRF heating, the TORIC full-wave code for Ion Cyclotron waves [90] [91] as well as AORSA [92] and CQL3D [93] may be useful.

### 2.4.2 Passive TAE Measurements

When a sufficient gradient of energetic particle density exists, it can provide enough excitation to overcome the TAE damping terms. The resulting TAE is unstable and attains an amplitude for which the drive and damping terms are balanced. Such a spontaneous mode can be induced by supplying adequate energetic particle densities with ion-cyclotron radio frequency (ICRF) heating or neutral beam injection (NBI), or by alpha particles produced in fusion reactions. The mode can be detected by magnetic field probes or density measurements, such as phase contrast imaging (PCI) [94].

Unstable AEs have been studied in TFTR [95], DIII-D [15], JT-60U [96], JET [74], and W7-AS [97]. AE activity driven by energetic particles has been reported for NBI or ICRF heated discharges in various tokamak experiments [98] [95] [99]. A detailed

description of a magnetic measurement setup is given in [100]. TAEs led incrementally towards instability by fusion generated alphas have been observed in TFTR [101]. AEs have been observed during reduced sawtooth stabilization, indicating that fast particles are present. They have also been observed to eject fast particles from the core [102] [103] [104] [105]. The fast particles may be responsible for stabilizing the sawteeth [106]. Low shear was achieved by lower hybrid current drive (LHCD), affecting the alignment of the continuum gaps [50]. TAEs have also been observed with diagnostics other than magnetic coils [107].

### 2.4.3 Active MHD Excitation and Measurement

Passive TAE studies provide frequency and mode spectra as well as some information on instability thresholds, but cannot provide quantitative estimates of damping and driving of the Alfvén eigenmodes [17]. TAEs can be actively excited by generating perturbative magnetic fields near the resonant frequency with antennas outside of the plasma. Furthermore, the frequency of excitation can be varied to express the bandwidth of the resonances, which is directly related to the net damping rate. Plasma parameters that affect the TAE damping rate can thereby be estimated, a process known as MHD spectroscopy.

Early MHD spectroscopy was conducted on the TCA and PETULA experiments for Discrete Alfvén Waves (DAWs). Alfvén waves were launched by antennas and detected by magnetic field probes. The frequency at resonance allowed estimates of core current and mass densities using 1-D models of the modes. A heterodyne detection system was used to detect the resonances with an excellent signal to noise ratio. The system also permitted frequency tracking with a phase-locked loop to provide better frequency resolution [108] [109]. Similar experiments were conducted in TEXTOR [110].

More recent active MHD studies have been carried out on the JET and C-Mod tokamaks. The active MHD diagnostics on these machines also employ amplifier fed current winding antennas and arrays of Mirnov type magnetic pickup coils. They use a signal processing scheme called synchronous detection, which differs from hetero-

dyning but bears similarity to interferometry. Synchronous detection is performed in real-time at JET [74] and after each shot at C-Mod, and the resulting empirical system function is fit to a parametric model (a ratio of polynomials with real coefficients) to find the damping rate, resonant frequency and toroidal and poloidal structure of the mode [111]. Notable results from each machine are described in the next two sections.

#### 2.4.4 Active MHD on JET

The original JET active MHD diagnostic comprises 8 saddle coils generating 3kW in the range of 20 to 500 kHz, covering the BAE, TAE and EAE range. The antenna field has been modeled, and among the findings it was found that the field perturbation would be small  $dB/B_{tor} < 10^{-5}$ ; the most effectively driven mode would be at  $q=1.5$  [112], [113]. TAEs with  $n \leq 2$  are excited [17], [114], [115]. For an observed mode of 144kHz and damping of 1%, the maximum oscillating field measured was  $10^{-7}$ T and the frequency scaled with the toroidal field and inversely with the root of the density, indicating that these are TAEs. Ion Landau damping is small for Ohmic discharges considered in JET but electron Landau damping may be significant. In cases with aligned gap structures the damping was much smaller ( 0.5%) than when the gap structure had stronger radial dependence and continuum damping dominated [74]. The measurement of the mode damping rate as a function of various plasma parameters, in order to quantify the mechanisms that provide a background damping for the AEs in different operating regimes is reported in [116].

A clear dependence of damping on plasma shape and edge magnetic shear was observed. Damping increased with increased edge magnetic shear caused by increased triangularity or elongation [117], [118]. In diverted JET plasmas the damping rate exceeded 5-10% [119]. For low  $n \leq 2$  the measured damping rate increased with increasing edge shear [114]. For  $q_0 > 1.1$  the damping rate of  $n=1$  TAEs did not exceed  $\gamma/\omega \approx 2\%$ , but for  $q_0 < 0.9$  damping can be as high as 8%, suggesting that regimes with low  $q_0$  are less prone to low- $n$  TAE instabilities. Since the transition coincides with the  $q=1$  kink instability threshold, it suggests a role in destabilizing

the TAEs for the sawtooth-redistribution of the plasma current [120].

New antennas with narrower toroidal extent and broad toroidal mode number spectrum have recently been installed on JET. The antennas have been found to excite both low and moderate- $n$  modes, with  $|n| = 1 - 10$  [8].

### 2.4.5 Active MHD on Alcator C-Mod

This thesis examines active MHD experiments in C-Mod. Prior to this work, substantial results had already been obtained with the existing active MHD equipment.

The C-Mod active MHD diagnostic consists of two 15 cm wide antennas that generate magnetic fields having toroidal widths primarily in the range  $5 \leq n \leq 40$ . The amplifiers supply each antenna with 20A across a wide range of frequencies, with tuning flexibility provided by a capacitive tuning network [121]. The higher  $n$  modes expected from the relatively narrow antennas resonate at slightly lower  $q$  values, with mode frequencies a bit higher than those calculated for  $q = 1.5$ . TAEs with perturbations of  $B_\theta = 10^{-6}$  T and moderate toroidal mode number ( $4 \leq n \leq 14$ ) are excited in plasmas with ITER-like field and density. A complete description of the C-Mod active MHD experimental apparatus is provided in the next Chapter.

The damping rate is larger for inner wall limited discharges with larger outer gaps than for diverted discharges with outer gaps of less than 1 cm. For limited plasmas with  $\kappa_{edge} = 1.3$ , TAEs have been observed with damping rates in the range of  $1.4\% < \gamma/\omega < 4\%$ , in the same range as JET inner wall limited plasmas [117]. For diverted plasmas of  $\kappa_{95} = 1.6$  and outer gaps less than 1 cm, TAEs were observed to have damping rates in the range  $0.4\% < \gamma/\omega < 1.4\%$  [12]. An elongation scan with  $q = 1.5$  inner wall limited discharges and toroidal field ramping found no clear dependence of damping rate on edge shear, in contrast to increased damping with increased shear found on JET [71].

The damping rate does not increase for  $n = 6$  modes with increasing triangularity, in contrast to the JET result for  $n = 1$  where increased triangularity increases the damping rate. This suggests that the radial structure of moderate  $n$  modes is not dominated by edge shaping effects as expected for the low  $n$  modes. When comparing

lower single null (LSN) to upper single null (USN) diverted discharges, the measured damping rates vary from  $2\% < |\gamma/\omega| < 7\%$  in LSN and from  $3\% < |\gamma/\omega| < 8.5\%$  in USN. This is again in sharp contrast with the JET result for  $n = 1$  modes where the damping rate is 3 times higher when the ion  $\nabla B$  drift is directed away from the divertor. Note, however, that the  $n$  numbers are not all clearly defined for these resonances in C-Mod, so changes in the mode number could also affect the damping rate. This suggests that edge effects on the damping of moderate  $n$  modes are not as strong as for low  $n$  modes.

The collisionality has been varied over a range from  $0.02 < \nu_{*e} < 0.3$  and while there is no clear variation in damping rate at high collisionality, the damping rate appears to increase substantially at very low collisionality. The normalized ion gyroradius was varied over a range from nearly  $0.005 < \rho_{*i} < 0.01$  and the damping rate appears to increase with increasing  $\rho_{*i}$ . Beta was varied over the range  $0.3 < \beta_N < 0.9$ , showing slightly increased damping rates with increasing  $\beta_N$  [122], [6].

The importance of distinguishing between toroidal modes when making parameter comparisons should be emphasized. This thesis focuses on results obtained after new coils with wider toroidal spacing had been installed to increase the resolution of low and moderate  $n$  toroidal mode numbers.

## Chapter 3

# The Active MHD Diagnostic

As discussed in the previous section, the tokamak plasma is susceptible to toroidicity-induced Alfvén eigenmodes (TAEs), stable discrete MHD modes with low damping at frequencies in forbidden gaps in the Alfvén frequency continuum that arise due to poloidal coupling. The modes can attain considerable amplitudes in the presence of an energy source such as a significant fast particle gradient. They are observed in C-Mod and are expected to occur in ITER. At high amplitudes, the modes can enhance transport of fast particles, which can increase the heat flux on the vessel and could degrade the fusion gain in a burning plasma.

To observe these modes, the active MHD diagnostic weakly excites them and then measures the plasma response. It can evaluate the parameters that identify the TAEs including their frequency, damping rate and mode structure. These parameters depend on plasma conditions, and the TAE amplitude depends on the energy distribution and density profile of fast particles. With an understanding of these dependencies, the modes could be controlled to limit their impact or even harnessed as tools to redistribute energetic particles or as indicators of the plasma condition.

This chapter describes the equipment and operation of the active MHD system. First the principle of the diagnostic is introduced. The second section describes the hardware, including the amplifier system, the antennas, the magnetic probes, the control network, and the data collection hardware. The critical design parameters and resultant performance of each component are emphasized.

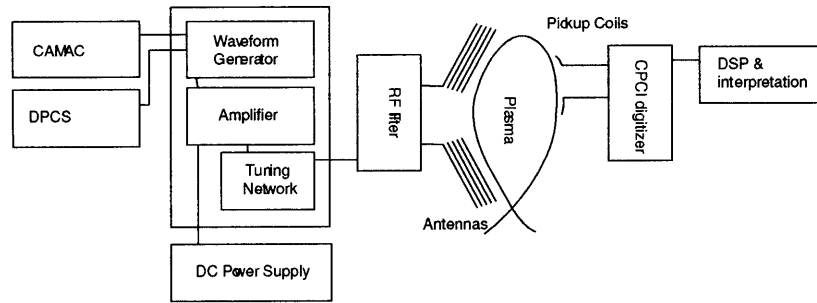


Figure 3-1: A schematic of the active MHD system shows the apparatus used to excite, detect and analyze TAEs.

Analysis techniques and the significant limiting factors of noise, spatial sampling rate and the hardware frequency response are reserved for Chapter 4. Complete derivations of the uncertainty calculations are provided in Appendix A.

### 3.1 Principle of Operation and System Overview

The active MHD diagnostic resonantly excites TAEs with two antennas that weakly perturb the equilibrium magnetic field through the frequency range in which the modes are expected to exist, 150 kHz to 1 MHz. An array of poloidally-oriented magnetic pickup coils positioned very close to the plasma edge detects the plasma response. The pickup coil signals are fed to electronics outside of the tokamak, where they are digitized and stored. The digital signals are later processed in the vicinity of the TAE resonance to identify its damping rate, frequency and mode number. This chapter presents a detailed description of the active MHD equipment and procedure, separated into the sections depicted in the system diagram of Figure 3-1. The system will be described in order of process flow, starting with the setup of the plasma shot, the excitation and measurement of the modes, the digital processing of raw signals and finally the derivation of quantities of interest from the processed data.

## 3.2 Excitation

During the plasma shot, the active MHD system perturbs the equilibrium magnetic field in the frequency range from 150 kHz to 1 MHz to excite TAE modes. The perturbing magnetic field is generated by versatile variable-frequency amplifiers driving a pair of antennas inside the vacuum vessel.

### 3.2.1 Amplifiers

The active MHD amplifiers were specifically designed for this application by Bill Burke [123]. They are digitally controlled arbitrary waveform bipolar current sources with a maximum output voltage of  $\pm 130$  V and a maximum output current of  $\pm 23$  A. The class AB output stage consists of four parallel common-drain N-channel MOSFETs and four parallel common-source N-channel MOSFETs. Each transistor is connected to the output by a protective current-limiting  $22 \Omega$  resistor in series. During the cycle while half of the transistors are in saturation, the other half are cutoff, so the amplifiers have an effective output resistance of  $5.5\Omega$ . Figure 3-2 shows a simplified circuit diagram of one amplifier. The amplifiers generate an approximately sinusoidal current waveform into a  $1 \Omega$  load as shown in Figure 3-3(a) by individually modulating the duty cycle of each MOSFET. Figure 3-3(b) shows that the spectrum is localized almost entirely in the fundamental; the fifth harmonic contains 0.013% of the energy, while the third, seventh and ninth harmonics are negligible. Because the bandwidth of the amplifier/antenna system is narrow, the harmonics encounter a much larger impedance and are easily filtered out. The perturbing magnetic field can therefore be considered as essentially sinusoidal in time.

The amplifiers include a capacitive tuning network at their output to match them to the largely inductive load of the antennas. The tuning network is illustrated in Figure 3-2, showing that nine capacitors of various sizes can be selectively combined to negate the antenna reactance at each frequency. At frequencies below 35 kHz where the antennas are mostly resistive, they can be directly connected to the amplifier output stages by a short across the capacitors.



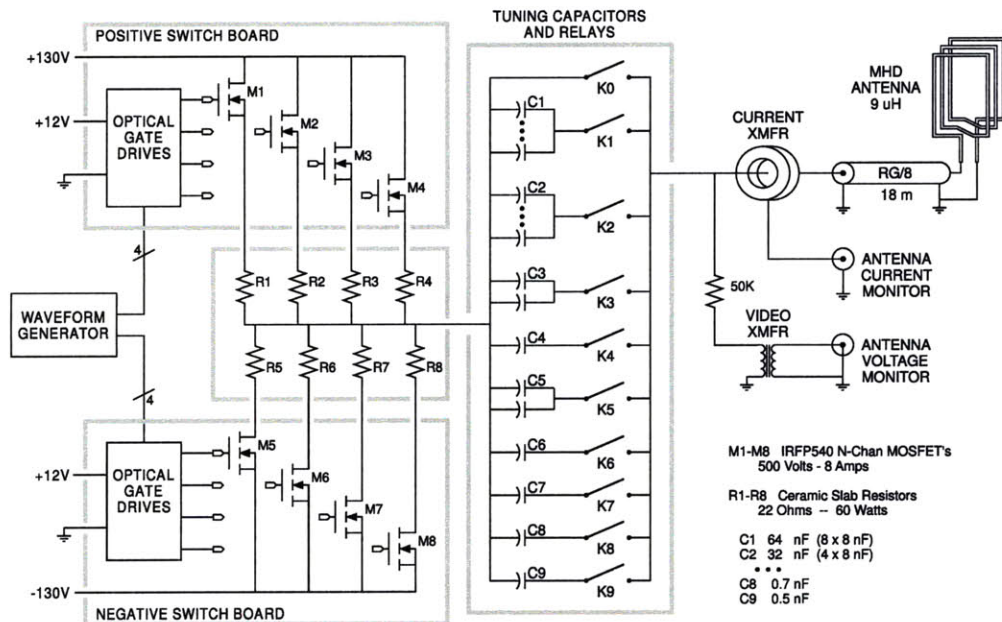


Figure 3-2: Each active MHD amplifier is composed of 8 N-channel MOSFETs. They can source  $\pm 130\text{V}$  and safely drive 23 A into a short. The effective output impedance is  $5.5\Omega$ . A capacitive variable tuning network at the output of each amplifier matches the amplifier to the antenna impedance.

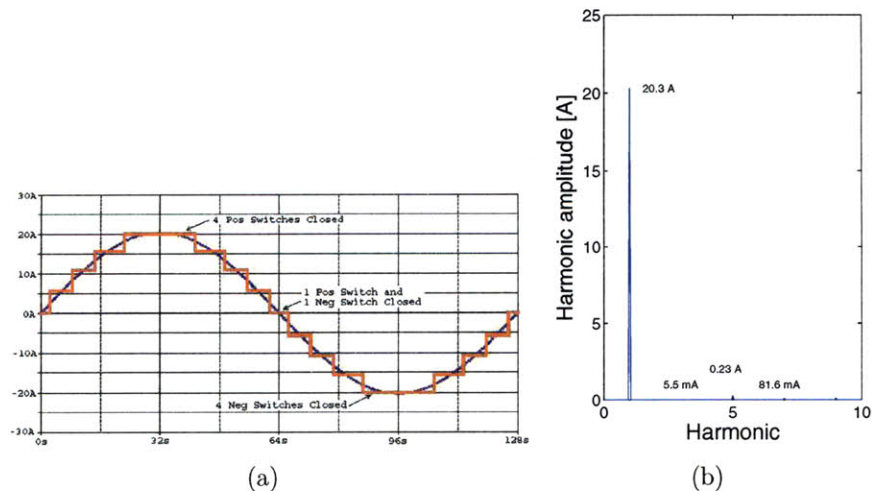


Figure 3-3: a) A simulation of the modulated MOSFET pulses. b) The corresponding calculated spectrum with very small harmonics, which is further filtered by the output stage and the antenna itself.

The capacitors are switched by mechanical relays with a switching time of about 20 ms during which the amplifier output is not reliable; at a frequency sweep rate of  $1.5 \text{ MHzs}^{-1}$  this corresponds to a 30 kHz dead band. To avoid constantly operating in a switching dead band, the amplifier/antenna must have a bandwidth significantly wider than 30 kHz. At the expense of current amplitude, the bandwidth is increased to 115 kHz by increasing the amplifier output impedance to  $5.5 \Omega$ :

$$\Delta f = \frac{R}{2\pi L} = \frac{5.5 + 1\Omega}{2\pi 9\mu H} = 115 \text{ kHz}.$$

To further decrease the interference of dead bands during resonances, the tuning network is programmed to switch only when the frequency sweep changes sign at the edges of the range.

The tuning is also affected by a 16 m length of transmission line that is required to connect the amplifiers, located in the northwest basement of the cell, to the antennas via H port. The transmission line effectively increases the inductance of the antenna seen at the amplifier, decreasing the bandwidth but beneficially increasing the current in the antenna. Figure 3-4 shows the calculated frequency response with and without the transmission line, illustrating that the effect of the transmission line becomes more acute at higher frequencies. The current in the antennas is given by

$$I_{ant} = \frac{v_{amp}}{R_s + \frac{1}{j\omega C_s} + Z(l)} e^{jkl} \frac{[1 - \Gamma_L]}{[1 - \Gamma_L e^{j2kl}]}$$

where

$$Z(l) = Z_0 \frac{1 + \Gamma_L e^{j2kl}}{1 - \Gamma_L e^{j2kl}}$$

$$\Gamma_L = \frac{Z_L - Z_0}{Z_L + Z_0}$$

and  $v_{amp} = 130V$  is the amplifier voltage;  $R_s = 5.5\Omega$  is the amplifier resistance;  $C_s = 1 \rightarrow 100nF$  is the matching network capacitance;  $Z_L = R + j\omega L = 1 + j\omega 9 \times 10^{-6}\Omega$  is the antenna impedance;  $Z_0 = 50\Omega$  is the characteristic impedance of the antenna

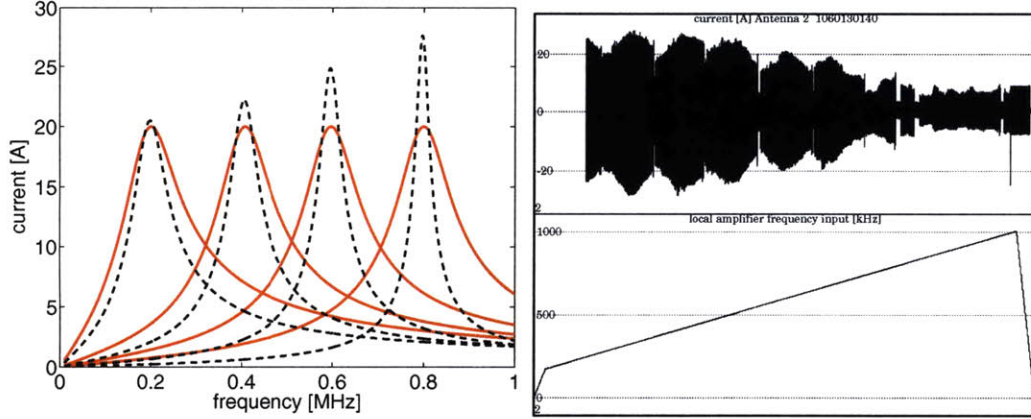


Figure 3-4: Figure a: The calculated antenna current with (dashed black curves) and without (solid red curves) a 20m transmission line over the frequency range of operation. Figure b: The actual current amplitude measured at the antenna end of the transmission line during a ramped-frequency test shot. While the maximum simulated current increases at higher frequencies, the actual maximum current decreases at higher frequencies due to operational limits of the amplifier such as MOSFET capacitance.

feeding lines;  $k = \omega/v_p$  is the wavenumber in the lines with  $v_p = 2/3c$  the phase velocity; and  $l = -16m$  is the length of the lines.

The amplifiers are not controlled directly by the settings in the tree or by the DPCS. Instead, the control is abstracted by a waveform generator in a separate chassis that produces the MOSFET gating and capacitive tuning relay signals. Table 3.1 lists these signals as well as the input parameters that control the waveform generator and their sources.

### 3.2.2 Antennas

The antennas are located inside the vacuum vessel on the H side of the GH limiter (Figure 3-5). They are positioned only 2-3 cms from the last closed flux surface at the closest point to penetrate as much flux as possible into the plasma. The antennas mirror each other about the midplane, and the plane of their coils is tilted  $30^\circ$  from vertical to be tangent to the flux surface near their center. Each antenna consists of five  $150\text{ mm} \times 250\text{ mm}$  rectangular turns of stainless steel plate conductor with a cross-section of  $3\text{ mm} \times 6\text{ mm}$  (Figure 3-6). The turns are separated by insulating

Table 3.1: Input and output control parameters of the waveform generator

<b>input</b>	<b>source</b>	<b>range</b>
TAE frequency	DPCS	1V = 100kHz (fibre)
DPCS excitation frequency	DPCS	1V = 100kHz (fibre)
CAMAC excitation frequency	CAMAC	1V=100kHz
hybrid_local	J221.OUTPUT_09	TTL
rfenable	J221.OUTPUT_05	TTL
powersupplyon	J221.OUTPUT_06	TTL
powersupplyoff	J221.OUTPUT_07	TTL
powersupplyreset	J221.OUTPUT_10	TTL
<b>output</b>	<b>number of channels</b>	<b>destination</b>
MOSFET gating	8	amplifiers
tuning relay gating	10	capacitive tuning network

ceramic coated washers and are secured to a stainless steel frame by ceramic coated studs. The frame is constructed of 16 mm square stainless steel stock to withstand  $J \times B$  disruption forces. In the past, the antennas have been shielded from the plasma heat flux by boron nitride tiles, but these have been removed due to concerns over their role in degrading plasma performance. The antennas continue to survive and operate properly without the boron nitride tiles.

The antennas have a resistance of  $0.4 \Omega$  at low frequencies and an inductance of  $9 \mu\text{H}$ . The resistance increases above 100 kHz when the skin depth diminishes to 1.5mm, and is  $2 \Omega$  at 1 MHz. The skin depth of stainless steel is given by

$$\delta = \sqrt{\frac{2\rho}{\omega\mu}}$$

$$f_{\delta=1.5\text{mm}} = \frac{\rho}{\pi\delta^2\mu} = 81\text{kHz}$$

where  $\rho = 72 \times 10^{-8} \Omega\text{m}$  is the resistivity of stainless steel and  $\mu = 4\pi \times 10^{-7} \text{Hm}^{-1}$  is its permeability.

Each antenna is designed to generate a magnetic field that penetrates into the plasma to couple the TAEs as much as possible. Near the antenna the field decays as  $\frac{1}{r^2}$ ; beyond about 15 cm, the antenna resembles a dipole and the field decays like

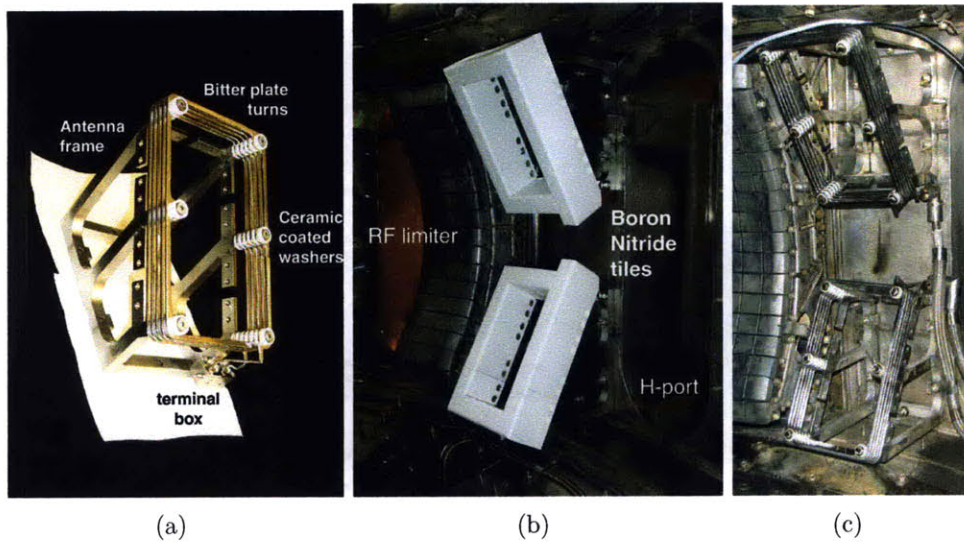


Figure 3-5: Photos of the antennas. a) The upper antenna before installation and without boron nitride tiles. b) The installed antennas protected by boron nitride tiles, which were removed before the 2006 campaign due to concerns about their role in reduced plasma performance. c) The antennas without boron nitride tiles as installed for the 2006 campaign.

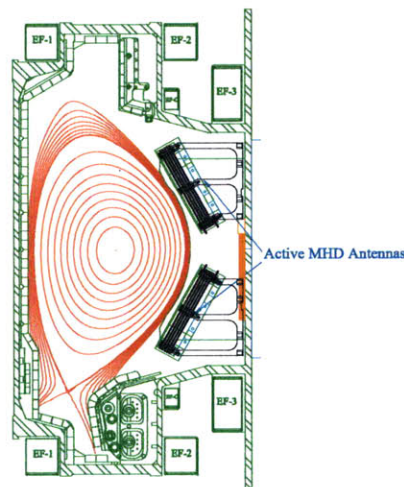


Figure 3-6: The active MHD antennas located between ports G and H are positioned only millimeters outside of the last-closed flux surface.

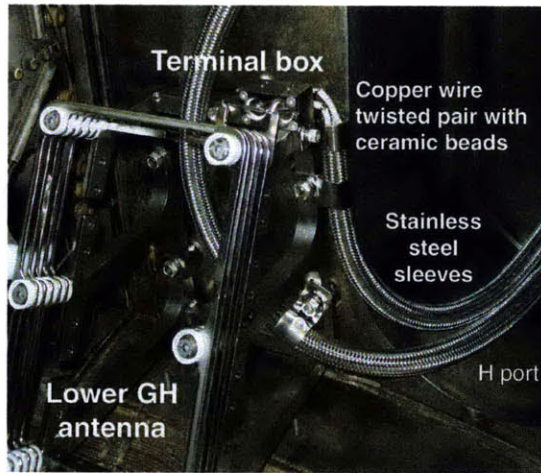


Figure 3-7: A closeup photo of the electrical connection at the antenna. The antennas make an electrical connection outside of the vacuum vessel via coaxial feedthroughs, with the outer conductor grounded to the machine at the feedthrough to reduce guidance of ICRF pickup into the cell.

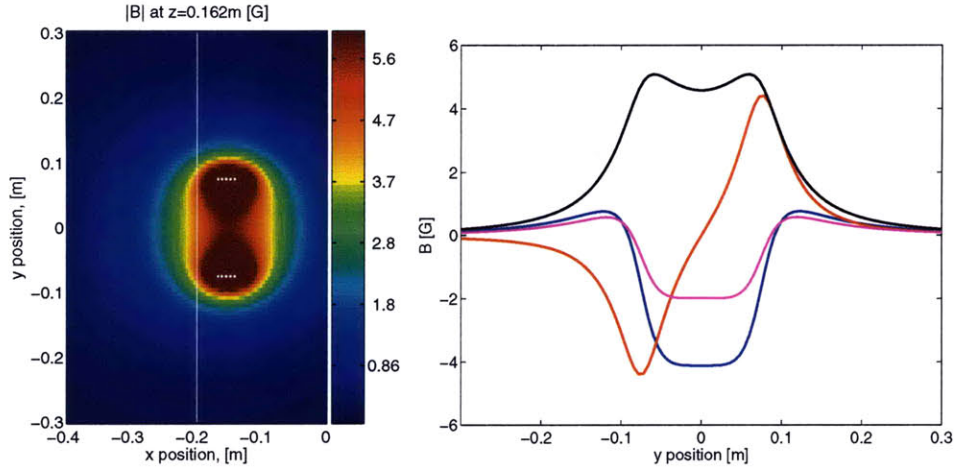
$\frac{1}{r^3}$ . The field at the last closed flux surface can reach 5 G, which represents only 0.01% of the equilibrium magnetic field. The magnetic field strength on a horizontal plane through the midpoint of the upper antenna (16.2 cm above the midplane) is plotted in 3-8(a), representing the field when the antenna conducts 20A. The white dots show the cross-section of the antenna turns in that plane. Similarly, the field strength along a vertical plane that bisects the antennas is shown in 3-8(c). Here, the profile of the antenna turns is drawn in white. Each of these figures also depicts in white features a line tangent to the last closed flux surface along which the cartesian field components in the frame of the antennas have been plotted, in Figure 3-8(b).

To estimate how strongly the antennas couple to the TAEs, the structure of the field generated by the antennas can be compared to the TAE structure. In particular, the toroidal mode spectrum of the antenna field should indicate which toroidal modes are excited by the antenna. The toroidal mode spectrum of the total field along the tangent line is shown in Figure 3-8(d), where the tangent line was approximated to be a segment of a circle with major radius  $R = 85\text{cm}$  and  $z = 16.2\text{cm}$ . There are several features to note. First, since the field falls off sharply and is limited in toroidal extent, the spectrum has significant side-lobes. Second, the spectrum depends strongly on

the distance from the antenna but generally has a width of  $n = \pm 30$ , which reflects the 15 cm width of the antenna. Finally, an accurate calculation of the coupling would have to consider the poloidal mode structure and the radial profile of the TAEs, as well as the angle between the antenna field and the TAE perturbed field. Rather than comparing the antenna field to the TAE field, an equivalent but more direct analysis would be to determine the flux of the TAE that links the antenna. Such an in-depth analysis would serve as a useful design check if the antennas were ever to be replaced.

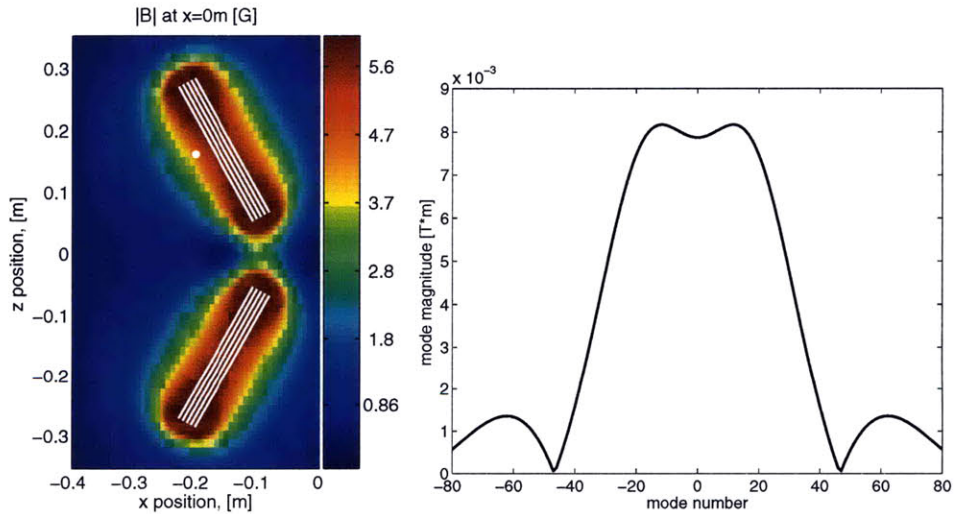
### 3.2.3 Filters

One disadvantage of well-designed antennas is that they also couple to the ICRF antennas at up to -23dB. For 2 MW of ICRF power at 50 to 80 MHz, roughly 10 kW is coupled to the active MHD antennas and is fed back down the active MHD transmission lines. To prevent this power from radiating into the cell or damaging the amplifiers, modified commercial low-pass filters (Figure 3-9(a)) interrupt the transmission lines just outside of the vacuum feedthroughs. Figure 3-9(b) shows the circuit diagram of the filters. Figure 3-9(c) and 3-9(d) show the calculated and measured response of the filters, respectively, demonstrating that they pass signals below 10 MHz with almost zero attenuation and cutoff signals in the 70 to 80 MHz RF range by almost -80dB. The filters are constructed symmetrically except that the antenna side, which must withstand tens of kilovolts, has a 7-16 connector, while the amplifier side has a regular N-type connector.



(a) The calculated antenna field in a horizontal plane when the antennas are driven in phase. A white line shows the path along which the spectrum of Figure (d) is calculated.

(b) The field components along the white line in Fig. a. Blue(radial,  $R$ ); Red(toroidal,  $\theta$ ) Magenta(vertical,  $Z$ ) Black( $\sqrt{B_R^2 + B_\theta^2 + B_Z^2}$ )

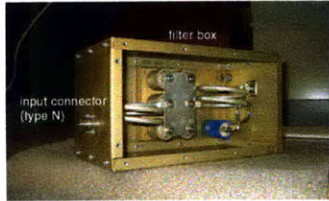


(c) The calculated antenna field on a vertical plane. The white dot corresponds to the white line of Figure (a).

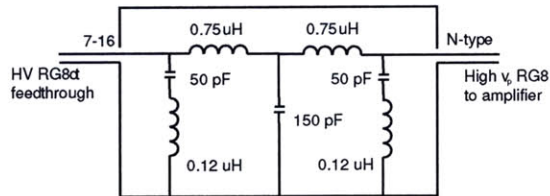
(d) Toroidal spectrum along the white line in Figure (a). The spectrum has a width at half intensity of about  $\pm 30$ , but depends on the radial and vertical location along which it is calculated.

Figure 3-8:

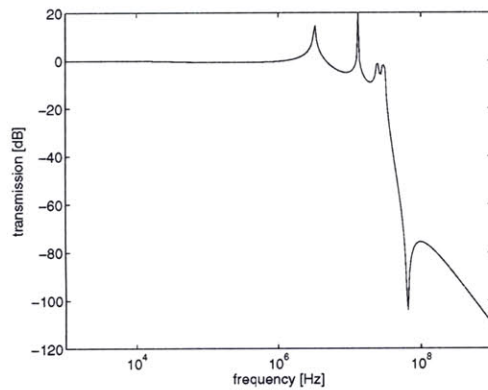




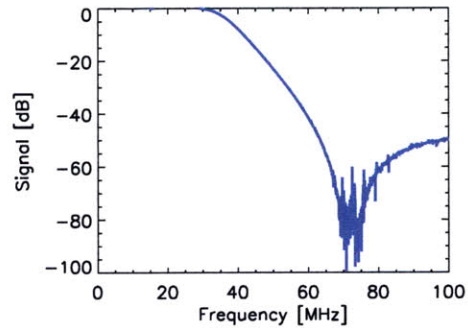
(a) A commercial RF filter was adapted to reduce ICRF pickup outside the cell



(b) The electrical circuit of the RF filter.



(c) A simulated transmission coefficient of the filter into an antenna, showing that it does strongly cutoff above the required 70 MHz of the ICRF antenna, and passes frequencies below 1MHz at effectively 0 dB. The resonances may be avoided in practice due to non-ideal resistances that were not included in the model.



(d) A transmission measurement of the filter into a 50  $\Omega$  load also confirms that it strongly cutoff above the required 70 MHz of the ICRF antenna, and passes frequencies below 1MHz at effectively 0 dB. The measurement differs significantly from the simulation.

Figure 3-9: A filter at the air side of the vacuum feedthrough cuts off RF power that couples to the antennas, while passing active MHD frequencies with very low attenuation.



Figure 3-10: A pickup coil is mounted in a limiter with some shielding removed to show the assembly.

### 3.3 Detection

#### 3.3.1 Pickup Coil System

Perturbations in the poloidal magnetic field are detected by a set of pickup coils. Each coil consists of a 13 mm long, 4 mm diameter ceramic bobbin wound with 140 turns of 29 AWG Kapton coated copper wire (Figure 3-10). The total area of one coil is  $A = 4500 \text{ mm}^2$ ; the open circuit voltage of the pickup coil is then  $V = A \cdot \dot{B}$ . Active MHD driven modes are observed with intensities up to  $50 \text{ [Ts}^{-1}\text{]}$ , corresponding to 220 mV.

Each coil has an inductance of  $43 \mu\text{H}$  and a DC resistance of  $0.7 \Omega$ . The skin depth of copper diminishes to the radius of the wire (0.14 mm) at 220 kHz. Above this frequency the resistance of the coil increases proportional to the square root of the frequency. The twisted pair leads of each coil contribute a capacitance that causes a self-resonance. The impedance of an isolated coil with 1.3 m leads is plotted in Figure

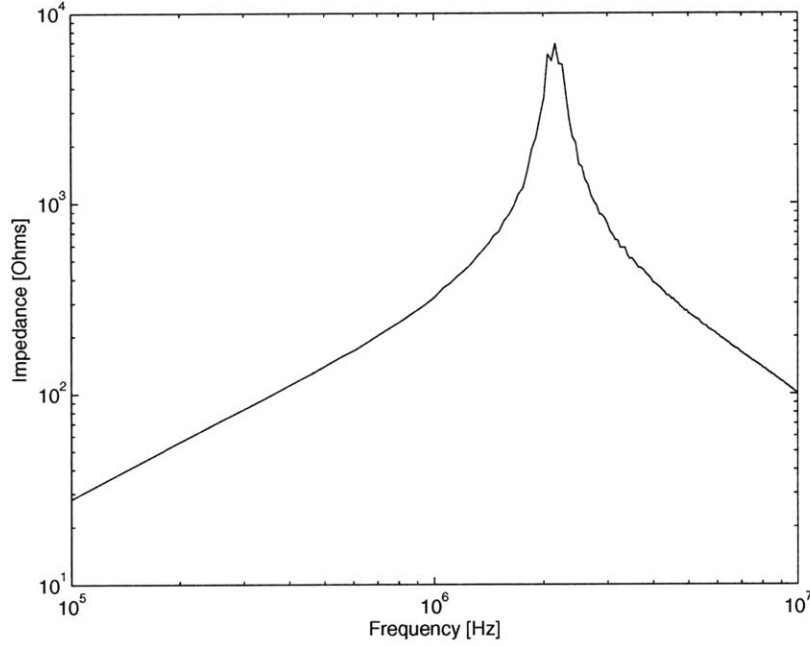


Figure 3-11: A pickup coil with 1.3 m twisted pair leads has an inductance of  $43 \mu\text{H}$  and a capacitance of  $126 \text{ pF}$ ; correspondingly it has a self resonance around  $2.2 \text{ MHz}$ .

3-11, derived from scattering parameters measured with a network analyzer as:

$$z_{coil} = z_0 \frac{(1 + S_{11})}{(1 - S_{11})}$$

The impedance appears to have a blunt peak because small variations in  $S_{11}$  when it is near 1 cause large variations in  $z_{coil}$ . The resonance in the coil's frequency response is undesirable because it can obscure the behavior of the plasma. Fortunately a coil's frequency response can be calibrated out of the measured data, as will be discussed in the next section.

Groups of pickup coils are arranged in poloidal arrays of 15 and 12 coils on the sides of the the GH and AB limiters, respectively, in the positions shown in Figure 3-12(a); and in toroidal arrays of six coils, 10 cm above and below the midplane, behind the limiter molybdenum tiles, in the toroidal positions shown in Figure 3-12(b). A second set of coils installed before the 2007 campaign augment the toroidal array, with positions 10 cm above and below the midplane at more widely spaced

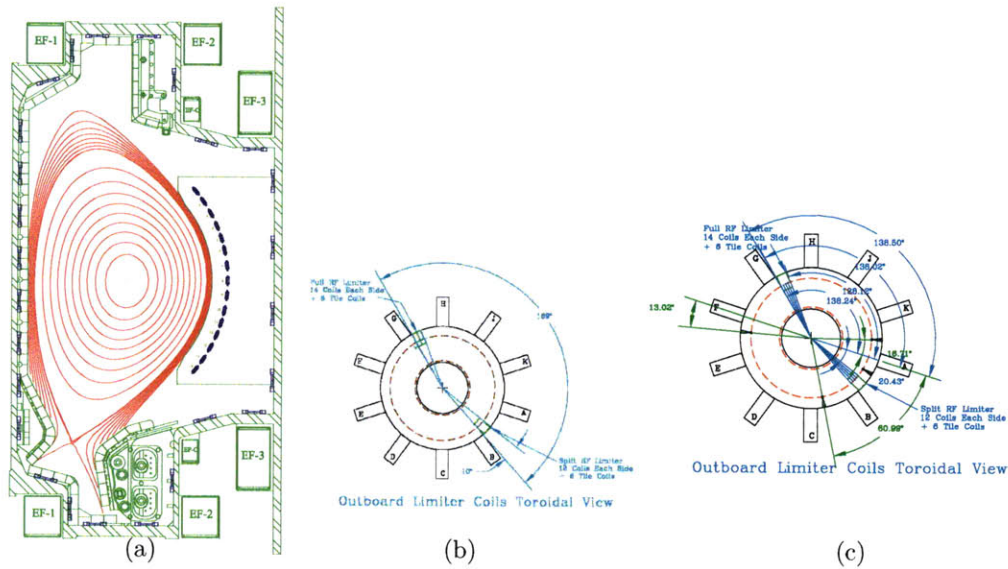


Figure 3-12: a.) Pickup coils are located on the edges of the AB and GH limiters and on the vessel wall, here drawn in blue, and b.) behind the limiter tiles 10cm above and below the midplane, covering a range of toroidal angles. c.) New pickup coils are mounted in dedicated standoffs at four toroidal locations. Much of the outboard last-closed flux surface real-estate in C-Mod is already appropriated by various diagnostics.

toroidal angles, as shown in Figure 3-12(c). Being more broadly spaced around the circumference than the limiter coils, they increase the precision of low to moderate n-number measurements.

The new coils are supported near the plasma interface by dedicated structures, and protected from radiation and particle flux by a shield of stainless steel shim stock and a pair of molybdenum tiles illustrated in Figure 3-13. The structure has been designed to guarantee the safety of the pickup coils while maximizing the poloidal flux that they couple, which may be reduced by the shielding components.

To determine the effect of the shielding components on the coupling of the coil to an external field, a calibration coil was positioned next to a pickup coil in a limiter. The mutual inductance of the two coils was then measured with various shielding components in place as shown in Figure 3-14. The 0.43 mm thick stainless steel reaches one skin depth at 986 kHz. At similar and higher frequencies the shield reduces the penetrating field, with an attenuation of almost 3 dB at 1 MHz. The

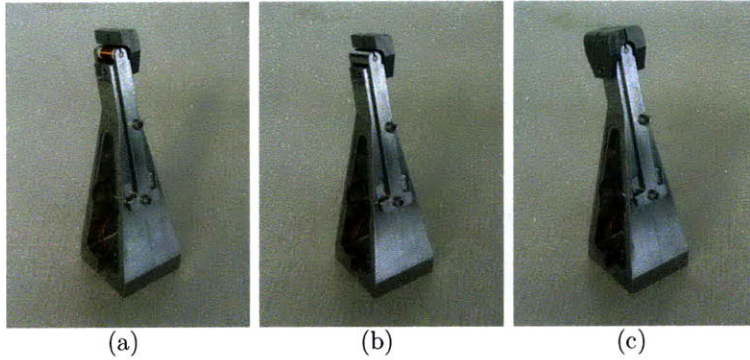


Figure 3-13: The new pickup coils are mounted in dedicated stainless standoffs that are robust enough to resist disruptions.

molybdenum tiles, being thicker, seem to concentrate the field into the cross-section of the coil, and partly compensate for the attenuation due to the stainless steel. The attenuation is acceptable but may be reduced by splitting the stainless steel shield.

All the coils are connected to a digitizer by 20 to 25 m of twisted pair wire. The twisted pairs are shielded inside the vessel by flexible stainless conduit, and are connected to the air side at the K-top outboard flange by a 37 pin vacuum feedthrough. The twisted pair continues from there to the digitizer. The digitizer consists of three 14 bit D-Tacq ACQ216 CPCI 16 channel instruments capable of sampling  $\pm 2.5$  V up to 10 MHz, with each channel having a 12 k $\Omega$  input impedance.

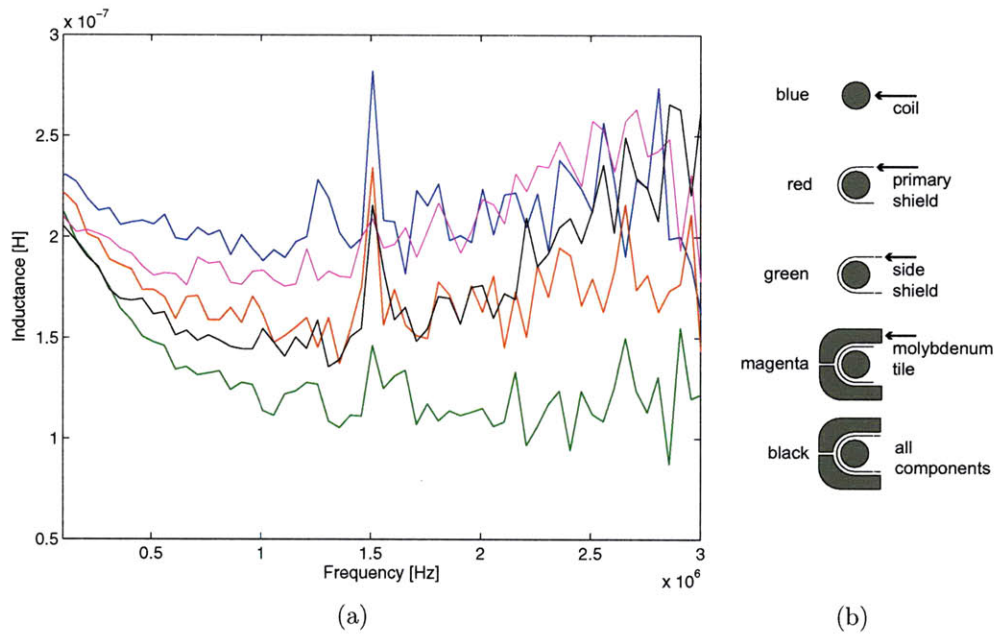


Figure 3-14: a.) The mutual coupling of the pickup coil with an external field as affected by various shielding components. b.) The corresponding configuration of the shields. It appears that the thin steel shim stock reduces coupling (red and green curves) while the molybdenum tiles actually concentrate the field in the coil (magenta and black curves) and increase the coupling comparable to that with no shielding at all (blue curve) .

# Chapter 4

## Analysis

The active MHD hardware described in the preceding chapter reveals the nature of Alfvén eigenmodes by external excitation with antennas. This chapter will cover the analysis of the measured signals to retrieve the characteristics of the resonant plasma modes. Section 4.1 of this chapter will consider the analysis from an ideal perspective, assuming that the measured signals are noiseless and uncorrupted. Section 4.2 will deal with the non-idealities of the diagnostic system that make the analysis more difficult.

### 4.1 Signal Processing to obtain the System Response

TAEs are damped by four primary mechanisms as discussed in Chapter 2, including coupling to the continuum, ion and electron Landau damping, radiative losses on kinetic Alfvén waves, and collisional absorption. The damping mechanisms oppose processes that excite the modes, such as energetic particle gradients and resonant particle orbits. Although the excitation and damping terms cannot be directly measured individually, their net effect is measurable when the damping exceeds the excitation. In this regime the plasma is stable, and the net damping rate defines the stability of the plasma in the TAE frequency range.

From a transient perspective, the net damping rate of the plasma is exhibited by the decay of its impulse response,  $h(t)$ , the natural response of the plasma to an impulse. Specifically, the ratio of the period of oscillation of  $h(t)$  to the exponential decay time is called the net damping rate. As the plasma approaches instability, the net damping rate approaches zero. If the plasma is represented by a linear, time invariant (LTI) and stable system function  $H(s)$ , its impulse response is

$$h(t) = \frac{1}{2\pi j} \int_{-i\infty+\alpha}^{i\infty+\alpha} H(s)e^{st} ds = \mathcal{L}^{-1}H(s) \quad (4.1)$$

This suggests a method to determine  $h(t)$ , and thus the stability of the plasma. Namely,

1. measure  $H(s)$
2. calculate  $h(t)$  via equation 4.1, the inverse Laplace transform of  $H(s)$ , and
3. observe the damping rate in  $h(t)$ .

To measure the plasma system function  $H(s)$ , the plasma is excited by the antenna's magnetic field,  $x(t) = \mathcal{L}^{-1}X(s)$ ; simultaneously, the plasma response  $y(t) = \mathcal{L}^{-1}H(s)X(s)$ , which contains information about the system function  $H(s)$ , is observed. The frequency of  $x(t)$  ranges over a band about the TAE frequency to manifest  $H(s)$  at those frequencies. The following sections discuss several important details in the process of determining the net damping rate from the measurements,  $x(t)$  and  $y(t)$ .

First, the signals  $x(t)$  and  $y(t)$  are real, while a complex-valued  $H(s)$  is required to calculate  $h(t)$  in Equation 4.1. Section 4.1.1 describes how a complex-valued  $H(s)$  is obtained from  $x$  and  $y$ .

Secondly, in practice the excitation  $x(t)$  is restricted to real frequencies so that  $s \rightarrow j\omega$  and Equation 4.1 becomes the inverse Fourier transform. This is permissible so long as  $H(s)$  is stable. Therefore the method of active MHD is applicable only to Alfvén eigenmodes that experience more damping than excitation, and thus have net



stability. In the absence of external excitation, stable eigenmodes have zero amplitude and are not observed by passive diagnostics. The stability and other important characteristics of  $H(s)$  are discussed in Section 4.1.2.

Thirdly, the observation of the system function  $H$  is limited to a discrete, finite frequency basis due to the digital nature of the hardware and the limited time of the experiment. With sampling period  $T$  and  $N$  samples, the fundamental frequency is

$$\omega_0 = \frac{2\pi}{NT}$$

and

$$\begin{aligned} s &\rightarrow \{jk\omega_0 | k = k^-, k^- + 1, \dots, k^+\} \\ t &\rightarrow \{nT | n = 0, \dots, N - 1\} \\ H(s) &\rightarrow H(jk\omega_0) \\ h(t) &\rightarrow h(nT) \\ x(t) &\rightarrow x(nT) \\ y(t) &\rightarrow y(nT) \end{aligned}$$

On this frequency basis, Equation 4.1 becomes the equivalent Fourier series, truncated to the frequency band of excitation,

$$h(t) \approx \sum_{k=k^-}^{k^+} H(jk\omega_0) e^{jk\omega_0 nT}. \quad (4.2)$$

The result of this calculation for a measured resonance is plotted in Figure 4-1. This approximation for  $h(nT)$  includes the response of all mechanisms that couple the antenna to the pickup coils, including undesired ones such as direct coupling. It is also negatively affected by the truncation of the frequency range.

An analytic function  $H(s)$  of a complex and continuous  $s$  can be sought to approximate  $H(j\omega_0 k)$ , and allows the behavior of the TAE to be isolated. Many physical

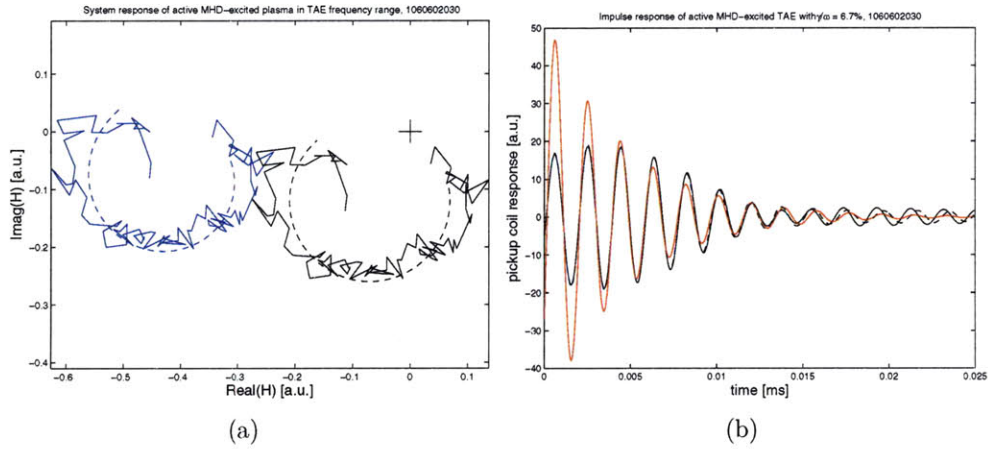


Figure 4-1: a) For a TAE resonance with damping rate of 6.7%: the measured system response (solid blue); the analytic approximation to the system response (dashed blue); the response of the dominant pole term,  $residue/(s - pole)$ , isolated from the analytic approximation (dashed black), which is exactly part of a circle that passes through 0, marked by a cross; the measured response minus the non-dominant terms of the analytic approximation (solid black). b) The corresponding impulse responses of the system responses in Fig (a), calculated by: the truncated Fourier series of Equation 4.2 using the measured dominant term (solid black); using the analytic dominant term (dashed black) in Equation 4.2; and the analytic solution to the inverse Laplace transform (Equation 4.1) for the analytic dominant term (red). The large discrepancy between the results of the inverse Laplace transform and the Fourier series is due to the truncation.

LTI systems can be accurately described by differential equations taking the form

$$\sum_i^m b_i \frac{\partial^i x}{\partial t^i} = \sum_i^n a_i \frac{\partial^i y}{\partial t^i} \quad (4.3)$$

with the associated system function,

$$H = \frac{Y}{X} = \frac{\sum_i^m b_i s^i}{\sum_i^n a_i s^i},$$

obtained from the Laplace transform of both sides of equation 4.3. This suggests that the analytic approximation to  $H(j\omega_0 k)$  should take the form of a ratio of polynomials of  $s$ . The process of finding the best analytic approximation for a given  $H(j\omega_0 k)$  is described in Section 4.1.3. Conveniently, the inverse Laplace transforms of rational functions are analytic and well-known, so that the damping rate (as well as the frequency of oscillation and phase) of  $h(t)$  can be determined by inspection of  $H(s)$  in its partial fraction form [124].

Finally, noise in the measurement leads to error in the final result. The error is quantified in Appendix A.

#### 4.1.1 Synchronous Detection

The frequency response  $H(j\omega)$  of a system can be extracted from the input and output signals using a process known as synchronous detection. Obtaining a complex system function from real signals requires the construction of a complex reference signal,  $r(nT)$ , with Fourier series coefficients  $R(j\omega_0 k)$  defined by:

$$R(j\omega_0 k) = \begin{cases} 0, & 0 < k < \frac{N}{2} \\ 2X(j\omega_0 k), & -\frac{N}{2} < k < 0 \end{cases} \quad (4.4)$$

The difference  $j(r - x)$  is called the Hilbert transform of  $x$  [124]. This one-sided property of  $R$  will prove to be useful in the following manipulation.

Synchronous detection is accomplished by mixing the output with the reference:

$$\begin{aligned} y(nT) \cdot r(nT) &= \sum_{k=0}^{N-1} (Y * R) e^{jk\omega_0 nT} \\ &= \sum_{k=0}^{N-1} e^{jk\omega_0 nT} \sum_{p=0}^{N-1} Y(j\omega_0 p) \cdot R(j\omega_0 (k-p)) \end{aligned}$$

and then filtering with an ideal low-pass filter,  $F(j\omega_0 k)$ , defined by the Fourier series coefficients

$$F(j\omega_0 k) = \begin{cases} 1, & k = lN, \quad l \in \text{integers} \\ 0, & k \neq lN \end{cases}$$

During a short time interval the frequency of excitation of the antenna is essentially limited to a single frequency  $\omega_0 k_0$ , so that  $X(j\omega_0 k)$  has the coefficients

$$X(j\omega_0 k) = \begin{cases} \text{finite}, & k = lN \pm k_0, \quad l \in \text{integers} \\ 0, & k \neq lN \pm k_0 \end{cases}$$

Then the coefficients of  $Y$  that do not correspond to  $lN - k_0$  are wiped out:

$$\begin{aligned} f * (y(nT) \cdot r(nT)) &= \sum_{k=0}^{N-1} F(j\omega_0 k) e^{jk\omega_0 nT} \sum_{p=0}^{N-1} Y(j\omega_0 p) R(j\omega_0 (k-p)) \\ &= \sum_{p=0}^{N-1} Y(j\omega_0 p) R(-j\omega_0 p) \\ &= Y(j\omega_0 k_0) R(-j\omega_0 k_0) \\ &= H(j\omega_0 k_0) X(j\omega_0 k_0) R(-j\omega_0 k_0) \end{aligned} \tag{4.5}$$

where the property of  $R$  described in Equation 4.4 has been used in the third line. The same process is carried out with the input,  $x(nT)$ , to achieve

$$f * (x(nT) \cdot r(nT)) = X(j\omega_0 k_0) R(-j\omega_0 k_0). \tag{4.6}$$

Finally, the right side of Equation 4.5 is divided by the right side of Equation 4.6 to

give the system response at the frequency of excitation:

$$H(j\omega_0 k_0) = \frac{H(j\omega_0 k_0)X(j\omega_0 k_0)R(-j\omega_0 k_0)}{X(j\omega_0 k_0)R(-j\omega_0 k_0)}$$

#### 4.1.2 Properties of $H(s)$

As previously discussed, the plasma system function is naturally modelled by a ratio of polynomials in  $s$ ,

$$H(s) = \frac{b_m s^m + b_{m-1} s^{m-1} + \dots + b_0}{s^n + a_{n-1} s^{n-1} + \dots + a_0}$$

where the polynomial coefficients  $b_i$  and  $a_i$  are to be chosen so that  $H(s)$  matches the measured data,  $H(j\omega_0 k)$ , as closely as possible. This form corresponds to a differential equation in the time domain and can accurately describe the system. The resulting rational transform,  $H(s)$ , is in general not proper, and can be decomposed by the method of partial fractions into a polynomial with real coefficients plus conjugate pairs of strictly proper rational functions,

$$H(s) = (d_{m-n} s^{m-n} + \dots + d_0) + \left( \frac{c_1}{s - p_1} + \frac{c_1^*}{s - p_1^*} \right) + \dots + \left( \frac{c_{\frac{n}{2}}}{s - p_{\frac{n}{2}}} + \frac{c_{\frac{n}{2}}^*}{s - p_{\frac{n}{2}}^*} \right). \quad (4.7)$$

The properties of the plasma system function are conveniently discussed in terms of this partial fraction expansion of  $H(s)$ .

Each conjugate pair of strictly proper fractions represents a TAE resonance. The impulse response of the TAE is therefore

$$h(t) = 2\mathcal{R} \{ c e^{\gamma t} e^{j\omega t} \}$$

$$p = \gamma + j\omega.$$

The magnitude and phase of the resonance are exhibited by  $c$ , the residue of  $H$  at the pole,  $p$ . The decay rate and resonant angular frequency of oscillation are exhibited

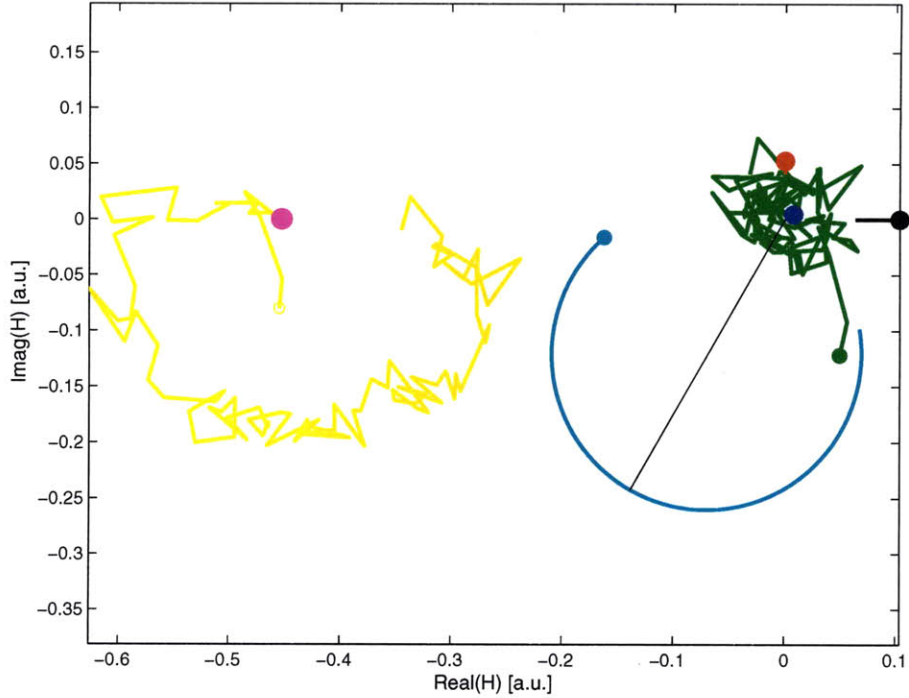


Figure 4-2: Measured data is shown for a resonance in shot 1060602030 (yellow), in which the frequency was swept from 452 kHz to 576 kHz. In comparison, each term in Equation 4.7 of the fitted system function  $H$  is also plotted: the dominant pole (cyan); the conjugate pole (blue); the constant term (magenta); the linear term (red); the quadratic term (black); and the measurement noise (green). The dots mark the 576 kHz data point. The angle of the black diameter in the dominant resonance circle corresponds to the angle of the resonance.

by the real and imaginary parts of the pole. The damping rate is defined by the ratio  $\gamma/\omega$ . Since the TAEs observed by active MHD are stable, the poles must have negative real parts.

The form  $\frac{c}{s-p}$  is a bilinear mapping of  $s$  which maps a straight line in the  $s$  plane to a circle passing through the origin. A circular trajectory of the measured  $H(j\omega_0 k)$  is therefore recognized as evidence of a TAE resonance. Data for a typical shot is shown in Figure 4-2. The magnitude  $\left| \frac{c}{s-p} \right|$  reaches a maximum on the path  $s = j\omega$  when  $s - p$  is real and corresponds to the point on the circle opposite the origin, so it is clear that the angle of the circle around the origin is equal to the phase of the resonance. The diameter of the circle is determined by the magnitude of the resonance and the damping rate. Since the poles are in the left-half plane, the circle

is traversed clock-wise as the frequency increases.

Near  $\omega = \mathcal{I}\{p\}$ , the trajectory of  $H(s)$  is dominated by the TAE resonance term,  $\frac{c}{s-p}$ , and should be roughly circular. The other terms on the right side of Equation 4.7 also contribute to the shape of the trajectory, and have significance to physical mechanisms, besides the TAE, that couple the antennas to the pickup coils.

First, the conjugate term  $\frac{c^*}{s-p^*}$  is present because the TAE response is real. It contributes a small arc that distorts the circular trajectory. Furthermore, the coefficients of this term are not free to be determined, since they are conjugates of the coefficients in the dominant term.

The constant term  $d_0$  represents direct coupling of the input to the output: its impulse response is an impulse. The constant term displaces the circular trajectory from the origin without distortion.

The linear term  $d_1s$  represents inductive coupling of the antenna magnetic field to the pickup coil, where the output is the derivative of the input. Its impulse response is the unit doublet. The linear term contributes a vertical skew (along the imaginary axis) to the trajectory of  $H(s)$ .

The quadratic term  $d_2s^2$  represents coupling of the input's second derivative to the output. It contributes a horizontal skew (along the real axis) to the trajectory.

More terms can be included in the polynomial of Equation 4.7 to improve the fit to the measured data. However, higher order terms are not motivated by theoretical derivations of TAE behavior, and they may incorrectly absorb some of the response that should rather be attributed to the dominant pole. The task of finding the best coefficients for the rational function is discussed next.

### 4.1.3 Parametric Fitting of the System Function $H(s)$

To find the best coefficients  $b_i$  and  $a_i$  for the rational function  $H(s)$ , the approximation

$$H(j\omega_0k) \approx H(s) = \frac{B(s)}{A(s)} = \frac{b_ms^m + b_{m-1}s^{m-1} + \dots + b_0}{s^n + a_{n-1}s^{n-1} + \dots + a_0}, \quad \{s = j\omega_0k\} \quad (4.8)$$

is optimized over a suitable metric for a selected set of coils. Several considerations are brought to bear when forming the metric.

First, Equation 4.8 could be linearized by multiplying by  $A(s)$ , which has the adverse effect of emphasizing terms with large  $A(s)$ , and therefore small  $H(s)$ . To avoid this emphasis, the optimization is performed iteratively; then, in each iteration, Equation 4.8 is linearized instead by the normalized factor

$$\frac{A(s)}{A_{-1}(s)} \approx 1$$

where  $A_{-1}(s)$  is the solution of  $A(s)$  from the previous iteration. The first iteration assumes that  $A_{-1}(s) = 1$ .

A second consideration is that multiple pickup coils in the detection array measure the local plasma response to the antenna excitation, each coil producing its own output signal and associated system function. Because the TAE is a global mode, each coil should observe the same eigenmode,  $e^{pt}$ . This requires that the system functions relating each coil to the antenna all share the same denominator,  $A(s)$ .

Thirdly, the coefficients  $b_i$  and  $a_i$  must be real because  $H$  is a real system.

Finally, the orders of  $B(s)$  and  $A(s)$  are chosen to be small but allow for a suitable fit of the data. Also, the excitation frequency,  $j\omega_0 k$ , at each finite time interval is obtained from the largest term in the Fourier series of the input,  $X(j\omega_0 k)$  over that time interval.

For each coil and each frequency, the approximation error is

$$\epsilon = -H(s) \frac{A(s)}{A_{-1}(s)} + \frac{B(s)}{A_{-1}(s)}.$$

The approximation is optimized in the least squares sense at each iteration. That is,

$$\sum_{coils} \sum_{freq's} (\epsilon^* \epsilon)$$

is minimized. The optimal solution at each iteration is given by a closed form matrix equation that is developed below. In the following notation, the subscripts on  $H$  and



the coefficients  $b_i$  identify the coil and run over the integers from  $1 \rightarrow v$  where  $v$  is the number of coils in the set. Likewise, the subscripts on  $s$  identify the frequency and run over the integers from  $1 \rightarrow w$ , where  $w$  is the number of discrete samples of  $H(j\omega_0 k)$ . The equations relating the samples of  $H(j\omega_0 k)$  to the fitted  $H(s)$  can be compactly represented by a single matrix relation, where each row represents the measurement at one coil for one frequency:

$$\begin{bmatrix} \epsilon_1(s_1) \\ \vdots \\ \epsilon_1(s_w) \\ \hline \vdots \\ \vdots \\ \hline \epsilon_v(s_1) \\ \vdots \\ \epsilon_v(s_w) \end{bmatrix} = \begin{bmatrix} \frac{H_1 s_1^m}{A_{-1}} \\ \vdots \\ \frac{H_1 s_w^m}{A_{-1}} \\ \hline \vdots \\ \vdots \\ \hline \frac{H_v s_1^m}{A_{-1}} \\ \vdots \\ \frac{H_v s_w^m}{A_{-1}} \end{bmatrix} + \begin{bmatrix} \frac{H_1 s_1^{m-1}}{A_{-1}} & \cdot & \frac{H_1(s_1)}{A_{-1}} & \frac{-s_1}{A_{-1}} & \cdot & \frac{-1}{A_{-1}} & \vdots & \vdots \\ \vdots & \cdot & \cdot & \cdot & \cdot & \cdot & \cdot & 0 \\ \frac{H_1 s_w^{m-1}}{A_{-1}} & \cdot & \frac{H_1(s_w)}{A_{-1}} & \frac{-s_w}{A_{-1}} & \cdot & \frac{-1}{A_{-1}} & \vdots & \vdots \\ \hline \vdots & \cdot & \cdot & \cdot & \cdot & \cdot & 0 & \cdot \\ \vdots & \cdot & \cdot & \cdot & \cdot & \cdot & \cdot & 0 \\ \hline \frac{H_v s_1^{m-1}}{A_{-1}} & \cdot & \frac{H_v(s_1)}{A_{-1}} & \vdots & \vdots & \frac{-s_1}{A_{-1}} & \cdot & \frac{-1}{A_{-1}} \\ \vdots & \cdot & \cdot & \cdot & \cdot & \cdot & \cdot & \cdot \\ \frac{H_v s_w^{m-1}}{A_{-1}} & \cdot & \frac{H_v(s_w)}{A_{-1}} & \cdot & 0 & \cdot & \frac{-s_w}{A_{-1}} & \frac{-1}{A_{-1}} \end{bmatrix} \begin{bmatrix} a_{m-1} \\ \vdots \\ a_0 \\ \hline b_{1,n} \\ \vdots \\ b_{1,0} \\ \hline \vdots \\ \hline b_{v,n} \\ \vdots \\ b_{v,0} \end{bmatrix}$$

which will be abbreviated here by

$$\epsilon = -D + Su.$$

and  $u$  is to be optimized. The best solution for  $u$  satisfies

$$0 = \frac{\partial \epsilon^* \epsilon}{\partial u}.$$

Noting that  $\frac{\partial u}{\partial u} = I$ , an expression for  $u$  is

$$\begin{aligned}
\frac{\partial \epsilon^* \epsilon}{\partial u} &= \frac{\partial}{\partial u} (Su - D)^* (Su - D) \\
&= \frac{\partial}{\partial u} ((Su)^* Su - (Su)^* D - D^* Su + D^* D) \\
&= \left( S \frac{\partial u}{\partial u} \right)^* Su + \left( (Su)^* S \frac{\partial u}{\partial u} \right)^T - \left( S \frac{\partial u}{\partial u} \right)^* D - \left( D^* S \frac{\partial u}{\partial u} \right)^T \\
&= S^* Su + ((Su)^* S)^T - S^* D - (D^* S)^T \\
&= S^* Su + (S^* S)' u - S^* D - (S^* D)' \\
&= \mathcal{R} \{ S^* S \} u - \mathcal{R} \{ S^* D \} \\
&= 0
\end{aligned}$$

Solving for  $u$  gives

$$u = \mathcal{R} \{ S^* S \}^{-1} \mathcal{R} \{ S^* D \}$$

Here  $u$ , containing the coefficients  $b_i$  and  $a_i$ , is purely real. If the constraint that the system function polynomials have real coefficients is removed, the system function can be expanded about the dominant pole as in a Laurent series. It is unclear which convention more easily accomodates a variable number of overlapping poles and fits the measured data more closely. A system function expanded about a single pole can be formulated in a way similar to the process described above, as follows:

$$H = \frac{\alpha_{-1}}{s - p} + \alpha_0 + \alpha_1(s - p) + \alpha_2(s - p)^2 + \dots$$

where the pole  $p$  and the coefficients  $\alpha_k$  are complex and are to be determined by iteration as before. The equation is linearized by multiplying by  $\frac{(s-p)}{(s-p_{-1})}$  where  $p_{-1}$  was determined in the previous iteration; in the first iteration,  $p_{-1}$  is assumed to be  $p_{-1} = (j + 0.05) * 2\pi 5 \times 10^5$  Hz, a typical value. The coefficients are separated into real and imaginary parts and the matrix equation for one coil for at one frequency is:

$$Hs = \begin{bmatrix} H \\ iH \\ \hline 1 \\ s \\ s^2 \\ \dots \\ \hline i \\ is \\ is^2 \\ \dots \end{bmatrix}^T \begin{bmatrix} p_r \\ p_i \\ \hline \kappa_{-1,r} \\ \kappa_{0,r} \\ \kappa_{1,r} \\ \dots \\ \hline \kappa_{-1,i} \\ \kappa_{0,i} \\ \kappa_{1,i} \\ \dots \end{bmatrix}$$

where

$$\begin{bmatrix} \kappa_{-1} \\ \kappa_0 \\ \kappa_1 \\ \dots \end{bmatrix} = \begin{bmatrix} 1 & -p & p^2 & \dots \\ 0 & 1 & -2p & \dots \\ 0 & 0 & 1 & \dots \\ \dots & \dots & \dots & \binom{col}{row}(-p)^{col-row} \end{bmatrix} \begin{bmatrix} \alpha_{-1} \\ \alpha_0 \\ \alpha_1 \\ \dots \end{bmatrix}$$

The equations for all coils at all frequencies are then solved simultaneously as before and the calculation is iterated to refine the pole.

## 4.2 Compensation

The ideal linear, time-invariant (LTI) model of the diagnostic system is shown in Figure 4-3. In this model the transfer function,  $Y(j\omega)/X(j\omega)$ , is exactly proportional to the resonant plasma frequency response.

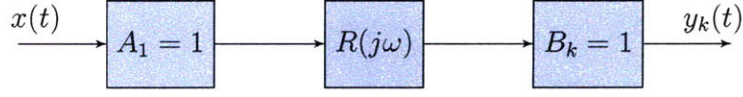


Figure 4-3: Block diagram of the ideal model of the diagnostic system. The only non-constant element in this model is the resonant plasma frequency response,  $R(j\omega, t)$ .

The various signals and factors are defined as,

$$x(t) = \frac{1}{2\pi} \int_{-\infty}^{\infty} X(j\omega) e^{j\omega t} d\omega \quad \text{antenna current}$$

$$A_1 \quad \text{antenna frequency response function}$$

$$R(j\omega, t) = \frac{r}{s - p} \quad \text{resonant plasma frequency response function}$$

$$B_k \quad \text{magnetic probe frequency response function}$$

$$y_k(t) = \frac{1}{2\pi} \int_{-\infty}^{\infty} Y(j\omega) e^{j\omega t} d\omega \quad \text{voltage of magnetic probe } k \text{ at data acquisition}$$

The analysis of the previous section extracted the resonant plasma frequency response from the observed time signals of a simple but slightly more realistic model of the diagnostic, depicted in Figure 4-4. For clarity, the observed signals were assumed to be the sum of at most two linear factors: a non-resonant response showing a weak function of frequency, representing the direct coupling of the antenna to the magnetic probes; and when sufficiently excited, the resonant component representing the Alfvén eigenmode, characterized by a complex root and exhibiting a strong function of frequency. In that model, the time-variation of these two responses due to their dependence on the plasma configuration was acknowledged. The gain of the hardware that couples the diagnostic to the plasma, however, was tacitly assumed to be real and constant.

Non-ideal behavior was introduced into the model as the direct coupling term,

$$D(j\omega, t) = d_2 s^2 + d_1 s + d_0 \quad \text{non-resonant plasma frequency response function}$$

In this thesis, the complex, time- and frequency-dependent collective frequency response function from the input to the output of the diagnostic system, including the

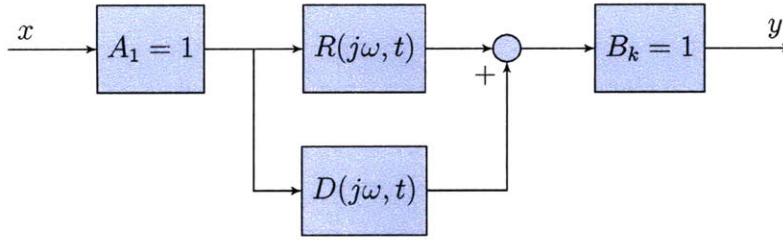


Figure 4-4: Block diagram of the simple two-factor system that was adopted in the analysis of the previous section.

plasma behavior, is called the *system response* and is denoted by  $H(j\omega, t)$ . It is,

$$\frac{Y(j\omega)}{X(j\omega)} = H(j\omega, t) = B_k(R + D)A_1$$

The frequency response function of an individual component of the system, such as the antenna, is called, for example, the *antenna response* (denoted above by  $A_1$ ). The combined response of all the instrumentation is called the *diagnostic response*, and is,

$$H_D = A_1 \cdot B_k.$$

For the simple system that was analyzed in the previous section, the diagnostic response was real and constant. Then the system response was just proportional to the *plasma response*,  $P = R + D$ .

In contrast to the simple system of Figure 4-4, the mechanisms of the actual diagnostic have responses that are complex functions of frequency and time. In addition, the two antennas must be recognized as distinct inputs to the system - being sourced by separate amplifiers, their currents can be different. A block diagram representation of the actual system is shown in Figure 4-5. The current and frequency response of the upper and lower antennas are distinguished in Figure 4-5 by the respective

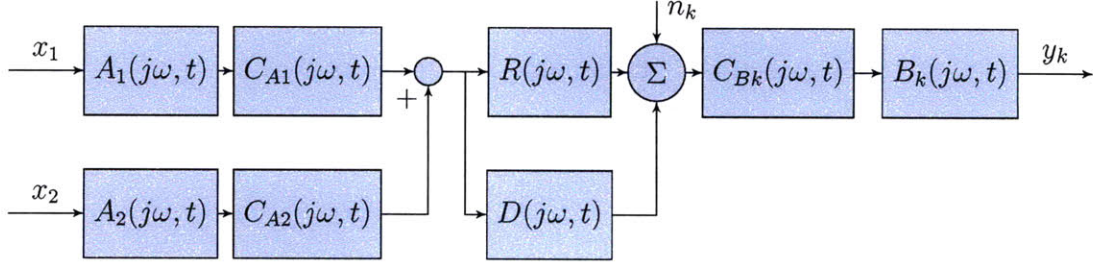


Figure 4-5: Block diagram of the full system, showing the frequency and time-dependence of all components, and treating the two antennas separately. Noise is also included.

subscripts 1 and 2. The additional terms are:

$C_A$	coupling of the antenna to the plasma
$C_{Bk}$	coupling of plasma to the magnetic probe
$n_k$	noise

The coupling terms  $C_A$  and  $C_B$  describe the significant dependence on the plasma configuration of the coupling between the diagnostic instrumentation and the plasma. While noise is distributed to some extent on every node of the system, it is equivalent to aggregate all the noise at the second summation. The response of the full system is,

$$H(j\omega) = (A_1 \cdot C_{A1} + A_2 \cdot C_{A2}) \cdot (R + D + N) \cdot C_{Bk} \cdot B_k.$$

The non-ideal factors  $A$ ,  $C_A$ ,  $D$ ,  $n_k$ ,  $C_{Bk}$  and  $B_k$  introduced in Figure 4-5 distort the system response from the desired resonant plasma response,  $R(j\omega, t)$ . Each factor contributes phase and gain that are functions of frequency and vary over time. These distortions influence the acquisition of the Alfvén eigenmode characteristics. In particular, the AE damping rate is sensitive to the frequency profile of the phase and amplitude, while the toroidal mode number is sensitive to the relative phase among probes. (The relative amplitude among the probes is also distorted but is of lesser consequence in the analysis.) To acquire the true Alfvén eigenmode behavior,  $R(j\omega, t)$ , the observed system response  $H(j\omega, t)$  must be compensated for the

response of all of the non-ideal factors.

The compensation process must therefore separate the character of observed Alfvén eigenmodes from the extraneous functions  $A$ ,  $C_A$ ,  $D$ ,  $n_k$ ,  $C_{Bk}$  and  $B_k$ , within satisfactory bounds of uncertainty. The investigation proceeds in the order of achievable precision as follows. First it must be determined whether a resonance has truly been observed. This requires discriminating the general shape of the resonant plasma behavior from peaks in amplitude and shifts in phase that result from non-ideal behavior of the diagnostic. If the discrimination is successful, the second task is to seek the pole of the resonance, which describes the resonant frequency and the damping rate of the eigenmode. The pole is determined by the frequency derivative of the system response, but is insensitive to its phase or absolute value. Finally, the residues are obtained to determine the toroidal structure of the mode. The toroidal mode number is sensitive to the relative phase among probes.

This section of the thesis examines the non-ideal factors of the diagnostic and their requisite compensation during the analysis process just described. The first two subsections address the compensation from two paradigms of non-ideal behavior. First, the normal non-ideal behavior that represents the expected response of the diagnostic is quantified. Normal behavior includes the ambiguity of the contributions from the multiple-inputs  $x_1(t)$  and  $x_2(t)$ , the frequency-dependent transconductance of the antennas,  $A_1$  and  $A_2$ , the magnetic probe self-resonances,  $B_k$ , the variable coupling between diagnostic instruments and plasma,  $C_A$  and  $C_{Bk}$ , and the direct coupling of antenna to probe,  $D$ . These factors are divided, subtracted or otherwise eliminated from the system response to isolate the resonant component,  $R$ . In the normal paradigm, the antenna and probe responses,  $A$  and  $B$ , are taken to be time-invariant; all time dependence in the instrument-plasma coupling is assumed by the coupling factors,  $C_A$  and  $C_B$ . The direct coupling,  $D$ , is also a function of time. The noise,  $n_k(t)$  is assumed to have zero mean and its influence on precision is therefore taken up in the error analysis of Appendix A.

The second subsection concerns the pathological or irregular modes of the diagnostic that often have serious implications for the interpretation of data. The

pathological modes include glitches in the tuning network relays, corruption of the waveform gating pulses and accompanying current attenuation, saturation of data acquisition channels, and delays in the data acquisition clocks. Pathological behavior tends to be intermittent and is therefore compensated on a case-by-case basis. None of the terms are assumed to be time-invariant in the pathological paradigm, and some of the irregular behavior is also non-linear.

The purpose of the first two subsections is to extract the accurate character of the AEs from distorted data. For simplicity, each non-ideal behavior will be examined in isolation. When it comes to real experiments, however, these distortions often occur simultaneously, making it much more difficult to accurately disentangle their effects. Since some of the non-ideal factors resemble the behavior of Alfvén eigenmodes, there is concern that events that are claimed to be AEs are in fact the result of incomplete compensation for non-ideal behavior of the diagnostic. To address this concern, the third subsection discriminates AEs from non-ideal events by directly comparing their distributions in time and frequency.

How good must the compensation be? Assuming the mere existence of an Alfvén eigenmode has been satisfied, we can estimate the required precision of the compensation that allows meaningful measurements of mode damping rate and toroidal mode number. These estimates will guide the compensation effort.

The mode damping rate depends on the frequency derivative of the system response, as described above. Uncertainty in the derivative must therefore be significantly smaller than the typical derivative that is due to an Alfvén eigenmode, which will now be calculated. The plasma response is,

$$\begin{aligned} P &= D + R \\ &= D + \frac{r}{j\omega - (j\omega_0 - \gamma)} \end{aligned}$$

where  $r$  is the residue and  $(j\omega_0 - \gamma)$  is the pole. The plasma response changes most



rapidly at the resonant frequency and its normalized derivative there is,

$$\frac{1}{P} \frac{\partial P}{\partial \omega} = -j \frac{1}{P} \frac{r}{\gamma^2} = -j \frac{1}{\gamma} \frac{1}{D/\frac{r}{\gamma} + 1} \approx -j \frac{1}{\gamma} \frac{R}{D} \quad [\text{kHz}^{-1}],$$

where  $R(j\omega_0) = r/\gamma$ . The required precision increases with the ratio of direct to resonant signal,  $|D|/|R|$ : on probes near the antenna, that ratio is about 5.

When  $D(j\omega_0)/R(j\omega_0)$  is approximately real, the plasma response changes primarily in phase at resonance. Then the maximum frequency derivative of the plasma response phase is,

$$\frac{\partial}{\partial \omega} (\angle P) \approx \arctan \left( \frac{1}{\gamma} \frac{1}{D/\frac{r}{\gamma} + 1} \right) \approx \frac{|R|}{|D|} \frac{1}{\gamma} \quad [\text{rad} \cdot \text{kHz}^{-1}].$$

For modes with damping rates of  $\gamma/\omega_0 = -5\%$  and resonant frequencies of  $f_0 = 750 \text{ kHz}$ , the rate of phase change is about  $-0.3^\circ \cdot \text{kHz}^{-1}$  at resonance. A reasonable precision to require in the slope of the phase is therefore  $\pm 0.1^\circ \cdot \text{kHz}^{-1}$ .

When  $D(j\omega_0)/R(j\omega_0)$  is large and approximately imaginary, it is the amplitude of the plasma response that is changing quickly at resonance. The rate of change of the amplitude is,

$$\frac{\partial}{\partial \omega} (20 \log_{10} |P|) = \frac{20}{\ln(10)} \frac{1}{P} \frac{\partial P}{\partial \omega} \approx \frac{20}{\ln(10)} \frac{1}{\gamma} \frac{|R|}{|D|} \quad [\text{dB} \cdot \text{kHz}^{-1}]$$

which is about  $0.05 \text{ dB} \cdot \text{kHz}^{-1}$  for a mode having  $\gamma/\omega_0 = -5\%$  and  $f_0 = 750 \text{ kHz}$ . A reasonable precision to require in the slope of the amplitude is therefore  $\pm 0.02 \text{ dB} \cdot \text{kHz}^{-1}$ .

With respect to the toroidal mode number, the accuracy of the analysis depends on the relative phase of the plasma response among the probes. The most complete toroidal array available in this experiment consists of ten probes separated by various toroidal angles, as depicted in Figure 4-6. The sensitivity of the toroidal mode number to phase error is not equal among probes, since the probes are not equally spaced. Nonetheless, the minimum mean phase error that can be tolerated on any set of probes while still ensuring that the toroidal mode number will be correctly identified

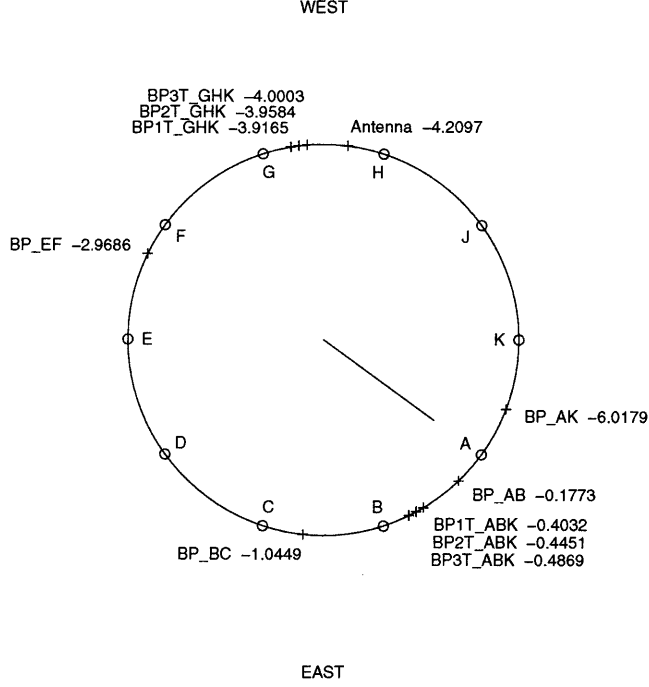


Figure 4-6: The positions of the magnetic probes that compose a toroidal array are marked with + symbols. For angular reference, the centerline of the diagnostic ports are marked with circles and labelled with the corresponding port name. The angles of the probes are listed in radians in the machine coordinates, with zero degrees at the A port centerline. The active MHD antenna is also shown between G and H ports.

is calculated as,

$$\sigma_{\varphi} = \frac{1}{2} \min_{n \in [-20, 20]} \min_{b \in [0, 2\pi]} \sqrt{\frac{1}{N} \sum_{k=1}^N (n\phi_k + b)^2}$$

where  $\phi_k$  is the toroidal angle of each probe;  $N$  is the number of probes,  $n$  is the integer toroidal mode number and ranges from  $-20$  to  $20$ , the reasonable set of modes that could be observed; and  $b$  is the phase offset of the plasma response and ranges from  $0$  to  $2\pi$ . For the unequally spaced arrangement of ten probes used in the experiment, the mean tolerable error is  $\sigma_{\varphi} = \pm 24^{\circ}$ . In summary, the distortions from

the diagnostic response that can be tolerated are:

$$\begin{aligned} \left| \frac{\partial}{\partial \omega} (\angle P) \right| &< 0.1^\circ \cdot \text{kHz}^{-1} \\ \left| \frac{1}{P} \frac{\partial P}{\partial \omega} \right| &< 0.02 \text{ dB} \cdot \text{kHz}^{-1} \\ |\sigma_\varphi| &< 24^\circ \end{aligned} \tag{4.9}$$

In observations where the uncertainties are considerably greater than the required precision calculated in Criteria 4.9, the experimental results are rendered inconclusive. The challenge of the compensation problem to overcome this dilemma is epitomized in the system response plotted in Figure 4-7. The figure compares the behavior of the Alfvén eigenmode to the non-resonant system response during a shot. Features that require compensation in the particular data of this figure include a phase lag due to a glitch in the data acquisition clock; distortion from the probe response; addition of the direct coupling term; and confusion of the purported resonance with pathological jumps in phase and amplitude. The analysis that follows in this section will address these and other issues to demonstrate that the measured system response can be compensated to a satisfactory precision. A thorough error analysis is subsequently carried out in Appendix A to arrive at confidence intervals for the derived quantities.

## 4.2.1 Compensating for Normal Non-Ideal Effects

### Two-Input, One-Output problem

When evaluating the measured signals to recover the system response, the currents of the two antennas must be recognized as separate inputs because they often have subtly different spectra, due to several causes. First, while the current profiles originate from the same control system, the two currents are sourced by independent transistor gating signals. These gating signals are subject to corruption from electromagnetic noise inside the amplifier rack, so that in the pathological case, the transistors do not operate in unison. Second, the antenna circuits, including the coaxial transmission lines, have similar but not identical impedance. Third, the antenna impedances can

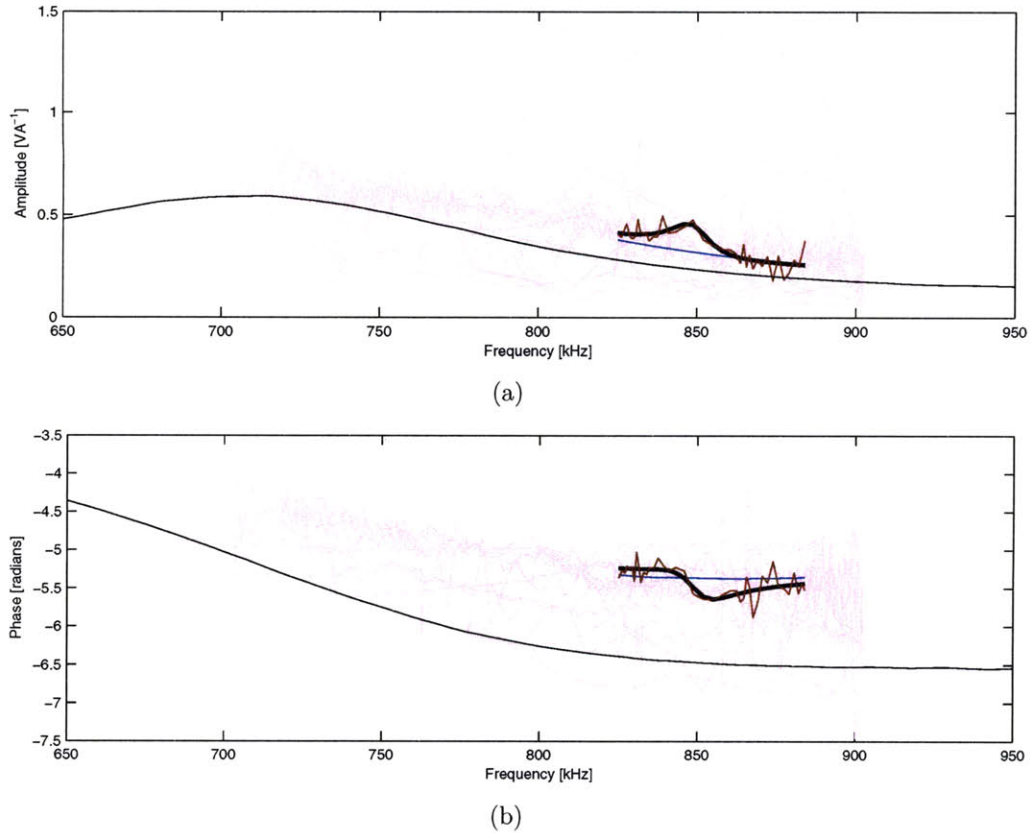


Figure 4-7: An Alfvén eigenmode observation in shot 1080403010 on probe BP1T\_GHK (dark red). The system response is divided into the resonant part (thick black) and the direct coupling component (blue), based on their respective frequency responses. This chapter will demonstrate how the resonant signal is separated from the system response of the rest of the shot, which is shown here in pink. The thin black line is the response of the diagnostic in vacuum.

be modified independently by the presence of plasma, a phenomenon that will be discussed in the next subsection. The effect of having different current spectra in each antenna is readily visible in the measured system response functions. Figure 4-8 shows the measured system response on two probes when both antennas are driven, for two cases of misguided analysis: first, considering only the upper antenna current to be the system input (in blue); and second, considering only the lower antenna current (in red). The derived responses are clearly different for the two cases, and the difference is accentuated for probes near the antennas (Figure 4-8(a)).

A fourth incentive for treating the inputs separately, and the one that is most

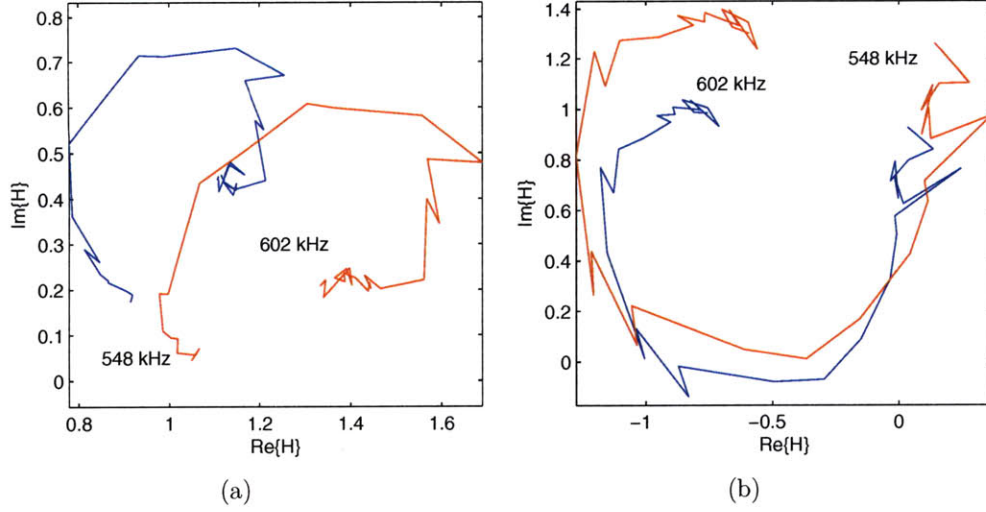


Figure 4-8: The measured system response of shot 1070626015 on probes a) BP3T\_GHK and b) BP\_BC.TOP during the interval 0.274-0.314 [s]. Using two antennas presents the dilemma of choosing which antenna current to view as the input to the system: here, the blue response is calculated using the upper antenna current, while the red response is calculated using the lower antenna current. Since both responses ostensibly describe the same plasma, they should be identical.

severe, relates to the mis-tuning of the amplifiers. The amplifier tuning networks can mis-tune when relays stick opened or closed, so that each antenna circuit is resonant at a different frequency. This leads to the appearance of an uncompensated resonance in the system response and will be discussed after the two-input system is introduced.

With the two-input model in mind, the diagnostic system can accordingly be reduced to the topology of Figure 4-9 where only the measurable states are considered.

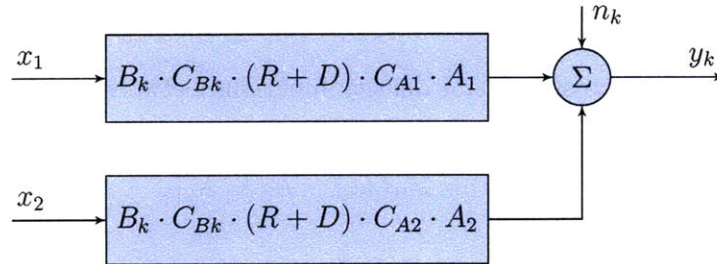


Figure 4-9: A block diagram of the system for probe  $k$ , collapsed to show only the measurable signals.

The condensed system response can be represented by its two factors,

$$H_{1,k} = B_k \cdot C_{Bk} \cdot (R + D) \cdot C_{A1} \cdot A_1,$$

$$H_{2,k} = B_k \cdot C_{Bk} \cdot (R + D) \cdot C_{A2} \cdot A_2.$$

Given the Fourier transforms of the measured signals,

$$X_i(j\omega) = \int_0^T x_i(t) e^{-j\omega t} dt,$$

$$Y_k(j\omega) = \int_0^T y_k(t) e^{-j\omega t} dt,$$

the output of each probe is expressed in terms of the system response as:

$$Y_k(j\omega) = H_{1,k}(j\omega)X_1(j\omega) + H_{2,k}(j\omega)X_2(j\omega) + N_k(j\omega).$$

The diagnostic is a set of  $k$ , two-input, single-output systems. For a single two-input, single-output system, the cross-spectral density functions between the inputs and the output are expressed in terms of the expectation value over many sampling periods, denoted  $E[ \ ]$ ,

$$\begin{aligned} S_{1y} &= E [X_1^*(j\omega)Y(j\omega)] \\ &= H_1 S_{11} + H_2 S_{12} + S_{1n}, \\ S_{2y} &= E [X_2^*(j\omega)Y(j\omega)] \\ &= H_1 S_{21} + H_2 S_{22} + S_{2n}, \end{aligned} \tag{4.10}$$

where  $S_{12}$ ,  $S_{21}$  are the cross-spectral density functions between the inputs,

$$S_{12}(j\omega) = S_{21}(j\omega) = E [X_1^* X_2], \tag{4.11}$$

$S_{1n}$  and  $S_{2n}$  are the cross-spectral density functions between the noise and the inputs,

$$S_{in}(j\omega) = E [X_i^* N], \tag{4.12}$$

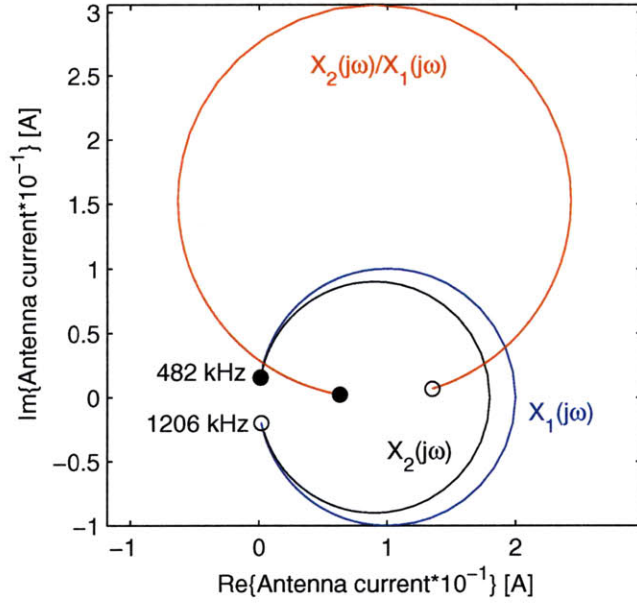


Figure 4-10: Calculation shows that the incomplete cancellation of distinct resonant frequencies of the two amplifiers produces a resonant signature that could be mistaken for a plasma resonance.

and  $S_{11}$  and  $S_{22}$  are the autospectral density functions [125],

$$S_{ii}(j\omega) = E [|X_i(j\omega)|^2] . \quad (4.13)$$

The important case for considering the antenna currents separately due to mistuned amplifiers can now be made. When the amplifiers are resonantly tuned to different frequencies, the two antenna currents could be, for example,

$$X_1 = \frac{I_1 \cdot \gamma_1}{(j\omega - (j\omega_1 - \gamma_1))} \quad \omega_1 = 2\pi \cdot 686 \text{ kHz}, \quad \gamma_1/\omega_1 = 0.05,$$

$$X_2 = \frac{I_2 \cdot \gamma_2}{(j\omega - (j\omega_2 - \gamma_2))} \quad \omega_2 = 2\pi \cdot 804 \text{ kHz}, \quad \gamma_2/\omega_2 = 0.05.$$

The voltage on probe  $k$  would then be,

$$Y_k(j\omega) = H(j\omega) \cdot (X_1 + X_2).$$

If the two-antenna diagnostic is then simply evaluated as a single-input system as-

suming the input to be  $2 \cdot x_1(t)$ , the system response is calculated as,

$$\begin{aligned} H(j\omega)_{calc} &= \frac{1}{2} \frac{S_{1y}}{S_{11}} \\ &= \frac{1}{2} H \cdot \left[ 1 + \frac{S_{12}}{S_{11}} \right] \\ &= \frac{1}{2} H \cdot \left[ 1 + \frac{I_2 \cdot \gamma_2 (j\omega - (j\omega_1 - \gamma_1))}{I_1 \cdot \gamma_1 (j\omega - (j\omega_2 - \gamma_2))} \right]. \end{aligned}$$

This constitutes an incomplete pole-zero cancellation, creating a non-physical bilinear term in the calculated system response that can be mistaken for a plasma resonance. Figure 4-10 shows how convincing the incomplete cancellation appears in the complex plane of the system response.

It is clear that if two antennas are used, the two-input model must be instantiated. The system of equations 4.10 can be solved for the system response, which is what we seek, when the noise is uncorrelated to the inputs so that  $S_{1n} = S_{2n} = 0$ . The solution is:

$$H_1(j\omega) = \frac{S_{1y} \left[ 1 - \frac{S_{12}S_{2y}}{S_{22}S_{1y}} \right]}{S_{11} [1 - \gamma_{12}^2]} \tag{4.14}$$

$$H_2(j\omega) = \frac{S_{2y} \left[ 1 - \frac{S_{21}S_{1y}}{S_{11}S_{2y}} \right]}{S_{22} [1 - \gamma_{12}^2]},$$

where  $\gamma$  is the coherence function,

$$\gamma_{12}^2(j\omega) = \frac{|S_{12}|^2}{S_{11}S_{22}}.$$

Unfortunately, this decomposition is not well-posed for the active MHD diagnostic system. First, the noise may be correlated to the inputs since the acquisition and excitation racks share the same ground. Then the terms  $S_{1n}$  and  $S_{2n}$  are finite and the system of equations 4.10 is underdetermined. Second, the system is not time-invariant, so the expectation values of the cross-spectral density functions 4.13 are not well defined. Third, the inputs are often very well correlated, so that  $\gamma_{12}^2$  approaches



unity and renders Equations 4.14 undefined. And finally, where a field null coincides with a probe (ie., at a location where the magnetic field contribution of the two antennas is opposite), the cross-spectral density functions  $S_{1y}$  and  $S_{2y}$ , being of low power, are especially vulnerable to noise.

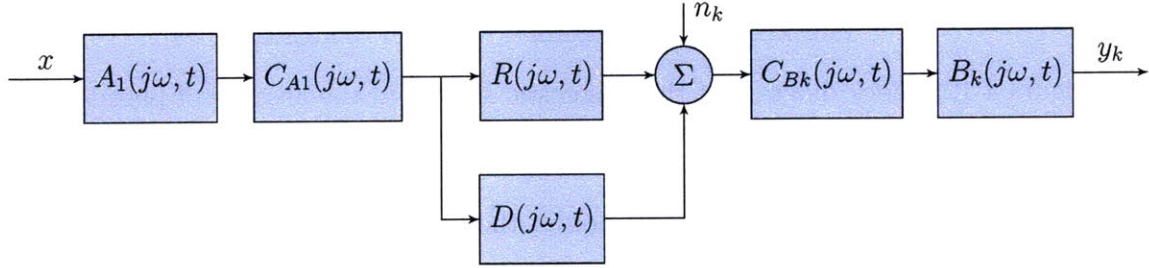


Figure 4-11: Block diagram of the single-input, single-output (SISO) diagnostic when only one antenna is active. This disambiguates the contributions of the separate antennas.

The easiest solution is to operate with only one antenna, which is how the diagnostic has usually functioned since the middle of the 2007 campaign. Of course, this limits the perturbation to half of the available power. To make use of both antennas, they could be configured in series, so that they are guaranteed to have the same current. The series configuration complicates the grounding of the transmission lines considerably. Alternatively, one of the antennas could be operated in a chopped mode to distinguish its contribution on the output. A third option would be to operate the two antennas at different frequencies. These last two solutions require clever but feasible signal processing to recover the resonant plasma response.

Henceforth the analysis will be limited to the single-input/single-output representation of one probe, in Figure 4-11, which measures

$$H = A \cdot C_A \cdot (D + R) \cdot C_{Bk} \cdot B_k. \quad (4.15)$$

The diagnostic response for a single-antenna system,  $H_D = A \cdot C_A \cdot C_{Bk} \cdot B_k$ , representing the distortion from the antenna and probes and their coupling to the plasma, remains to be determined.

## Vacuum response

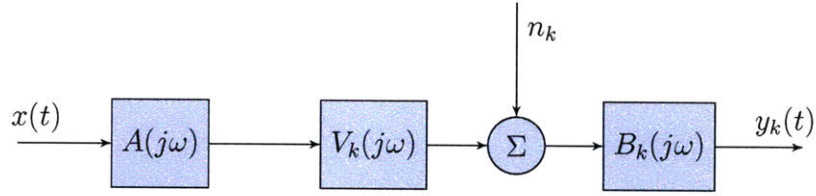


Figure 4-12: Block diagram of the diagnostic system in the absence of plasma. Neglecting pathological behavior, all of the elements are linear time-invariant (LTI).

To converge towards a compensation of the diagnostic response, the plasma response  $R + D$  can be eliminated by operating the diagnostic in vacuum during test shots or when the vessel is vented to air. Then the coupling factors,  $C_A$  and  $C_{B_k}$ , are also eliminated and all the plasma-dependent terms are replaced by the vacuum coupling term, introduced in the block diagram of Figure 4-12 and represented as,

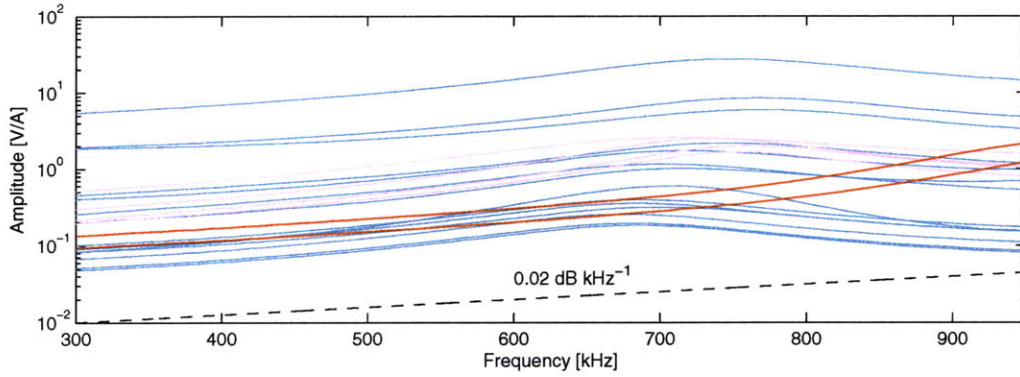
$V_k$  vacuum response: antenna coupling to probe  $k$  through vacuum or air

The system response becomes,

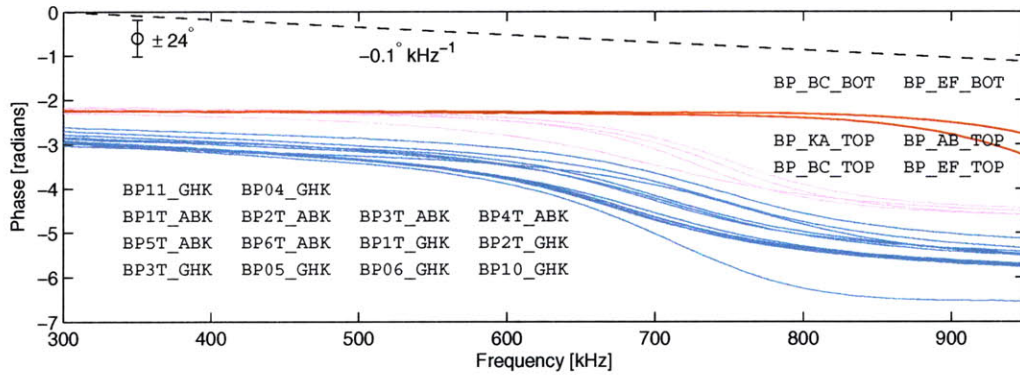
$$H_V = A \cdot V_k \cdot B_k. \quad (4.16)$$

The antenna and probe responses,  $A$  and  $B_k$ , as well as the vacuum response,  $V_k$ , are obviously plasma-independent. When pathological behavior is ignored, these responses are also linear and time-invariant (LTI). Then the uncertainty due to noise can be reduced to an arbitrary level by sufficient repetition of the measurement. The consideration of noise is relegated to Appendix A.

Several methods for measuring the system response in vacuum,  $H_V$ , are compared in Appendix B. The resultant measured functions corresponding to the set of probes are plotted in Figure 4-13. It is evident that the system response in vacuum lies outside the bounds of precision that were calculated in Criteria 4.9, and that the system response differs significantly among probes. Compensation for these distorting factors is therefore required to derive accurate resonant mode characteristics from the



(a)



(b)

Figure 4-13: Measurements of the system response in vacuum,  $A \cdot V_k \cdot B_k$ , for limiter probes (blue), low-n probes (pink) and low-n, high-frequency probes (red). Dashed black lines show the limiting precision that is required to recognize resonant plasma modes, tabulated in Criteria 4.9. Both the amplitude and the phase of the vacuum response are greater than the limits.

measured data.

### Coupling Fraction

Compensating the system response of a plasma discharge by the vacuum system response leaves,

$$\begin{aligned} \frac{H}{H_V} &= \frac{A \cdot C_A \cdot (D + R) \cdot C_{Bk} \cdot B_k}{A \cdot V_k \cdot B_k} \\ &= \frac{C_A \cdot C_{Bk}}{V_k} (D + R). \end{aligned} \tag{4.17}$$

Unfortunately, the factor  $C_A \cdot C_{Bk}/V_k$  remains unknown. Does it also significantly distort the plasma response? The remainder of this section examines this factor; let it be called the *coupling fraction* for probe  $k$ , defined as,

$$H_{Ck} = \frac{C_A \cdot C_{Bk}}{V_k}.$$

Physical intuition suggests that the phase shift and frequency dependence of the coupling fraction should be negligible. To elaborate, the denominator of  $H_{Ck}$  represents the field structure of the magnetic dipole antenna. On the scale length of the vessel diameter, at the excitation frequency below 1 MHz, and in vacuum, the dipole field is magnetoquasistatic, which precludes any phase shift or frequency dependence. However, the conductive vessel walls and molybdenum tiles surrounding the probes may complicate that assumption (see [77] and [8]). Likewise, the numerator of  $H_{Ck}$  represents the behavior of the small volumes surrounding the antenna and probe  $k$  that connect them to the flux surfaces of the TAE during a plasma discharge. The magnetoacoustic phase velocity in those volumes is everywhere greater than the on-axis Alfvén velocity, which is conservatively  $8.3 \times 10^6 \text{ ms}^{-1}$  (for  $B_0 = 5.4 \text{ T}$ ,  $n_e = 1 \times 10^{20} \text{ m}^{-3}$ , in deuterium). At frequencies around 1MHz, the antenna field pattern is again magnetoquasistatic in the tens of centimeters between the instruments and the localization of the TAE. The coupling terms  $C_A$  and  $C_{Bk}$ , therefore,

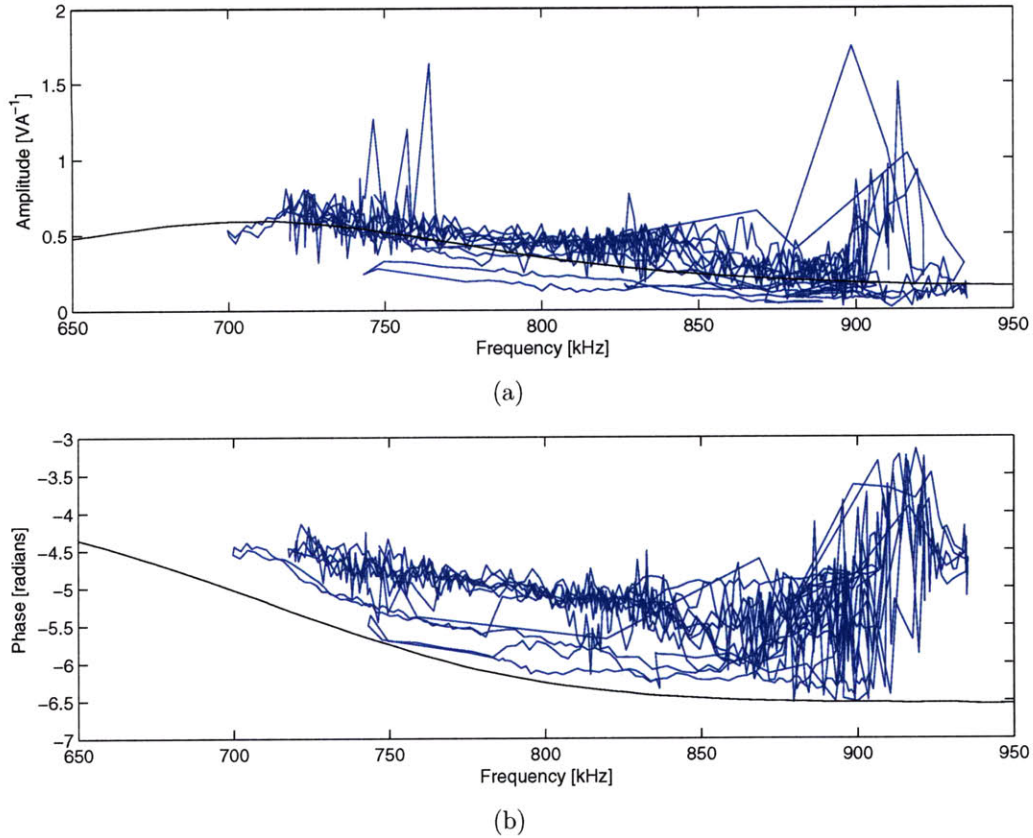


Figure 4-14: Measured system response during shot 1080403015 on probe BP1T\_GHK (blue), compared to the system response for the same probe measured in vacuum (black).

should also be essentially free of phase shift or frequency dependence. By the same reasoning the direct coupling term,  $D$ , should also be real and constant over short distances.

On the other hand, the coupling fraction does not intuitively have unity amplitude. The antenna dipole field in vacuum falls off at least as fast as  $R^{-1}$ , and like  $R^{-3}$  in the far field. Therefore  $V_k$  is much smaller for probes that are far from the antenna, and their coupling fractions are correspondingly larger.

To test this intuition, the diagnostic response,  $H_D = A \cdot C_A \cdot C_{Bk} \cdot B_k$ , can be further isolated when the resonant term,  $R$ , is eliminated from Equation 4.15, by operating the diagnostic outside of the resonant plasma regime. This is achieved, for instance, in shots with greater magnetic safety factor near the plasma edge: the Alfvén continuum

gap closes off and prevents the TAEs from coupling to the diagnostic. Since stably-resonant discharges are not trivial to achieve, shots having only the direct coupling term are common. This leaves,

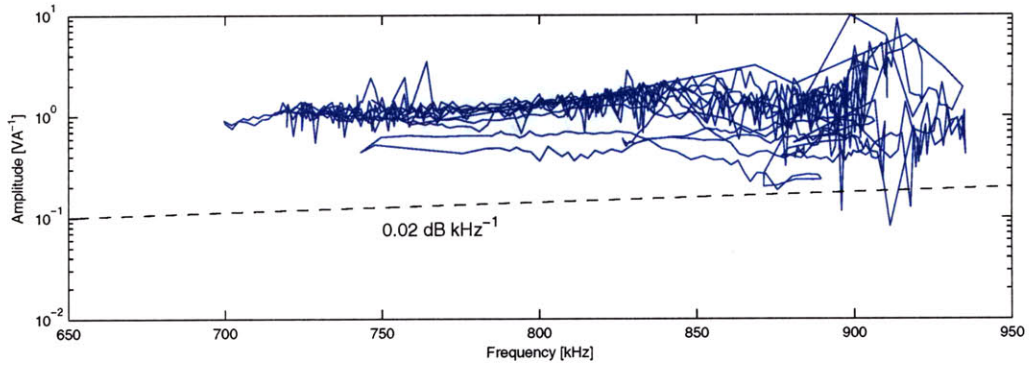
$$H = A \cdot C_A \cdot (D) \cdot C_{Bk} \cdot B_k.$$

Typical measurements in this regime are plotted in Figure 4-14. Dividing the measurement of the direct term by the system response in vacuum gives,

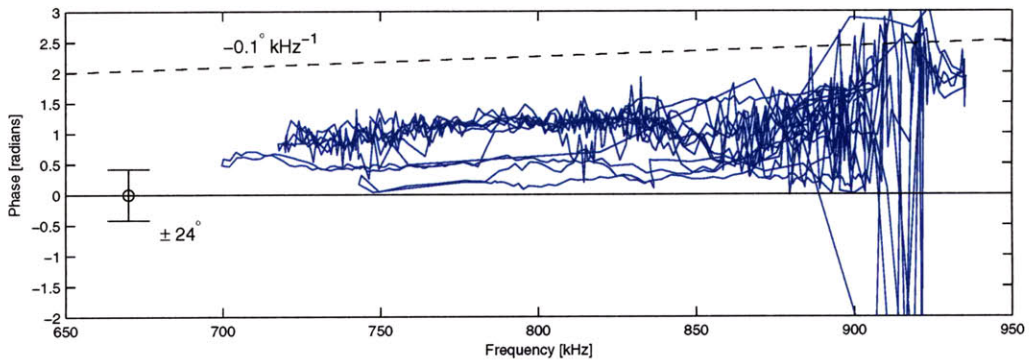
$$\frac{C_A \cdot C_{Bk}}{V_k} \cdot D = H_{Ck} \cdot D.$$

Only 15 centimeters separate the probes on the H-port face of the GH limiter from the upper active MHD antenna. The positioning is visible in Figure 4-16. Yet contrary to intuition, for some of these probes, the products of the direct term and the coupling fraction display significant phase shift and frequency dependence. Figure 4-15 plots the products  $H_{Ck} \cdot D$  for one of these probes. The phase shift is beyond the margins of acceptable distortion, Criteria 4.9. If the phase shift and frequency dependence arise from the coupling fraction, they must be compensated from the measured resonant term, as well.

The coupling fraction cannot be measured independently of the direct plasma response,  $D$ , so it cannot be directly scrutinized. However, any frequency dependence and any relative amplitude and phase shift among probes that arise from the coupling fraction mechanisms can be inferred given several rational premises on  $R$ ,  $D$ , and the coupling fraction itself. In the process, the system response that is measured in vacuum,  $H_V$ , can be validated, for if it were incorrect, the error,  $\epsilon(j\omega)$ , would be evident as an additional term in  $H_{Ck}$  when the quotient  $H/H_V$  is formed. In other



(a)



(b)

Figure 4-15: This figure presents the same data as in Figure 4-14. The measured system response from shot 1080403015 on probe BP1T\_GHK has been compensated by the system response measured in vacuum for that probe, to produce the function  $H_{Ck} \cdot D$ . Precision criteria are shown in black. The phase offset of this response lies outside of the necessary precision of  $\pm 24^\circ$ .

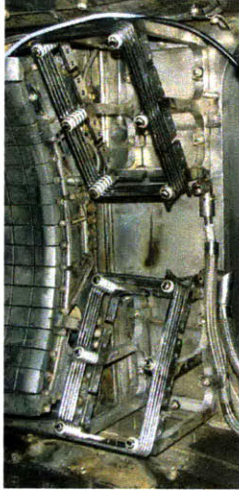


Figure 4-16: The gap between the antenna and the probes on the GH limiter is 5 – 15 centimeters. On such a small distance, direct coupling might be expected to be without phase shift.

words,

$$\begin{aligned} \frac{H}{H_V \cdot \epsilon} &= \frac{C_A \cdot C_{Bk}}{V_k \cdot \epsilon} (D + R) \\ &= \frac{H_{Ck}}{\epsilon} \cdot (D + R). \end{aligned}$$

The inferred frequency dependence, relative amplitude and relative phase shift of the coupling fraction are now investigated in turn. The insinuation of the vacuum measurement error,  $\epsilon$ , into  $H_{Ck}$ , remains implicit to simplify notation.

### Frequency Dependence

The frequency dependent phase of  $H_{Ck}$  is examined first. It will be shown that if the coupling fraction only mildly distorts the plasma response, then a limited separation of  $H_{Ck} \cdot D$  and  $H_{Ck} \cdot R$  can be achieved. Any frequency dependence that is common to both terms over an ensemble of resonant mode observations will then be attributed to the coupling fraction.

To proceed, the following supposition is made:



**Premise 1.** *The frequency dependence of the phase of the coupling fraction,  $H_{Ck}$ , is weak compared to the antenna and probe responses,  $A$  and  $B_k$ .*

The premise is supported by comparison of  $H_V$  and  $H$ , plotted in Figures 4-13 and 4-14, respectively. Their similarity suggests that most of the frequency dependence of the phase arises from their common terms,  $A \cdot B_k$ , especially when intuition maintains that  $C_A$ ,  $C_{Bk}$ ,  $V_k$  and  $D$  are real and constant. The frequency dependence of the amplitude of  $H_{Ck}$  is not treated here because it is sensitive to plasma fluctuations and because it has less influence in the determination of the resonant mode parameters.

Recall that the analysis of Section 4 separates the plasma response into the resonant component,  $R$ , and the direct coupling component,  $D$ , based on their frequency dependence, which is determined primarily by the pole,  $p = (j\omega_0 + \gamma)$ . The resonant term,  $R$ , is assigned the resonant part of the response, if it exists, and the rest is assigned to the direct term,  $D$ .

$$H(s) \approx \underbrace{\frac{r}{s-p}}_R + \underbrace{\frac{r^*}{s-p^*} + d_2s^2 + d_1s + d_0}_D$$

Under Premise 1, the same method can be applied to the partially compensated plasma response,  $H_{Ck} \cdot (R + D)$ , to accurately recover the resonant frequency and the phase of  $H_{Ck}(j\omega_0) \cdot R(j\omega_0)$ . This is evident after linearizing  $H_{Ck}$  in frequency about  $\omega_0$  and applying the perturbation to the resonant term. Defining the first derivative of the coupling fraction to be,

$$\left. \frac{\partial H_{Ck}}{\partial \omega} \right|_{\omega_0} = H_{Ck_0} \frac{j\alpha}{\omega_0},$$

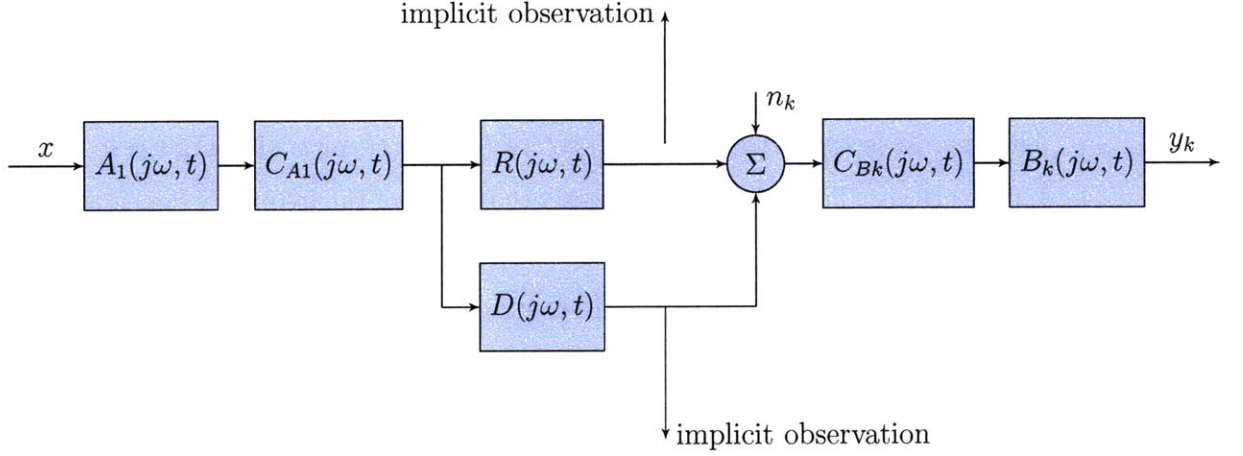


Figure 4-17: Block diagram showing the implicit observation points that are enabled by the frequency-response distinction between the two spatially-separated volumes.

the resonant term becomes,

$$\begin{aligned}
 H_{Ck}(j\omega) \cdot R &\approx H_{Ck_0} \left( 1 + j \left( \frac{\omega}{\omega_0} - 1 \right) \alpha \right) \frac{r}{j\omega - (j\omega_0 + \gamma)} \\
 &\approx \frac{H_{Ck_0} r}{j(\omega - \omega_0) \left( 1 + \frac{\alpha\gamma}{\omega_0} \right) - (\gamma - (\omega - \omega_0)^2 \frac{\alpha}{\omega_0})} \\
 &= \frac{H_{Ck_0} r / \left( 1 + \frac{\alpha\gamma}{\omega_0} \right)}{j(\omega - \omega_0) - (\gamma - (\omega - \omega_0)^2 \frac{\alpha}{\omega_0}) / \left( 1 + \frac{\alpha\gamma}{\omega_0} \right)}
 \end{aligned}$$

The weak frequency dependence of  $H_{Ck}$  primarily influences the real part of the pole and the amplitude of the residue. Therefore the resonant frequency, and the phase of the product  $H_{Ck_0} \cdot R(j\omega_0)$ , are accurately separated from the combined measurement of  $H_{Ck} \cdot (R + D)$ . Likewise, the phase of  $H_{Ck_0} \cdot D(j\omega_0)$  is also accurately determined.

Implicit in this frequency-based distinction is a spatial separation of the two signals. Whereas the resonant behavior originates on a set of radially-localized flux surfaces in the plasma core, the direct coupling occurs in the rest of the vessel, including the essential vacuum outside the scrape-off layer. It is interesting that the differing frequency responses of these two regimes allows internal states of the di-

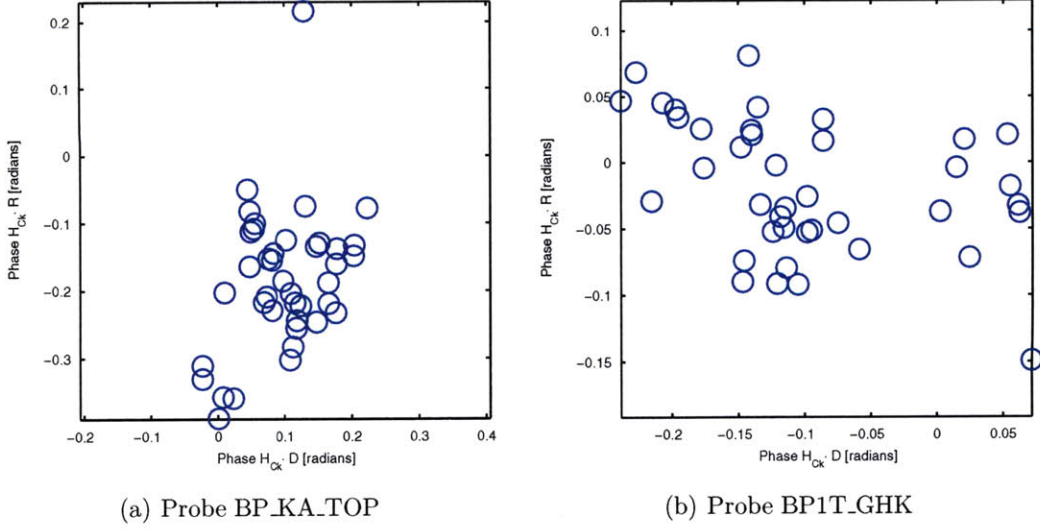


Figure 4-18: For an ensemble of resonances over a range of frequencies, the phases of  $H_{Ck} \cdot D$  and  $H_{Ck} \cdot R$  are uncorrelated, suggesting that the phase of the common factor,  $H_{Ck}$ , is not frequency dependent.

agnostic system to be observed independently, even though they are not directly measurable. One might consider this to be primitive MHD spectroscopy [126]. Figure 4-17 illustrates the concept. In addition, the two components  $R$  and  $D$ , while both magnetohydrodynamic in origin, arise from distinct plasma behavior.

Given these distinctions, one should not expect  $R$  and  $D$  to be similarly dependent on frequency. Therefore it could be supposed that,

**Premise 2.** *Any common frequency dependence between  $H_{Ck_0} \cdot R(j\omega_0)$  and  $H_{Ck_0} \cdot D(j\omega_0)$  over the ensemble of observed resonant modes is due to the factor they share, which is the coupling fraction,  $H_{Ck}$ .*

Figure 4-18 shows that the phases of  $H_{Ck_0} \cdot R(j\omega_0)$  and  $H_{Ck_0} \cdot D(j\omega_0)$  are essentially uncorrelated. Premise 2 implies that their disparate phase variation is rather due to the individual behavior of  $R$  and  $D$ , and not to the coupling fraction.

The phase of the coupling fraction can be assumed constant with frequency.

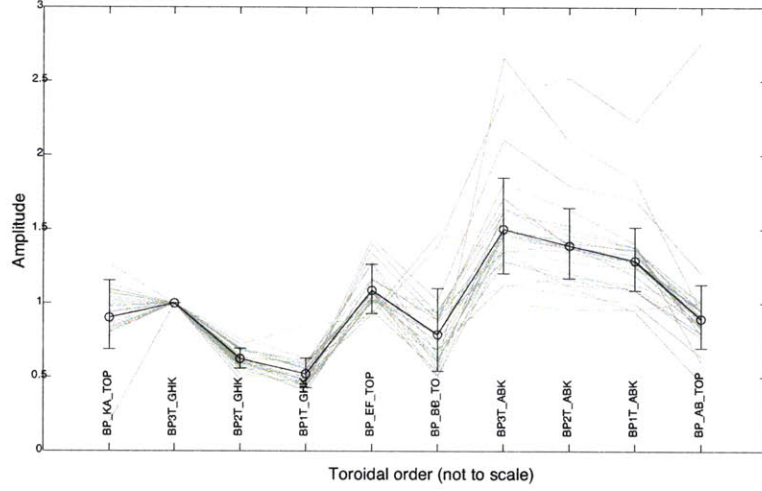


Figure 4-19: Mean amplitude of  $H_{Ck}$  over the ensemble of  $n = 0$  resonances for the upper toroidal array of probes. Normalized to the mean amplitude of  $R(j\omega_0)$  on probe BP1T\_GHK. Probes nearest the antenna have the strongest coupling in vacuum and hence the smallest coupling fraction.

### Amplitude

The relative amplitude of the coupling fraction from probe to probe is dictated in large part by the vacuum response,  $V_k$ , which is very small for probes far from the antenna. The probe coupling term,  $C_{Bk}$ , also contributes, because the probes are not all at the same major radius. Their distance from the plasma edge varies by 8 mm, depending on the adjacent diagnostics that they must not shadow, and so the coupling to the plasma also varies among probes..

On the other hand, it is true that,

**Premise 3.** *The amplitude of the resonant term,  $R$ , is independent of toroidal angle.*

In fact, the existence of AEs is predicated on their global nature, including axisymmetry. Any variation among probes in the amplitude of the measurement,  $H_{Ck} \cdot R$ , can therefore be attributed to the coupling fraction. Figure 4-19 shows the mean variation of  $H_{Ck}$  among probes over the ensemble of observed plasma resonances. The resonant signal amplitudes on each probe are balanced with this result to achieve equal weighting in the fitting procedures of Section 4.

## Phase

The relative phase of the resonant term,  $R$ , from probe to probe is determined by the mode's toroidal wavelength. Again, the axisymmetry of the resonant mode constrains the possible values of the coupling fraction. Several new variables are useful to proceed with the analysis:

$n_i$	integer toroidal mode number
$\varphi_k$	toroidal angular position of probe $k$
$\phi_{R_k, n_i}$	phase of $R$ mod $2\pi$ at probe $k$ for mode $n_i$
$\phi_{H_{Ck}}$	phase of $H_{Ck}$ mod $2\pi$
$p_{n_i, k}$	integer factor of $2\pi$ at probe $k$ for mode $n_i$
$b_{n_i}$	phase offset at $\varphi = 0$ for resonant mode $n_i$

From the axisymmetry of Alfvén eigenmodes it is true that,

**Premise 4.** *Observed resonant modes have integer toroidal mode numbers.*

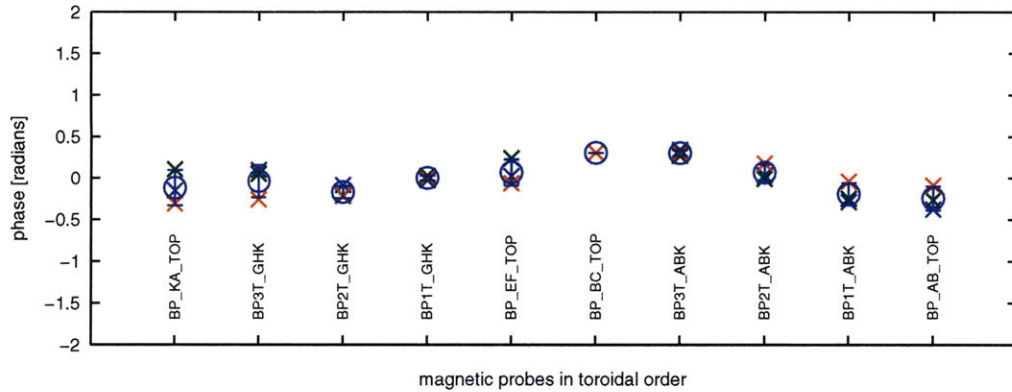
Consequently the phase of the resonant term on each probe has an integral relation to the toroidal angular position of the probe:

$$\phi_{R_k, n_i} = n_i \varphi_k + p_{k, n_i} 2\pi + b_{n_i}.$$

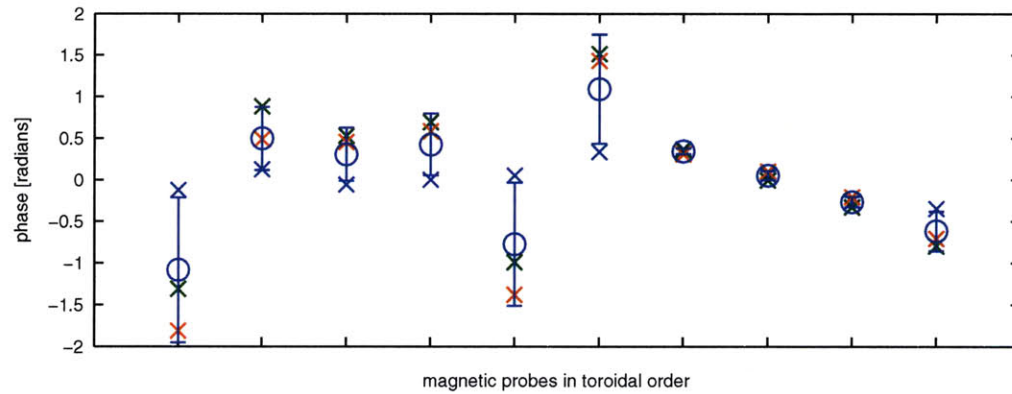
Of course, only the combination  $\phi_{R_k, n_i} + \phi_{H_{Ck}}$  can be measured. Since  $\phi_{H_{Ck}}$  is independent of toroidal mode number,  $n_i$ , the difference,

$$\underbrace{(\phi_{H_{Ck}} + \phi_{R_k, n_i})}_{\text{measured quantity}} - n_i \varphi_k + p_{k, n_i} 2\pi + b_{n_i} = \phi_{H_{Ck}}, \quad (4.18)$$

should be common to every resonant mode in the ensemble of observations, given the correct choice of mode numbers  $n_i$ . A similar method is proposed in [11]. The coincidence of the RHS of Equation 4.18 for multiple distinct toroidal modes is not trivial when the probes are unequally spaced. (For equally spaced probes, degenerate



(a) Best fit: blue  $n = 0$ ; green  $n = -6$ ; red  $n = 4$ . Circles show mean phase of coupling fraction.



(b) Next best fit: blue  $n = 0$ ; green  $n = -4$ ; red  $n = 6$ .

Figure 4-20: Relative phase of coupling fraction for toroidal array of probes, showing the best two permutations of surmised toroidal mode numbers for the three sample modes. The blue x's represent stable  $n = 0$  modes observed on runday 1080403010; the green x's correspond to unstable  $n = -6$  modes observed on 1080110031; and the red x's correspond to unstable  $n = 4$  modes observed on 1080110021. The contrast between the best permutation of mode numbers (top) and the next best permutation (bottom) is stark and convincing.

solutions would exist). Three types of recognizably similar resonant modes were tested against relation 4.18: a stable mode with toroidal mode number  $n = 0$ , and two unstable modes with toroidal mode numbers of  $n = -6$  and  $n = 4$ . Figure 4-20(a) shows that the phase of the coupling fraction is common and small for this ensemble of resonant mode observations. Uncertainty in the phase of the coupling fraction for all probes, marked with error bars, is less than  $\pm 15^\circ$ , within the bounds of  $\pm 24^\circ$  set by Criteria 4.9. Therefore the phase of the coupling fraction is generally finite but not large enough to obscure the toroidal mode number.

The measurement of unstable modes does not include the antenna coupling term,  $C_A$ . Nevertheless,  $C_A$  is the same for the coupling fraction of every probe, and since common terms do not contribute in this comparison of *relative* phase among probes, use of unstable modes in the analysis is valid. In addition, this test simultaneously confirms that the suspected mode numbers  $n = \{0, -6, 4\}$  are accurate, since they result in the most consistent RHS of Equation 4.18.

In this section, the normal non-ideal behavior of the diagnostic has been quantified. The distortion from the antenna, the magnetic probes, and the coupling of those instruments to the plasma have been addressed. It has been shown that the resonant component of the measured signal can be isolated to a satisfactory degree such that the characteristics of the plasma resonance can be reliably derived.

In practice, several pathological effects must first be reconciled before the measured signals are useable.

## 4.2.2 Compensating for Pathological Non-Ideal Effects

Several instrument faults occur frequently enough in the course of experiments that they must be addressed rather than discarding the affected data.

### Time-base offset

The data acquisition system consists of three 16-channel boards that normally sample at rates between 2.5 MHz and 10 MHz. Each board produces its own sampling trigger in synchronization with an external clock. On approximately one third of shots, the triggers of some boards may be offset by an integer multiple of samples. It appears that this fault is a deficiency in the design of the boards and cannot be remedied.

When the time base of two signals is offset, their cross-spectral density function will have a frequency-dependent phase offset. For an offset of  $n$  samples at sampling frequency  $F_s$ , the phase offset at frequency  $\omega$  is,

$$\sigma_\phi = \frac{n}{F_s} \omega \text{ [radians].}$$

The system response measured on many of the probes suffers from such phase offsets. They can be repaired in post-shot processing by removing the offset in the time base, if it is known.

After this fault was discovered, one channel of each board was tied to a common square-wave signal. Then the detection of the time-base offset can be automated by comparing the timing of the square-wave edges. In fact, it is possible to recognize timing-offsets by correlating the noise on the common signal: the square wave is not even necessary.

To recover data in shots prior to the discovery of the time-base offset, the phase of the system response for one probe on each board can be compared to their usual performance. Extra slope in phase with respect to frequency indicates a relative offset in the time-base between the corresponding boards. Figure 4-21 shows the response of a probe suffering from a timing offset, compared to its usual system response.

This fault represents a pathological binary time-dependence in the probe response,  $B_k$ .



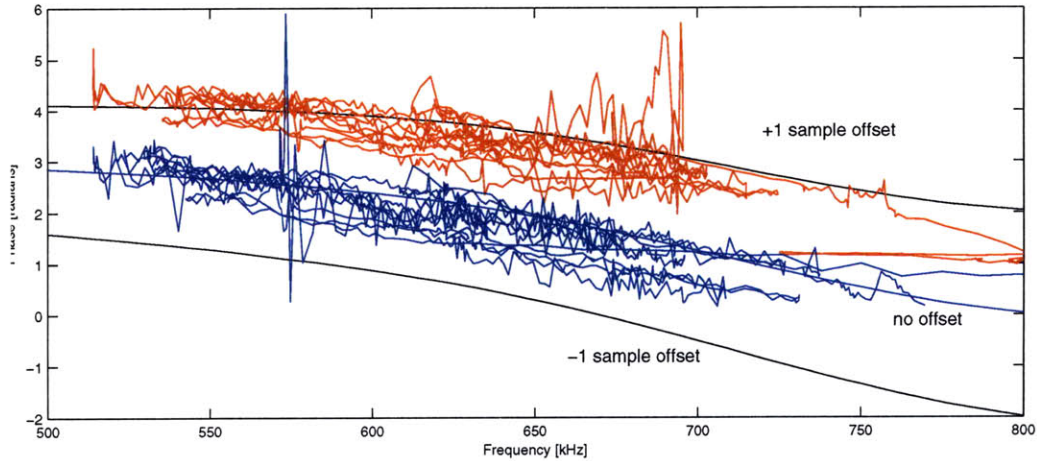


Figure 4-21: The usual phase of the system response measured on a probe, compared to the frequency dependence of the phase when the time-base of the data acquisition board has an offset.

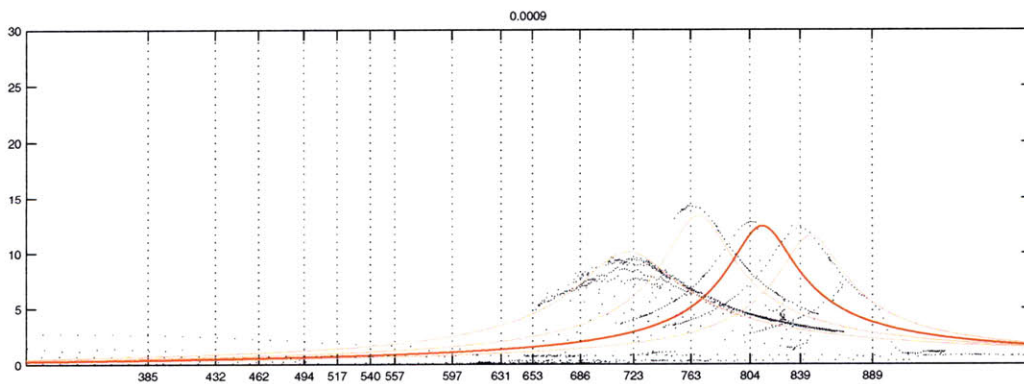


Figure 4-22: Calculated current at the vacuum feedthrough for  $11 \Omega$  effective output resistance of the amplifier (pink curve with peak at 723 kHz) and  $5.5 \Omega$  (other pink and red peaks), matches the measured currents (black) at full output and when some of the MOSFETs fail.

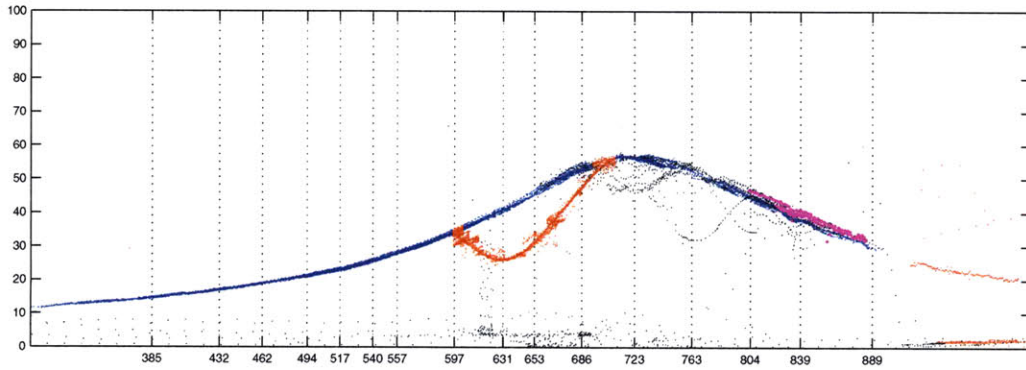


Figure 4-23: The saturation of some probe signals at the data acquisition results in an attenuated system response (red). The behavior is intermittent because saturation does not occur (blue) when the antenna current is reduced due to MOSFET gate corruption (see Figure 4-22). Resonances are verified to fall outside of the attenuated probe signal (purple).

### Current attenuation

The gating signals that operate the MOSFETs in the amplifiers pass between the control crate and the amplifier crates inside a shielded rack. On that path they can be corrupted by noise from the amplifiers, and subsequently fail to drive the gates as intended. Schematic 3-2 depicts the amplifiers, which consist of four parallel n-type MOSFETs sourcing the positive half of the antenna waveform, and four parallel p-type MOSFETs that source the negative half of the waveform. Each MOSFET is in series with a  $22\ \Omega$  resistor. During normal operation, the effective output resistance of the amplifier is therefore  $5.5\ \Omega$ . When MOSFETs fail to saturate or cut-off, they increase the effective impedance of the amplifiers, attenuating the current. The effective impedance becomes  $7.3$ ,  $11$  or  $22\ \Omega$ . Figure 4-22 shows that the intermittent current attenuation measured at the vacuum feedthrough matches this pattern of fault in the MOSFETs.

The current attenuation does not affect the measurement of the diagnostic system response, since the system is for the most part linear. A non-linearity is encountered when the data acquisition saturates.

## Acquisition Saturation

The direct coupling term,  $D$ , is large enough for some probes near the antenna that the signal at the acquisition input exceeds 2.5 V, the maximum measurable voltage. The amplitude of the system response on these probes is artificially reduced in that situation. Since the reduction in recorded voltage reflects the profile of the current amplitude, the modified system response resembles resonant behavior. Figure 4-23 shows the modified system response for a saturating probe near the antenna.

The behavior is intermittent because the acquisition channel does not saturate when the current is attenuated due to MOSFET faults, as described above. This fault represents a pathological time-dependent non-linearity in the response of select probes,  $B_k$ . The affected probes are not routinely used in the analysis of observed modes because they are situated at different elevations than the primary toroidal array of probes.

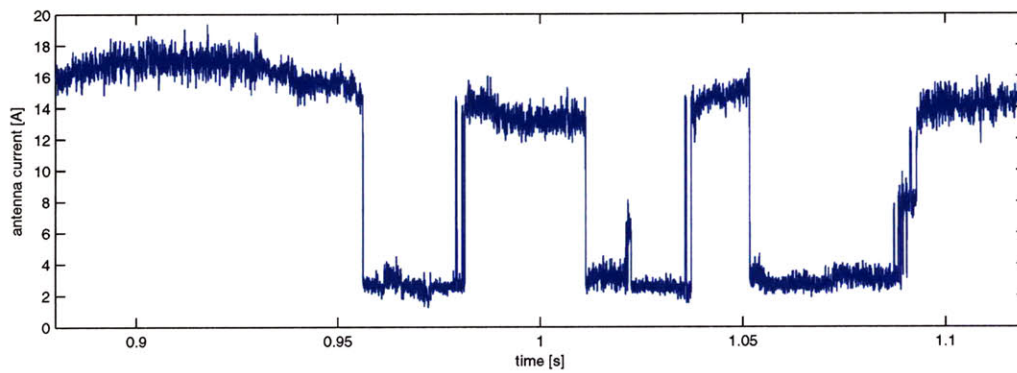
## Tuning gaps

The amplifiers incorporate variable capacitive tuning networks to match the amplifier output impedance to the antenna inductance throughout the wide range of operating frequencies. The tuning bands are approximately 100 kHz wide. During frequency excursions outside that range, the amplifier is tuned by reconfiguring the capacitance via mechanical relays, which take approximately 20 ms to transition states. Sometimes the transition takes longer if an arc develops.

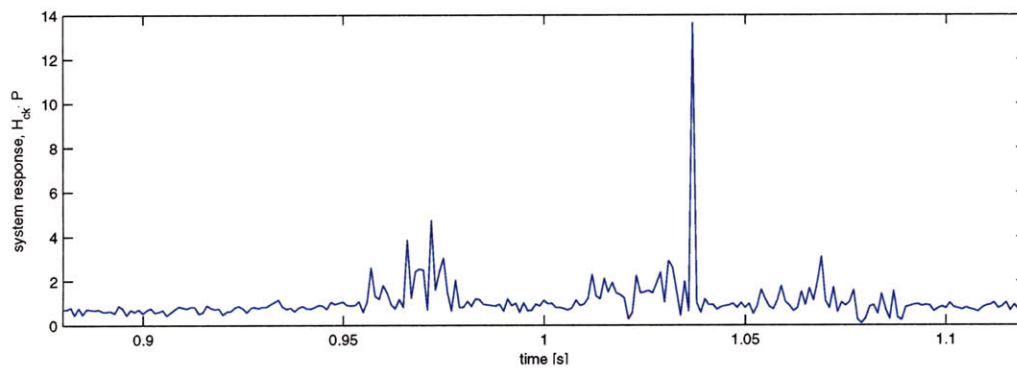
During the relay transition, the amplifier can be strongly out of tune, and consequently the antenna current can be very low, as well as noisy. These periods generally result in unuseable measurements of the system response. When the transition period coincides with a resonant plasma mode, the corresponding interval of the system response is disregarded. Figure 4-24 shows one such interval.

---

In the preceding sections, methods to compensate the measured data for normal and pathological behavior of the diagnostic system were developed. Properties of the



(a)



(b)

Figure 4-24: The antenna current is strongly attenuated during the  $\sim 20$  ms transition of the tuning network relays. In that period, the system response is heavily distorted. Shown here for 1080403024 on probe BP1T\_ABK.

resonant plasma response can be confidently derived when these methods are applied.

Given the variety of coupled fluctuations inherent to the diagnostic system, however, it is prudent to demonstrate directly that the observed resonant modes are in fact products of the plasma, and that they do not mistakenly arise from any of the diagnostic mechanisms.

### 4.2.3 Discriminating Plasma Resonances from other Processes

The distributions in time and frequency of the ensemble of observed plasma resonant modes are compared to several inherent fluctuations of the diagnostic. Finding that the distributions are not coincident, the resonant modes are concluded to arise from the mechanisms of the Alfvén eigenmode.

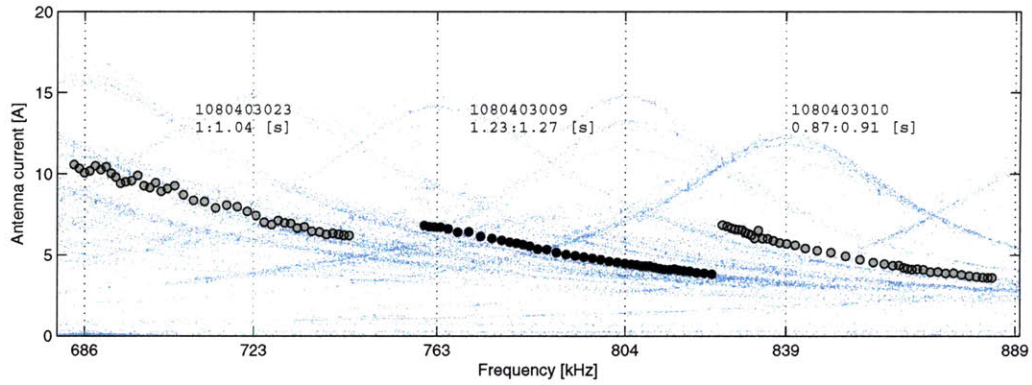
#### Amplifier Matching Network Resonance

The antenna and amplifier system, with its impedance matching network, has a damping rate of  $\sim 5\%$ . This response should not be observed in the measurement of  $H = A \cdot C_A \cdot P \cdot C_{Bk} \cdot B_k$ , since it is outside the measurement points. Could it somehow be the source of the observed resonant modes?

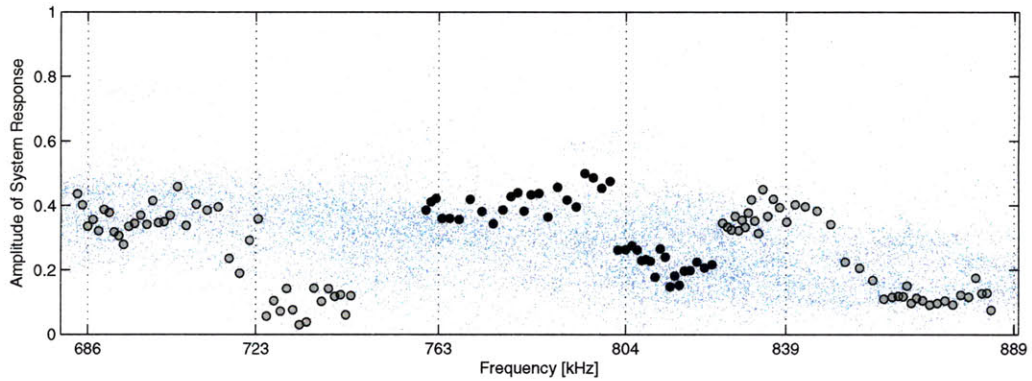
Figure 4-25 compares the frequency profile of the antenna current to the amplitude of  $H$  over the same frequency axis. Since the peaks do not coincide, the resonance of the impedance matching network is not the source of the observed resonant modes.

#### Dissonant Probe Response

When new probes were installed to obtain greater toroidal mode resolution, several of them were produced with higher resonant frequencies. After compensating the observed resonant modes by the system response measured in vacuum, probes of both standard and high resonant frequency detect the same pole. Therefore the observed resonance is not a product of the probe response. Figure 4-26 compares the system response in vacuum for standard and high-frequency probes to several observed plasma resonances to show that they are not coincident.

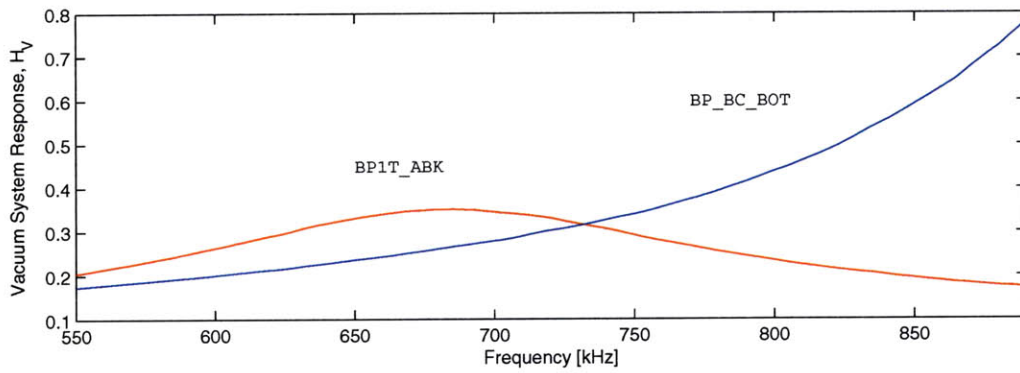


(a) Antenna current

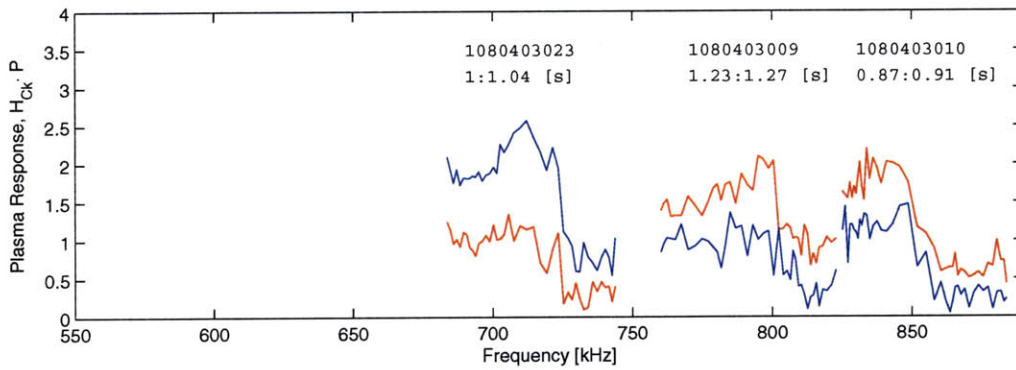


(b) System response amplitude

Figure 4-25: The amplitude of the system response is not correlated with the amplifier tuning response. Three resonant modes are plotted in black and grey. The typical antenna current and system response are shown in light blue. For reference, the peak of each tuning band is shown on the frequency axis.



(a) System response measured in vacuum



(b) System response measured through plasma, compensated for diagnostic response.

Figure 4-26: Comparing the plasma response to the system response measured in vacuum demonstrates that the observed plasma resonances are not artifacts of the frequency response of the diagnostic system.

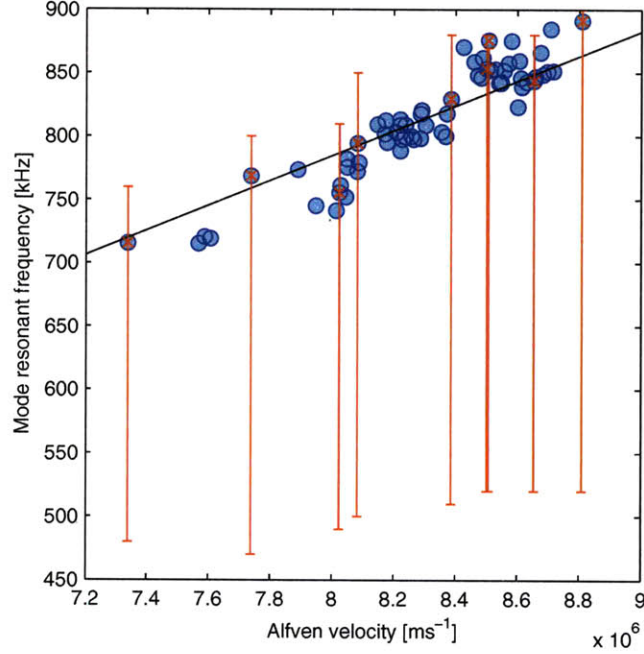


Figure 4-27: The frequency of observed  $n = 0$  stable resonances scales with the Alfvén phase velocity, calculated for line-averaged density and magnetic field on axis. The vertical red bars give the width of the TAE gap at  $r/a = 0.6$ , calculated by NOVA-K, and show that the modes fall near the top of the TAE gap, which is expected for Global Alfvén eigenmodes. The black line is the best fit line through the origin; its slope is determined by the pitch angle on the flux surface of the modes.

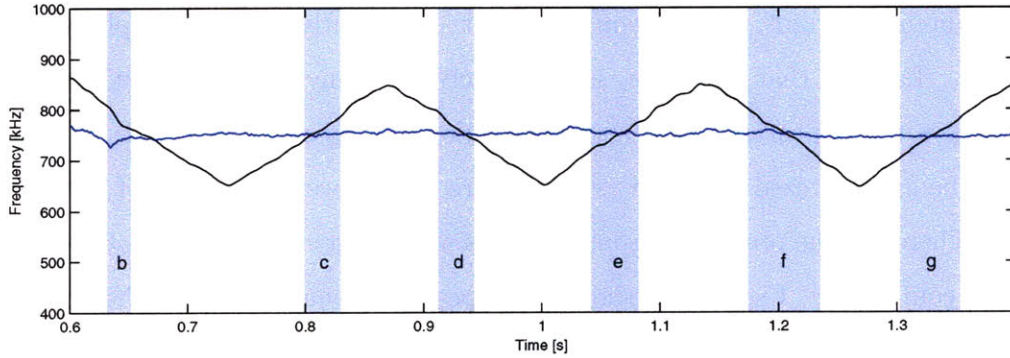
### Alfvén Frequency Scaling

The resonant frequencies of the ensemble of observed resonant modes scale with the Alfvén speed for the corresponding plasma parameters,

$$c_A = \frac{B}{\sqrt{\rho\mu_0}}.$$

None of the diagnostic components is likely to have a similar dependence on the magnetic field and plasma density. Figure 4-27 shows that the  $n = 0$  modes scale near the top of the TAE gap, where GAEs are expected to reside.





(a) Excitation frequency (black) repeatedly crossing the TAE frequency (blue). Blue bands indicate resonant mode intervals.

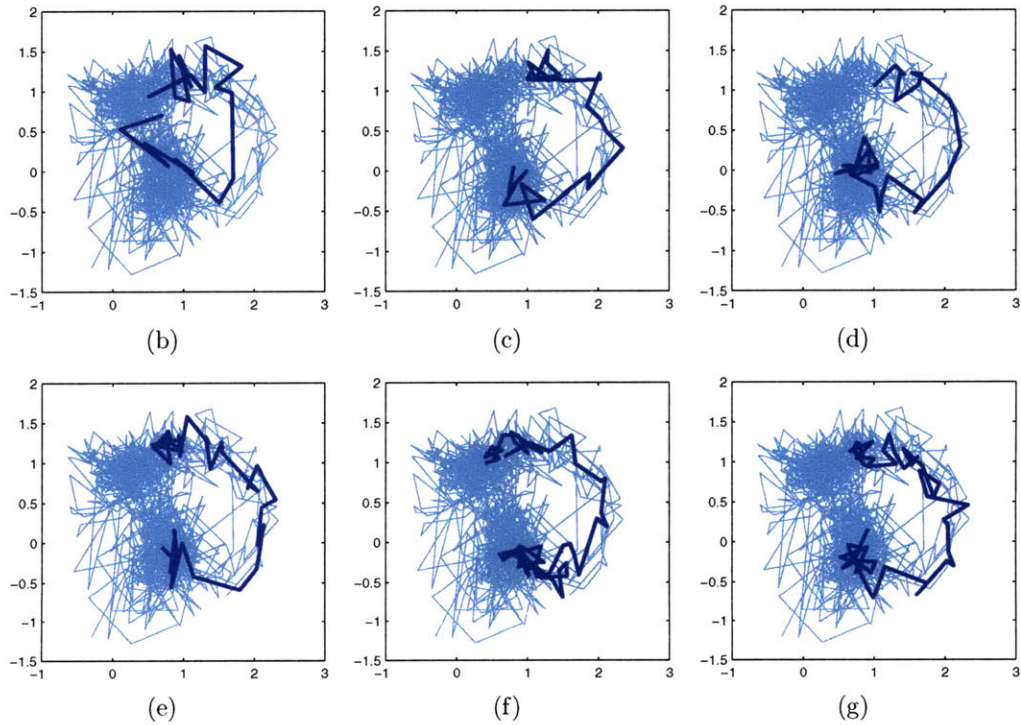


Figure 4-28: Resonant modes observed during shot 1080403019 on six consecutive crosses of the TAE frequency for  $q=1.25$  confirm the Alfvénic origin of the resonant mode. In figures b-g, the compensated plasma response as observed on probe BP3T\_ABK at each resonant interval is plotted (dark blue). The system response for the entire shot is shown for reference (light blue).

## Resonance Tracking

In some shots, resonances are repeatedly observed on consecutive frequency sweeps of the antenna current. The antenna does not significantly perturb the plasma equilibrium. Lacking that influence, it is unlikely that any plasma fluctuations that might give the appearance of a resonant mode, such as a change in the outer gap, should be synchronized with the excitation frequency over the course of several periods. Therefore the observed resonant modes are not artifacts of fluctuations in the plasma equilibrium. Figure 4-28 shows the repeated resonant modes as the excitation frequency repeatedly crosses the TAE frequency.

## Transient Response

The stable  $n = 0$  resonant modes are observed to have damping rates in the neighborhood of 1%. In the sudden absence of excitation, such modes should persist and be observable above  $e^{-1}$  of their original amplitude for  $100/2\pi \sim 16$  cycles. This test should be performed by clamping the antenna current in the course of exciting a resonant mode, and observing the transient response on the magnetic probes.

An attempt at this last test on 1091217 failed for lack of discharges. Nonetheless this section provides conclusive evidence to attribute the resonant observations to Alfvén eigenmodes.

### 4.2.4 Conclusion to Equipment

In this chapter, the derivation of resonant mode properties from the measured system response was developed. The regular and irregular response of the diagnostic components have been characterized. None of them are responsible for the appearance of a global resonance on the magnetic probes. Therefore the resonant modes are clearly a behavior of the plasma. Also, the derivation of the properties of the resonant modes is accurate.

The ensemble of resonances from the 2008 campaign can be reliably declared to have toroidal mode numbers of  $n = 0$ . In the remaining chapters, the radial eigenmode

structure is investigated using calculations with the NOVA-K code; and the effect of energetic particle drive from ICRF-heated protons is presented based on observations of the compact neutral particle analyzer in combination with results of the code.

# Chapter 5

## Results

In this thesis, the excitation of Alfvén eigenmodes by energetic ions is investigated empirically in two ways. Most simply, the spontaneous onset of an Alfvén eigenmode during strong ICRF heating marks the minimum ion distribution that is required to achieve instability. Unstable eigenmodes were observed in several discharges in the 2007 and 2008 experimental campaigns. The threshold ion distributions leading to the onset of these unstable modes were generated by modest levels of ICRF around 3.5 MW; the distribution tails were measured to have temperatures around 135 keV by the Compact Neutral Particle Analyzer (CNPA). The unstable modes are found to have moderate toroidal mode numbers including  $n = -4$  and  $n = 6$ .

The active MHD diagnostic furnishes a second, complementary method to examine the interaction between energetic ions and Alfvén eigenmodes. It analyzes the plasma frequency response over the entire Alfvénic range to expose the stable spectrum of discrete modes, as described in Chapter 3. Consequently, the impact of intensified energetic ion distribution on every discrete mode of the spectrum, and at all levels of excitation prior to instability, can be observed. In several series of shots in 2006, 2007 and 2008, plasmas were generated while ICRF heating power varied between 0 MW and 5.5 MW from shot to shot. Stable resonant modes were observed in many shots, though the plasma frequency response as measured by the active MHD system is found to be sparsely populated. After analysis following the methods of Chapter 4 the observed modes are found to have toroidal mode numbers of  $n = 0$

(for those in 2008) and  $n = 1$  (for those in 2007). While the augmented toroidal array of probes had not been implemented in 2006, linear fits to the residue phases of the limiter probes found moderate mode numbers. TAEs cannot have toroidal mode numbers of  $n = 0$ , so the  $n = 0$  modes of 2008 are concluded to be global Alfvén eigenmodes (GAEs). The  $n = 1$  modes in 2007 are concluded to be TAEs because their frequencies fall in the TAE gap in the Alfvén continuum. Figure 5-1 shows the summarized chronology of the experiment.

**history of AMHD rundays and conditions**

runday	MP	config	RF power	B_T	I_p	antenna	CNPA operator	mode numbers
1060526	404a	limited	0-2.5 MW	-5.4T	-800 kA	both	vtang	moderate
<b>low-n probes installed (1070201)</b>								
1070605	489	limited	0-2.5 MW	-5.9T	-600 kA	both	none	1
1070626	489	limited	0-4 MW	-5.9T	-600 kA	both	none	1
<b>single antenna operation (1070801)</b>								
<b>CNPA back online (1070816)</b>								
1080110	489	diverted	0-5.5 MW	-5.9T	-600 kA	upper	sears/abader	0
1080403	489	diverted	0-3.5 MW	-5.9T	-600 kA	upper	sears/abader	0

**Notes**

This lists only the dedicated rundays for MP 404a and 489 since the 2006 campaign, and is not an exhaustive list of all runs. Piggy back runs have been useful for diagnostic checkout but did not contribute significant AE data.

see /home/sears/shot\_list.sxc for shot-to-shot details for ALL AMHD shots since 1050614

Figure 5-1: Brief chronological outline of the experiment.

The resonant modes observed in each respective campaign were similar in frequency response and occurred in similar plasma conditions, with the primary variation among shots being ICRF power. Therefore the group of stable modes from each campaign is treated as an ensemble in the analysis and interpreted collectively. One ensemble comprises the  $n = 0$  modes from 2008; a second ensemble comprises the  $n = 1$  modes from 2007; and a third ensemble comprises the moderate- $n$  modes of 2006. Unstable modes are discussed together but treated individually in analysis because they have distinct toroidal structure.

Calculations with the perturbative equilibrium and kinetic code NOVA-K for the conditions in the 2007 shots find unstable toroidicity-induced Alfvén eigenmodes at

similar frequencies to the observed modes in a range of toroidal mode numbers, but only stable modes with  $n = 1$ . The calculations also provide an estimate of the radial and poloidal structure of the TAEs that is not possible to measure with external magnetic probes of limited poloidal coverage. Compared to the moderate- $n$  modes that tend to be most easily destabilized, the calculations show that low- $n$  modes, such as  $n = 1$ , tend to peak in amplitude much closer to the plasma edge where interaction with the diagnostic takes place.

Several significant findings resulting from these experimental series and NOVA-K calculations are as follows. An antenna of wide toroidal wave spectrum is operated for the first time with fully resolved toroidal array of magnetic probes. GAEs having  $n = 0$  are shown to exist and to not couple strongly to energetic ions generated by ICRF heating. Low- $n$  modes such as the  $n = 0$  GAEs and the  $n = 1$  TAEs from the 2007 campaign are found to couple most strongly to the diagnostic antenna and magnetic probes by virtue of their proximity to the plasma edge. Finally, the modes that are most strongly excited by energetic ions have moderate toroidal mode numbers in the range  $|n| = 4$  to  $|n| = 8$ .

This chapter presents the results and interpretations that support those findings. Observations of  $n = 0$  GAEs from the 2008 campaign are discussed first because they are the most clear: scrutiny of the diagnostic performance is easiest and interpretation of the results is most confident for that ensemble. Next, the stability measurements of the 2006 ensemble are presented, complemented by preliminary analysis of the 2007 ensemble, where it is suggested the fast ions could be contributing damping to moderate- $n$  modes. However, a more conservative analysis of the 2007  $n = 1$  stable mode observations from the 2007 campaign find that only modes observed during the Ohmic regime can reasonably be interpreted. Corresponding calculations from NOVA-K lend evidence that the diagnostic, being restricted to the plasma edge, is biased to observe low- $n$  modes for the particular equilibria in these two campaigns. It is argued that the observed spectrum of stable discrete modes depends strongly on the plasma equilibrium profiles even though the antenna has a broad toroidal spectrum. Finally unstable mode observations from both campaigns are presented. They exhibit

preferential excitation by the energetic ions in the midst of active stimulation of the  $n = 0$  and  $n = 1$  stable modes.

## 5.1 2008 ensemble

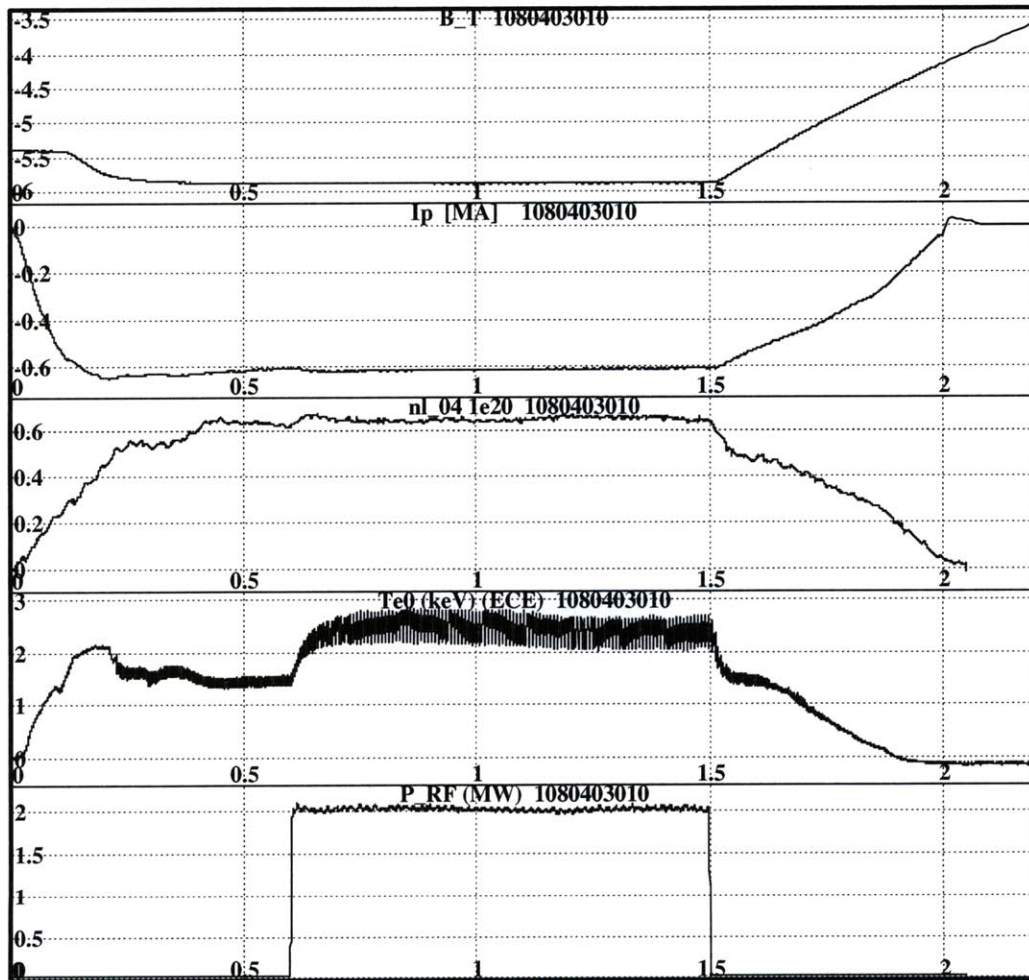


Figure 5-2: Plasma conditions for shot 1080403010.

The discharges in the 2008 runs were programmed to maximize the interaction between the energetic ion distribution and the eigenmodes, while ICRF power was varied from shot to shot between 0 MW and 5.5 MW. Some of the notable plasma conditions are plotted in Figure 5-2 for a typical shot, 1080403010.

The distance between the plasma edge and the outer wall is one of the most

Shot= 1080403010 Time= 0.900 Ip = 0.62

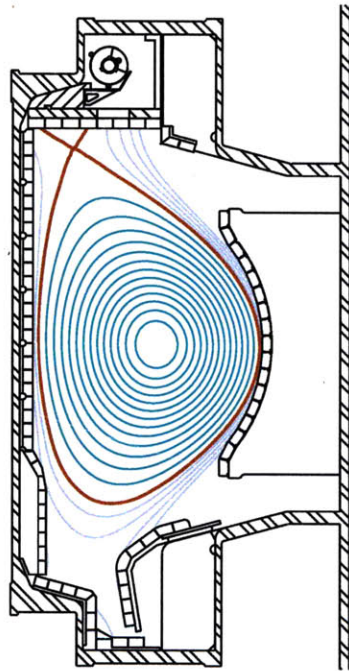


Figure 5-3: Equilibrium magnetic field reconstruction during a resonance in 1080403010. The red curve separates the confined field lines from the field lines the intersect vessel.



important conditions because it determines the strength of coupling between plasma modes and the diagnostic antenna and probes. Gaps well below 8 mm were routinely achieved by confining the plasma in a diverted configuration with a magnetic field null at the top, allowing it to be pulled away from the inner wall. The magnetic field profile for shot 1080403010 is depicted in Figure 5-3.

The upper-null diverted configuration also favorably increases the threshold of ICRF power at which the plasma transitions from a mode of low confinement (L-mode), with a peaked radial density profile, to one of high confinement (H-mode). Since the density profile partly determines the radial shape of the toroidicity induced gap in the Alfvén continuum, maintaining L-mode in all shots ensured that comparable modes would be observed. Argon injected during strong ICRF heating also helped to maintain L-mode by radiating power and allowed measurement of the rotation profile by x-ray spectroscopy.

The major radius of ICRF deposition is determined by the location at which the fast wave is resonant with the local minority cyclotron frequency, which varies with magnetic field. Typically the ICRF transmitter frequency is chosen to center the deposition on axis for a  $-5.4$  T field; in these shots the deposition was pushed outboard, closer to the presumed maximum amplitude of Alfvén eigenmodes, by increasing the toroidal field to  $-5.9$  T. At the same time, the density was kept low to increase the minority tail temperature that is achievable by ICRF heating, and to minimize the attenuation of charge-exchanged neutrals that are collected by the Compact Neutral Particle Analyzer (CNPA). The combination of high field and low density lead to a high Alfvén velocity and consequently high expected TAE frequencies.

The total plasma current also determines the radial profile of the magnetic pitch angle (inversely related to the safety factor,  $q$ ), and consequently the radial profile of the toroidicity-induced gap, as well. These shots had relatively low plasma current around 600 kA to move the  $q = 1.5$  surface towards the magnetic axis and the ICRF deposition layer. Unfortunately this also moved eigenmodes that are resonant on the  $q = 1.5$  surface further from the active MHD diagnostic.

This collection of conditions optimizes the plasma for substantial minority ion

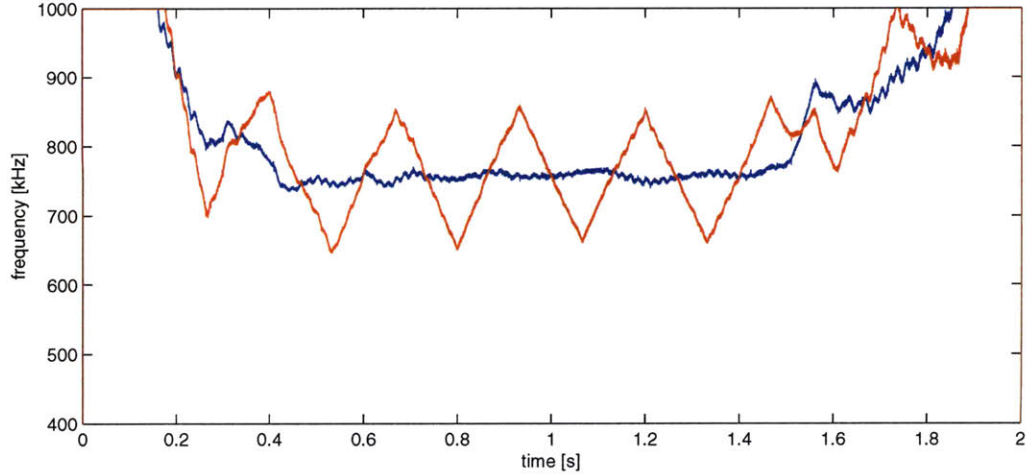


Figure 5-4: TAE frequency calculated with the line-averaged density and on-axis magnetic field (blue) and the active MHD excitation frequency (red) for shot 1080403010.

tail distributions and strong interaction between ions and eigenmodes. Moreover it appears to be a successful formula for eigenmodes to be observed *at all*, in contrast to shots programmed for other experiments (so called 'piggy-back' shots) in which no stable eigenmodes are observed. That the conditions described here for shot 1080403010 are well suited to active MHD operation may be largely due to the very small outer gap; otherwise the symbiosis is not well understood.

The active MHD diagnostic was operated with only the upper antenna in the 2008 runs, to simplify the system identification process as described in Chapter 4. The estimated TAE frequency for shot 1080403010 and the active MHD excitation frequency are shown in Figure 5-4. TAEs can be localized near surfaces of rational safety factor,  $q$ , typically between  $q = 1$  and  $q = 1.5$ . The nominal excitation frequency was varied accordingly from shot to shot to interrogate the plasma frequency response for TAEs throughout that range of safety factor.

Sixty-five resonant modes were observed on rundays 1080110 and 1080403. The distribution of resonances throughout the shots of the two rundays is shown in Figure 5-5.

The resonant plasma response is obtained from the signals of 27 magnetic probes. Since accurate calculation of the toroidal mode number requires the phase to be

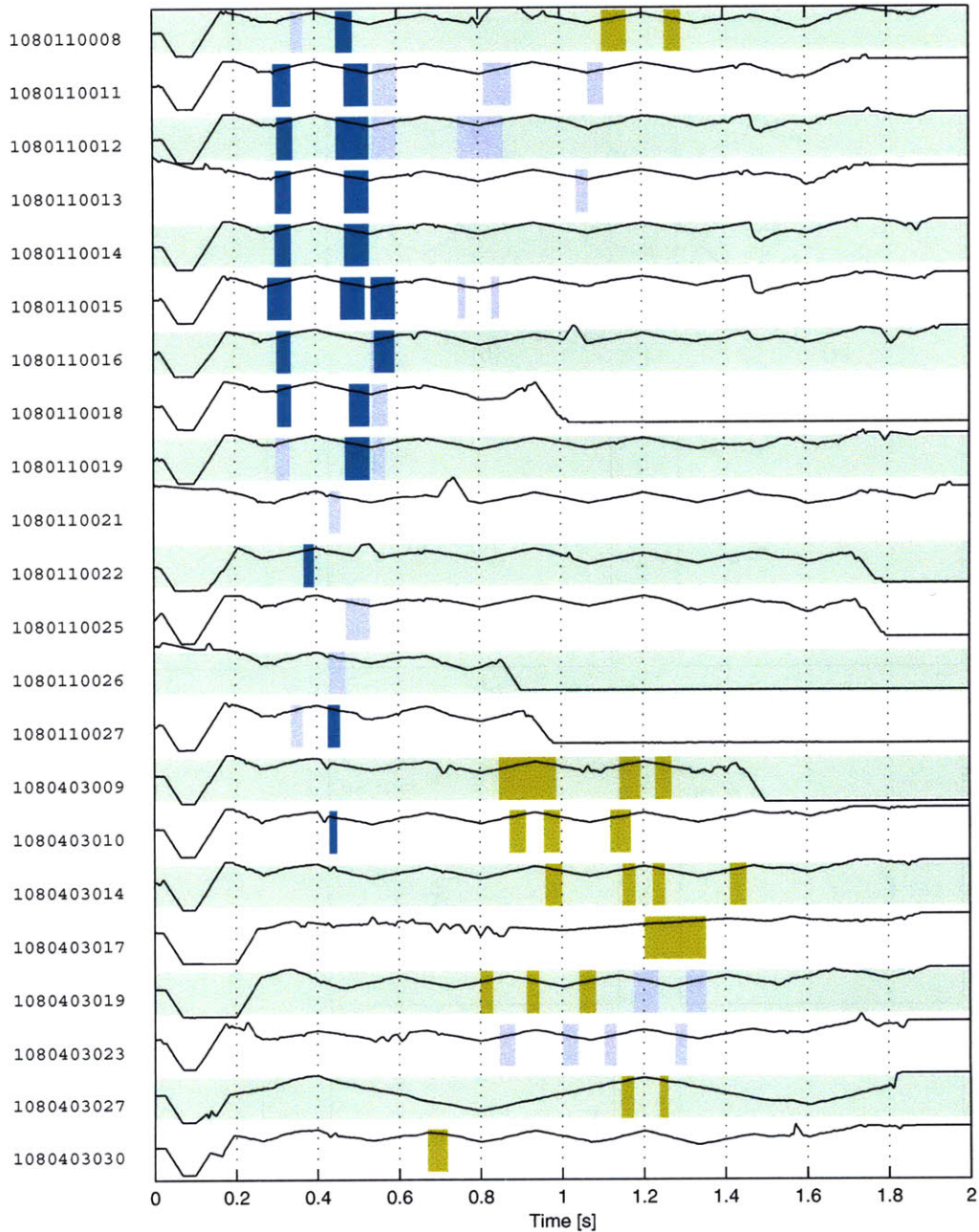


Figure 5-5: Distribution of the ensemble of resonant modes among shots of 2008. All of these shots were L-mode diverted plasmas with upper nulls. Resonant mode observations are marked in dark blue, light blue and lime, with the color signifying modes having similar toroidal amplitude profiles as a result of subtle changes in the plasma position. The black trace shows the excitation frequency of the active MHD antennas. The green background simply helps distinguish consecutive shots.

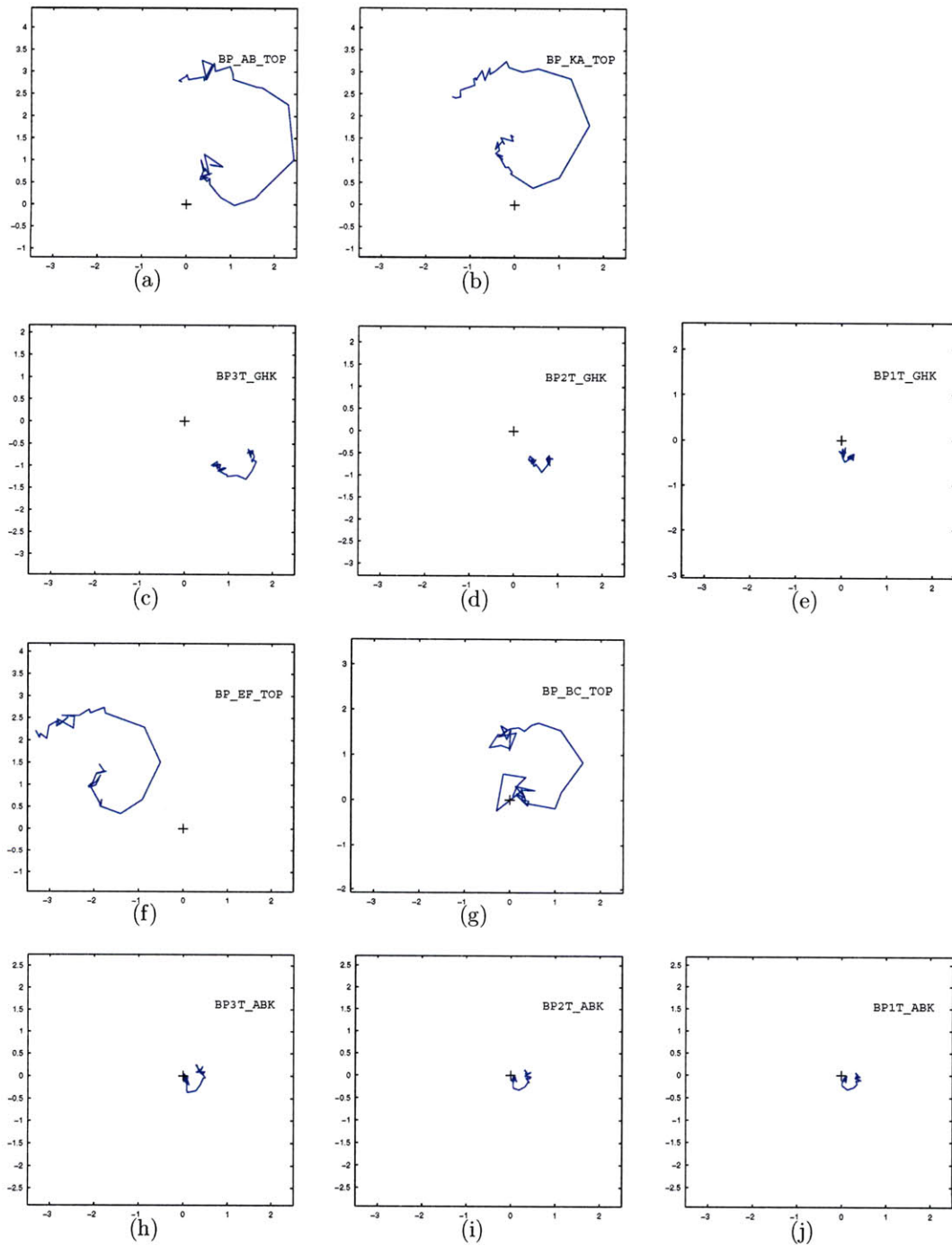


Figure 5-6: Frequency response for a resonance in 1080403010, uncompensated.

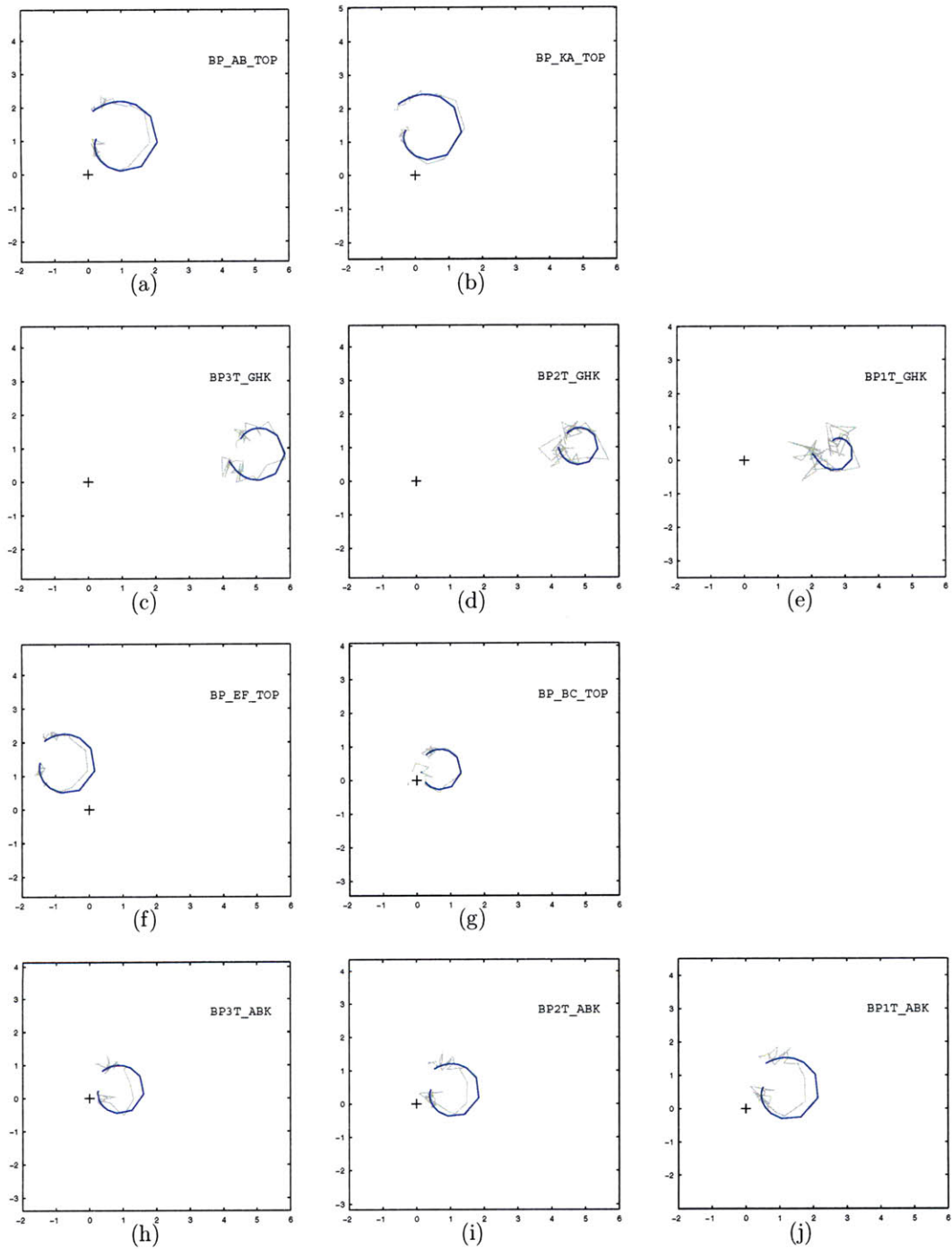


Figure 5-7: Compensated frequency response for a resonance in 1080403010 (grey), and fitted function (blue).

compared among probes of identical poloidal position, the signals from a toroidally distributed array of 10 probes 10 cm above the midplane - having the best resolution for this purpose - are emphasized. The positions of those probes are depicted in Figure 4-6. A typical example of the raw frequency response measured on this set of probes from shot 1080403010 is given in Figure 5-6.

Figure 5-7 shows the signals after the compensation described in Section 4.2 is applied. The probes closest to the antenna have the largest direct component and the highest noise level. The corresponding fitted system responses are also shown.

The coefficients derived in the fitting procedure can be transformed to give the toroidal mode structure, the resonant frequency and the damping rate of the mode. These characteristics are now discussed for the  $n = 0$  ensemble of resonant modes.

### 5.1.1 Toroidal mode $n = 0$

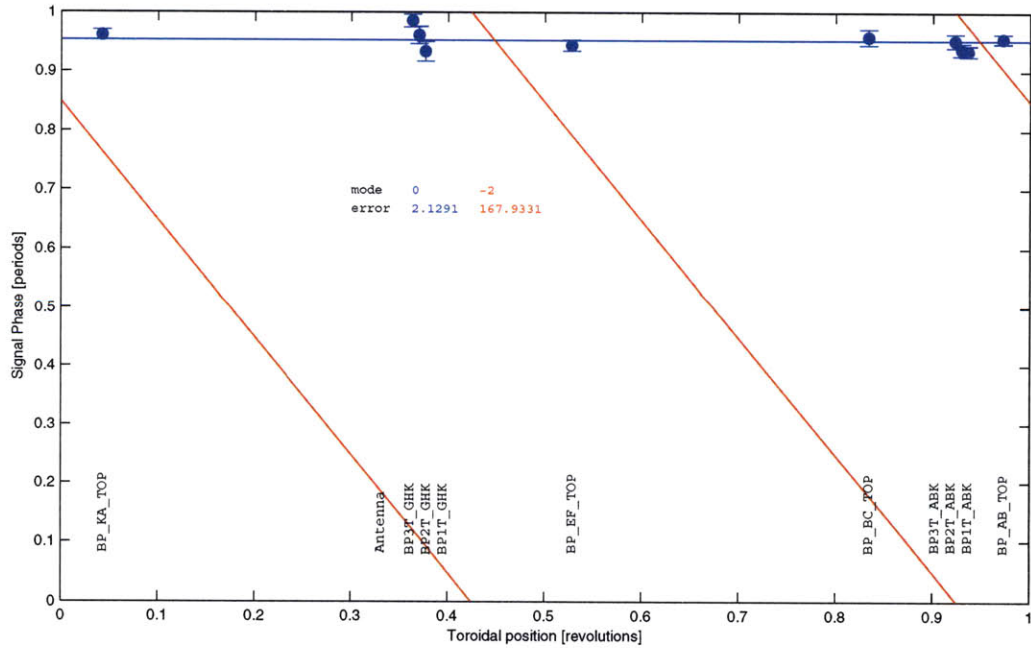


Figure 5-8: All modes in the 2008 ensemble of resonants fit  $n = 0$  far better than any other mode number.

Using the set of 10 probes that have identical poloidal positions, the toroidal mode number is determined as the best fitting linear relation between the phase of

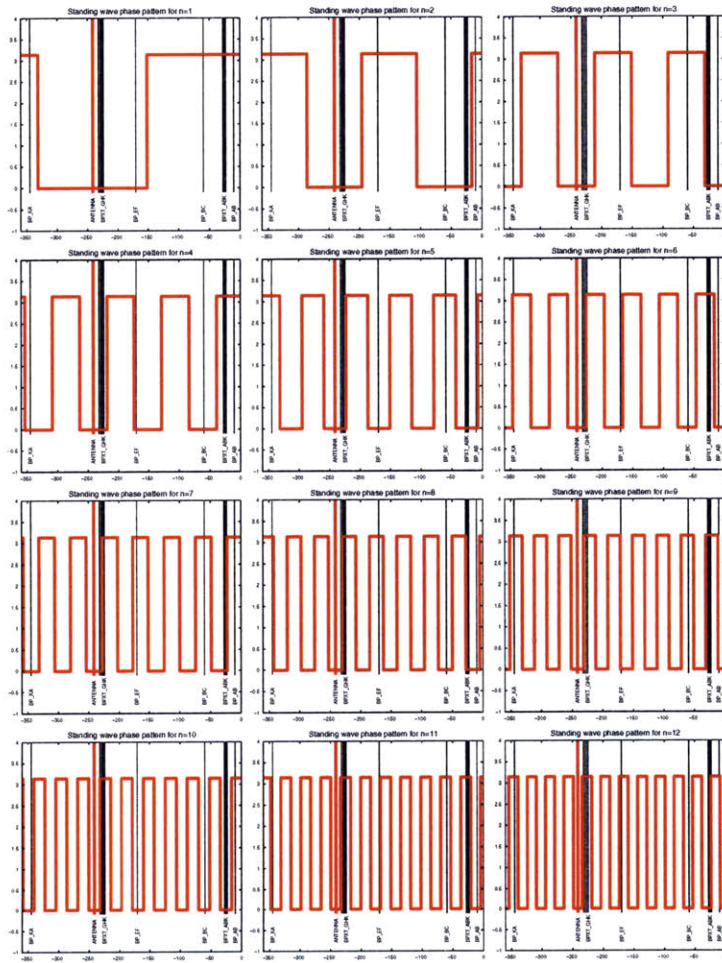


Figure 5-9: Probe spacing ensures that both 0 and  $\pi$  phasing would be observed for standing waves having their maxima at the antenna, for toroidal mode numbers between -12 and 12.

the residue of the probes' signals, and their toroidal positions. The mode number is constrained to be integral. Given the periodic nature of phase, branch cuts are permitted between probes. Figure 5-8 shows the fit for the example resonance from 1080403010. It is found to be  $n = 0$ . Error analysis is described in detail in Appendix A. The second-best fitting toroidal mode number, found to be  $n = -2$ , is also shown in the figure. In similar fashion, every mode in the 2008 ensemble is found to have a toroidal mode number of  $n = 0$ .

This progression of phase could also be explained as the product of a standing wave. A standing wave yields phases of either 0 or  $\pi$  and amplitudes with sinusoidal variation along the toroidal direction. In a pathological case, probes could be positioned only in regions of 0 phase to achieve the observed pattern. Given the non-uniform spacing of the probes, however, this possibility is ruled out for any realistic mode number, as shown in Figure 5-9.

A toroidal mode number of  $n = 0$  is significant because it precludes the possibility that these modes are TAEs: TAEs require finite toroidal variation in order to couple two degenerate waves to form the eigenmode. Secondly, the excitation by energetic particles also requires toroidal variation, so it should be weak or non-existent for these modes. An alternate identity for the modes as global Alfvén eigenmodes (GAEs) is proposed, and discussed shortly.

### 5.1.2 Frequency

In the ensemble of  $n = 0$  modes, the resonant frequency scales with the Alfvén velocity, as shown in Figure 5-10, where the Alfvén velocity is calculated for the line-averaged density and the magnetic field on axis. In the figure, the location of the TAE gap at  $r/a = 0.6$  is marked by red vertical bars for several sample modes. TAEs normally reside near the bottom of the gap, whereas these modes evidently have frequencies near the top.

Instead, these modes are more likely explained as global Alfvén eigenmodes (GAEs).



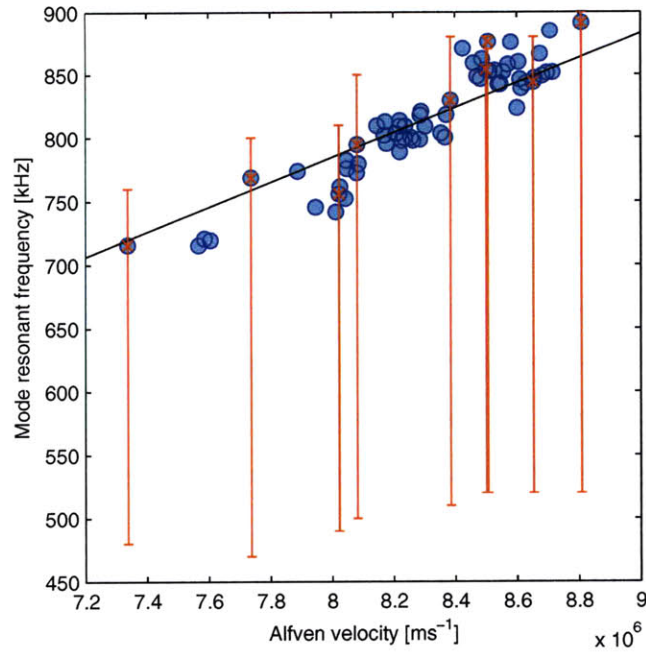


Figure 5-10: The mode frequencies scale with the Alfvén velocity and sit near the top of the TAE gap, indicated by the red vertical bars.

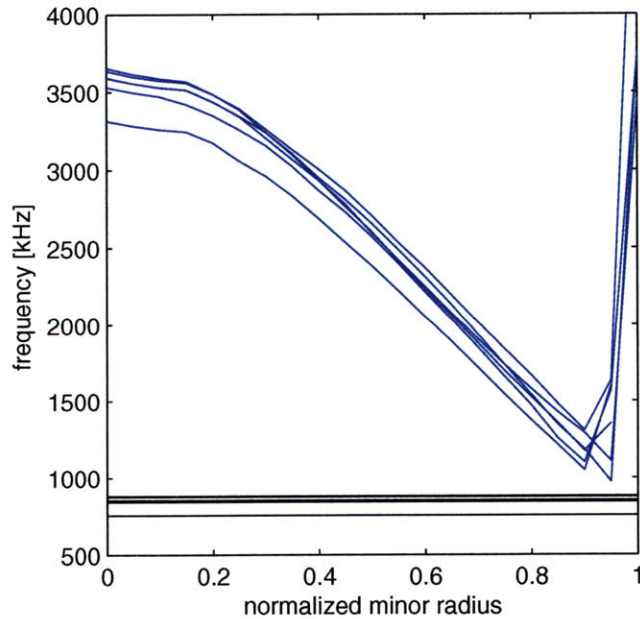


Figure 5-11: For several typical observed modes, the GAE continuum based on Thomson measurements and efit reconstruction (blue) and the observed mode frequencies (black).

The GAE continuum is given as,

$$\omega_A^2 = \frac{B_z^2 m^2}{\mu_0 \rho q^2 R^2}$$

where  $\rho$  is the mass density,  $q$  is the safety factor and  $m$  is the poloidal mode number. For a mode eigenfrequency,  $\omega$ , the mode tends to localize where  $|\omega - \omega_A|$  is minimized. Figure 5-11 shows the GAE continuum for  $|m| = 2$ . The observed mode frequencies are shown to reside just below the minimum of the continuum;  $|\omega - \omega_A|$  is minimum outside of  $r/a = 0.9$ , placing the GAEs far from the ICRF generated fast ions but within strong coupling of the diagnostic antenna and probes.

### 5.1.3 Damping rate

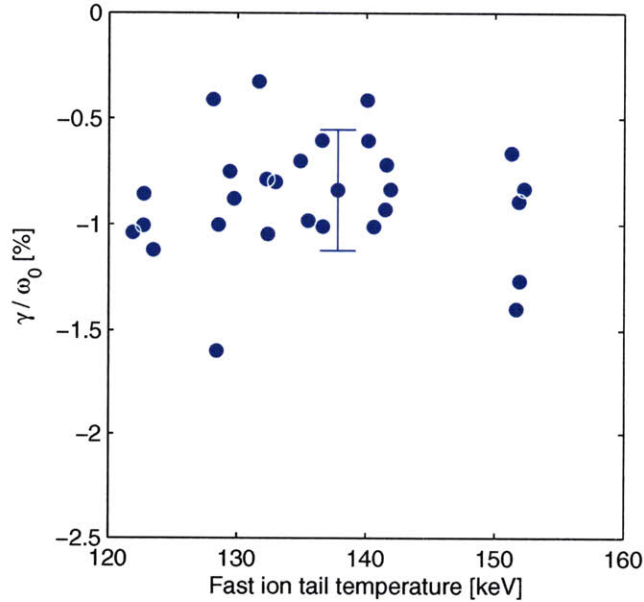


Figure 5-12: Damping rate is not sensitive to fast ion tail temperature within the bounds of uncertainty. The 34% error bar is due primarily to stochastic density fluctuations that distort the magnitude of both the residue and the real part of the pole.

The net damping rate signifies the margin to instability. For resonances in otherwise similar conditions, increased excitation by the energetic ions should be evident

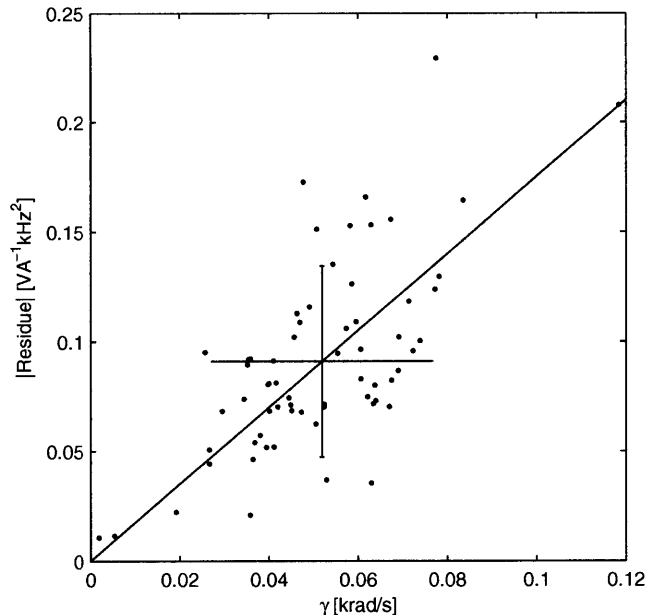


Figure 5-13: Correlation between the magnitude of the residue and the real part of the pole is caused by density perturbations that shift the mode frequency while it is being interrogated by the active MHD diagnostic.

as a reduction in damping rate and approach to instability. The range of RF power in the 2008 shots generates energetic ion temperatures between 122 keV and 153 keV as measured by the compact neutral particle analyzer (CNPA). The net damping rate of all modes in the  $n = 0$  ensemble is found to be insensitive to variations in the tail temperature over that entire range, within the margin of precision. For the resonances that occur during RF heating such that sufficient energetic ions are generated to obtain a meaningful signal on the CNPA, Figure 5-12 shows an effectively flat relationship and a representative error bar. The fast ion temperature is assigned by fitting the energy distribution measured by the CNPA to a modified Stix distribution after compensating for charge-exchange cross-section, neutral beam energy and exit attenuation. Operation of the CNPA is described in detail in Vincent Tang's thesis [127]. It is concluded that excitation of the  $n = 0$  mode by energetic ions is negligible.

The precision of the damping rate measurement is significantly limited by stochastic perturbations in the plasma density near the radius of peak amplitude of the mode. These perturbations lead to unsteadiness in the pole and disrupt the fitting proce-

ture. The effect is due to the dependence of the resonant frequency on the plasma mass density,  $\rho$ ,

$$\omega_0 = k_{||} \frac{B}{\sqrt{\mu_0 \rho}}.$$

The linearized relation for the imaginary part of the pole with small changes in density is,

$$\begin{aligned} \delta\omega_0 &= -\omega_0 \frac{\delta n}{2n} \\ &= \Omega_0(t) + \alpha(\omega(t) - \omega_0) \end{aligned}$$

where  $\omega(t)$  is the excitation frequency of the active MHD diagnostic. The pole perturbation is divided into components that are either correlated ( $\alpha(\omega(t) - \omega_0)$ ), or uncorrelated ( $\Omega_0(t)$ ) with the excitation frequency. In cases when the correlated density fluctuation is significant, the observed frequency response is,

$$\begin{aligned} H(j\omega) &= \frac{r}{j\omega - [\gamma + j(\omega_0 + \delta\omega_0)]} && + R^*(j\omega) + D(j\omega) \\ &= \frac{r}{j\omega(1 - \alpha) - [\gamma + j(\omega_0(1 - \alpha) + \Omega_0)]} && + R^*(j\omega) + D(j\omega) \end{aligned}$$

The excitation frequency is independently measured, and its coefficient in the denominator is forced to unity in the fitting process. This results in an artificial scaling of the real part of the pole as well as the amplitude of the residue, but only a small discrepancy in the imaginary part of the pole:

$$H(j\omega) = \frac{r/(1 - \alpha)}{j\omega - [\gamma/(1 - \alpha) + j(\omega_0 + \Omega/(1 - \alpha))]} + R^*(j\omega) + D(j\omega)$$

In the vicinity of the pole, the excitation traverses a frequency on the order of  $\gamma$ ,

$$\frac{\omega - \omega_0}{\omega_0} \approx O\left(\frac{\gamma}{\omega_0}\right)$$

Then the factor  $\alpha$  relates the density perturbation and the damping rate as,

$$\alpha \approx -\frac{\delta n}{2n} O\left(\frac{\gamma}{\omega_0}\right)^{-1}$$

For a |1%| stochastic fluctuation in density and  $\gamma/\omega = -1\%$  damping rate, the distorting factor  $(1 - \alpha)$  has amplitude  $0.5 < (1 - \alpha) < 1.5$ . The inequality depends on whether the fluctuation is positively or negatively correlated with the excitation frequency.

In this treatment, the magnitude of the residue is expected to be equally distorted. Figure 5-13 shows that the magnitudes of the residue and of  $\gamma$  are correlated, evidence that this effect does take place. Then the standard deviation in  $|r|$  is an estimate of the related uncertainty in each measurement of  $\gamma$ , assuming the parameters would otherwise be uncorrelated.

This uncertainty far outweighs the uncertainty obtained in the parameter fitting process, as described in Appendix A. The representative error bar in Figure 5-12 reflects this more conservative value, namely,

$$\sigma_\gamma = \frac{\sigma_{|r|}}{\beta\sqrt{2}}$$

where  $\sigma_{|r|}$  is the standard deviation in the magnitude of the residue,  $\beta$  is the slope of the correlation in Figure 5-13, and the factor of  $\sqrt{2}$  is included because not all the variation in  $|r|$  is due to stochastic density fluctuations. Since the trend is only evident over an ensemble of modes, only measures  $\delta\rho$  and not  $\rho$ , and only in the eigenfunction-averaged sense, it probably cannot serve as a more sensitive measure of density than the Thomson scattering diagnostic.

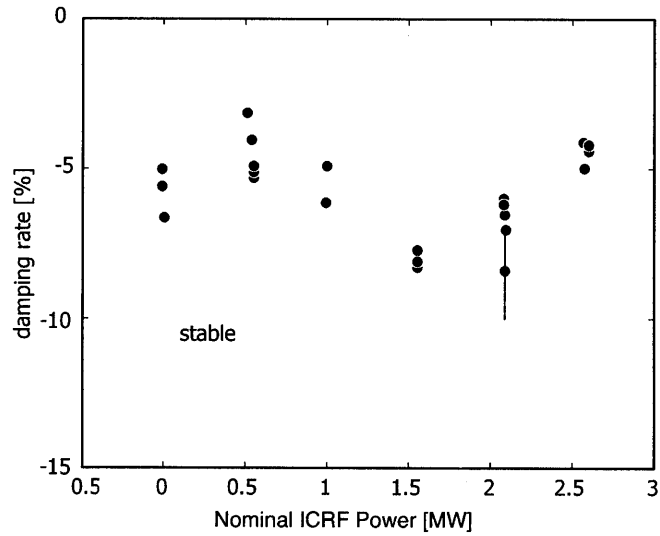


Figure 5-14: Damping rate for stable modes of 1060526, having a range of moderate toroidal mode numbers, with varying RF power.

In summary, the 2008 ensemble of resonant modes are concluded to be GAEs with toroidal mode number of  $n = 0$ . The modes are localized near the plasma edge, away from the ICRF generated distribution of fast ions, and they are invariant in the toroidal direction. Therefore little interaction of the modes with energetic ions should be expected, in agreement with the observed damping rates.

## 5.2 2006 ensemble

Preliminary analysis of the moderate- $n$  modes observed on runday 1060526 suggested that fast ions may contribute damping to the modes. Figure 5-14 shows the strongest damping rate for modes at 1.5 MW of ICRF heating. The modes are not segregated by toroidal mode number, though they are identified to be of moderate  $n$ , so it is possible that the damping trend is confounded by a mixture of modes. Runs in 2007 would attempt to reproduce the stabilizing effect of fast ions.

Figures 5-15 and 5-16 illustrate the system response for a typical mode on 10605026. While a mode clearly exists, it is not fit as well as the modes in 2008.

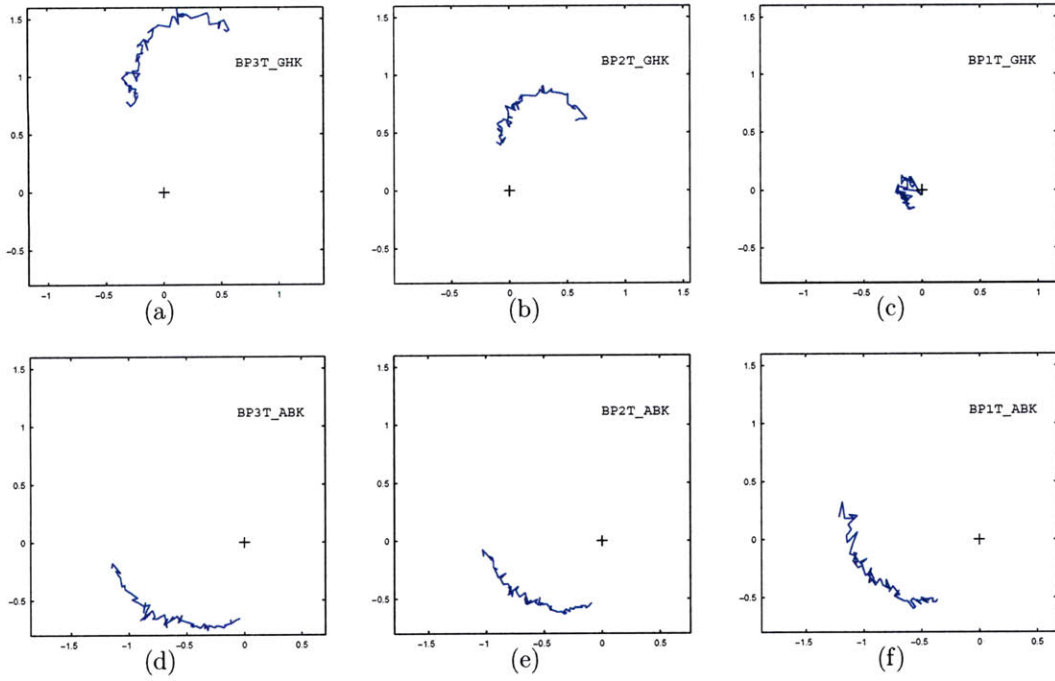


Figure 5-15: Uncompensated frequency response for a resonance in shot 1060526022.

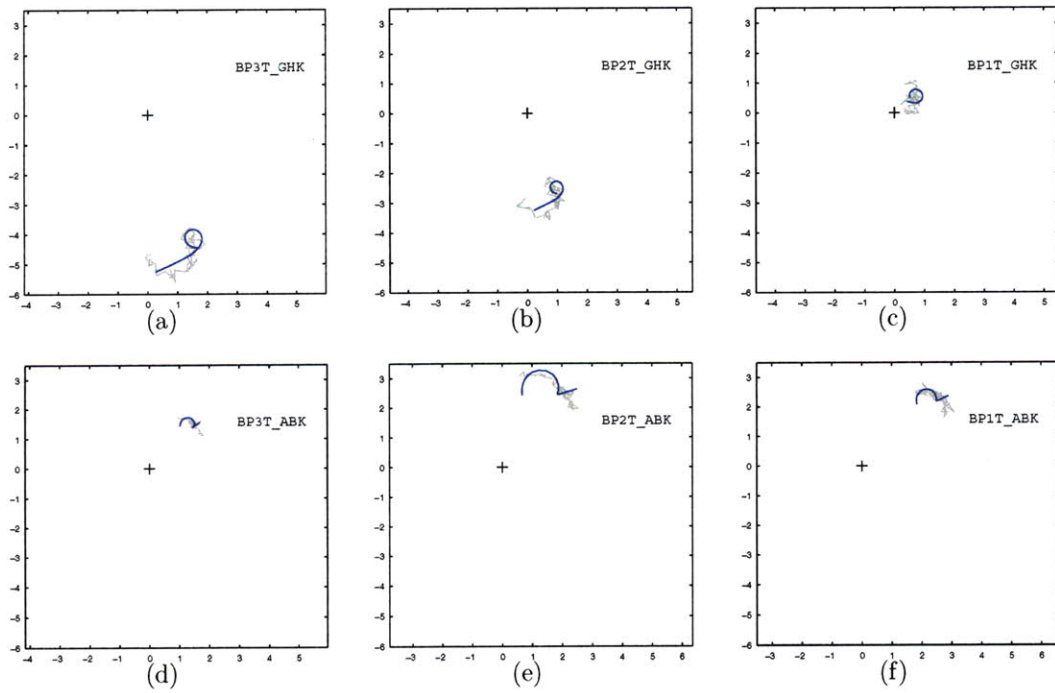


Figure 5-16: Compensated frequency response (grey) for a resonance in shot 1060526022, with fitted system response (blue).

### 5.3 2007 ensemble

Like the shots of 2008, the shots of 2007 are similarly programmed to examine the interaction of resonant modes with fast ions, with several fewer refinements compared to the 2008 shots. First, the plasmas are configured as inner-wall limited discharges to be consistent with earlier experiments. This increases the gap between the plasma and the outer wall, where the diagnostic instruments reside. Secondly, the active MHD diagnostic runs with two antennas, which complicates the system identification process as described in Chapter 4. However, the equilibrium does use an increased toroidal field of 5.9 T, which moves the RF absorption resonance outboard, and may enable a hollow fast ion profile. Traces of typical parameters of the discharges are shown in Figure 5-20. A typical equilibrium profile is shown in Figure 5-21.

During initial analysis, modes of dubious standard were included in analysis of damping with respect to RF power. In fact, all modes observed during non-zero RF power are of inferior resolution compared to the modes during Ohmic intervals of the 2007 shots, and especially in comparison to the modes of 2008. Figures 5-17 and 5-18 illustrate a typical system response during RF heating on shot 1070626003. The damping rate trend for all modes (including those during RF activity) is given in Figure 5-19. At first glance, it appears that damping may again peak at moderate levels of RF heating, in this case around 2.5 MW, as was observed in 2006. However, one troubling aspect of the data set is that the damping rates seem to follow not just a contour, but take on all values between the envelope and zero.

After the 2008 data became available as a benchmark for system response resolution, it was clear that the non-zero RF power dataset of 2007 could not be reliably interpreted. Thereafter, only modes during the Ohmic phase were included in the 2007 ensemble, and the hypothesis that fast ions were observed to contribute damping was abandoned for lack of credible evidence.

There then remained an ensemble of 28 resonant modes representing the Ohmic phase of the 2007 shots. A typical frequency response for this class of modes is shown in Figures 5-22 (uncompensated) and 5-23 (compensated). While of much better res-



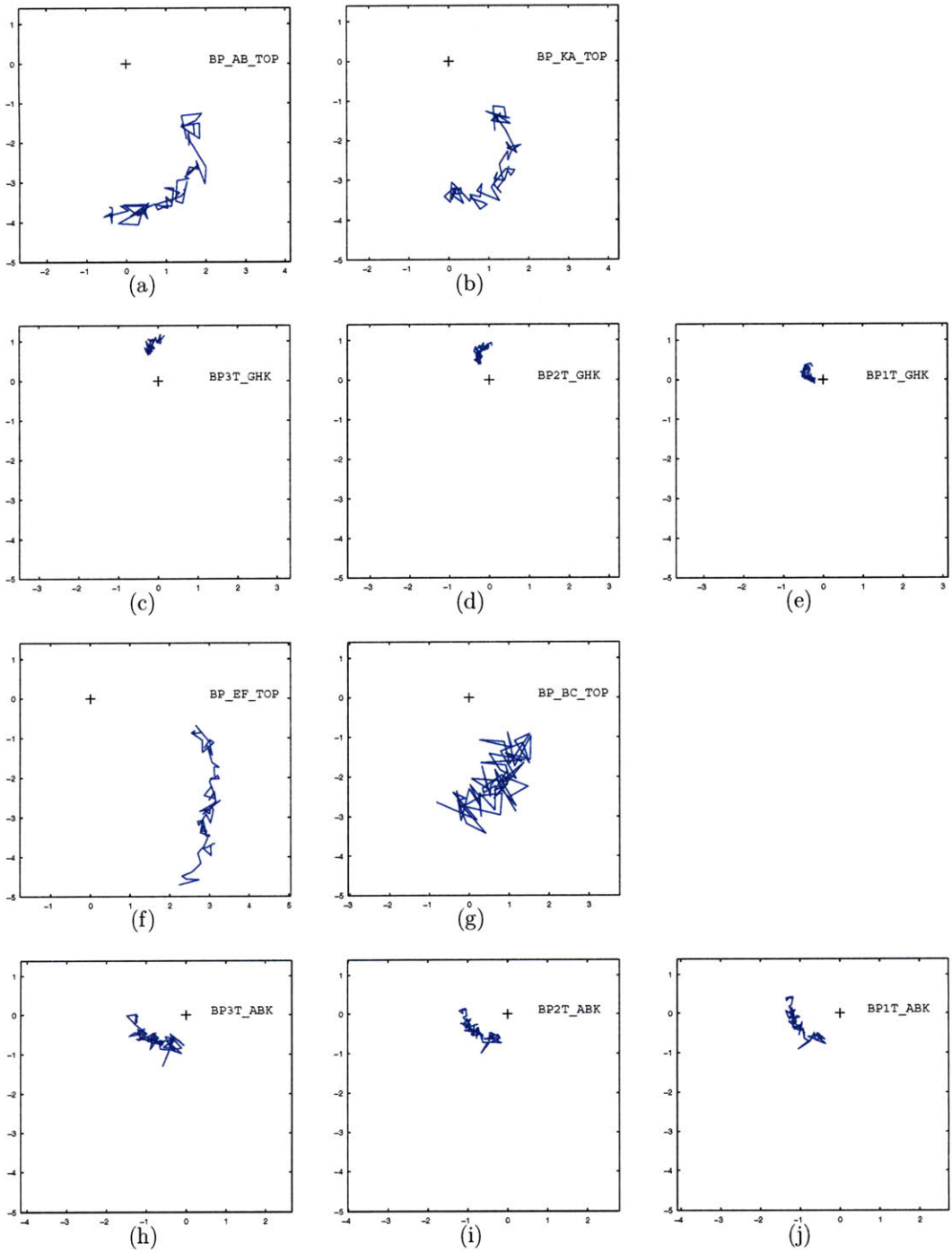


Figure 5-17: Uncompensated frequency response for a resonance in shot 1070626003 during RF activity.

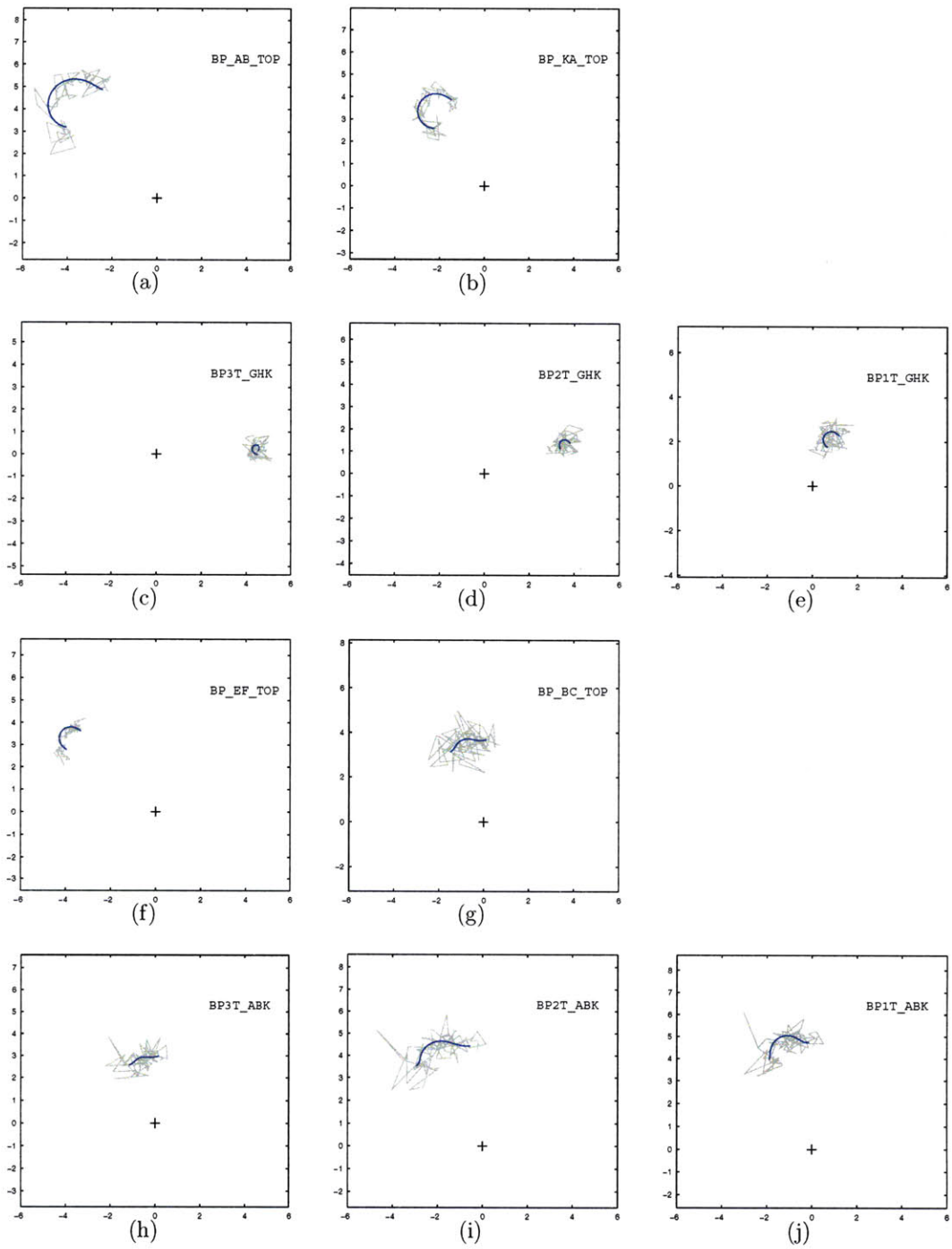


Figure 5-18: Compensated frequency response (grey) and fitted response (blue) for a resonance in shot 1070626003 during RF activity.

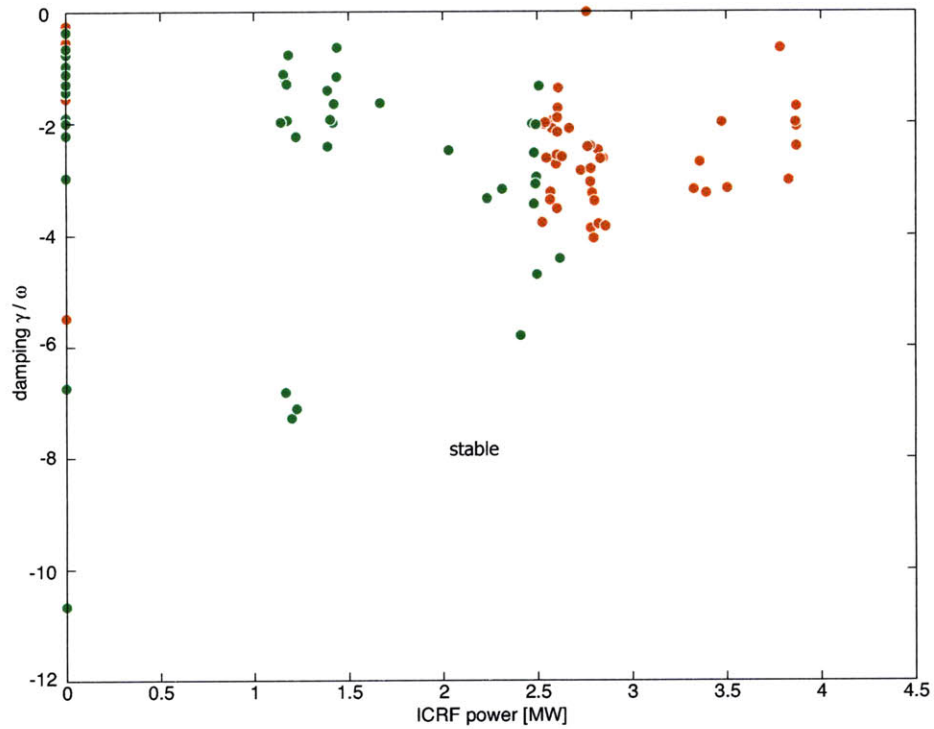


Figure 5-19: Damping measurements during RF activity in the 1070605 (green) and 1070626 (red) runs, which were thought to corroborate the evidence of 1060526 that fast ions were providing stabilization to the modes. After comparing the system response resolution to modes in 2008, however, this data was discredited and abandoned.

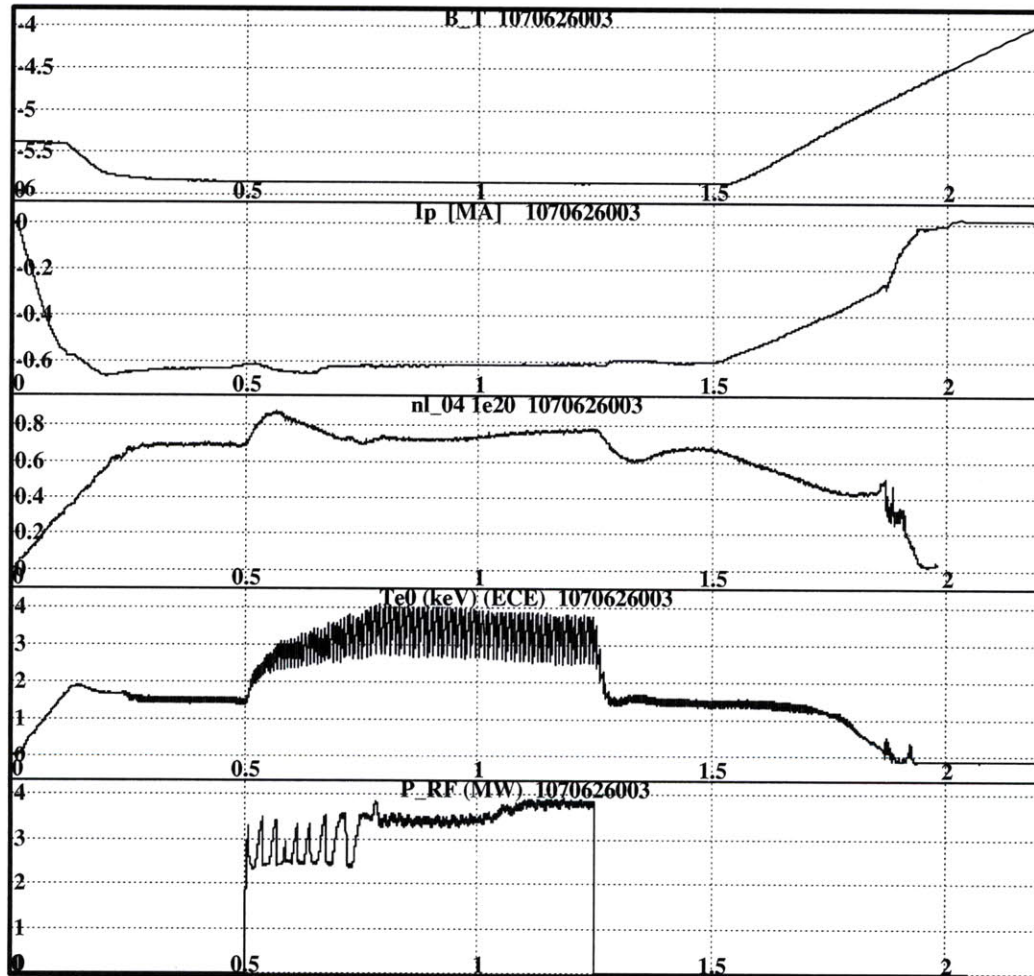


Figure 5-20: Plasma conditions for shot 1070626003.

Shot= 1070626003 Time= 0.280 Ip = 0.65

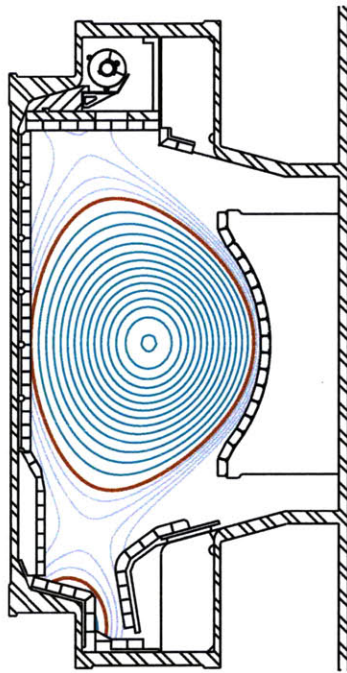


Figure 5-21: Equilibrium magnetic field reconstruction during a resonance in 1070626003. The red curve separates the confined field lines from the field lines that intersect the vessel. This equilibrium is limited by the inner wall.

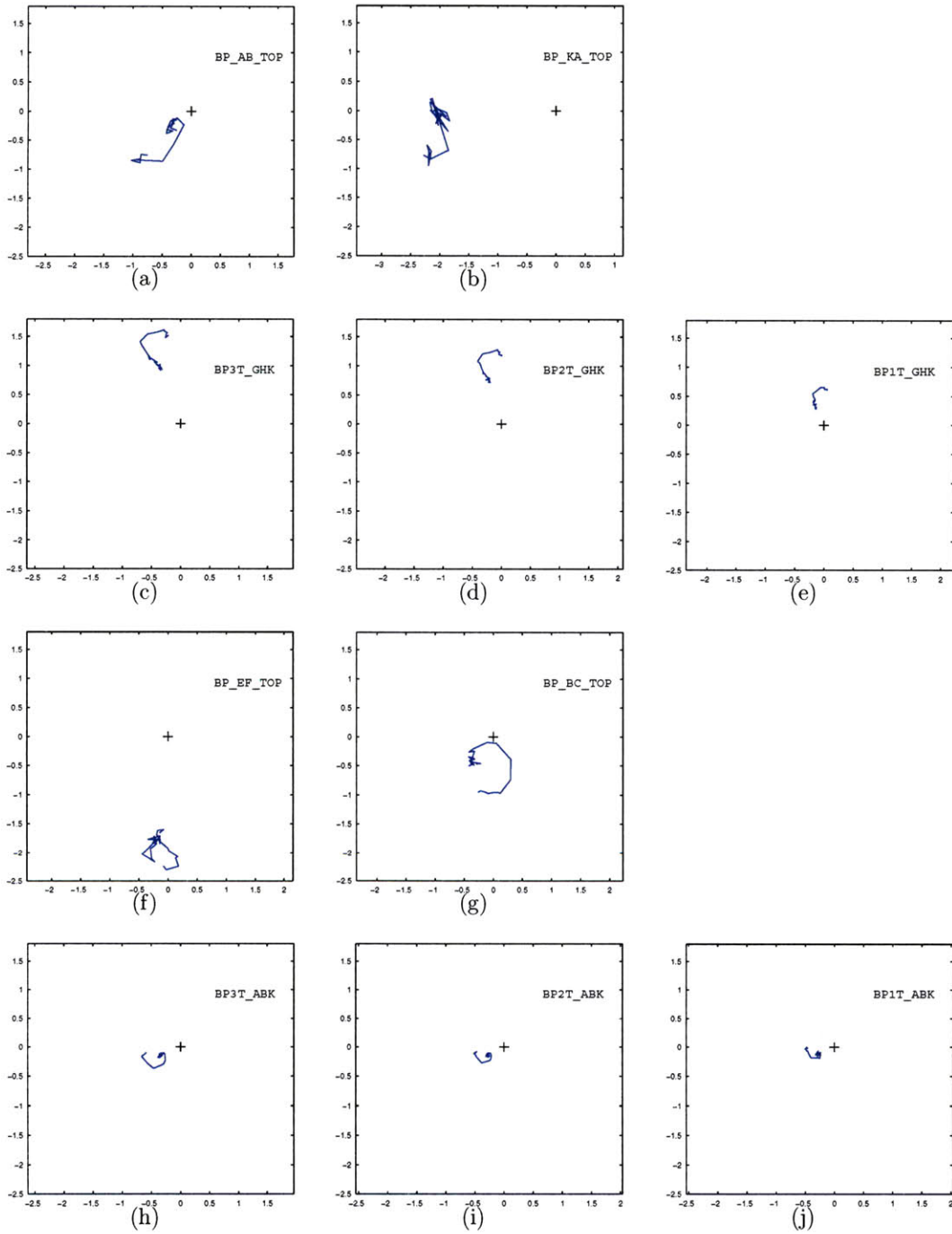


Figure 5-22: Uncompensated frequency response for a resonance in shot 1070626003 at 0.28 s.

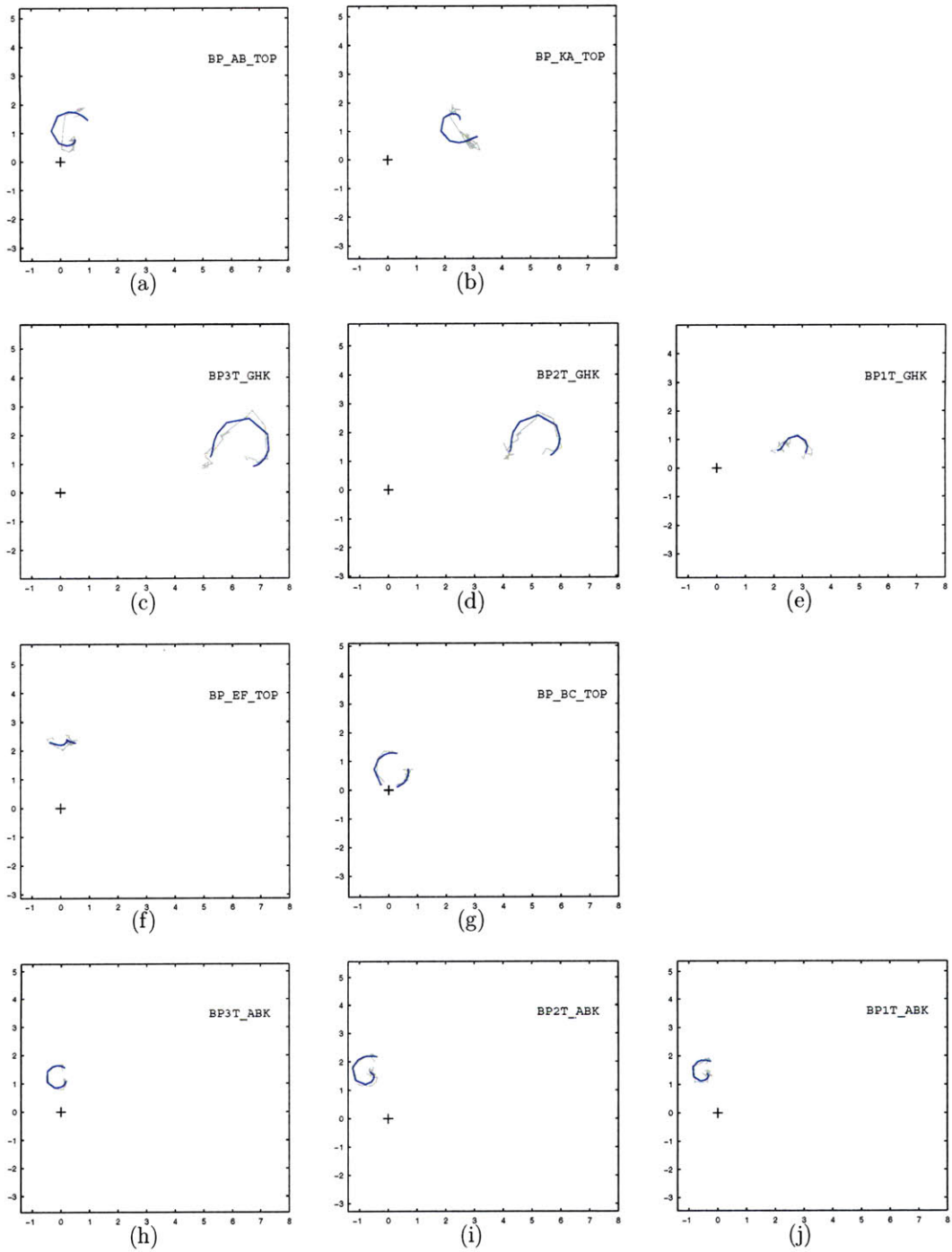


Figure 5-23: Compensated frequency response (grey) and fitted response (blue) for a resonance in shot 1070626003 at 0.28 s. For three of the low-n probes, the frequency response is strongly distorted from the typical circular shape.

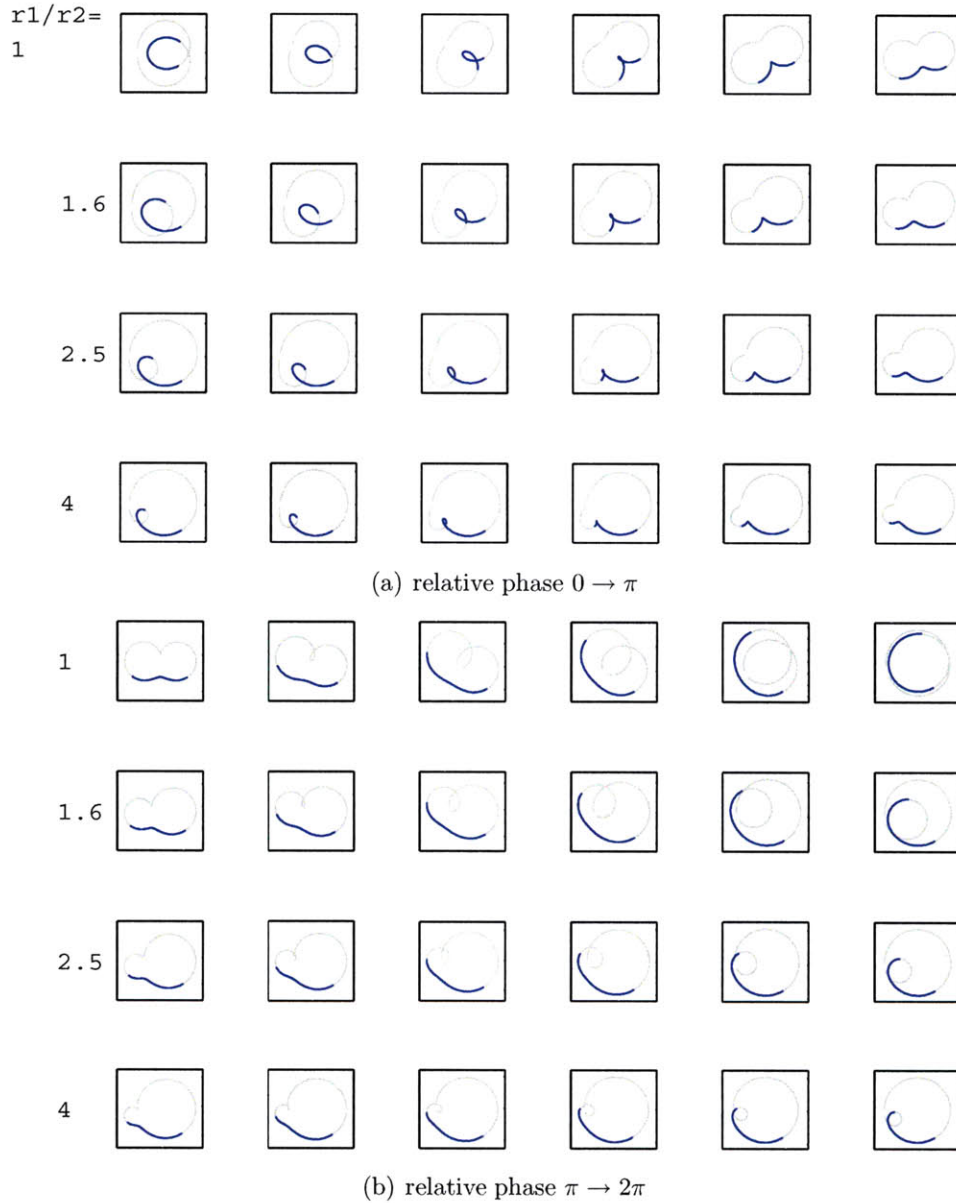


Figure 5-24: Family of frequency response shapes for two modes with adjacent poles, split into two subfigures to fit on the page. In each subfigure: Rows: the ratio of residue amplitude between the two modes varies from 1 (top row) to 4 (bottom row); Columns: the relative phase of the residue between the two modes varies from left to right, analogous to the variation that would be observed from probe to probe around the torus. The two poles are separated by  $\delta\omega/\gamma = 6$ . The damping rate for both modes is  $\gamma/\omega_0 = 1\%$ . The blue curve shows a frequency interval of  $\omega_0 \pm 2.5\gamma$ , similar to what would normally be observed by the sweep of the active MHD diagnostic. The grey curve shows a much wider frequency interval.



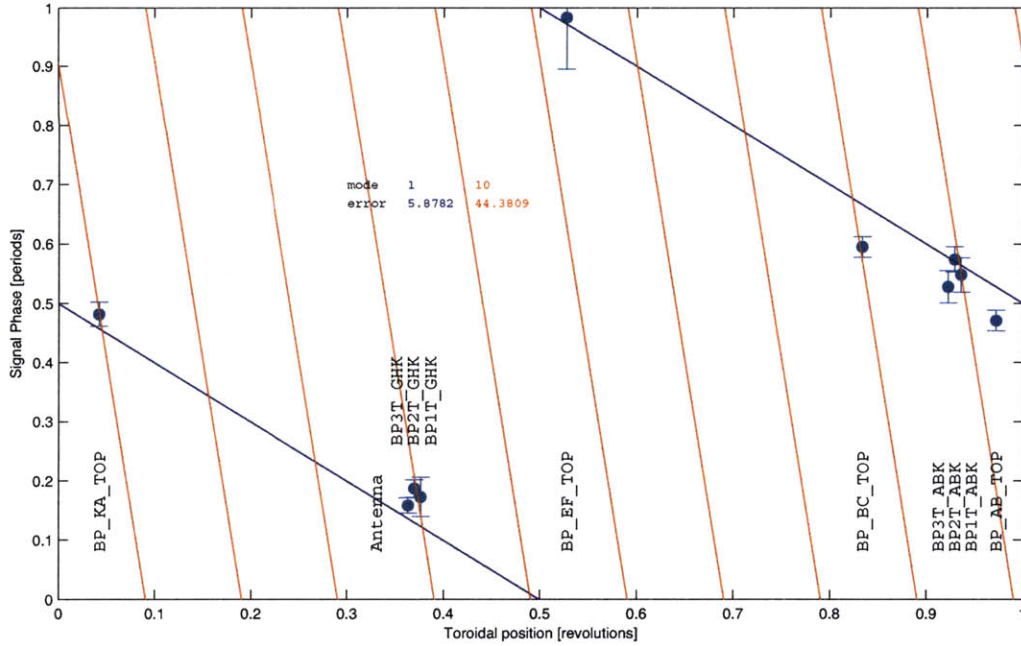


Figure 5-25: Most of the resonances in the 2007 ensemble fit  $n = 1$  best. The others fit  $n = 1$  almost as well as their best fit mode number.

olution than their RF counterparts, compared to the typical frequency response for a resonant mode in the 2008 ensemble, the responses on the low- $n$  probes, including BP\_KA\_TOP, BP\_AB\_TOP and BP\_EF\_TOP, are much less circular (the expected shape for a resonant mode), and their fit to the model response is much poorer. The discrepancy is evident by comparing Figures 5-23 and 5-7. The difference between ensembles may be caused by the contrasting experimental configuration mentioned above. However, in shots on non-dedicated rundays in 2007, similarly distorted resonances are observed even in conjunction with the modifications from the 2008 shots: using only the upper antenna, configuring the discharge in a diverted equilibrium, and minimizing the outer gap all produce distorted frequency responses on the low- $n$  probes in the 2007 campaign. In addition to the distortion, also note that the direct component of the frequency response measured at the AB-limiter probes is significantly greater in the 2007 ensemble than in the 2008 ensemble.

It is possible for adjacent poles to give rise to a frequency response with a distorted appearance. Adjacent poles arise in several cases: when distinct resonant modes with

identical or different toroidal mode numbers exist at nearby frequencies; or when otherwise identical modes exist with opposite toroidal mode numbers, which gives rise to a standing wave pattern; and thirdly, when either adjacent or identical poles (with different mode numbers) are subject to plasma rotation, the poles are also separated. The resultant family of shapes of the frequency response, computed for synthetic adjacent poles, is plotted in Figure 5-24. The family of shapes in Figure 5-24 appears to include quite a variety of trajectories, some of which approach the level of distortion in the measured frequency responses. It should be noted, however, that the frequency parametrization of the system response curve, which cannot be visualized in the 2-D plot, is equally important in the fitting procedure. For example, if the frequency parametrization in any of the synthetic curves is inverted, the fitting procedure finds a positive pole, indicating an unstable mode, which is clearly unphysical. Therefore similarity between the synthetic and measured shapes may provide a clue as to the origin of a distorted frequency response but is not sufficient to assert that adjacent poles exist. As a more conclusive test, the fitting routine described in Chapter 4 handles all of the synthetic frequency responses well, but fails to find good fits for the distorted frequency responses of measured data in the 2007 ensemble.

Despite the unexplained degradation in fit of the frequency response, most of the modes of the 2007 ensemble are found to have toroidal mode numbers of  $n = 1$ . A typical linear fit to the toroidal phase progression is shown in Figure 5-25, along with the next best fit.

None of the resonances occurred during ICRF heating, so no corresponding measurements of fast ion temperature are available. However calculations based on the plasma conditions using the NOVA-K code can give some estimate of the effect that ICRF heating would have on the damping rate. NOVA-K is an algorithm that reconstructs a full toroidal equilibrium geometry from measured input profiles. It calculates eigenmodes and eigenfrequencies in the MHD range based on a single-fluid model. The eigenmode displacement as well as perturbations in magnetic field, electric field, plasma density and pressure are provided. The continuum damping is calculated for each mode. A kinetic extension of the code also solves for the damping and growth

rates contributed by energetic ions. The ion distribution is described by a measured temperature and radial position of the ICRF resonance layer, from, for example, the CNPA; and an analytic form for the velocity distribution from ICRF heating.

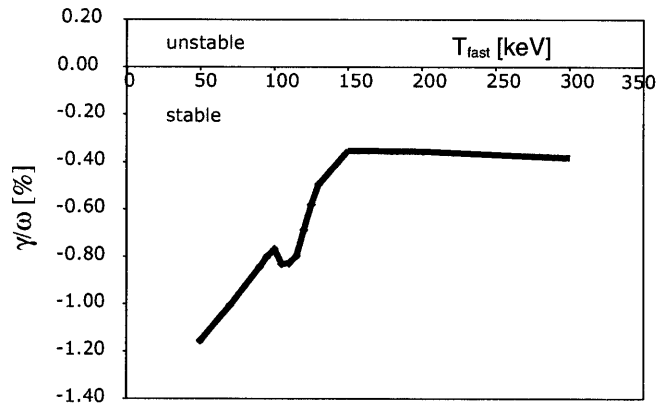
For plasma conditions typical of the 2007 shots, NOVA-K found that  $n = 1$  modes are stable up to fast ion temperatures of 300 keV (Figure 5-26(a)). In contrast,  $n = 5$  modes were found to reach instability at around 70 keV (Figure 5-26(b)). Results from NOVA-K for the range of mode numbers for  $|n| = 1$  to  $|n| = 10$  are shown in Figures 5-27. Low- $n$  modes, such as the  $n = 1$  that is observed by the active MHD diagnostic, are only weakly excited by the fast ions, whereas it is the moderate- $n$  modes that are most strongly excited.

## 5.4 Unstable mode observations

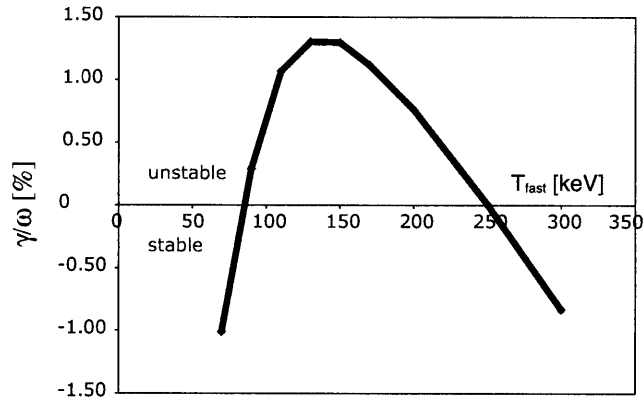
Unstable modes are observed in several shots in both the 2007 and 2008 campaigns, during RF heating above 3.5 MW. In some cases the unstable modes appear during active MHD stimulation of the plasma, at nearby frequencies. The modes typically have mode numbers of  $n = -4$ , in the ion diamagnetic drift direction that is expected for peaked fast ion pressure profiles. The mode number magnitude is also in agreement with the NOVA-K calculation that found that the most unstable modes would have moderate mode numbers (Figure 5-27). One mode in shot 1080110031 was found to have a toroidal mode number of  $n = 6$ , which is opposite the ion diamagnetic drift direction: this is strong evidence that there exists a hollow fast ion pressure profile in that shot. Figures 5-28 and 5-29 illustrate the mode number analysis for these unstable modes, which is strikingly more precise than the same analysis for stable modes (eg as shown in Figures 5-8 and 5-25).

From this coexistence of unstable and stable modes, it is evident that moderate- $n$  modes should be the first to destabilize. It may be somewhat unexpected then that in the runs of 2007 and 2008 the active MHD diagnostic seems to preferentially observe low- $n$  modes.

NOVA-K calculations show that moderate- $n$  modes are more localized in the core



(a) Net damping rate for  $n = 1$  mode.



(b) Net damping rate for  $n = 5$  mode.

Figure 5-26: Net damping rates for  $n = 1$  (a) and  $n = 5$  (b) modes with various fast ion temperatures, calculated by NOVA-K for the conditions of the 2007 ensemble of resonances. The  $n = 1$  is found to be stable for all fast ion temperatures below 300 keV.

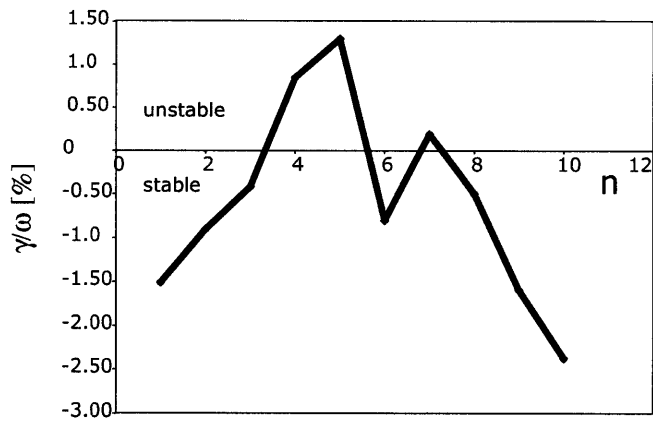


Figure 5-27: Net damping rate for a range of mode numbers, calculate by NOVA-K. The moderate- $n$  modes are found to be most unstable.

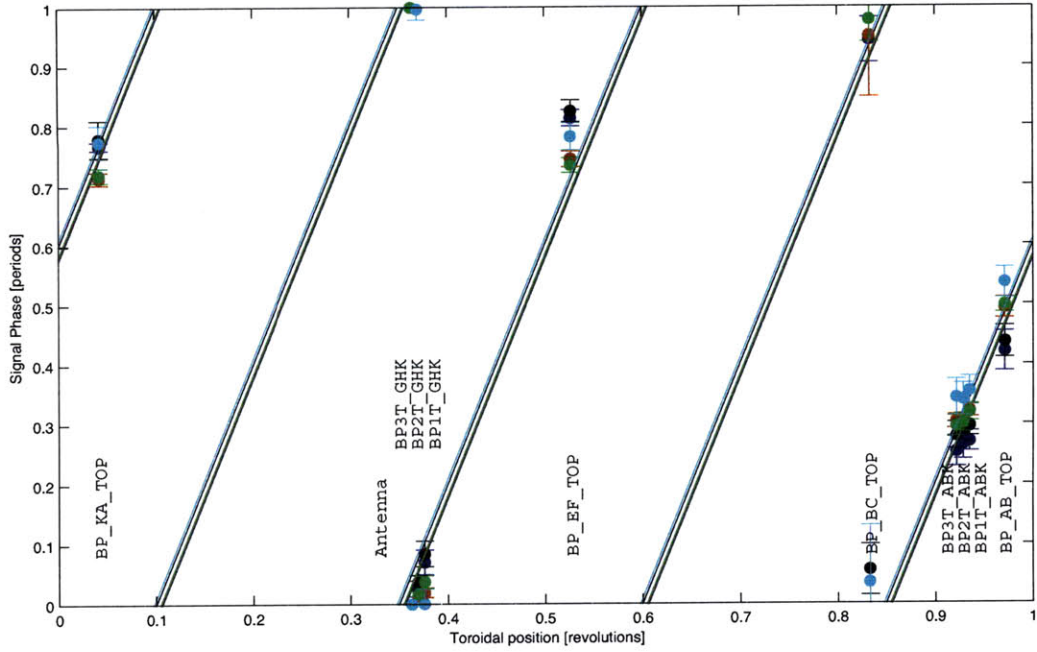


Figure 5-28: Several unstable modes in shots 1070626003, 1070626004, 1080110021, 1080110022 and 1080110025 are found to have toroidal mode numbers of  $n = -4$ , with phase velocity in the ion diamagnetic drift direction as expected for unstable modes driven by fast ions with a peaked pressure profile.

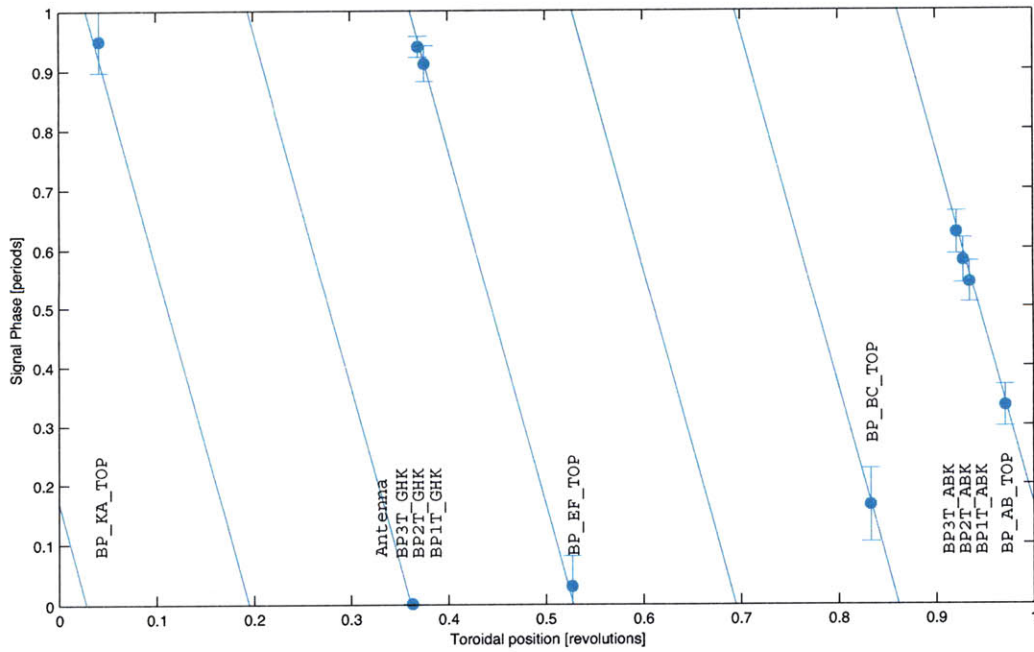


Figure 5-29: A spontaneous TAE in 1080110031 is found to have a toroidal mode number of  $n = 6$

compared to low- $n$  modes. This makes the low- $n$  modes more accessible to stimulation by external antennas. While NOVA-K treats the plasma boundary as fixed, the proximity of the mode to the plasma edge is indicative of its ability to tunnel through the continuum, and may indicate a strong perturbation outside of the plasma, as well. Figure 5-30 illustrates the comparative localization of the low- and moderate- $n$  modes.

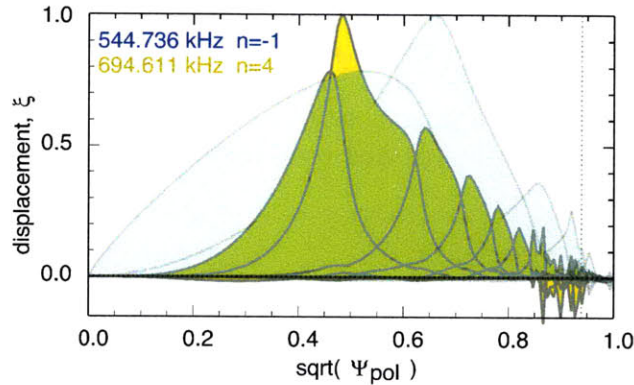


Figure 5-30:

## 5.5 Conclusion

GAEs having  $n = 0$  are observed in the upper-null diverted plasmas of the 2008 campaign. They are not significantly coupled to fast ions that are generated by up to 5.5 MW of ICRF heating. The frequency response of these modes is especially clear, possibly because only one antenna of the active MHD diagnostic was used, and possibly also because the gap between the plasma and outer wall was minimized. During shots in 2007,  $n = 1$  TAEs were observed in the absence of ICRF heating.

NOVA-K calculations estimate that these modes would also not couple strongly to fast ions. In contrast, moderate- $n$  modes are predicted by NOVA-K to be destabilized by fast ions above 70 keV.

Unstable modes with mode numbers in the range  $|n| = 4$  to  $|n| = 6$  are observed in several shots of the 2007 and 2008 campaigns. The active MHD diagnostic, however, preferentially couples to low- $n$  modes such as the  $n = 0$  GAE and the  $n = 1$  TAE because they are localized closer to the plasma boundary and therefore have stronger amplitudes at the diagnostic instruments. Moderate- $n$  modes are only observed once they become unstable and grow to significant amplitudes.

# Chapter 6

## Summary & Conclusions

The goal of the research reported in this thesis was to observe the stability dependence of a wide- $n$  spectrum ( $|n| = 0-10$ ) on the fast ion temperature,  $T_{fast}$ , and distribution,  $f_{fast}(r, v)$ . With the threat of AEs to fusion reactors in mind, inflections in the stability of the toroidal mode spectrum that could be exploited to preserve or modify the fast ion distribution were sought. AEs with toroidal mode number in the range ( $|n| = 0-6$ ) were measured by the active MHD system, and mode behavior in an even broader toroidal spectrum ( $|n| = 0 - 10$ ) was calculated using NOVA-K. Modes of moderate toroidal wavelength were invariably the most susceptible to destabilization by fast ions. It was also shown, however, that the composition of the TAE toroidal mode spectrum can be influenced by the selection of equilibrium profiles and plasma shape. This dependence might offer a handle to control mode activity, and will be discussed shortly. First, the novel contributions of this thesis to both the measurement and calculation of Alfvén eigenmode behavior that have driven the investigation are summarized.

### 6.1 Diagnostic Contributions

For the first time, TAEs of various toroidal mode number have been excited by a wide-toroidal-spectrum antenna and detected by a fully resolved toroidal array of probes. The resolution of toroidal mode structure was augmented by adding seven



widely-spaced probes to the existing closely-spaced probe arrays, as described in Section 3.3.1. Most of the new probes were identical to the existing probes, but two of them were intentionally built with higher frequency responses so that plasma resonances could be unequivocally distinguished from resonances of the diagnostic system. Starting near the end of the 2007 campaign, only one of the two active MHD antennas was activated at any one time to disambiguate the system input, thereby avoiding any incomplete pole-zero cancellation in the homodyne synchronous correlation process (Section 4.2.1).

The measured system response was compensated for the frequency response of the diagnostic system to isolate the resonant plasma response (Section 4.2.1). The compensation was derived from a detailed calibration that accounts for probe-to-probe variation in construction, spacing of the probes to the plasma last closed flux surface, the response of surrounding metal components, and the influence of the plasma itself on probe performance. Since the compensation factor is greater than the allowable error for confident mode identification, it is a necessary step in the process. Comparison among observed modes of various toroidal wavelength confirm that the compensation factor is accurate. Density fluctuations correlated with the excitation frequency were shown to distort the damping rate and residue measurements. The effect is magnified because the complex poles of the resonant modes are very close to the imaginary axis (Section 5.1.3).

The Compact Neutral Particle Analyzer (CNPA) was reinstalled with the help of Aaron Bader to measure the fast ion distribution during ICRF activity. Significantly, fast ion temperature was more effectively raised by reducing plasma density than by increasing RF power. Chord-to-chord comparison of the CNPA channels also corroborated evidence that the ICRF-generated fast ion density profile could be radially hollow.

## 6.2 Summary of Observations

The discharges on two rundays of the 2008 campaign used upper-null diverted, L-mode configuration, and were operated with an increased toroidal field of  $-5.9$  T to move the ICRF heating off axis. The plasma-wall gap was reduced below 8mm, improving the active MHD coupling to AEs. An ensemble of global Alfvén eigenmodes (GAEs) with toroidal mode number of  $n = 0$  was observed. These modes had the highest signal-to-noise ratio of any resonant plasma response measured by the active MHD system to date, which was critical in verifying the accuracy of the instrument compensation and equalizing the probe relative amplitudes. Probe-to-probe amplitude profiles were found to correlate to plasma-wall gap and plasma shape. The damping rate of the GAEs was typically  $-1\%$  and was not sensitive to fast ion temperature, as expected for modes having no toroidal variation.

Toroidicity-induced Alfvén eigenmodes having toroidal mode number of  $n = 1$  were observed on several rundays of the 2007 campaign in plasmas having a limited configuration and an elevated toroidal field of  $-5.9$  T. The modes were observed during the Ohmic phase of the discharges; resonant signatures that were tentatively recognized in the ICRF heating phase were too noisy to confidently segregate by mode number, even after the compensation procedure was improved using the 2008 observations. In the absence of fast ions, the damping rate of the  $n = 1$  modes was typically  $-1.5\%$ .

In addition to the modes that were excited by the active MHD diagnostic, unstable modes excited by fast ions were also observed in select shots on the same rundays, with mode numbers of  $n = -4$  and  $n = 6$ . Positive unstable mode numbers are indicative of a hollow fast ion pressure profile that could result from off-axis ICRF heating. CNPA measurements similarly found the fast ion pressure to be hollow. It is evident that modes with positive unstable mode numbers must be localized near the core of the plasma to be centered in the region of inverted fast ion pressure gradient. In contrast, the stable modes detected by active MHD must be localized near the plasma edge if there is to be strong coupling to the antenna and probes.

Numerical analysis was performed with the NOVA-K code to estimate the interaction of fast ions with the measured stable and unstable modes. Given the measured equilibrium profiles, NOVA-K finds AEs at similar frequencies and with the same mode numbers as those that were observed. A composite spectrum was rendered from the collection of stable and unstable mode observations, and the NOVA-K calculations in Figure 6-1, and shows reasonable agreement among the paradigms despite their corresponding to different equilibria. This patchwork spectrum displays peaked instability at moderate mode numbers around  $|n| = 5$ .

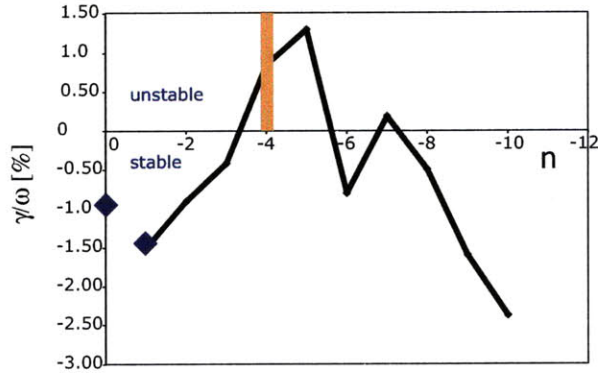


Figure 6-1: The composite AE spectrum include stable  $n = 0$  and  $n = 1$  modes, unstable  $n = -4$  modes (for which a damping rate could not be measured), and the stability spectrum calculated by NOVA-K for the equilibrium of 1080403010 and a fast ion temperature of 150keV. The  $n = 6$  mode is not included since it corresponds to a hollow fast ion profile that is not modeled in this NOVA-K dataset.

In comparison, the analytical scaling for instability typically finds that modes having  $k_{\theta}\rho_i \approx 1$  are most unstable.  $k_{\theta}\rho_i$  is found to be around  $8^{-1}n$  for protons of 150 keV,  $q = 1.5$ ,  $r = a/2 \approx 0.12$ , and  $B = -5.9T$ , and correspondingly, the most unstable modes are expected to have toroidal mode numbers around  $|n| = 8$ . Considering the simplicity of that scaling, the agreement is good.

### 6.3 Conclusions

Alfvén eigenmodes having moderate toroidal mode numbers were found to be the most unstable, in agreement with prior work on C-Mod [122] and other machines.

Future experimental and computational investigation of fast ion drive of AEs should focus on the moderate- $n$  portion of the AE spectrum. For active MHD investigation, the inherent difficulty of coupling to the plasma core, where the moderate- $n$  modes tend to reside, must be resolved. Attempts at correlation with internal diagnostics such as phase contrast imaging and electron cyclotron emission spectroscopy should be revisited.

The toroidally-broadband active MHD antenna in C-Mod couples selectively to the toroidal spectrum of AEs in a given equilibrium. In the experiments of this thesis, the coupled modes had low toroidal mode numbers of  $n = 1$  and  $n = 0$ , and in many of the equilibria that were interrogated no AEs were exposed. This suggests that the selection of the spectrum that is coupled to the diagnostic depends more on the plasma equilibrium parameters and shape than on the toroidal width of the antenna. Proximity of a mode to the plasma edge is one important factor for strong coupling. The narrow selectivity prevented a full spectrum of AEs from being measured simultaneously, and a comparison of Alfvén eigenmodes across a collection of equilibria was therefore required to arrive at the general conclusion that moderate- $n$  modes are most unstable.

The instability thresholds on fast ion temperature as a function of plasma parameters that were observed in these experiments cannot be smoothly extrapolated to predict the threat of AEs to burning plasmas. The most severe discontinuity that bars such an extrapolation is the non-linear nature of unstable modes: as the fast ion population intensifies, the spectrum of AEs also changes. Having focused for the most part on stable modes, this thesis makes no specific conclusion on the threat of AEs to burning plasmas.

Still, this thesis has assembled evidence that can be generally applied to AE control in burning plasmas. For example, global Alfvén eigenmodes with  $n = 0$  are not excited by fast ions. Figure 6-1 shows that intervals of stability in the moderate- $n$  range (here around  $n = 6$ ) exist. Evidence has been presented that islands of stability may also exist at moderate fast ion temperatures, where the fast ions contribute damping to the AEs (Chapter 5.2). The same subtle modifications of equilibrium parameters

that lead to antenna-mode coupling selectivity might be exploited to position the burning plasma parameter-space within such an island of stability. Previous scaling experiments of stability with parameters such as beta, collisionality and edge shear ([12], [71], [122]) could be applied to that effort even though the specific location in parameter space where such islands exist, and their immunity to fast ion drive, might be hard to predict.

Finally, the active MHD system is found to be useful for MHD spectroscopy, in which plasma conditions are deduced from mode behavior. For example, it is found that correlated variations in the mode residue and damping rate indicate otherwise unmeasured density fluctuations. As another example, the amplitude profile among the toroidal set of probes is correlated with the gap between the plasma and the vessel, and possibly with triangularity or edge shear. Such useful capabilities should be investigated further.

## 6.4 Future Work

The results of this thesis open several avenues for further investigation with the active MHD diagnostic and AE activity.

One way to investigate fast ion redistribution is to detect lost ions directly [1]. A fast ion scintillator installed at the plasma edge can resolve ion energy and pitch angle using a shaped cavity and a 2D scintillator screen, coupled to the air side via a coherent fiber bundle. Spectral analysis is also available to find correlations with other diagnostics, such as magnetic probes.

Since antenna-mode coupling in general equilibria is often hit-or-miss, a coupling calculation should be done with the antenna geometry and the full eigenfunction solutions for multiple equilibria calculated in NOVA-K. The free-boundary mode, which has been recently added to G. Kramer's version of the code, should be used. The coupling study with NOVA-K profiles can be compared to a full calculation in COMSOL. As well, alternative antenna designs such as poloidal-field straps could be tested for better coupling. Care should be taken to minimize the coupling of the

antenna to the ICRF waves. A successful antenna design is also useful as a probe, since the coupling should be reciprocal; the present antenna has been used as a probe occasionally but, by coincidence, never during intervals of AE activity.

Mode resolution could also be improved by increasing signal-to-noise levels. It could be that the system response noise is a product of plasma fluctuations that alter plasma-probe coupling, in which case it would scale with antenna current. This can be evaluated easily with existing data. If there is significant noise from plasma fluctuations, one may be able to reduce it by running a reference frequency simultaneously with the ramped, probing frequency, through the same active MHD antenna structure (so called two-color active MHD). Common mode noise could then be rejected.

Resolution could also be increased by simply improving statistics. Most C-Mod scientists are beginning to embrace the active MHD as a regular tool since it is not perturbative. Therefore frequent piggy-back shots may be available to help in covering wider parameter space, although in the past, modes have in large part only been observable in very specific equilibria on dedicated MP rundays. Nonetheless, increased statistics and a finer mapping of the active MHD operating space could make it a more versatile tool. A comprehensive mapping of AE dependence on plasma parameters, especially related to the coupling of the spectrum to the antennas, and separately, to the most unstable constituents, should be pursued. A corresponding predictive capability with NOVA-K or another code should be developed to prove a physical understanding of the relationship.

Stable AEs are identified by active MHD exclusively in the frequency domain, and they are assumed to be second-order and linear time invariant (LTI) in the fitting procedure. Their LTI nature can be verified with their transient time response by abruptly cutting off the antenna excitation, whereupon it should be expected that their oscillations decay to  $e^{-1}$  in  $N = \omega/(2\pi\gamma)$  periods.

Alfvén eigenmodes could also be excited by modulating the ICRF fast wave at the TAE frequency. Since ICRF heating relies on non-linear mechanisms in the core, a component at the TAE frequency having significant energy is produced, and should excite the TAEs. This method is very promising because it can excite the modes

from the core of the plasma, and might make observations of stable modes with phase contrast imaging possible.

It has been found that the relative amplitude among probes while detecting a stable mode depends on the gap between the plasma and the vessel wall. This is presumably because the probes are not all the same distance from the last closed flux surface. Since the field falls off non-linearly, the relative amplitude depends on how close the plasma is to the probes. Correlation with edge safety factor, edge shear, and pedestal density should also be investigated.

# Appendix A

## Error Analysis

A stable resonant mode that is excited by the active MHD system can be characterized by its damping rate,  $\gamma$ , resonant frequency,  $\omega_0$ , and toroidal mode number,  $n$ . It is only with knowledge of their accuracy that any perceived trend in these parameters can be considered meaningful. The uncertainties associated with these parameters are contributed by several sources: noise on the antenna current and magnetic probe signals distorts the observed plasma response; the calibrated frequency response of the diagnostic itself has some uncertainty that is carried over in the compensation process; the plasma conditions may vary in an unknown but significant way over the period of observing a resonant mode; the resonant mode response is measured on a variably truncated frequency band; and the linear analytic model that is fit to the observed response may not be an exact representation of the resonant plasma behavior and direct coupling terms. The error induced by these sources must be propagated along with the derivation of the characteristic parameters of the resonance to achieve corresponding confidence intervals.

This appendix presents typical values for the sources of uncertainty and considers their step-by-step propagation through the derivation of the resonant mode parameters. First, the influence of signal noise on the coefficients of the analytic model is derived. Next the uncertainty in the model coefficients and the effect of truncating the frequency response are projected onto uncertainties in  $\gamma$ ,  $\omega_0$  and the relative phase between the magnetic probe and the antenna current,  $\phi$ . Finally, the uncertainties in



$\phi$  and the compensation of the diagnostic response are applied to the derivation of the toroidal mode number. Specifically, the steps to determine the confidence intervals in the parameters of an observed resonant mode are:

1. evaluate noise characteristics of measured signals
2. determine the uncertainty in the system response
3. assess the fit of the model to the measured system response
4. determine the uncertainty in the model coefficients
5. transform the model coefficient uncertainties to uncertainties in the resonance parameters
6. assess the fit of the toroidal mode structure

To provide a concrete example, this error analysis procedure is applied to measurements from a toroidal array of probes that lie 10cm above the machine midplane, during a typical resonance that was observed at 0.87s on shot 1080403010. The probes' toroidal positions are shown in Figure A-1.

A summary of the errors associated with the probes at each step of the analysis is given in Table A.1.

## A.1 Uncertainty in the system response

The system diagram in Figure A-2 shows how noise corrupts the true input and output signals. For the input and output respectively, the true signals are  $x(t)$  and  $y(t)$ , the noise is  $m(t)$  and  $n(t)$  and the measured signals are  $c(t)$  and  $v(t)$ .

The nature of the noise determines how it will distort the measured system response from the true response, so it is useful to define some characteristics of both the noise and the true signals.

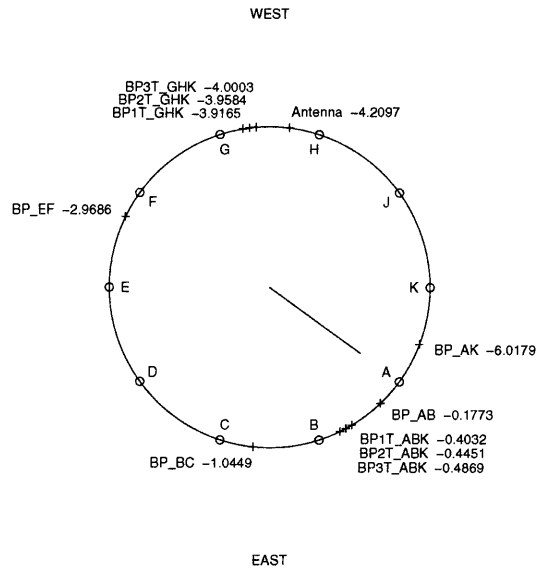


Figure A-1: Top view of the probes used in this appendix to demonstrate the error analysis procedure. Ports are labelled by their letter names. Toroidal angle relative to port 'A' is listed in radians.

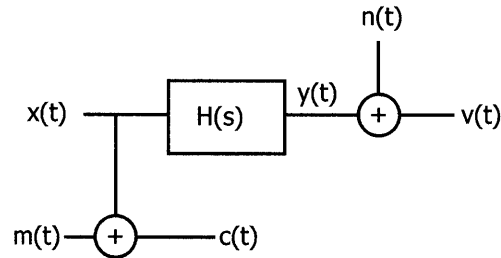


Figure A-2: The system diagram of the active MHD system. Here  $H(s)$  embodies the response of the diagnostic and the plasma.

### A.1.1 Characterizing the signal and noise

Given two signals  $x(t)$  and  $y(t)$ , their cross correlation function is [128],

$$R_{xy}(\tau) = \lim_{T \rightarrow \infty} \frac{1}{T} \int_0^T x(t)y(t + \tau)dt.$$

Then the one-sided cross spectral density function is,

$$\begin{aligned} G_{xy}(j\omega) &= 2 \int_{-\infty}^{\infty} R_{xy}(\tau)e^{-j\omega\tau} d\tau && \omega \geq 0 \\ &= 0 && \omega < 0. \end{aligned}$$

When working with digitized signals it is convenient to interpret these functions in terms of the discrete time Fourier series over a time interval  $N\Delta t$  in which the signals are essentially stationary. For DTFS defined as,

$$\begin{aligned} X(k) &= \frac{1}{N} \sum_{n=0}^{N-1} x(n)e^{-j2\pi\frac{kn}{N}}, \\ Y(k) &= \frac{1}{N} \sum_{n=0}^{N-1} y(n)e^{-j2\pi\frac{kn}{N}}, \end{aligned}$$

the one-sided cross spectral density function is,

$$\begin{aligned} G_{xy}(k) &= 2X^*(k)Y(k) && k \geq 0 \\ &= 0 && k < 0. \end{aligned}$$

Similarly, the power spectral density function (also called the autospectrum) is related to the autocorrelation function,  $R_{xx}$ , as,

$$G_{xx}(j\omega) = 2 \int_{-\infty}^{\infty} R_{xx}(\tau) e^{-j\omega\tau} d\tau \quad \omega \geq 0$$

$$= 0 \quad \omega < 0,$$

or equivalently to the DTFS as,

$$G_{xx}(k) = 2X^*(k)X(k) \quad k \geq 0$$

$$= 0 \quad k < 0,$$

which helps to emphasize that the autospectrum is real valued. These spectral functions are used to characterize the true signals and the noise.

To begin with, the expected value of the power spectral density of the noise is called the noise floor, and describes how the noise power is distributed in frequency. For the current and probe noise, respectively, they are defined as,

$$\overline{G}_{mm}(k) = \langle G_{mm} \rangle(k)$$

$$\overline{G}_{nn}(k) = \langle G_{nn} \rangle(k)$$

The ratio of the noise power to the true signal power is called the signal-to-noise ratio,  $\beta$ . For the output voltage and input current respectively, the signal-to-noise ratios

are calculated as,

$$\beta_v = \frac{\sum_k G_{yy}(k)}{\sum_k G_{nn}(k)} \quad (\text{A.1})$$

$$(\text{A.2})$$

$$\beta_c = \frac{\sum_k G_{xx}(k)}{\sum_k G_{mm}(k)} \quad (\text{A.3})$$

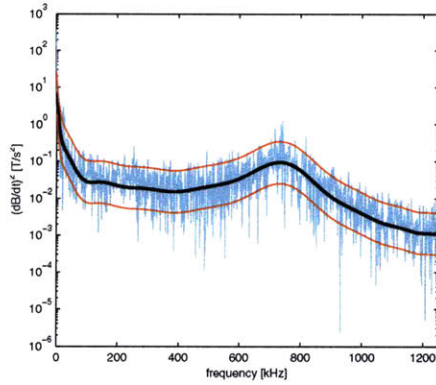
The correlation of the input and output noise is called their coherence,  $\gamma_{mn}$ . This is an important quantity because it represents the fraction of power that is common to both the input and the output signals, but that does not pass through the system, adding a spurious term to the measured system response. The coherence of the noise is calculated as,

$$\gamma_{mn} = \frac{\sum_k G_{mn}(k)}{\sqrt{\sum_k G_{mm}(k) \sum_k G_{nn}(k)}} \quad (\text{A.4})$$

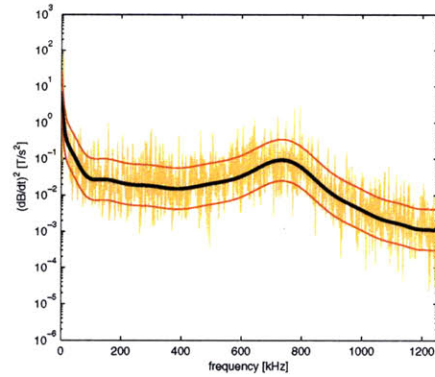
To determine the influence of noise on the measured system response in practice, the noise floors  $\overline{G}_{mm}$  and  $\overline{G}_{nn}$ , the coherences,  $\gamma_{mn}$ , and the signal-to-noise ratios,  $\beta$ , must be identified.

The noise floor is readily determined from the measured signals when no excitation is present, for example in shot 1080411004 when active MHD is not operating. Then the measured signal consists entirely of noise. The noise floors  $\overline{G}_{mm}$  and  $\overline{G}_{nn}$  for the current and probe noise respectively, are shown in Figure A-3, along with their standard deviations and typical noise autospectrums. It is an unfortunate characteristic of the diagnostic that for both signals, the noise floor peaks around  $700\text{kHz}$  near the typical excitation frequency; consequently, bandpass filtering the signals around the excitation frequencies eliminates only the weakest components of the noise. After normalizing by the noise floor, the energy distribution of the noise is essentially Gaussian (Figure A-3(e)). The Gaussian character is maintained in the synthetic noise that is generated in Figures A-3(d) and A-3(b).

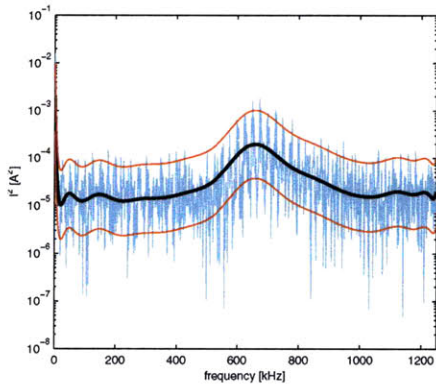
The noise coherence  $\gamma_{mn}$  is calculated from these noise floor autospectrums as in Equation A.4. The amplitude of the coherence roughly falls on a normal distribution with a standard deviation of 0.03, and its phase is randomly distributed (Figures A-4).



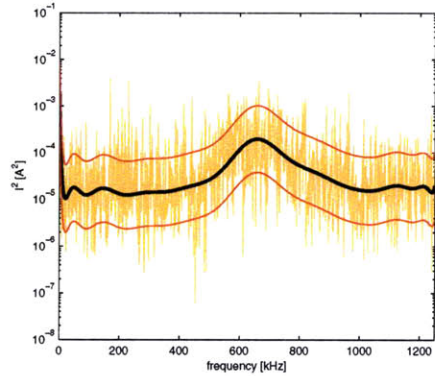
(a) Typical measured probe noise.



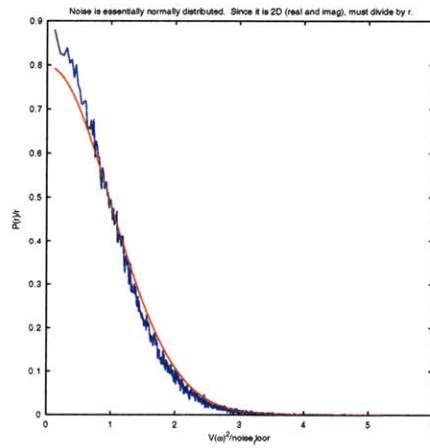
(b) Synthesized probe noise.



(c) Typical measured antenna current noise.



(d) Synthesized antenna current noise.



(e) The distribution of the noise after compensating for the noise floor is Gaussian, with some small error at low amplitudes where the power density is less.

Figure A-3: Typical measured signal autospectrums (light blue); noise floor (black) with standard deviation of the noise (red); and synthesized autospectrums based on the noise floors and the distribution of the noise.

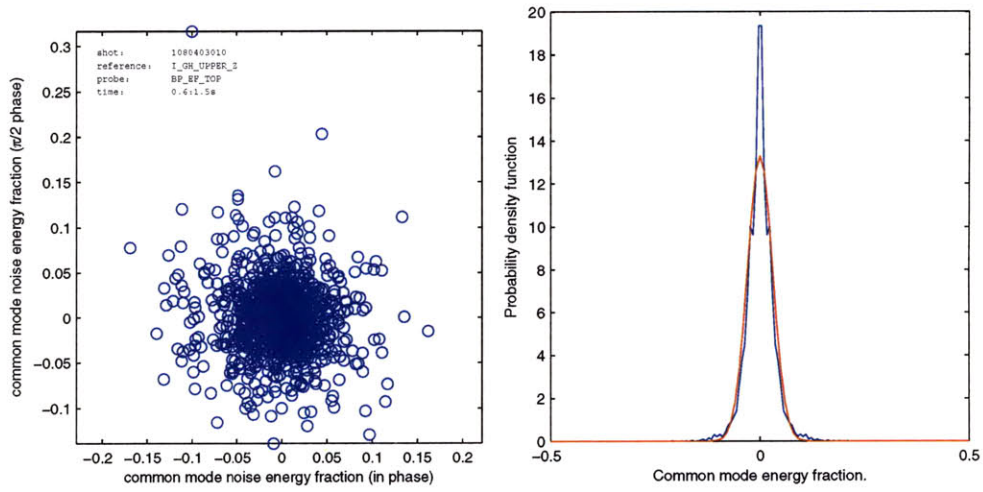
It may be surprising that the noise on the current tap and the magnetic probes is not more strongly correlated, especially when the RF beatwave at 500kHz is present; however spectrums of each signal show that the RF beatwave is not a strong component of the current tap noise (Figures A-5).

To obtain the signal-to-noise ratios of the input and output signals, the true signal and noise components must be identified. A typical measured spectrum of the antenna current is shown in Figure A-6. For reference, Figure A-7 shows the synthesized spectrum for a noiseless chirped signal, and the fraction of power within a frequency band centered on the peak frequency component of the synthesized spectrum. The excitation typically chirps between 1.5 to 6MHz $s^{-1}$ . At these chirp rates, at least 95% of the power is confined to a 7kHz band in each 0.8ms period. For this analysis, then, it is a good estimate to consider the true antenna current signal  $G_{cc}$  to be restricted to a 7kHz band centered around the maximum frequency component, and the antenna current noise  $G_{mm}$  to occupy all other frequencies. The measured signals of the magnetic probes are similarly divided:  $G_{vv}$  inside a 7kHz band, and  $G_{nn}$  outside. Consequently the cross spectrums between true signal and noise are zero,

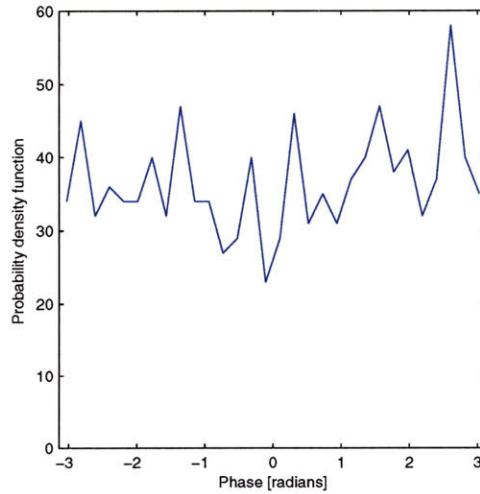
$$G_{yn} = G_{xm} = 0. \quad (\text{A.5})$$

From this perspective it is clear that the noise power could be decreased by filtering the measured signal with a passband centered around the excitation frequencies to selectively eliminate some of the noise power. The improvement in signal resolution would come at the expense of processing speed, and this trade-off must be evaluated to achieve whatever precision is required, if possible. Since the results in this thesis were obtained using a very wide passband from 150 to 900kHz, the remaining analysis will assume the use of such a filter.

Given this definition of the true signal and noise components, the signal-to-noise ratios can be calculated. To evaluate the signal-to-noise ratio of the current signal during shot 1080403010, power inside the 7kHz band (the true signal) is divided by the power outside of the 7kHz band (the noise), while the center of the 7kHz band is



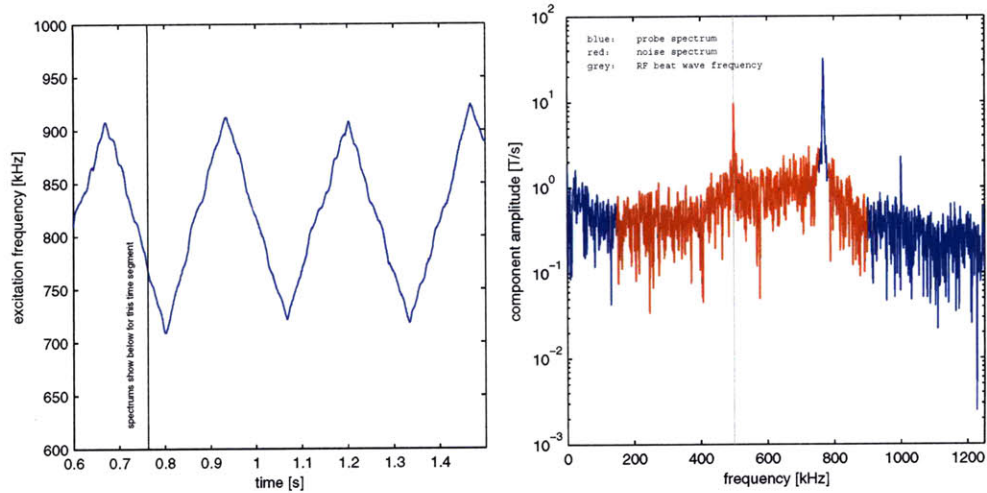
(a) Amplitude and phase of the noise coherence plotted in the complex plane. (b) Standard deviation is  $\tilde{3}\%$ . The peak in the common mode distribution is due to very few counts being compensated by very small amplitude. Counting error is magnified.



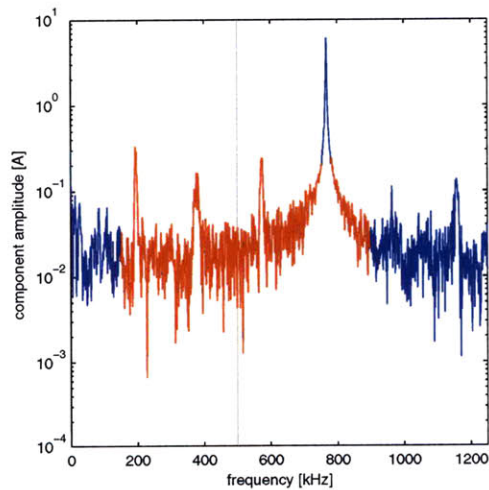
(c) The phase of the coherence is randomly distributed.

Figure A-4: The coherence  $\gamma_{mn}$  between the current and the probe voltage for a typical probe.





(a) Blue: active MHD frequency trajectory; Black vertical line: time slice inspected in adjacent figures. (b) typical probe spectrum shows peaks at the active MHD excitation frequency and at the ICRF beatwave frequency.



(c) The antenna current spectrum does not show evidence of ICRF beatwave noise.

Figure A-5: The noise coherence may be unexpectedly small, especially during ICRF operation. While a strong component of the beatwave appears in the typical probe signal, it is absent in the current signal. The grey line marks the ICRF beatwave frequency. Also illustrated in these spectrums is the distinction that has been made between the true signal (the center blue portion) and the noise (the red portion).

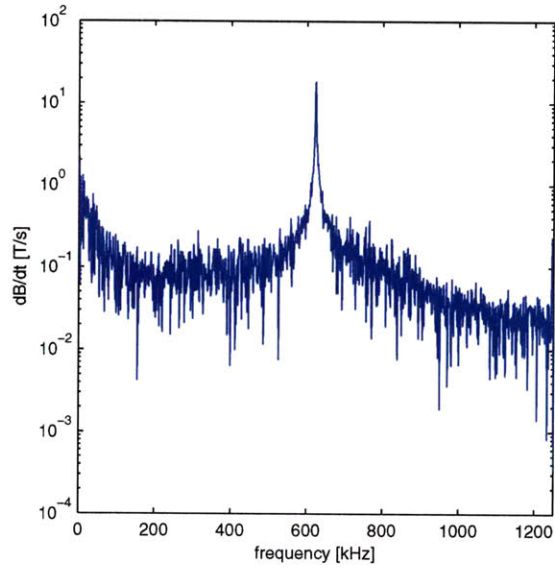
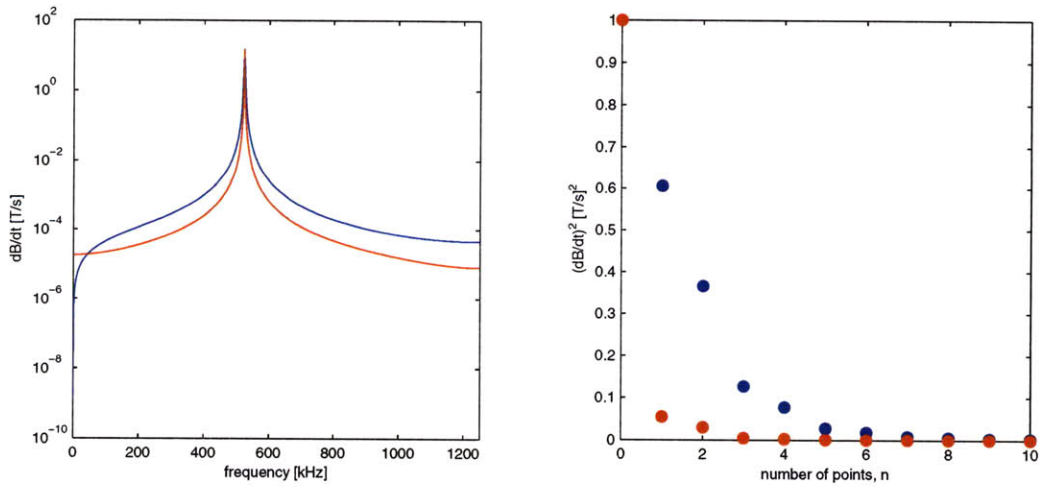


Figure A-6: Typical spectrum of a magnetics probe with active MHD excitation.



(a) The spectrum of a synthetic chirp: red  $1.5\text{MHzs}^{-1}$ ; blue  $6\text{MHzs}^{-1}$

(b) The signal power is strongly concentrated near the central frequency, which should justify the separation between true signal and noise based on frequency.

Figure A-7: Spectrum of synthetic chirping signal.

shifted at each time sample as the excitation frequency chirps. Figure A-8(a) shows how the signal and noise components fluctuate as the amplifier traverses its tuning band. Figure A-8(b) indicates that the signal-to-noise ratio ranges from 4 to beyond 30. Figure A-8(c) shows the autospectrum for high and low  $\beta_c$  and illustrates that the fluctuation of  $\beta_c$  is actually due to the true signal power leaking out of the  $7kHz$  band when the excitation frequency jitters. This leakage makes it difficult to implement a sufficiently narrow bandpass filter, since it causes the signal bandwidth to change rapidly in time. Furthermore, the homodyne synchronous correlation method is not sensitive to the bandwidth of the true signal, so signal leakage does not present a problem for system identification.

A similar analysis is performed for the probe voltage signals, for which the signal-to-noise ratios are observed to range from 0.05 to more than 2 (Figures A-9). Like the current tap signal, the probe voltage signals would also require a very narrow bandpass filter to significantly improve the signal-to-noise ratio.

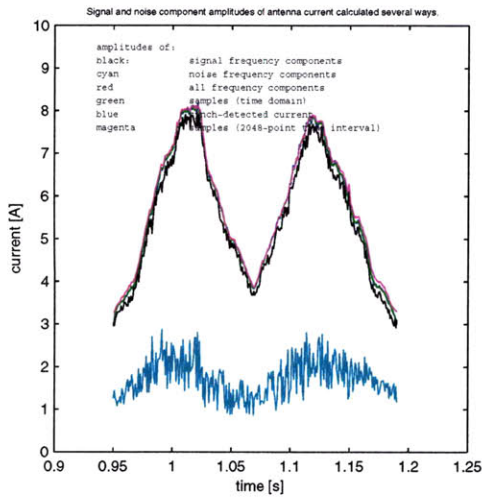
To summarize, in addition to the noise floor profiles, the attributes that characterize the noise are listed in Table A.1. Now the error in the measured system response can be assessed from the attributes of the noise.

### A.1.2 Quantifying the uncertainty in the system response

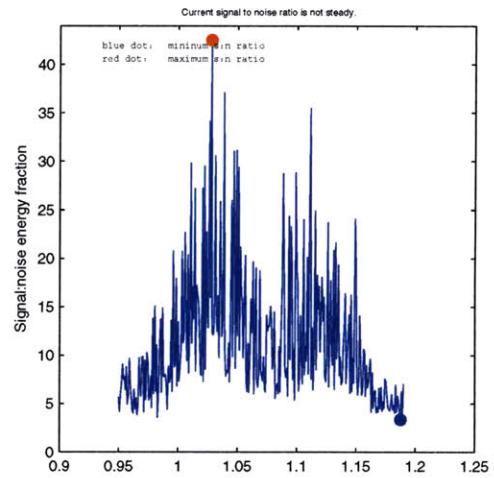
The true system response is,

$$H_{true} = \frac{\sum_k Y^* X}{\sum_k X^* X},$$

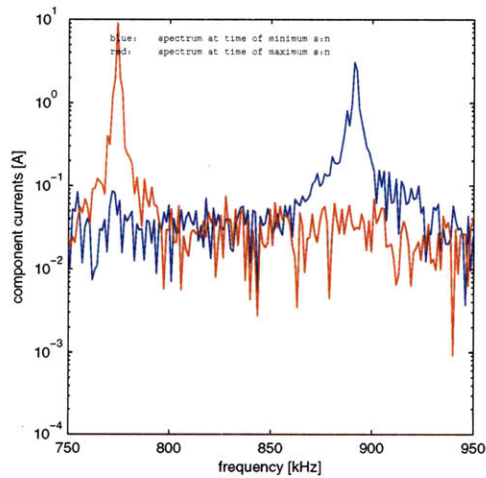
where  $Y$  and  $X$  are the Fourier series of  $y(t)$  and  $x(t)$ , the antenna current and probe voltages. But  $Y$  and  $X$  are not measurable. Instead, the measurable signals  $V$  and



(a) Energy of the noise (cyan) and true signal (black) of the antenna current as the active MDH frequency sweeps through a resonance.

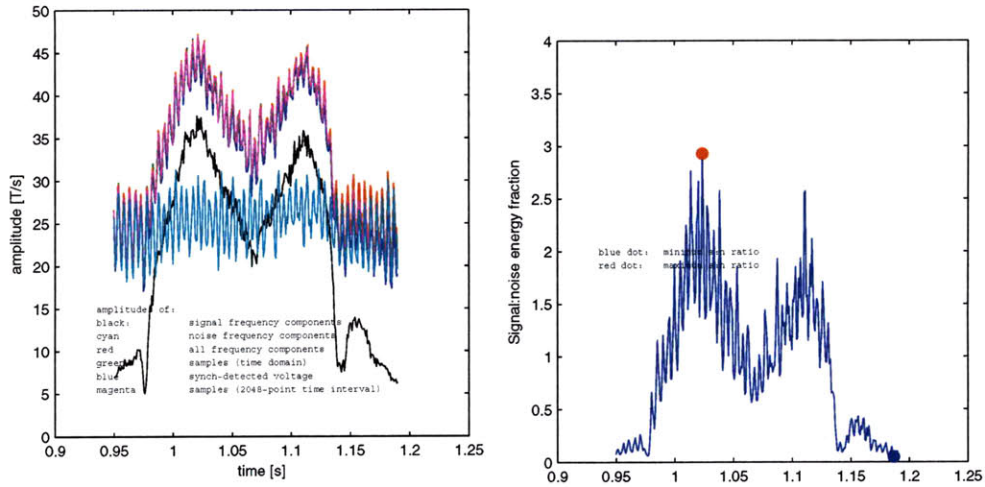


(b) Signal-to-noise ratio  $\beta_c$



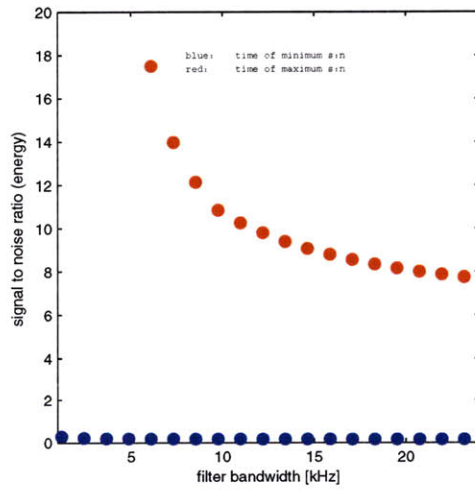
(c) Jitter in the excitation frequency causes the signal to leak of the central frequencies (blue curve). When the frequency is stable, the signal is confined to a narrow frequency band (red).

Figure A-8: Investigation of the antenna current signal-to-noise ratio during shot 1080403010.



(a) Energy of the noise (cyan) and true signal (black) of a typical probe as the active MDH frequency sweeps through a resonance.

(b) Signal-to-noise ratio  $\beta_v$



(c) At times of low signal-to-noise ratio (blue dots) even a narrow filter does not improve the ratio significantly.

Figure A-9: Investigation of a typical probe signal-to-noise ratio during shot 1080403010.

$C$  are contaminated by noise, so the measured system response is,

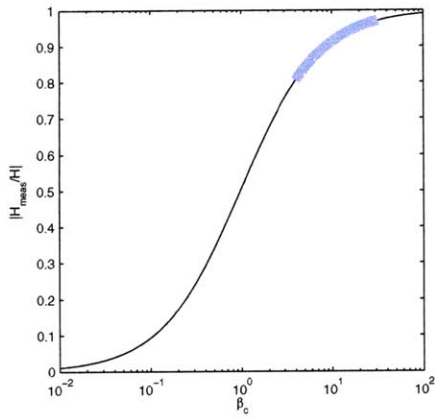
$$\begin{aligned}
H_{meas} &= \frac{\sum_k V^* C}{\sum_k C^* C} \\
&= \frac{\sum_k (Y + N)^* (X + M)}{\sum_k (X + M)^* (X + M)} \\
&= \frac{\sum_k (Y^* X + Y^* M + N^* X + N^* M)}{\sum_k (X^* X + X^* M + M^* X + M^* M)} \\
&= \frac{\sum_k (X^* Y / X^* X + N^* M / X^* X)}{1 + \sum_k (M^* M / X^* X)}
\end{aligned}$$

so that

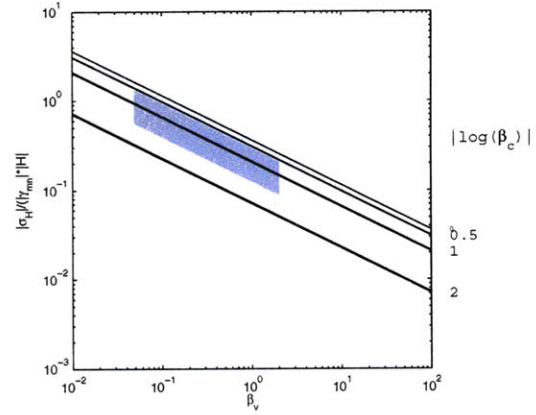
$$H_{meas} = \frac{H_{true}}{1 + 1/\beta_c} \left( 1 + \gamma_{mn} / \sqrt{\beta_c \beta_v} \right) \quad (\text{A.6})$$

where relations A.3, A.4 and A.5 have been put to use. Two effects are evident. First, the system response is attenuated by the noise on the input in the form of  $\beta_c$ . This provides motivation to reduce the noise on the input signal by bandpass filtering more tightly. Figure A-10(a) shows the change in  $|H|$  due to this factor. Secondly, a term having the phase of the noise coherence,  $\gamma_{mn}$  is added. As mentioned above,  $\gamma_{mn}$  is observed to have randomly distributed phase and a Gaussian amplitude distribution, so this term amounts to random noise added to the system response. Figure A-10(b) shows the worst case change in  $|H|$  due to this additive term. These two effects are due to the expected value of  $\beta$  and  $\gamma$ . In addition, there is some added variation contributed by the random variation of  $\beta$  and  $\gamma$ . The distribution of this third effect was generated statistically with synthesized signals and was found to be Gaussian, as Figure A-11 illustrates. The effect it has on the measured value of  $|H|$  is shown in Figure A-10(c). Finally, the measured  $|H|$  is statistically generated using synthetic signals and is found to agree with the prediction of equation A.6, as shown in Figure A-12.

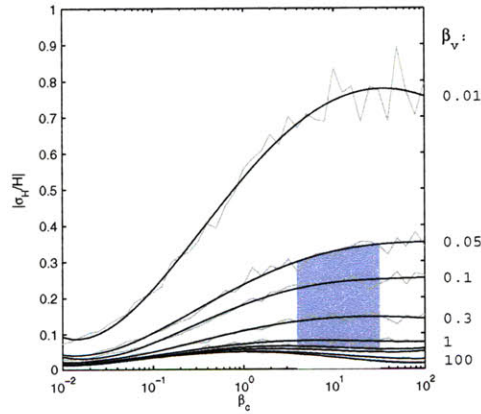
The total measurement uncertainty  $\sigma_h$  in the system response for each probe is



(a) The attenuation of the measured system response due to the  $1/\beta_c$  factor in the denominator. Light blue patch shows the typical region of operation.

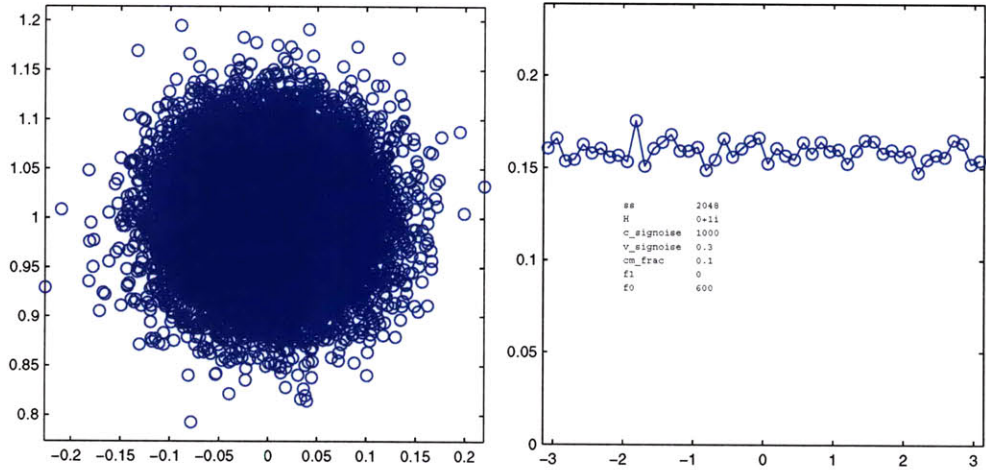


(b) Amplitude of the distortion due to the second term in Equation A.6.

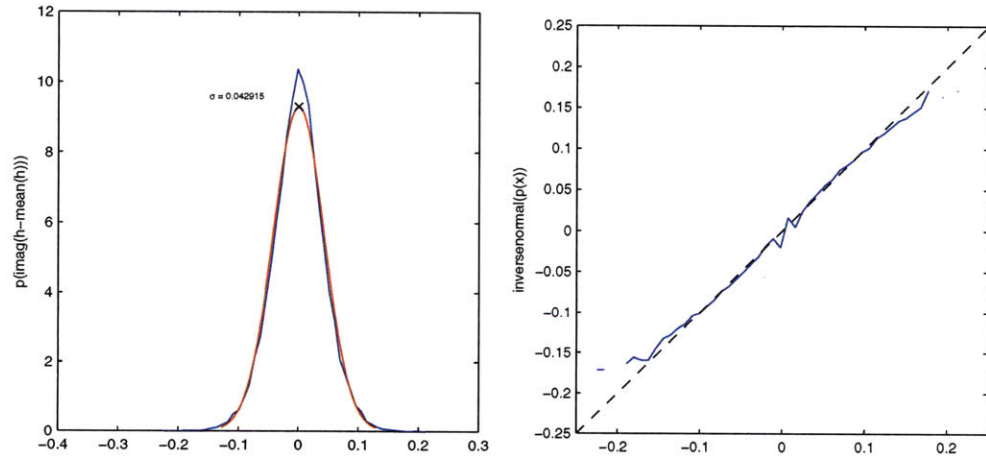


(c) Amplitude of the random noise due to the fluctuation of the  $\beta$  and  $\gamma_{mn}$ .

Figure A-10: The amplitudes of the distortion of the system response due to the various terms in Equation A.6. Blue patches indicate the typical region of operation.



(a) Distribution of  $\sigma_H$  due to fluctuation of  $\beta$  and  $\gamma_{mn}$ . (b) The phase of  $\sigma_H$  is uniformly distributed.



(c) The amplitude of the  $\sigma_H$  is gaussian distributed. (d) Inverse Gaussian function of the amplitude distribution shows that it fits pretty well.

Figure A-11: Distribution of  $\sigma_H$  for synthetic signals constructed based on the parameters  $\beta_v$ ,  $\beta_c$ ,  $\gamma_{mn}$  and the noise floor spectrums. Defining the distribution of the error on  $\sigma_H$  will allow the  $\chi^2$  test to evaluate the quality of fit. It appears to be essentially Gaussian.



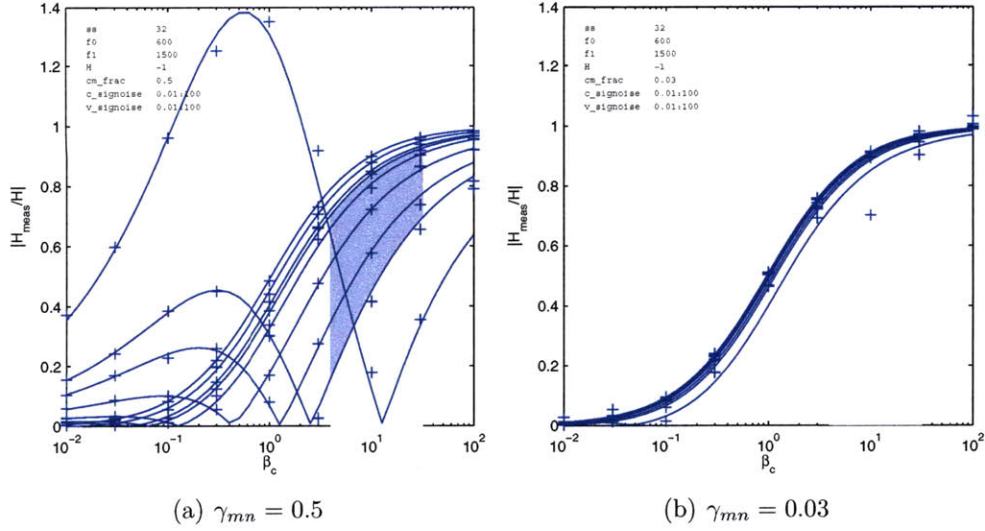


Figure A-12: Expected value of the total distortion of the amplitude of  $H(s)$  due to all the factors presented in Figure A-10. The blue patches indicate typical regions of operation.  $\gamma_{mn} = 0.03$  is the typical value for the noise coherence, but  $\gamma_{mn} = 0.5$  is also shown for comparison. Blue curves are the calculated distortion based on Equation A.6, crosses are the statistical result of simulations with synthetic signals generated based on the signal and noise characteristics.

calculated using the relation A.6 and the distribution in Figure A-10(c) for the values of  $\beta$  and  $\gamma$  inferred from the noise in shot 1080403010, and these uncertainties are tabulated in Table A.1.

For comparison, the fitting errors between the system response model and the measured system response are plotted as circular regions in Figure A-13. In the figure, the frequency increases in the clockwise direction, which is expected for a pole in the left-half plane. At the instant in time depicted here, the active MHD excitation frequency is chirping down, so the response is being traversed counter-clockwise as time increases. Note that the first half of the response has larger fitting error due to the smaller signal-to-noise ratios at that time, as shown in Figure A-9. Note also that probes near the antenna have stronger direct coupling compared to the resonant coupling, which evident by the origins of the resonant circles being further from the origin. For a good fit it should be expected that the fit errors would be similar to the measurement uncertainties  $\sigma_H$ . Hence the quality of the fit can be evaluated with the  $\chi^2$  test. Namely, for  $N$  measurements of the system response and  $c$  coefficients in the

Table A.1: Signal-to-noise ratios as in Figure A-9 and the corresponding distortion of the system response as articulated in Figure A-12. The resonance is divided into two periods of contrasting signal-to-noise ratios, and the uncertainty changes accordingly. High  $P(\chi^2)$  indicates a confident fit.

probe name	0.95 – 0.975s			0.975 – 1.0s			$\tilde{\chi}^2$	P( $\tilde{\chi}^2$ )
	$\beta_v$	$\gamma_{mn}$	$\sigma_H/H$	$\beta_v$	$\gamma_{mn}$	$\sigma_H/H$		
	dB	%	%	dB	%	%		
BP_KA_TOP	-5.2	2	15	5.4	2	6	2.84	0
BP3T_GHK	-7	2	18	1.1	2	8	0.106	100
BP2T_GHK	-10	2	25	-3	2	13	0.435	100
BP1T_GHK	-17	2	65	-10.5	2	27	1.12	29
BP_EF_TOP	-5.2	2	85	2	2	20	1.11	96
BP_BC_TOP	-21	2	95	-7.0	2	20	0.544	96
BP3T_ABK	-24	2	95	-10.5	2	27	2.3	0
BP2T_ABK	-23	2	90	-10	2	25	2.01	0.04
BP1T_ABK	-20	2	80	-8.2	2	23	1.88	0.14
BP_AB_TOP	-13	2	33	0.41	2	8	2.95	0
L_GH_UPPER_Z	10			15.4				

model, the reduced  $\tilde{\chi}^2$  is [129],

$$\tilde{\chi}^2 = \frac{1}{N - c} \sum \left| \frac{H(j\omega)_{meas} - H(j\omega)_{fit}}{\sigma_h} \right|^2. \quad (\text{A.7})$$

When  $\tilde{\chi}^2$  is small it means that the agreement between the model and the measured system response is good, and therefore implies that the model represents the measurements accurately. The values of  $\tilde{\chi}^2$  and the probability of achieving an agreement of  $\tilde{\chi}^2$  or worse with data that truly fit the assumed distribution are tabulated for each probe in Table A.1. For probabilities less than 5%, the fit validity of the fit should be questioned. However there is some question whether the  $\chi^2$  test is applicable to this system because the direct coupling and resonant coupling are not likely subject to the same noise distribution. Indeed, for probes that have higher fractions of direct coupling power, the  $\chi^2$  test declares a more likely match to the model.

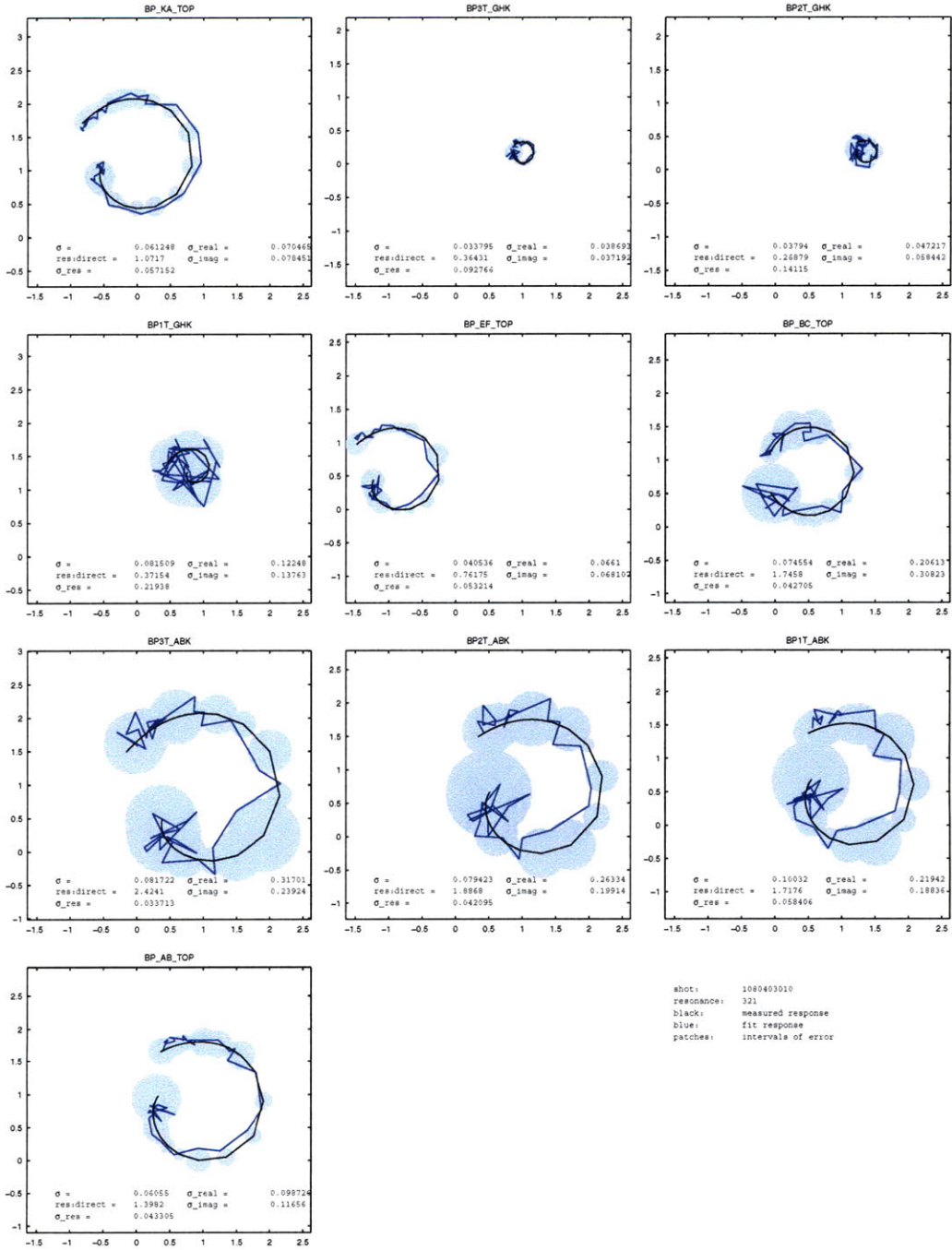


Figure A-13: System response for the 10 probes enumerated in Figure A-1. Blue line: measured response; Black line: fit response; Blue patches: region of uncertainty based on the fitting error, which is to be compared to the uncertainty in the measured response inferred from Equation A.6 and plotted in Figure A-12. The frequency increases in the clockwise direction, which is expected for a pole in the left-half plane.

## A.2 Propagation of error to quantities of interest

### A.2.1 Confidence interval of polynomial coefficients

The quality of the fit also projects onto uncertainties in the coefficients  $\mathbf{u}$  of the polynomials  $B(s)$  and  $A(s)$  that compose the model. Recall that in multiple regression the coefficients  $\mathbf{u}$  are given by,

$$u = \mathcal{R} \{S^* S\}^{-1} \mathcal{R} \{S^* D\}$$

and the fitting error by,

$$\epsilon = -D + Su.$$

Then the uncertainty in the coefficients is given by the covariance matrix [130]:

$$\begin{aligned} \sigma_{\mathbf{u}} &= \frac{1}{N} \sum_{i=1}^N \left( \frac{\partial \mathbf{u}}{\partial \epsilon_i} \epsilon_i \right)^* \left( \frac{\partial \mathbf{u}}{\partial \epsilon_i} \epsilon_i \right) \\ &= \frac{1}{N} \left( \frac{\partial \epsilon^*}{\partial \mathbf{u}} \frac{\partial \epsilon}{\partial \mathbf{u}} \right)^{-1} \epsilon^* \epsilon \\ &= \frac{1}{N} (S^* S)^{-1} \epsilon^* \epsilon \end{aligned}$$

The diagonal elements of  $\sigma_u$  are the squares of the uncertainties of the corresponding coefficients. In the preceding it has been assumed that the distribution of uncertainty is the same for each measurement, so that each measurement can be assigned equal weight in determining the best fit. This is not strictly accurate since the signal to noise level, and hence the standard deviation of the measurement, changes unavoidably throughout the resonance. Omitting the weights provides a conservative estimate of the uncertainties in the coefficients [131],[132] and is sufficient for the present requirements.

## A.2.2 Confidence interval of resonance parameters

Resonances are more meaningfully represented by the residues, poles and direct terms of the quotient  $B(s)/A(s)$  rather than the coefficients of those polynomials. The poles are the roots of  $A(s)$ , the corresponding residues are the values of  $H(s)$  evaluated at each pole, and the direct term is the remainder in the polynomial division  $B(s)/A(s)$ . Grouping the residues, poles and direct terms into the vector resonance parameter  $\nu$ , uncertainties in  $u$  are transformed into uncertainties in  $\nu$  by the Jacobian  $J(\nu, u)$  so that the uncertainties in  $\nu$  are obtained from a transformation of the original covariance matrix  $\sigma_u$  to,

$$\sigma_\nu = \frac{\epsilon^* \epsilon}{N} J (S^* S)^{-1} J^* \quad (\text{A.8})$$

where again, the diagonal elements of  $\sigma_\nu$  are the squares of the uncertainties of the corresponding coefficients.

A further transformation yields the damping rate  $\gamma/\omega_0$ , resonant frequency  $\omega_0$  and phase  $\phi$  of the resonance from the roots of the polynomials, and again, the uncertainties can be likewise transformed to yield uncertainties  $\sigma_{\gamma/\omega}$ ,  $\sigma_\omega$  and  $\sigma_\phi$  as follows. For the pole  $p = \gamma + i\omega_0$ ,

$$\sigma_{\gamma/\omega}^{\frac{1}{2}} = \frac{\gamma}{\omega_0} - \frac{\gamma(1 - \sigma_p)}{\omega_0(1 + \sigma_p)}$$

$$\approx -2 \frac{\gamma}{\omega_0} \sigma_p,$$

and,

$$\sigma_\omega^{\frac{1}{2}} = \sigma_p,$$

and for the residue  $r$ ,

$$\sigma_\phi^{\frac{1}{2}} = \sin^{-1} \left( \frac{\sigma_r}{r} \right).$$

The uncertainties in these coefficients for the resonance in shot 1080403010 are summarized in Table A.2.

### A.2.3 Significance of the toroidal mode number fit

The toroidal mode number of the resonance is obtained from a linear regression of the phase of the probe responses against the probes' toroidal angles. The uncertainty in the probe toroidal positions is negligible, so the uncertainty in the phase of the response,  $\sigma_\phi$ , is identical to the uncertainty in the fit to the regression function. As before, the quality of this fit can be evaluated by the  $\chi^2$  test, where the mode number is an integer,  $n$ , the phase offset is  $b$ , and the toroidal angular position of the coils are  $\varphi$ .

$$\tilde{\chi}^2 = \frac{1}{N - c} \sum \left| \frac{n\varphi_i - b - \phi_i}{\sigma_{\phi,i}} \right|^2.$$

The  $\tilde{\chi}^2$  and  $P(\tilde{\chi}^2)$  are listed in Table A.3 for the mode numbers  $\{-20 : 20\}$  fit to the resonance in 1080403010. The phase distribution of the best fitting mode,  $n = 0$ , is shown in Figure A-14. That  $n = 0$  has a significant  $\chi^2$  probability confirms that it is the correct toroidal mode number of this resonance.

Table A.2: The parameters of the resonance and their respective uncertainties.

probe name	$\gamma/\omega_0$	$\sigma_{\gamma/\omega}^{\frac{1}{2}}$	$f_0$	$\sigma_f^{\frac{1}{2}}$	$\phi$	$\sigma_\phi^{\frac{1}{2}}$
	%	%	kHz	kHz	deg	deg
all	0.85	0.018	848.98	0.15		
BP_KA_TOP					-12.9	3.2
BP3T_GHK					-3.9	22.6
BP2T_GHK					-12.7	26.6
BP1T_GHK					-22.6	17.8
BP_EF_TOP					-19	3.25
BP_BC_TOP					-13.8	3.65
BP3T_ABK					-16.2	2.55
BP2T_ABK					-21.4	2.73
BP1T_ABK					-22.5	2.71
BP_AB_TOP					-14.8	2.77

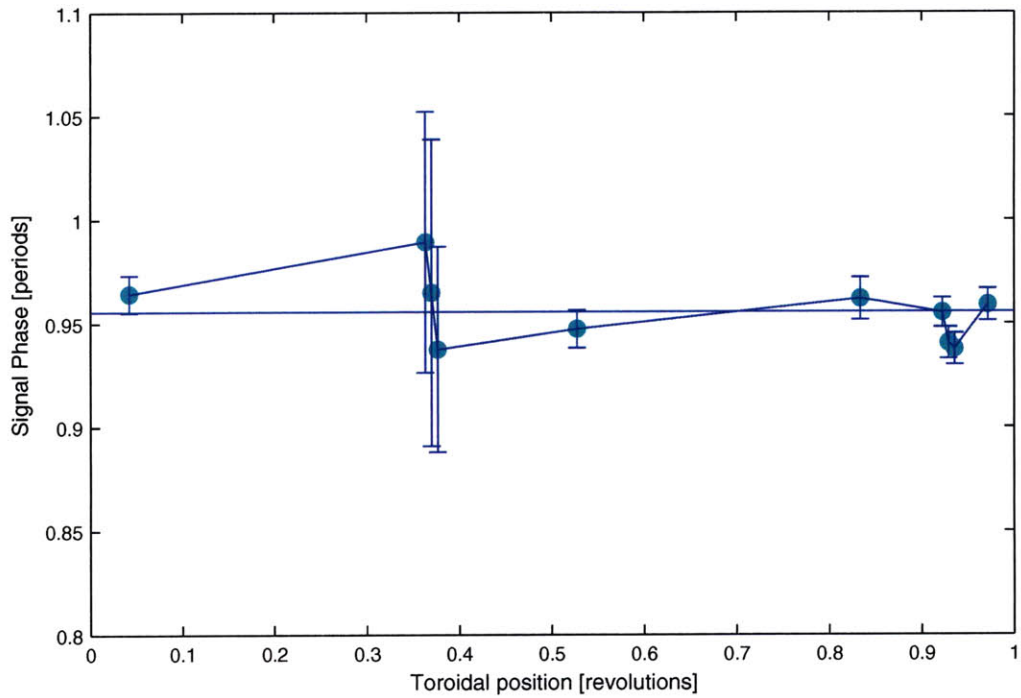


Figure A-14: The best fit toroidal mode number to the example resonance in 1080403010 is  $n=0$ . Cyan: phases for each probe used in the example; Blue error bars are determined by propagating the fitting error to the resonance parameters via Equation A.8.  $P(\tilde{\chi}^2)$  indicates there is an 18% probability of fitting this poorly with phases that are truly  $n=0$ .

Table A.3: The fit of the toroidal mode numbers within  $\{-20 : 20\}$  for the example resonance in 1080403010. High  $P(\tilde{\chi}^2)$  indicates a confident fit.

mode number	$\tilde{\chi}^2$	$P(\tilde{\chi}^2)$
		%
0	1.4	18.3
-2	183.23	0
2	183.29	0
-20	243.42	0
1	252.22	0
20	258	0
-1	267.12	0
-18	302.98	0
18	313.5	0
7	339.7	0
-7	348.87	0
9	363.45	0
-9	368.56	0
8	376.93	0
-8	388.38	0
10	397.58	0
19	399.62	0
3	409.41	0
-19	411.58	0
-17	412.68	0
17	440.97	0
-10	445.13	0
-15	446.91	0
-3	447.8	0
-16	484.56	0
-13	509.06	0
16	538.74	0
15	543.54	0
5	561.55	0
4	570.39	0
12	574.9	0
-5	577.65	0
13	601.64	0
-12	618.39	0
-4	653.04	0
-14	672.19	0
-11	727.84	0
14	729.1	0
11	733.1	0
-6	752.5	0
6	771.43	0



# Appendix B

## Calibration of Pickup Coils

The voltage induced in the pickup coil by a changing poloidal magnetic field is transformed by the wires that connect the coil to the digitizer. If the behavior of the coils and wire circuit is known, this transformation can be inverted and removed from recorded data. In particular, it is especially important to correct for phase shifts because the relative phase of adjacent coils is used to determine the mode number of TAEs.

The frequency response of the coils can be measured by one of three methods; the feasibility of each method depends on the physical access that is available to the pickup coil circuit. When the vacuum vessel is closed, the frequency response can be approximated from measurements at the digitizer end of the pickup coil circuit. When the vacuum vessel is open, the pickup coil can be excited by an external field, and the exact response can be measured at the digitizer end. Finally, if the pickup coil circuit is interrupted very close to the pickup coil by a connector, a signal can be injected at the connector and the response measured at the digitizer end. The merits of each method are discussed in this section. In all cases the transformation is assumed to be linear.

### External Calibration

A true measurement of the frequency response of a two-port network is not possible from only one port. When the vacuum vessel is closed, only the air side length of

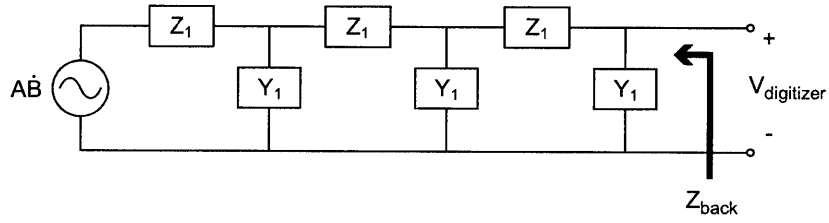


Figure B-1: The circuit topology used by Heeter to develop a method to calibrate the pickup coils from one end of the circuit only.

the twisted pair can be contacted. With some knowledge of the pickup coil circuit topology, however, an appropriate frequency response can be synthesized from single port measurements [133]. To determine the transfer function of a circuit with topology shown in Figure B-1, the impedance looking back from the digitizer,  $z_{back}$ , is measured over the frequency range of interest. A ratio of polynomials of given order is then fit to the measured data,  $z_{back} \cong N/D$ , to determine the coefficients of the polynomials  $N$  and  $D$ . As Heeter et. al. show in [133], the transfer function can then be written down as  $1/D$ . This method relies on the assumptions that the circuit topology is as shown in Figure B-1, that the numerator and denominator have no common factors, and that the circuit elements can be accurately represented by polynomials of limited order.

### Internal Calibration, inductively excited

If the interior of the vessel is accessible, the pickup coil response can be measured by exciting the coils with an oscillating field generated by a calibrating winding. An apparatus for the measurement is illustrated in Figure B-2. This provides a direct measurement of the circuit response, which necessarily also includes the response of the calibrating winding near each pickup coil. Since the calibrating coil response is similar near each coil, and since the difference between coil responses is of primary interest rather than their absolute behavior, the calibrating winding response can be essentially cancelled out leaving only a small residual error, which will now be calculated.

The calibrating winding/pickup coil system to be measured is approximated by

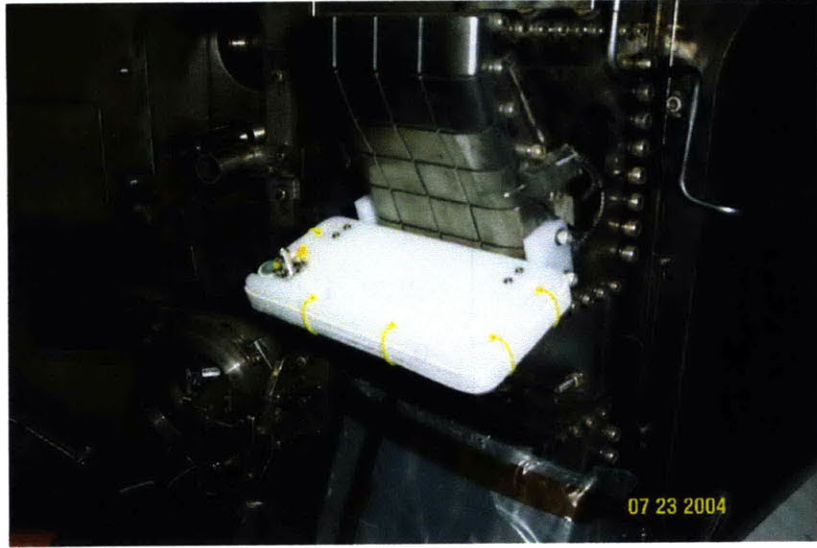


Figure B-2: The pickup coils can be precisely calibrated when in-vessel access is available, by exciting them in pairs with field-generating windings.

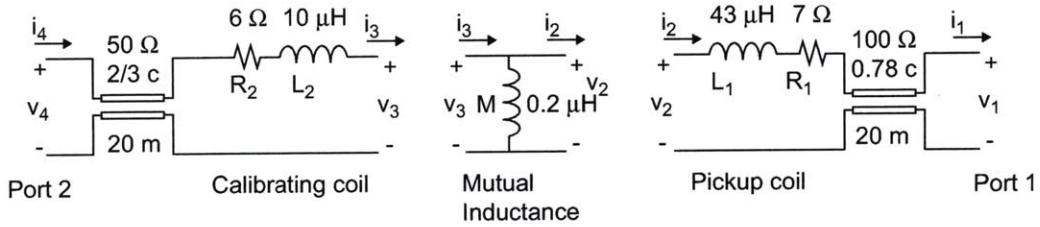


Figure B-3: The circuit for in-vessel, inductively-driven calibration, with component values.

the circuit diagram of Figure B-3. To simplify the analysis, the circuit is divided into three two-port networks. The response of each network is written below, along with

the estimated magnitudes at 1 MHz for the purpose of scaling the terms.

$$\begin{aligned}
 \begin{matrix} v_4 \\ i_4 \end{matrix} &= \begin{bmatrix} A_3 & B_3 \\ C_3 & D_3 \end{bmatrix} \begin{matrix} v_3 \\ i_3 \end{matrix} = \begin{bmatrix} 0.805 & 42 + j47 \\ j0.012 & 40.3 - j29.7 \end{bmatrix} \begin{matrix} v_3 \\ i_3 \end{matrix} \\
 \begin{matrix} v_3 \\ i_3 \end{matrix} &= \begin{bmatrix} A_2 & B_2 \\ C_2 & D_2 \end{bmatrix} \begin{matrix} v_2 \\ i_2 \end{matrix} = \begin{bmatrix} 1 & 0 \\ -j0.80 & 1 \end{bmatrix} \begin{matrix} v_2 \\ i_2 \end{matrix} \\
 \begin{matrix} v_2 \\ i_2 \end{matrix} &= \begin{bmatrix} A_1 & B_1 \\ C_1 & D_1 \end{bmatrix} \begin{matrix} v_1 \\ i_1 \end{matrix} = \begin{bmatrix} -0.523 + j0.036 & -283 + j6 \\ -j0.005 & -j0.51 \end{bmatrix} \begin{matrix} v_1 \\ i_1 \end{matrix}
 \end{aligned}$$

Given two pickup coils labelled  $i$  and  $j$ , the complex-valued ratio of their frequency response into digitizers with input impedances  $z_{in,i}$  and  $z_{in,j}$  is sought. It is:

$$\frac{v_{3,i}}{v_{3,j}} = \frac{\frac{v_{3,i}}{v_{1,i}}}{\frac{v_{3,j}}{v_{1,j}}} = \frac{A_{1,i} + \frac{B_{1,i}}{Z_{in,i}}}{A_{1,j} + \frac{B_{1,j}}{Z_{in,j}}}$$

However only  $v_4$ ,  $i_4$ ,  $v_1$  and  $i_1$  are accessible, so only the overall network parameters  $A_0$ ,  $B_0$ ,  $C_0$  and  $D_0$  and the input impedance  $z_{in}$  of the digitizer can be measured.

These are related by:

$$\begin{matrix} v_4 \\ i_4 \end{matrix} = \begin{bmatrix} A_0 & B_0 \\ C_0 & D_0 \end{bmatrix} \begin{matrix} v_1 \\ i_1 \end{matrix} = \begin{bmatrix} A_1(A_3 + \frac{B_3}{sM}) + B_3C_1 & B_1(A_3 + \frac{B_3}{sM}) + B_3D_1 \\ A_1(C_3 + \frac{D_3}{sM}) + D_3C_1 & B_1(C_3 + \frac{D_3}{sM}) + D_3D_1 \end{bmatrix} \begin{matrix} v_1 \\ i_1 \end{matrix}$$

$$Z_{in} = \frac{v_1}{i_1}$$

To obtain a ratio of frequency responses for coils  $i$  and  $j$ , the measurable ratio

$$\frac{\frac{v_{4,i}}{v_{1,i}}}{\frac{v_{4,j}}{v_{1,j}}} = \frac{A_{0,i} + \frac{B_{0,i}}{Z_{in,i}}}{A_{0,j} + \frac{B_{0,j}}{Z_{in,j}}},$$

can be reduced approximately to

$$\frac{v_{3,i}}{v_{3,j}} \approx \frac{A_{1,i} + \frac{B_{1,i}}{Z_{in,i}}}{A_{1,j} + \frac{B_{1,j}}{Z_{in,j}}} \cdot \frac{M_j}{M_i} \cdot \frac{A_{3,i}sM_i + B_{3,i}}{A_{3,j}sM_j + B_{3,j}} \quad (\text{B.1})$$

by noting that

$$\left( A_3 + \frac{B_3}{sM} \right) \left( A_1 + \frac{B_1}{Z_{in}} \right) / (B_3 C_1) \approx 100.$$

The terms on the right of Equation B.1 are, from left to right: the ratio of pickup coil voltages that is sought; the ratio of mutual inductances between each pickup coil and its calibrating winding; and the ratio of currents in each calibrating winding. Each of the error quantities is close to 1. The calibration of phase between coils is therefore very accurate.

If a function generator is used to excite the calibrating winding, and the digitizer to measure the coil response,  $v_4$  and  $v_1$  of each coil are measured. The ratio of these measurements, ie  $(v_{4,i}/v_{1,i}) / (v_{4,j}/v_{1,j})$ , for one pair of coils is shown in Figure B-4. If, instead, the measurement is conducted with a network analyzer, the wave components  $v_+$  and  $v_-$  are separately identified, so values for  $i_4$  and  $i_1$  can also be obtained. These can be divided in the same manner as the voltages, using the parameters  $C_0$  and  $D_0$  to find another approximation to the frequency response ratio. In the case of the network analyzer, the two ratios can be compared to improve accuracy.

### **Internal Calibration, directly excited**

The inaccuracy of the ratio of mutual coupling and the ratio of current in each calibrating winding is close to 1 but can be eliminated by applying a voltage directly to the pickup coil. This is not usually possible because the pickup coil is very well shielded, and thus inaccessible. However, if a very short piece of wire separates the pickup coil from a connector, the calibrating signal can be injected at this junction instead. The circuit will then behave essentially as if a voltage was being induced on the pickup coil. Unfortunately it will be inaccurate to the extent that the inductive coupling through the molybdenum tiles and stainless steel shim stock will not be

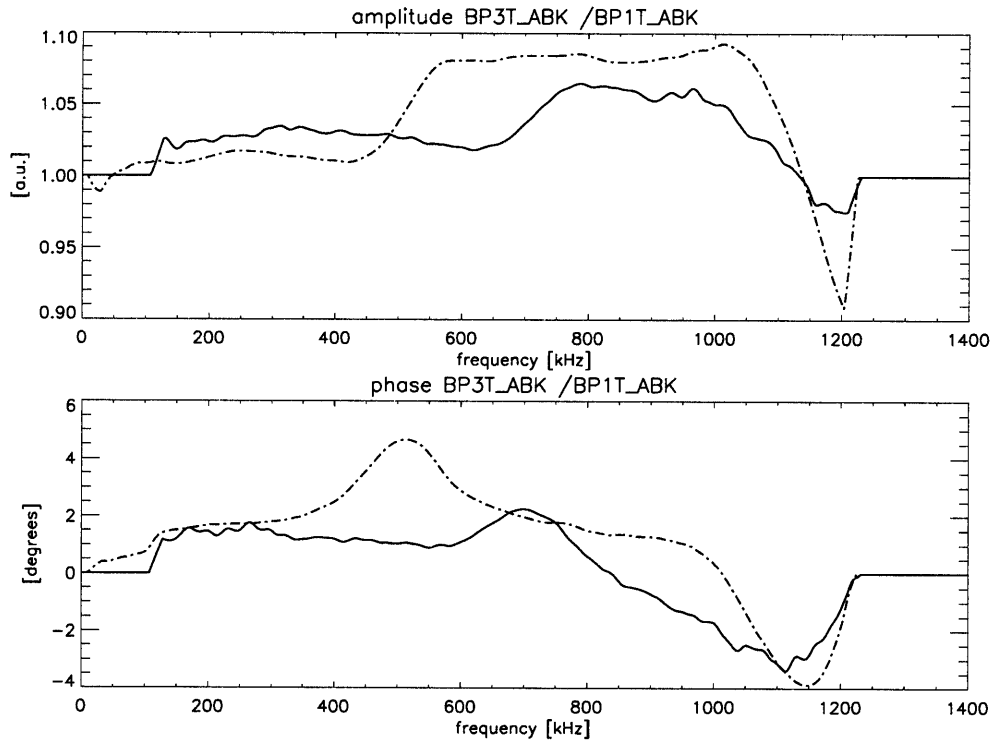


Figure B-4: The frequency response of coil BP3T\_ABK compared to BP1T\_ABK, with a long cable running to the digitizer (dotted line) and a short cable (solid). The short cable increases the frequency of the self-resonance.

measured. However results of this method, when possible, can be compared with the inductively driven method to distinguish the response of the metal surrounding the coils from that of the coils themselves.

# Appendix C

## Test Shot Procedure

```
\HYBRID::TOP.DPCS.LOADABLES.PROCEDURES:TEST_PROS .
```

The amplifiers that power the antennas must also be initialized. This requires turning on the AC power that services the amplifier racks, and the DC power supply in the cell, and enabling the amplifier in the tree by inserting [0.0,2.0] into the following node of the tree:

```
\MAGNETICS::TOP.ACTIVE_MHD.DATA_ACQ.CAMAC:J221:OUTPUT_05:RFENABLE
```

The digitizer should also be set to collect data at the desired rate, which is usually 2.5 MHz.

Finally, test shots can be fired in the absence of a plasma, for example to debug parts of the equipment. Because the DPCS is not accessible to magnetics test shots, the frequency waveform must be preprogrammed into the tree in node:

```
\MAGNETICS::TOP.ACTIVE_MHD.DATA_ACQ.CAMAC:WAVEFORM:CHANNEL_2 .
```

Accordingly, the amplifier must be set to obey local control by setting:

```
\MAGNETICS::TOP.ACTIVE_MHD.DATA_ACQ.CAMAC:J221:OUTPUT_09:HYBRID_LOCAL
```

to [0.0,2.0]. The test shot is executed and assigned the number 4xxx by running

```
/home/snipes/mag/active]\$ IDL> .r active_test
```

```
/home/snipes/mag/active]\$ IDL> init,4xxx
```

```
/home/snipes/mag/active]\$ IDL> trigger
```

```
/home/snipes/mag/active]\$ IDL> store
```

Test shot data are temporarily stored in a 'test' directory that is cleaned periodically.

However, they can be copied into the 'saved' tree for permanent archiving by:

1. logging on to alldata
2. copying the `.characteristics`, `.datafile` and `.tree` files corresponding to the test shot of interest from `/cmod/trees/test/magnetics` to `/cmod/trees/saved/magnetics`
3. renaming the new files with a proper date-sequence shot number in the 400's.



# Bibliography

- [1] M. Garcia-Munoz, H.-U. Fahrbach, H. Zohm, and the ASDEX Upgrade Team. Scintillator based detector for fast-ion losses induced by magnetohydrodynamic instabilities in the ASDEX upgrade tokamak. *Review of Scientific Instruments*, 80(5):053503–9, May 2009.
- [2] H.H. Duong et al. Loss of energetic beam ions during TAE instabilities. *Nuclear Fusion*, 33(5):749+, May 1993.
- [3] R. B. White, E. Fredrickson, D. Darrow, M. Zarnstorff, R. Wilson, S. Zweben, K. Hill, Yang Chen, and Guoyong Fu. Toroidal alfvén eigenmode-induced ripple trapping. *Physics of Plasmas*, 2(8):2871–2873, 1995.
- [4] W.W. Heidbrink et al. An Alfvén eigenmode similarity experiment. *Plasma Physics and Controlled Fusion*, 45:983–997, 2003.
- [5] G.Y. Fu and C.Z. Cheng. Excitation of high-n toroidicity-induced shear Alfvén eigenmodes by energetic particles and fusion alpha particles in tokamaks. *Phys. Fluids B*, 4(11):3722+, November 1992.
- [6] J.A. Snipes, N.N. Gorelenkov, and J.A. Sears. A comparison of measured and calculated toroidal Alfvén eigenmode damping rates in alcator C-Mod. *Nuclear Fusion*, 46(12):1036+, December 2006.
- [7] N.N. Gorelenkov, H.L. Berk, and R.V. Budny. Beam anisotropy effect on Alfvén eigenmode stability in ITER-like plasmas. *Nuclear Fusion*, 45(4):226–237, 2005.

- [8] A. Klein, H. Carfantan, D. Testa, A. Fasoli, J. Snipes, and JET EFDA Contributors. A sparsity-based method for the analysis of magnetic fluctuations in unevenly-spaced mirnov coils. *Plasma Physics and Controlled Fusion*, 50(12):125005, 2008.
- [9] N.N. Gorelenkov, H.L. Berk, R. Budny, C.Z. Cheng, G.-Y. Fu, W.W. Heidbrink, G.J. Kramer, D. Meade, and R. Nazikian. Study of thermonuclear Alfvén instabilities in next step burning plasma proposals. *Nuclear Fusion*, 43(7):594–605, 2003.
- [10] D. Testa, A. Fasoli, and E. Solano. Diagnosis and study of Alfvén eigenmodes stability in JET (invited). *Rev. Sci. Inst*, 74(3):1694, March 2003.
- [11] D. Borba et al. Destabilization of TAE modes using ICRH in ASDEX upgrade. *Plasma Physics and Controlled Fusion*, 46(5):809833, 2004.
- [12] J.A. Snipes et al. Initial active MHD spectroscopy experiments exciting stable Alfvén eigenmodes in alcator C-Mod. *Plasma Physics and Controlled Fusion*, 46(4):611+, April 2004.
- [13] K. L. Wong et al. Evolution of toroidal Alfvén eigenmode instability in tokamak fusion test reactor. *Physics of Plasmas*, 4(2):393404, February 1997.
- [14] R.F. Heeter, A.F. Fasoli, and S.E. Sharapov. Chaotic regime of Alfvén eigenmode wave-particle interaction. *Phys. Rev. Lett.*, 85(15):3177–3180, October 2000.
- [15] W. W. Heidbrink et al. An investigation of beam driven Alfvén instabilities in the DIII-D tokamak. *Nuclear Fusion*, 31(9):16351648, 1991.
- [16] H.L. Berk, B.N. Breizman, and M.S. Pekker. Simulation of Alfvén-wave-resonant-particle interaction. *Nuclear Fusion*, 35(12):1713–1720, 1995.
- [17] A. Fasoli et al. Direct measurement of the damping of Toroidicity-Induced Alfvén eigenmodes. *Phys. Rev. Lett.*, 75(4):645648, July 1995.

- [18] H. Alfvén. Existence of Electromagnetic-Hydromagnetic waves. *Nature*, 150:405–406, 1942.
- [19] Jeffrey P Freidberg. *Plasma Physics and Fusion Energy*. Cambridge University Press, Cambridge, 2007.
- [20] J.P. Freidberg. *Ideal Magnetohydrodynamics*. Plenum Press, 1987.
- [21] N.F. Cramer. *The Physics of Alfvén Waves*. Wiley-VCH, 2001.
- [22] J. P Goedbloed and Stefaan Poedts. *Principles of Magnetohydrodynamics: With Applications to Laboratory and Astrophysical Plasmas*. Cambridge University Press, Cambridge, UK, 2004.
- [23] Philip Morse and Herman Feshbach. *Methods of theoretical physics*. McGraw-Hill, New York, 1953.
- [24] Carl M Bender and Steven A Orszag. *Advanced Mathematical Methods for Scientists and Engineers I: Asymptotic Methods and Perturbation Theory*. Springer, New York, 1999.
- [25] Liu Chen and Akira Hasegawa. Plasma heating by spatial resonance of Alfvén wave. *Phs. Fluids*, 17(7):1399–1403, July 1974.
- [26] J. Kappraff and J. Tataronis. Resistive Effects On Alfvén Wave Heating. *Journal of Plasma Physics*, 18(OCT):209–226, 1977.
- [27] W.E. Boyce and R.C. DiPrima. *Elementary differential equations and boundary value problems*. Wiley, Hoboken, NJ, 8th edition, 2005.
- [28] A. Hasegawa and C. Uberoi. *The Alfvén Wave*, pages 33–43. Unites States DOE, 1982.
- [29] L. Villard and J. Vaclavik. Alfvén frequency modes and global Alfvén eigenmodes. *Nuclear Fusion*, 37(3):351–360, 1997.

- [30] L. Villard and J. Vaclavik. On the spectrum of  $n=0$  Alfvén eigenmodes. *Proceedings 1996 Int. Conf. on Plasma Physics*, 1996.
- [31] K. Appert et al. Excitation of global eigenmodes of the Alfvén wave in tokamaks. *Plasma Physics*, 24(9):1147+, 1982.
- [32] O. Pogutse and E. Yurchenko. Energy Principle And Kink Instability In a Toroidal Plasma With Strong Magnetic-Field. *Nuclear fusion*, 18(12):1629–1638, 1978.
- [33] D.A. D’Ippolito and J.P. Goedbloed. Mode coupling in a toroidal, sharp-boundary plasma - i. weak-coupling limit. *Plasma Physics*, 22:1091–1107, 1980.
- [34] Pochi Yeh. *Optical waves in layered media*. Wiley series in pure and applied optics. Wiley, New York, 1988.
- [35] C. Kittel. *Introduction to Solid State Physics*. John Wiley, New York, 8th edition, 2005.
- [36] C. Z. Cheng and M. S. Chance. Low- $n$  shear Alfvén spectra in axisymmetric toroidal plasmas. *Physics of Fluids*, 29(11):36953701, November 1986.
- [37] C. E. Kieras and J. A. Tataronis. The shear Alfvén continuum in the low beta limit. *Physics of Fluids*, 25(7):1228–1230, July 1982.
- [38] R. Betti and J.P.Freidberg. Ellipticity induced Alfvén eigenmodes. *Phys. Fluids B*, 3(8):1865+, August 1991.
- [39] C.E. Kieras and J.A. Tataronis. The shear Alfvén continuous spectrum of axisymmetric toroidal equilibria in the large aspect ratio limit. *J. Plasma Physics*, 28(3):395–414, 1982.
- [40] C. Z. Cheng, Liu Chen, and M. S. Chance. High- $n$  ideal and resistive shear Alfvén waves in tokamaks. *Annals of Physics*, 161(1):2147, April 1985.

- [41] G.Y. Fu and J.W. Van Dam. Stability of the global Alfvén eigenmode in the presence of fusion alpha particles in an ignited tokamak plasma. *Phys. Fluids B*, 1(12):2404+, December 1989.
- [42] F. Zonca. *Continuum Damping of Toroidal Alfvén Eigenmodes in finite- $\beta$  tokamak Equilibria*. PhD thesis, Princeton University, June 1993.
- [43] G.Y. Fu and J.W. Van Dam. Excitation of the toroidicity-induced shear Alfvén eigenmode by fusion alpha particles in an ignited tokamak. *Phys. Fluids B*, 1(10):1949+, October 1989.
- [44] F. Zonca et al. Theory of continuum damping of toroidal Alfvén eigenmodes in finite-beta tokamaks. *Physics of Fluids B*, 5(10):3668+, October 1993.
- [45] F. Zonca and L. Chen. Resonant damping of toroidicity-induced Shear-Alfvén eigenmodes in tokamaks. *Phys. Rev. Lett.*, 68(5):592+, February 1992.
- [46] M.N. Rosenbluth et al. Continuum Damping Of High-Mode-Number Toroidal Alfvén Waves. *Phys. Rev. Lett.*, 68(5):596+, February 1992.
- [47] H.L. Berk et al. Continuum Damping Of Low-n Toroidicity-Induced Shear Alfvén Eigenmodes. *Phys. Fluids B*, 4(7):1806, July 1992.
- [48] S. Poedts et al. Damping of global Alfvén waves in tokamaks due to resonant absorption. *Plasma Physics and Controlled Fusion*, 34(8):1397+, 1992.
- [49] L. Villard et al. Geometrical land profile effects on toroidicity And Ellipticity Induced Alfvén Eigenmodes. *Nuclear Fusion*, 32(10):1695+, October 1992.
- [50] G.J. Kramer et al. Observation of odd toroidal Alfvén eigenmodes. *Phys. Rev. Lett.*, 92(1):015001, 2004.
- [51] R. Betti and J.P. Freidberg. Stability of Alfvén gap modes in burning plasmas. *Phys. Fluids*, B4(6):1465+, June 1992.

- [52] G.Y. Fu et al. Analysis of alpha particle-driven toroidal Alfvén eigenmodes in tokamak fusion test reactor deuterium-tritium experiments. *Physics of Plasmas*, 3(11):4036+, November 1996.
- [53] R.R. Mett and S.M. Mahajan. Kinetic theory of toroidicity-induced Alfvén eigenmodes. *Phys. Fluids B*, 4(9):2885+, September 1992.
- [54] H. L. Berk, R. R. Mett, and D. M. Lindberg. Arbitrary mode number boundary-layer theory for nonideal toroidal Alfvén modes. *Physics of Fluids B*, 5(11):39693996, November 1993.
- [55] J. Candy and M.N. Rosenbluth. Nonideal theory of toroidal Alfvén eigenmodes. *Physics of Plasmas*, 1(2):356+, February 1994.
- [56] N.N. Gorelenkov and S.E. Sharapov. On the collisional damping of TAE-modes on trapped electrons in tokamaks. *Phys. Scr.*, 45:163+, 1992.
- [57] J. Candy and M.N. Rosenbluth. Alpha-Particle-Driven Nonideal Toroidal Alfvén Eigenmodes. *Plasma Physics and Controlled Fusion*, 35(8):957, August 1993.
- [58] A.B. Mikhailovsky and I.G. Shukhman. Effect Of Trapped Electrons On Alfvén Waves In Tokamak. *Zhurnal Eksperimentalnoi I Teoreticheskoi Fiziki*, 71(11):1813+, 1976.
- [59] M.N. Rosenbluth and P.H. Rutherford. Excitation of Alfvén waves by High-Energy ions in a tokamak. *Phys. Rev. Lett.*, 34(23):1424+, June 1975.
- [60] K.T. Tsang, D.J. Sigmar, and J.C. Whitson. Destabilization of low mode number Alfvén modes in a tokamak by energetic or alpha-particles. *Physics of Fluids*, 24(8):1508+, 1981.
- [61] G.Y. Fu and C.Z. Cheng. Theory of a high-n toroidicity-induced shear Alfvén eigenmode in tokamaks. *Phys. Fluids B*, 2(5):985+, May 1990.

- [62] F. Zonca, S. Briguglio, G. Fogaccia, and G. Vlad. Alfvén instabilities effects on energetic particles. 1999.
- [63] F. Zonca and L. Chen. Destabilization of energetic particle modes by localized particle sources. *Physics of Plasmas*, 7(11):46004608, November 2000.
- [64] L. Chen et al. ? In *Proceedings of the 12th International Conference on Plasma Physics and Controlled Nuclear Fusion Research*, volume 2, page 77, Vienna, 1989.
- [65] L. Chen. Theory of fusion plasmas. In J. Vaclavik, F. Troyon, and E. Sindoni, editors, *Theory of Fusion Plasmas*, pages 327+, Bologna, 1989.
- [66] C.Z. Cheng, G.Y. fu, and J.W. Van Dam. Theory of fusion plasmas. In J. Vaclavik, F. Troyon, and E. Sindoni, editors, *Theory of Fusion Plasmas*, pages 259+, Bologna, 1989.
- [67] H. Biglari, F. Zonca, and L. Chen. On resonant destabilisation of toroidal alfvén eigenmodes by circulating and trapped energetic ions/alpha particles in tokamaks. *Physics of Fluids B*, 4(8):23852388, August 1992.
- [68] Y.M. Li, S.M. Mahajan, and D.W. Ross. Destabilization Of Global AlfvN Eigenmodes And Kinetic AlfvN Waves By Alpha-Particles In Tokamak Plasma. *Phys. Fluids*, 30(5):1466+, May 1987.
- [69] R. Betti and J.P.Freidberg. A stability criterion for energetic particle-Alfvén modes. *Phys. Fluids B*, 3(3):538+, March 1991.
- [70] C.Z. Cheng. Alpha particle destabilization of the toroidicity-induced Alfvén eigenmodes. *Phys. Fluids B*, 3(9):2463+, September 1991.
- [71] J.A. Snipes et al. Active and fast particle driven Alfvén eigenmodes in alcator C-Mod. *Physics of Plasmas*, 12(5), May 2005.
- [72] F. Zonca et al. Energetic particle mode stability in tokamaks with hollow q-profiles. *Physics of Plasmas*, 9(12):4939+, December 2002.

- [73] R.B. White. *Theory of Tokamak Plasmas*. North-Holland, New York, 1989.
- [74] A. Fasoli et al. Overview of Alfvén eigenmode experiments in JET. *Nuclear Fusion*, 35(12):1485+, 1995.
- [75] N.N. Gorelenkov et al. Stability properties of toroidal Alfvén modes driven by fast particles. *Nuclear Fusion*, 40(7):1311+, July 2000.
- [76] R. Aymar et al. Overview of ITER-FEAT - the future international burning plasma experiment. *Nuclear Fusion*, 41(10):1301+, October 2001.
- [77] K. L Wong. A review of Alfvén eigenmode observations in toroidal plasmas. *Plasma Phys. Control. Fusion*, 41:R1–R55, 1999.
- [78] D.J. Sigmar et al. MIT plasma fusion center report. 1989.
- [79] D.J. Sigmar. Alpha-Particle Losses From Toroidicity-Induced Alfvén Eigenmodes .2. Monte-Carlo Simulations And Anomalous Alpha-Loss Processes. *Phys. Fluids B*, 4(6):1506+, June 1992.
- [80] C.Z. Cheng. Kinetic Extensions Of Magnetohydrodynamics For Axisymmetrical Toroidal Plasmas. *Physics Reports*, 211(1):1–51, February 1992.
- [81] C.Z. Cheng and M.S. Chance. NOVA - a nonvariational code for solving the MHD stability of axisymmetrical toroidal plasmas. *J. Comp. Phys.*, 71(1):124–146, July 1987.
- [82] N.N. Gorelenkov. Fast particle finite orbit width and larmor radius effects on low-n toroidicity induced Alfvén eigenmode excitation. *Physics of Plasmas*, 6(7):2802+, July 1999.
- [83] S.E. Sharapov, A.B. Mikhailovskii, and G.T.A. Huysmans. Effects of nonresonant hot ions with large orbits on Alfvén cascades and on magnetohydrodynamic instabilities in tokamaks. *Physics of Plasmas*, 11(5):2286+, May 2004.



- [84] G.T.A. Huysmans et al. Modeling of diamagnetic stabilization of ideal magnetohydrodynamic instabilities associated with the transport barrier. *Physics of Plasmas*, 8(10):4292, October 2001.
- [85] A. B. Mikhailovskii, G. T. A. Huysmans, W. O. K. Kerner, and S. E. Sharapov. Optimization of computational MHD Normal-Mode analysis for tokamaks. *Plasma Physics Reports*, 23(10):844857, 1997.
- [86] R.J. Hawryluk. *Physics of Plasmas Close Thermonuclear Conditions*, volume 1, pages 19–46. CEC, Brussels, 1980.
- [87] R.J. Goldston et al. New Techniques For Calculating Heat And Particle Source Rates Due To Neutral Beam Injection In Axisymmetric Tokamaks. *J. Comp. Phys.*, 43(1):61+, 1981.
- [88] J. Ongena, M. Evrard, and D. McCune. Numerical transport codes. *Fusion Science and Tech.*, 49(2T):337+, February 2006.
- [89] PPPL. <http://w3.pppl.gov/transp/refs>. 1998.
- [90] M. Brambilla. Numerical simulation of ion cyclotron waves in tokamak plasmas. *Plasma Physics and Controlled fusion*, 41(1):1–34, 1999.
- [91] M. Brambilla. A Full-Wave code for ion cyclotron waves in toroidal plasmas. Technical Report 5/66, Max-Planck-Institut fur Plasmaphysik, Garching, 1996.
- [92] E.F. Jaeger. Sheared poloidal flow driven by mode conversion in tokamak plasmas. *Phys. Rev. Lett.*, 90(19):195001, May 2003.
- [93] R.W. Harvey and M.G.McCoy. The CQL3D code. In *Proceedings of the IAEA Technical Committee Meeting on Numerical Modeling, Montreal*, page 489, Vienna, 1992.
- [94] E. Nelson-Melby et al. Experimental observations of mode-converted ion cyclotron waves in a tokamak plasma by phase contrast imaging. *Phys. Rev. Lett.*, 90(15):155004, April 2003.

- [95] K. L. Wong et al. Excitation of toroidal Alfvén eigenmodes in TFTR. *Phys. Rev. Lett.*, 66(14):18741877, April 1991.
- [96] M. Saigusa et al. Investigation of high-n TAE excited by minority-ion cyclotron heating in JT-60U. *Plasma Physics and Controlled Fusion*, 37:295313, 1995.
- [97] A. Weller et al. Neutral beam driven global Alfvén eigenmodes in the wendelstein W7-AS stellarator. *Phys. Rev. Lett.*, 72(8):1220+, February 1994.
- [98] W.W. Heidbrink. Observation Of Beta-Induced Alfvén Eigenmodes In The DIII-D Tokamak. *Phys. Rev. Lett.*, 71(6):855+, August 1993.
- [99] A.D. Turnbull et al. Global Alfvén modes - theory and experiment. *Physics of Fluids B*, 5(7):2546+, July 1993.
- [100] J.M. Moret. Magnetic measurements on the TCV tokamak. *Rev. Sci. Inst.*, 69(6):2333–2348, June 1998.
- [101] K. L. Wong et al. First evidence of collective alpha particle effect on toroidal Alfvén eigenmodes in the TFTR D-T experiment. *Phys. Rev. Lett.*, 76(13):2286+, March 1996.
- [102] M. Saigusa et al. Systematic study of toroidicity-induced alfvén eigenmodes at low-q discharges in JT-60U. *Plasma Physics and Controlled Fusion*, 40(9):1647+, September 1998.
- [103] L.G. Eriksson et al. Evidence for a Wave-Induced particle pinch in the presence of toroidally asymmetric ICRF waves. *Phys. Rev. Lett.*, 1998.
- [104] W.W. Heidbrink et al. High harmonic ion cyclotron heating in DIII-D: beam ion absorption and sawtooth stabilization. *Nuclear Fusion*, 39(10):1999, October 1999.
- [105] S. Bernabei et al. Nature of monster sawteeth and their relationship to Alfvén instabilities in tokamaks. *Phys. Rev. Lett.*, 84(6):1212+, February 2000.

- [106] F. Porcelli et al. Fast particle stabilization. *Plasma Physics and Controlled Fusion*, 33(13):1601+, November 1991.
- [107] S. E. Sharapov et al. Monitoring Alfvén cascades with interferometry on the JET tokamak. *Physical Review Letters*, 93(16):165001–1165001–4, October 2004.
- [108] G.A. Collins et al. Central mass and current-density measurements in tokamaks using the discrete alfvén-wave spectrum. *Plasma Physics and Controlled Fusion*, 29(3):323, March 1987.
- [109] G.A. Collins et al. The alfvén-wave spectrum as measured on a tokamak. *Physics of fluids*, 29(7):2260, July 1986.
- [110] P. Descamps et al. Determination of central q and effective mass on TEXTOR based on discrete alfvén-wave (DAW) spectrum measurements. *Physics Letters A*, 143(6):311+, 1990.
- [111] J.M. Moret. Fitting of transfer functions to frequency response measurements. Technical report, LPR, December 1994.
- [112] G.T.A Huysmans et al., editors. *MHD Spectroscopy Modelling the Excitation of TAE Modes by an Excited Antenna*. Europhysics Conference Abstracts. Geneva, June 1993.
- [113] Villard et al., editors. *Alfvén Gap modes in elongated plasmas*. Europhysics Conference Abstracts. Geneva, June 1993.
- [114] D. Testa and A. Fasoli. The effect of plasma shaping on the damping of low n Alfvén eigenmodes in JET tokamak plasmas. *Nuclear Fusion*, 41(7):809+, July 2001.
- [115] A. Fasoli et al. MHD spectroscopy. *Plasma Physics and Controlled Fusion*, 44:B159–B172, 2002.

- [116] D. Testa et al. Alfvén mode stability and wave-particle interaction in the JET tokamak: prospects for scenario development and control schemes in burning plasma experiments. *Plasma Physics and Controlled Fusion*, 46(7):S59+, July 2004.
- [117] A. Fasoli et al. Fast particle-wave interaction in the Alfvén frequency range on the joint european torus tokamak. *Physics of Plasmas*, 7(5):1816, May 2000.
- [118] A. Fasoli et al. Alfvén eigenmode experiments in tokamaks and stellarators. *Plasma Physics and Controlled Fusion*, 39:B287, 1997.
- [119] D. Testa et al. Experimental test of damping models for n=1 toroidal Alfvén eigenmodes in JET. *Nuclear Fusion*, 43(6):479, June 2003.
- [120] D. Testa, C. Boswell, and A. Fasoli. Experimental study of the dependence of the damping rate of n=1 TAEs on the on-axis safety factor and toroidal rotation shear. *Nuclear Fusion*, 45(8):907+, August 2005.
- [121] W. Burke et al. Broadband amplifiers for the active MHD diagnostic on alcator C-Mod. In *Fusion Engineering, 2003. 20th IEEE/NPSS Symposium on, ?*, pages 363–366. IEEE, October 2003.
- [122] J.A. Snipes et al. Moderate toroidal mode number Alfvén eigenmode damping rate measurements on alcator C-Mod. In *33rd Conference on Plasma Physics*, 2006.
- [123] W. Burke et al. Real time control of the active MHD diagnostic on alcator C-Mod. *SOFE*, 21, 2005.
- [124] A. Oppenheim, A. Willsky, and H. Nawab. *Signals and Systems*. Prentice Hall, 1997.
- [125] J.S. Bendat and A.G. Piersol. *Random Data Analysis and Measurement Procedures*. Wiley Series in Probability and Statistics. John Wiley & Sons, Inc, New York, 3rd edition, 2000.

- [126] J.P. Goedbloed et al. MHD spectroscopy: Free boundary modes (ELMs) & external excitation of TAE modes. *Plasma Physics and Controlled Fusion*, 35:B277+, 1993.
- [127] V. Tang et al. Experimental and numerical characterization of ion-cyclotron heated protons on the alcator C-Mod tokamak. *Plasma Physics and Controlled Fusion*, (49):873–904, May 2007.
- [128] J.S. Bendat and A.G. Piersol. *Engineering Applications of Correlation and Spectral Analysis*. John Wiley & Sons, 1980.
- [129] J.R. Taylor. *An Introduction to Error Analysis: The study of Uncertainties in Physical Measurements*, volume 2nd. University Science Books, 1997.
- [130] P.R. Bevington and D.K. Robinson. *Data Reduction and Error Analysis for the Physical Sciences*. McGraw Hill, 3rd edition, 2003.
- [131] R.J. Sheppard. The least-squares analysis of complex weighted data with dielectric applications. *J. Phys. D: Appl. Phys.*, 6:790–794, 1973.
- [132] R.J. Sheppard, B.P. Jordan, and E.H. Grant. Least squares analysis of complex data with applications to permittivity measurements. *J. Phys. D: Appl. Phys.*, 3(11):1759–1764, November 1970.
- [133] R.F. Heeter et al. Fast magnetic fluctuation diagnostics for Alfvén eigenmode and magnetohydrodynamics studies at the joint european torus. *Review of Scientific Instruments*, 71(11):4092–4106, November 2000.
- [134] William Strunk and E. B White. *The Elements of Style*. Allyn and Bacon, Boston, 4th ed edition, 2000.